*Supplementary Material to accompany:*

# Unified Maxwell-Stefan description of binary mixture diffusion in *micro*- and *meso*- porous materials

**R. Krishna\*, J.M. van Baten**

Van 't Hoff Institute for Molecular Sciences, University of Amsterdam, Nieuwe Achtergracht 166,

1018 WV Amsterdam, The Netherlands

CORRESPONDING AUTHOR *Tel +31 20 257007; Fax: + 31 20 5255604;

email: r.krishna@uva.nl

# 1. Zeolite Structures

Table 1 gives the characteristic sizes of channels or windows for the variety of zeolite structures investigated. The crystallographic data are available on the zeolite atlas website.[1]. The zeolite lattices are assumed to be rigid during simulations. $CH_4$ molecules are described with a united atom model, in which each molecule is treated as a single interaction center [2].The interaction between adsorbed molecules is described with Lennard-Jones terms. The Lennard-Jones parameters for $CH_4$-zeolite interactions are taken from Dubbeldam et al.[3]. The force fields for Ne and Ar are taken from the paper by Skoulidas and Sholl[4]. The force field for Kr is from Talu and Myers [5]. Table 2  summarizes the information on the Lennard-Jones parameters for atom-atom, and atom-zeolite interactions for C1, Ar, Ne, and Kr.  Some simulations are also reported for alkane mixtures containing ethane (C2) and propane (C3).  For simulations with linear alkanes with two or more C atoms, the beads in the chain are connected by harmonic bonding potentials. A harmonic cosine bending potential models the bond bending between three neighboring beads, a Ryckaert-Bellemans potential controls the torsion angle. The beads in a chain separated by more than three bonds interact with each other through a Lennard-Jones potential; see schematic in **Figure 1**. The force fields of Dubbeldam et al.[3] was used for the variety of potentials. The Lennard-Jones potentials are shifted and cut at 12 Å. The zeolite frameworks were considered to be rigid in all the simulations.

Most of the simulations were conducted for Ne-Ar, C1-Ar, C1-C2, and C1-C3 mixtures and unary diffusion of C1, Ar, and Ne. Additional simulation results are also reported here in the Supplementary material for pure components $CO_2$, $N_2$, Kr, He, $CF_4$, $H_2$, and equimolar binary mixtures C1- $CO_2$, $CO_2 -$ Ar, $CO_2 - H_2$, $CO_2 - N_2$, Ne- $CO_2$, C1- $N_2$, and C1- $H_2$.  The $CF_4$ force field is from Skoulidas and Sholl [6]. The remaining force fields and the simulation data are those contained in our previous publications [7-13]. These results are not discussed in detail the main text of this publication but are presented in the Supplementary material in order to emphasize the fact that the conclusions drawn in the paper are valid for a wider variety of guest species as well.  The Supplementary material includes some additional simulations for LTL (1D channels), ISV (intersecting channels), and ERI (cages separated by

narrow windows). These data are not included in the main text of the paper and the results are presented here as additional checks to demonstrate that the conclusions drawn in the main paper are valid also for these structures.

Most of the simulations were carried out with all-silica zeolites. A few simulations were also carried out to investigate the influence of cations on C1, C2, C3, C1-C2, and C1-C3 diffusion in FAU, MFI, and LTA zeolites. The following structures were investigated: NaX (106 Si, 86 Al, 86 Na$^+$, Si/Al=1.23), NaY (144 Si, 48 Al, 48 Na$^+$, Si/Al=3), LTA-5A (96 Si, 96 Al, 32 Na$^+$, 32 Ca$^{++}$, Si/Al=1), LTA-4A (96 Si, 96 Al, 96 Na$^+$, Si/Al=1), and MFI (with (Si=94, Al=2, 2Na$^+$); (Si=92, Al=4, 4Na$^+$); (Si=90, Al=6, 6Na$^+$); (Si=88, Al=8, 8Na$^+$)). The data on the number of cations per unit cell, along with the pore volume fraction data are given in Table 3. From Table 3 we note that the presence of cations reduces the accessible pore volume. The force fields information for the simulations with cations are taken from Calero et al. [14-16]. For determination of the pore volumes the Lennard-Jones parameters for interactions of the He probe atoms with Ca$^{++}$ and Na$^+$ are specified in Table 4. CBMC simulations were carried out to determine the adsorption isotherms in these structures, along with MD simulations for diffusion. In the MD simulations the cations were allowed to move within the framework and both Lennard-Jones and Coulombic interactions are taken into consideration; see schematic sketch in **Figure 2**.

The Dubbeldam et al. [3] and Calero et al. [14-16] force fields we have used for zeolites, including cations in some cases, has been validated by comparison with experimental data mentioned in these papers; see also the Supplementary materials accompanying our earlier publications [8, 10, 12, 17-19].

## 2. MOF Structures

The structural information for the metal organic frameworks (MOFs) have been taken from various publications: Cobalt Formate (Co-FA) from Li et al. [20]; Manganese Formate (Mn-FA) from Dybtsev et al.[21]; Zn(bdc)dabco from Bárcia et al.[22] and Lee et al. [23]; Co(bdc)dabco from Wang et al.[24]; MIL-47 from Alaerts et al. [25], Finsy et al. [26], and Barthelet et al. [27]; MIL-53 (Fe) from

Horcajada et al [28]; Zn(tbip) from Pan et al.[29, 30]. For IRMOF-1 simulations we used the structural data published by Dubbeldam et al. [31, 32]. The structural information for CuBTC simulations have been taken from Chui et al. [33] and Yang and Zhong [34]. The crystal structure of Chui et al. [33] includes axial oxygen atoms weakly bonded to the Cu atoms, which correspond to water ligands. Our simulations have been performed on the dry CuBTC with these oxygen atoms removed.

The structure data files for all MOFs we investigated are available on our website[35].

Table 5 gives information on the unit cell dimensions, and pore volume fractions. Table 6 summarizes the channel dimensions of the MOF structures investigated.

For the guest species, C1, Ar, Kr, and Ne, the atom-atom interaction parameters are the same as those used for zeolites, and listed in Table 2.

The metal organic framework structures were considered to be rigid in the simulations. For the atoms in the guest metal organic framework, the generic UFF [36] was used. The DREIDING [37] force fields was used for the organic linker atoms. The Lennard-Jones parameters for MOF atoms are summarized in Table 7. The Lorentz-Berthelot mixing rules were applied for calculating $\sigma$ and $\varepsilon/k_B$ for guest-host interactions.

The force fields for MOFs have not been subjected to extensive testing against experimental data as is the case with zeolites. Some indications of the accuracy of the force fields used in the current study can be gleaned by comparing simulated isotherms for methane in CuBTC, Zn(bdc)dabco, and Co(bdc)dabco with the published experimental data [24, 38]; these comparisons are presented in the accompanying Figures for each of these three MOFs.

Some simulation results are also reported here in the Supplementary material for pure components $CO_2$, Kr, and equimolar binary mixture C1- $CO_2$. The force fields for interaction of $CO_2$-$CO_2$ are those from our earlier work. [13]. The Lorentz-Berthelot mixing rules were used to determine the interactions of $CO_2$ with the constituent atoms in the MOF frameworks.

The simulation data for MIL-53 (Fe) presented here in the Supplementary material is not discussed in the main text; the results are entirely analogous to those for MIL-47.

# 3. COF Structures

Three different 3D covalent organic framework (COF) structures were investigated: COF-102, COF-103, and COF-108; the structural information is from El-Kaderi et al.[39] and Babarao and Jiang [40]. Table 8 gives information on the unit cell dimensions, and pore volume fractions. Table 9 summarizes the channel dimensions of the COF structures. The structure data files we used in our simulations are available on our website[35].

For the guest species, C1, Ar, Ne, and Kr the atom-atom interaction parameters are the same as those used for zeolites, and listed in Table 2.

For the atoms in the guest covalent organic framework, the generic UFF [36] was used. The DREIDING [37] force fields was used for the organic linker atoms. The Lennard-Jones parameters for MOF atoms are summarized in Table 7. The Lorentz-Berthelot mixing rules were applied for calculating $\sigma$ and $\varepsilon/k_B$ for guest-host interactions.

# 4. Cylindrical silica pores

For the 1, 1.5, 2, 3, 4, 5.8, 7.6, and 10 nm pore sizes, some of the data have been taken from our previous publication [41]. These data are also analysed and presented in a manner that is consistent with the present publication. Additional simulations were carried out with pores of 0.6, 0.75, 20 and 30 nm size. The silica structures have been prepared using a method based on Coasne et al.[42]. An initial $\beta$-cristobalite (unit cell of 8 Si and 16 O atoms, at glass density of 2200 kg/m3, with a box size of 7.132 Å) structure was considered. The total number of $\beta$-cristobalite unit cells in the complete box was determined by a minimum of 24 Å in the z-direction, and a minimum of 24 Å plus target pore diameter in the remaining two directions. A cylindrical cavity was cut out of the initial geometry. Subsequently, all Si atoms that was not bound to 4 O atoms were removed. Any non-bound O atoms were removed after that. This causes singly bound O atoms to remain in the structure. Half of these need to be removed to ensure electro-neutrality of the system. Pairs of singly-bound O-atoms were detected for which the O-O distance is less than 2.7 Å. These combinations where replaced by a single O atom to form a Siloxane

bridge. The single O atom was placed at the geometric mean location of the two removed O atoms. Half of the remaining singly bound O atoms were removed at random, introducing one bond defect per O atom. Of the remaining structure, all atoms were displaced on a random sphere with 0.7 Å radius to form the amorphous structure. The structure data files we used in our simulations are available on our website[35].

The interaction between the guest molecules C1 and Ar and the silica surface is assumed to be dominated by interactions between guest molecules and the O atoms in the silica. The same Lennard-Jones parameters were used as for zeolites, and these are listed in Table 10.

For cylindrical pores of 1.5 nm, 2 nm, and 3 nm silica pore diameters we also carried out a sensitivity analysis by varying the Lennard-Jones energy interaction parameter $\varepsilon/k_B$ for methane with the O atoms of the silica surface. Table 11 specifies the force fields used in the sensitivity analysis. The pure fluid phase diffusivity $Đ_{ii,fl}$ was also determined for each of the five cases, for comparison with the corresponding $Đ_{ii}$ values inside the pore.

Furthermore, for the 2 nm, and 3 nm cylindrical silica pores, we carried out simulations at a variety of temperatures to determine the zero-loading diffusivity value $Đ_i(0)$, for comparison with the Knudsen formula.

# 5. Determination of pore volume fraction

The pore volume is determined using a simulation of a single helium molecule at the reference temperature $T$ [40, 43, 44]

$$V_{pore} = \frac{1}{m} \int_0^{V_{pore}} \exp\left(-\frac{U(\mathbf{r})}{k_B T}\right) d\mathbf{r} \tag{1}$$

where $U$ is the interaction energy between a single helium atom and the framework, and $m$ is the mass of the framework. The pore volume can be readily computed from Monte Carlo sampling using Widom particle insertion [45]. Basically, the average Boltzmann factor associated with the random insertion of a probe molecule is computed. This value is averaged over all generated trial positions. In equation (1)

the integration is over the entire mass of the sample and yields the value of the accessible pore volume per unit mass of the framework; the units of $V_{pore}$ are m$^3$/kg, or in more commonly used units mL/(g framework). The volume fraction, $\phi$, is then given by $V_{pore}/V_{total}$ where $V_{total}$ is the total volume of the unit cell. Usually, a reference temperature of 298.15 K is chosen in experiment for the experimental determination of the helium void volume; this value is also used in the simulations.

The force field for He-He interactions are taken from Table 1 of Talu and Myers [46]; these are listed also in Table 4. For zeolites the He-O interaction parameters were also taken from this Table 1. We should mention here that the force field for He of Talu and Myers [46] is not the same as that in Skoulidas and Sholl[4]; in particular there are significant differences in the energy parameter $\varepsilon/k_B$. We had earlier used the Skoulidas force field to simulate diffusion of He in a variety of zeolites [8]. For determination of the pore volume fraction we have switched to the Talu and Myers force field parameters that has been tuned to represent experimental data on pore volumes in MFI.

For MOFs, the interaction between He and the atoms of the MOF structures were then determined using the Lorentz-Berthelot mixing rules. For determination of the pore volumes the Lennard-Jones parameters for interactions of the He probe atoms with Ca$^{++}$ and Na$^+$ are specified in Table 4.

For determination of the accessible pore volumes of FAU, NaX, NaY, LTA, LTA-5A and LTA-4A the sodalite cages were blocked and no He probe atoms could enter these cages. Only the supercage volumes are determined for these structures.

The $V_{pore}$, and $\phi$ data are included in Table 1 (all-silca zeolites), Table 3 (zeolites with cations), Table 5: (MOFs and COFs).


# 6. MD simulation methodology

Diffusion is simulated using Newton's equations of motion until the system properties, on average, no longer change in time. The Verlet algorithm is used for time integration. A time step of 1 fs was used in all simulations. For each simulation, *initializing* CBMC moves are used to place the molecules in the

domain, minimizing the energy. Next, follows an *equilibration* stage. These are essentially the same as the production cycles, only the statistics are not yet taken into account. This removes any initial large disturbances in the system that do not affect statistics on molecular displacements. After a fixed number of initialization and equilibrium steps, the MD simulation *production* cycles start. For every cycle, the statistics for determining the mean square displacements (MSDs) are updated. The MSDs are determined for time intervals ranging from 2 fs to 1 ns. In order to do this, an order-*N* algorithm, as detailed in Chapter 4 of Frenkel and Smit[45] is implemented. The Nosé-Hoover thermostat is applied to all the diffusing particles.

The DLPOLY code[47] was used along with the force field implementation as described in the previous section. DL_POLY is a molecular dynamics simulation package written by W. Smith, T.R. Forester and I.T. Todorov and has been obtained from CCLRCs Daresbury Laboratory via the website.[47]

The MD simulations were carried out for a variety of loadings within the various structures. All simulations were carried out on the LISA clusters of PCs equipped with Intel Xeon processors running at 3.4 GHz on the Linux operating system[48]. Each MD simulation, for a specified loading, was run for 120 h, determined to be long enough to obtain reliable statistics for determination of the diffusivities. In several cases the campaigns were replicated and the results averaged.

## 7. MD simulations for binary mixtures

The Maxwell-Stefan (M-S) equations for binary mixture diffusion inside a cylindrical silica pore can be written as

$$-\frac{c_i}{RT}\nabla\mu_i = \sum_{\substack{j=1 \\ j\neq i}}^{n}\frac{x_j N_i - x_i N_j}{Đ_{ij}} + \frac{N_i}{Đ_i}; \quad i = 1,2,...n \tag{2}$$

In equation (2) the $Đ_i$ are the M-S diffusivities of species 1 and 2, respectively, portraying the interaction between component *i* in the mixture with the surface, or wall of the structure. The $Đ_{ij}$ are M-

S exchange coefficients representing interaction between component $i$ with component j. The $c_i$ are the loadings within the pore and $x_i$ represent the component mole fractions

$$x_i = c_i / (c_1 + c_2 + ....c_n); \quad i = 1, n \tag{3}$$

The Onsager reciprocal relations require

$$Đ_{ij} = Đ_{ji} \tag{4}$$

It is important to stress here that the fluxes defined in equation (2) are expressed in terms of the number of moles of species $i$ transported per m$^2$ of *open pore area* per second. These fluxes are to be distinguished from the fluxes defined in the M-S formulations used in our earlier publications [8, 9].

For binary mixtures we can define a square 2×2 matrix [$B$]

$$-\frac{c_i}{RT} \nabla \mu_i = \sum_{j=1}^{2} B_{ij} N_j; \quad i = 1,2 \tag{5}$$

The four elements of the matrix [$B$] are given explicitly by

$$B_{11} = \frac{1}{Đ_1} + \frac{x_2}{Đ_{12}} \tag{6}$$

$$B_{22} = \frac{1}{Đ_2} + \frac{x_1}{Đ_{12}} \tag{7}$$

$$B_{12} = -\frac{x_1}{Đ_{12}} \tag{8}$$

$$B_{21} = -\frac{x_2}{Đ_{12}} \tag{9}$$

Furthermore, we define a matrix [Δ] as the inverse of [$B$]

$$[\Delta] \equiv [B]^{-1} = \begin{bmatrix} \dfrac{1}{\mathcal{D}_1} + \dfrac{x_2}{\mathcal{D}_{12}} & -\dfrac{x_1}{\mathcal{D}_{12}} \\ -\dfrac{x_2}{\mathcal{D}_{12}} & \dfrac{1}{\mathcal{D}_2} + \dfrac{x_1}{\mathcal{D}_{12}} \end{bmatrix}^{-1} \tag{10}$$

The inversion can be carried out explicitly to give the following expressions

$$\Delta_{11} = \frac{\mathcal{D}_1\left(1 + \dfrac{x_1 \mathcal{D}_2}{\mathcal{D}_{12}}\right)}{1 + \dfrac{x_1 \mathcal{D}_2 + x_2 \mathcal{D}_1}{\mathcal{D}_{12}}} \tag{11}$$

$$\Delta_{22} = \frac{\mathcal{D}_2\left(1 + \dfrac{x_2 \mathcal{D}_1}{\mathcal{D}_{12}}\right)}{1 + \dfrac{x_2 \mathcal{D}_1 + x_1 \mathcal{D}_2}{\mathcal{D}_{12}}} \tag{12}$$

$$\Delta_{12} = \frac{\mathcal{D}_1\, \dfrac{x_1 \mathcal{D}_2}{\mathcal{D}_{12}}}{1 + \dfrac{x_1 \mathcal{D}_2 + x_2 \mathcal{D}_1}{\mathcal{D}_{12}}} \tag{13}$$

$$\Delta_{21} = \frac{x_2}{x_1}\Delta_{12} = \frac{\mathcal{D}_2\, \dfrac{x_2 \mathcal{D}_1}{\mathcal{D}_{12}}}{1 + \dfrac{x_1 \mathcal{D}_2 + x_2 \mathcal{D}_1}{\mathcal{D}_{12}}} \tag{14}$$

The elements $\Delta_{ij}$ can be obtained from MD simulations of molecular displacements using the formula in each of the coordinate directions

$$\Delta_{ij} = \frac{1}{2}\lim_{\Delta t \to \infty}\frac{1}{n_j}\frac{1}{\Delta t}\left\langle\left(\sum_{l=1}^{n_i}\left(\mathbf{r}_{l,i}(t+\Delta t) - \mathbf{r}_{l,i}(t)\right)\right) \bullet \left(\sum_{k=1}^{n_j}\left(\mathbf{r}_{k,j}(t+\Delta t) - \mathbf{r}_{k,j}(t)\right)\right)\right\rangle \tag{15}$$

In this expression $n_i$ and $n_j$ represent the number of molecules of species $i$ and $j$ respectively, and $\mathbf{r}_{l,i}(t)$ is the position of molecule $l$ of species $i$ at any time $t$. In this context we note a typographical error in eq (15) as printed in earlier publications [49-51] wherein the denominator in the right member had $n_i$

10

instead of $n_j$. The simulation results presented in these publications are, however, correct as the proper formula given in eq (15) was used. Compliance with the Onsager Reciprocal Relations demands that

$$n_j \Delta_{ij} = n_i \Delta_{ji}; \quad i, j = 1,2,....n \tag{16}$$

For three-dimensional pore networks (MFI, FAU, NaX, NaY, BEA, LTA, LTA-5A, LTA-4A, CHA, ISV, IRMOF-1, CuBTC, Zn(bdc)dabco, Co(bdc)dabco, COF-102, COF-103, and COF-108) the arithmetic average of the diffusivities in the three coordinate directions were used in further analysis and reported in the Figures accompanying this Supplementary material. For one-dimensional pore structures (cylindrical silica nanopores, AFI, LTL, MIL-47, MIL-53, Co-FA, Mn-FA, Zn(tbip)) the diffusivities along the direction of diffusion are reported and analyzed. For DDR and ERI the reported diffusivities are the averages in x- and y- directions.

We define a matrix of thermodynamic correction factors $[\Gamma]$

$$\frac{c_i}{RT} \nabla \mu_i = \sum_{j=1}^{n} \Gamma_{ij} \nabla c_j; \quad \Gamma_{ij} \equiv \frac{c_i}{c_j} \frac{\partial \ln f_i}{\partial \ln c_j} = \frac{c_i}{f_i} \frac{\partial f_i}{\partial c_j}; \quad i, j = 1,..n \tag{17}$$

where $f_i$ represents the fugacity of component $i$ in the bulk fluid phase. With this definition equation (5) can be recast in 2×2 dimensional matrix notation in the form

$$-[\Gamma]\nabla(c)\frac{d(c)}{dx} = [B](N); \quad (N) = -[B]^{-1}[\Gamma]\nabla(c) = -[\Delta][\Gamma]\nabla(c) \tag{18}$$

## 8. Backing out $Đ_i$ and $Đ_{12}$ from MD mixture simulations

The MD simulations for binary mixtures yields the 2×2 matrix $[\Delta]$ using the formula (15). The first step is to determine the determinant

$$|\Delta| = \Delta_{11}\Delta_{22} - \Delta_{12}\Delta_{21} \tag{19}$$

The elements of $[B]$ are then obtained explicitly using

$$B_{11} = \frac{\Delta_{22}}{|\Delta|} \tag{20}$$

11

$$B_{22} = \frac{\Delta_{11}}{|\Delta|} \tag{21}$$

$$B_{12} = -\frac{\Delta_{12}}{|\Delta|} \tag{22}$$

$$B_{21} = -\frac{\Delta_{21}}{|\Delta|} \tag{23}$$

Combining equation (8) with (22) we can obtain $Đ_{12}$ explicitly

$$Đ_{12} = -\frac{x_1}{B_{12}} \tag{24}$$

Combining equation (9) with (23) we can obtain $Đ_{12}$ from the equivalent relationship

$$Đ_{12} = -\frac{x_2}{B_{21}} \tag{25}$$

From equations (6), (20), and (24) we get

$$Đ_1 = 1 \Big/ \left( B_{11} - \frac{x_2}{Đ_{12}} \right) \tag{26}$$

From equations (7), (21), and (24) we get

$$Đ_2 = 1 \Big/ \left( B_{22} - \frac{x_1}{Đ_{12}} \right) \tag{27}$$

The $Đ_i$ backed out using equations (26) and (27) can be compared with the MD simulated pure component values using equation (29). These two sets of results are compared at the same total loading. Such comparisons were presented in our earlier paper [41], but are not repeated here.

The $Đ_{12}$ backed out using equation (25) are also compared with values for binary mixture diffusion in fluid mixtures of the same composition and total loading; $Đ_{12,\,fl}$.

# 9. Unary diffusion

For unary diffusion, equation (2) simplifies to yield

$$-\frac{c_i}{RT}\nabla\mu_i = \frac{N_i}{Đ_i} \tag{28}$$

The pure component $Đ_i$ is obtained from MD simulations of molecular displacements using the formula in each of the coordinate direction

$$Đ_i = \frac{1}{2}\lim_{\Delta t\to\infty}\frac{1}{n_i}\frac{1}{\Delta t}\left\langle\left(\sum_{l=1}^{n_i}\left(\mathbf{r}_{l,i}(t+\Delta t)-\mathbf{r}_{l,i}(t)\right)\right)^2\right\rangle \tag{29}$$

In this expression $n_i$ represents the number of molecules of species $i$, and $\mathbf{r}_{l,i}(t)$ is the position of molecule $l$ of species $i$ at any time $t$. Let us apply equation (2) to a system consisting of two species that are identical with respect to diffusional properties and, furthermore, that we have equimolar diffusion $N_1 + N_2 = 0$

$$-\frac{c_1}{RT}\nabla\mu_1 = \frac{(x_1+x_2)N_1}{Đ_{11}} + \frac{N_1}{Đ_1} = \left(\frac{1}{Đ_{11}}+\frac{1}{Đ_1}\right)N_1 \tag{30}$$

Equation (30) defines the self-diffusivity within a pore for this special situation

$$-\frac{c_i}{RT}\nabla\mu_i = \frac{N_i}{D_{i.self}} \tag{31}$$

and so we derive the expression

$$\frac{1}{D_{i,self}} = \frac{1}{Đ_i} + \frac{1}{Đ_{ii}} \tag{32}$$

The self-diffusivities $D_{i,self}$ is computed from MD simulations by analyzing the mean square displacement of each species $i$ for each coordinate direction

$$D_{i,self} = \frac{1}{2n_i}\lim_{\Delta t\to\infty}\frac{1}{\Delta t}\left\langle\left(\sum_{l=1}^{n_i}\left(\mathbf{r}_{l,i}(t+\Delta t)-\mathbf{r}_{l,i}(t)\right)^2\right)\right\rangle \tag{33}$$

Equation (32) has been used to determine the self-exchange diffusivities $Đ_{ii}$ from MD simulated $D_{i,self}$ and $Đ_i$ for unary diffusion.

Equation (28) re-written in terms of molar concentration gradients is

$$N_i = -Đ_i \Gamma_i \nabla c_i \tag{34}$$

with the unary thermodynamic correction factor

$$\Gamma_i = \frac{c_i}{f_i} \frac{\partial f_i}{\partial c_i} \tag{35}$$

# 10.  MD simulations of fluid phase diffusivity

In addition to determination of diffusivities inside pores of zeolites and MOFs, the fluid phase self-diffusivities, $Đ_{ii,fl}$, for pure components C1, C2, C3, nC4, nC6, Kr, Ne, Ar, $CO_2$, $N_2$, Kr, $CF_4$, neopentane, and $H_2$ using the methodology as used in our earlier publications [51-53]. Furthermore, the M-S diffusivities $Đ_{12,fl}$ in binary fluid C1-Ar, C1-C2, C1-C3, Ne-Ar, Ar-Kr, Ne- $CO_2$, $H_2$- $CO_2$, Ar-$CO_2$, $N_2$ – $CO_2$, C1- $CO_2$, and C1- $H_2$ mixtures were also determined using the methodology in our earlier publications [51-53].

At this point we need to clarify the Darken interpolation formula for determination of the $Đ_{12,fl}$. In the original paper by Darken [54] the following expression is postulated

$$Đ_{12,fl} = x_2 D_{1,self,fl} + x_1 D_{2,self,fl} \tag{36}$$

where $D_{1,self,fl}$ and $D_{2,self,fl}$ are *tracer*, or *self-* diffusivities of components 1 and 2, respectively, in the **binary mixture**. Indeed the formula (36) is used in our earlier publication [52] for testing against MD simulations. The **pure component** $Đ_{ii,fl}$ that we use in the current publication are related to the $D_{i,self,fl}$ in the mixture by

$$Đ_{11,fl} = D_{1,self}^{x_1 \rightarrow 1} = Đ_{12}^{x_1 \rightarrow 1}; \quad Đ_{22,fl} = D_{2,self}^{x_2 \rightarrow 1} = Đ_{12}^{x_2 \rightarrow 1} \tag{37}$$

14

As an approximation, therefore, the Darken equation (36) may be re-written in terms of the pure component $Đ_{\text{ii,fl}}$ as follows

$$Đ_{12,fl} = x_1 Đ_{11,fl} + x_2 Đ_{22,fl} \tag{38}$$

We note the switch in the multiplicative mole fractions in equations (36) and (38). In this context we should mention that the equation (21) of our recent paper [41] is incorrect as printed; the correct form should have been the above equation (38). The calculations presented in [41] were carried out with the correct formula.

Futhermore, it is worthwhile pointing out that the Vignes relation as written in our publication [52]

$$Đ_{12,fl} = \left( Đ_{12,fl}^{x_1 \to 1} \right)^{x_1} \left( Đ_{12,fl}^{x_2 \to 1} \right)^{x_2} \tag{39}$$

is equivalent to the formula used in the current manuscript

$$Đ_{12,fl} = \left( Đ_{11,fl} \right)^{x_1} \left( Đ_{22,fl} \right)^{x_2} \tag{40}$$

## 11.  Interpolation formulae for $Đ_{\text{ij}}$ inside micropores

The proper generalization of the Darken.interpolation formula $Đ_{12} = x_1 Đ_{11} + x_2 Đ_{22l}$ for $n$-component mixture diffusion inside micro-pores is

$$Đ_{ij} = \frac{c_i}{c_i + c_j} Đ_{ii} + \frac{c_j}{c_i + c_j} Đ_{jj}; \quad i, j = 1,2,..n \tag{41}$$

Correspondingly the proper generalization of the Vignes type interpolation formula $Đ_{12} = \left( Đ_{11} \right)^{x_1} \left( Đ_{22} \right)^{x_2}$ for $n$-component mixture diffusion inside micro-pores is

$$Đ_{ij} = \left[ Đ_{ii} \right]^{c_i/(c_i + c_j)} \left[ Đ_{jj} \right]^{c_j/(c_i + c_j)}; \quad i, j = 1,2,..n \tag{42}$$

For all guest-host combinations, these two interpolation formulae are compared with the MD simulated values of the exchange coefficient $Đ_{12}$ inside the pores. These comparisons are presented, along with other simulation results, for each host material in turn.

15

## 12.   Self-diffusivities in *n*-component mixtures

Equation (32) also holds for the self-diffusivities $D_{i,self}$ in *n*-component mixtures. For *n*-component mixtures the following expression for self-diffusivities $D_{i,self}$ can be derived following earlier work [49, 55]

$$\frac{1}{D_{i,self}} = \frac{1}{Đ_i} + \sum_{j=1}^{n} \frac{x_j}{Đ_{ij}} = \frac{1}{Đ_i} + \frac{x_i}{Đ_{ii}} + \sum_{\substack{j=1 \\ j \neq i}}^{n} \frac{x_j}{Đ_{ij}}; \quad i = 1,2,...n \tag{43}$$

For the special case of a binary mixture we get

$$\frac{1}{D_{1,self}} = \frac{1}{Đ_1} + \frac{x_1}{Đ_{11}} + \frac{x_2}{Đ_{12}} \tag{44}$$

$$\frac{1}{D_{2,self}} = \frac{1}{Đ_2} + \frac{x_2}{Đ_{22}} + \frac{x_1}{Đ_{12}} \tag{45}$$

For *prediction* of the self-diffusivities $D_{i,self}$ from unary diffusion data, we determine the $Đ_i$ and $Đ_{ii,}$ at the total mixture loadings. In the accompanying Figures, the binary exchange coefficient is estimated using the Vignes interpolation formula $Đ_{12} = (Đ_{11})^{x_1} (Đ_{22})^{x_2}$. In these predictions, the MD simulated unary diffusion data on $Đ_i$ and $Đ_{ii}$ are used, rather than Reed and Ehrlich fits as in our earlier publications [8, 9]. For this reason, the "predicted" lines are not smooth.

## 13.   Estimation of [Δ] for mixtures

Equations (11), (12), (13), and (14) allow estimation of the elements of the matrix [Δ] from unary diffusion data on $Đ_i$ and $Đ_{ii,}$ along with an interpolation scheme, Darken or Vignes. In the accompanying Figures, the MD simulated data on [Δ], obtained from equation (15), are compared with these M-S model predictions, using the binary exchange coefficient as estimated using the Vignes interpolation formula $Đ_{12} = (Đ_{11})^{x_1} (Đ_{22})^{x_2}$. In these predictions, the MD simulated unary diffusion data on $Đ_i$ and $Đ_{ii}$ are used, rather than Reed and Ehrlich fits as in our earlier publications [8, 9]. For this reason, the "predicted" lines are not smooth.

# 14. Comparison with the published mixture diffusion formulation in *micro*porous materials

In the published literature, the M-S equations for binary mixture diffusion in mesoporous materials such as zeolites, carbon nanotubes (CNTs), titanosilicates (e.g. ETS-4), carbon molecular sieves (CMS), and MOFs are set up in a different manner [8, 9]

$$-\rho \frac{\theta_i}{RT} \nabla \mu_i = \sum_{\substack{j=1 \\ j \neq i}}^{n} \frac{q_j N_i - q_i N_j}{q_{i,sat} q_{j,sat} Đ_{ij}^*} + \frac{N_i}{q_{i,sat} Đ_i}; \quad i = 1,2,..n \tag{46}$$

where $\theta_i$ are the fractional occupancies

$$\theta_i \equiv q_i / q_{i,sat} = c_i / c_{i,sat} \quad i = 1,2,...n \tag{47}$$

and $q_i$ represents the loading defined in terms of mol per kg of framework. The fluxes $N_i$ in equation (46) are defined in terms of the number of moles of species $i$ transported per m$^2$ of *total* crystal area per second, not just the open pore area is in equation (2). The magnitude of the fluxes in equation (2) are lower than those calculated from equation (46) by a factor that equals the pore volume fraction, $\phi$. It is to be noted that the superscript * is not required for the $Đ_i$ in equations (46) because these diffusivities are the same as those defined in equations (2).

The definition of the first member on the right side of equations (2) and (46) are formulated differently, and consequently the two definitions of exchange coefficients in these equations are different. We have the inter-relationship

$$c_{2,sat} Đ_{12}^* / c_t = Đ_{12} = Đ_{21} = c_{1,sat} Đ_{21}^* / c_t \tag{48}$$

For unary diffusion the self-exchange coefficients $Đ_{ii}^*$ are inter-related as follows

$$c_{i,sat} Đ_{ii}^* / c_i = Đ_{ii}^* / \theta_i = Đ_{ii} \tag{49}$$

In the published literature the following "empirical" interpolation formula

$$cj_{2,sat} Đ_{ij}^* = \left[ c_{j,sat} Đ_{ii}^* \right]^{c_i/(c_i+c_j)} \left[ c_{i,sat} Đ_{jj}^* \right]^{c_j/(c_i+c_j)} = c_{i,sat} Đ_{ji}^* \tag{50}$$

has been recommended for estimating $Đ_{ij}^*$ using information on the *self*-exchange coefficients $Đ_{ii}^*$, obtainable from unary diffusion data on $Đ_i$ *and* self-diffusivities $Đ_{i,self}$ [8, 9, 55, 56].

Equation (50) has its origins in a multicomponent surface diffusion paper [57] wherein the following version, of the interpolation formula

$$Đ_{ij}^* = \left[Đ_{ii}^*\right]^{c_i/(c_i+c_j)} \left[Đ_{jj}^*\right]^{c_j/(c_i+c_j)} = Đ_{ji}^* \tag{51}$$

was postulated drawing inspiration from the Vignes interpolation formula (40) for fluid mixtures and without accounting for differences in the saturation capacities $c_{i,sat}$, of the constituent species. Skoulidas, Sholl, and Krishna [55] modified equation (51) modification to account for differences in the saturation capacities and derived equation (50) in order to (a) comply with the Onsager reciprocal relations, and (b) satisfy the limiting relations

$$\lim_{\frac{c_1}{c_1+c_2}\to 1} Đ_{12}^* \to Đ_{11}^*; \quad \lim_{\frac{c_2}{c_1+c_2}\to 1} Đ_{21}^* \to Đ_{22}^* \tag{52}$$

In applying the interpolation formula (50), it is recommended that the self-exchange coefficients $Đ_{ii}^*$ be evaluated at the total occupancy of the mixture

$$\theta = \theta_1 + \theta_2 + ...\theta_n = \frac{c_1}{c_{1,sat}} + \frac{c_2}{c_{2,sat}} + ....\frac{c_n}{c_{n,sat}} \tag{53}$$

If we formally insert equation (49) into equation (50) does not lead to a relation that is identical with equation (42) that is recommended in the present work.

# 15.   Animations

For visual appreciation of the diffusion phenomena in the various structures, animations were created on the basis of the MD simulations for most of the guest-host combinations considered in the present work; these can be viewed after downloading the movies from our website [35].

# 16. Simulation results for unary and binary mixture diffusion in fluid phase

The MD data on self-diffusivities of pure fluids, $Đ_{ii,fl}$ is shown in **Figure 3**. Also included here are the fluid phase simulations in which the Lennard-Jones energy parameter for interaction of two methane molecules is varied as specified in Table 11.

**Figures 4** and **5** compares the MD simulated $Đ_{12,fl}$ in equimolar fluid mixtures C1-Ar, C1-C2, C1-C3, Ne-Ar, Ar-Kr, Ne- $CO_2$, $H_2$- $CO_2$, Ar- $CO_2$, $N_2 - CO2$, C1- $CO_2$, and C1- $H_2$ with the Darken interpolation formula (38) and also the Vignes interpolation formula (40).

The data on pure component viscosity, determined from MD simulations, are provided in **Figure 6**; this data is required to determine the viscous contribution in silica mesopores. This contribution is discussed in our previous publication [41].

# 17. Simulation results for zeolites

The pore landscapes, along with the simulation data in graphical form for FAU, MFI, AFI, BEA, CHA, LTA,DDR, LTL, ISV, and ERI are presented in **Figures 7 – 63**. The influence of the presence of the cations on diffusion is not discussed extensively in the main text of the paper, and therefore more detailed discussions are given here.

**FAU, NaY, NaX**

Let us first consider the influence of cations $Na^+$ on unary diffusion of C1, C2, and C3 in FAU, which has an open structure. Snapshots of the location of C1 and $Na^+$ ions in NaY and NaX are shown in **Figure 8 and Figure 9**, respectively. More precise information on the location of cations is available in earlier work [14]. The MD simulated data for all-silica FAU are compared with NaX ($86Al$, $86Na^+$), and NaY ($48Al$, $48Na^+$) and are presented in **Figures 14, 15, 16, and 17** for C1, C2, C3, C1-C2, and C1-C3, respectively. The following general observations can be made.

1. The cations $Na^+$ offer stronger adsorption sites, in comparison to the zeolite framework and therefore the adsorption strength increases with increasing number of cations.

2. The loadings at which isotherm inflection occurs is different for all-silica FAU, NaX, and NaY.

3. The presence of cations has only a small influence on the self- and M-S diffusivities, when the data are compared using the loadings $c_i$, expressed in terms of the accessible pore volume. Due to different isotherm inflection behaviours of all-silica FAU, NaX, and NaY the $Đ_i$ - $c_i$ dependencies show inflection at different loadings. This aspect will be investigated in detail in future work.

4. The dependence of the self-exchange coefficient $Đ_{ii}$ on $c_i$ is nearly the same for all-silica FAU, NaX, and NaY. This is because the degree of confinement is largely unaltered due to the presence of cations.

5. The degree of correlations, quantified by $Đ_i /Đ_{ii}$ is practically independent of the number of cations present; see data for C1, C2, and C3 in **Figures 14, 15, and 16.**

6. **Figure 17** compares the Darken $Đ_{12} = x_1 Đ_{11} + x_2 Đ_{22l}$ and Vignes $Đ_{12} = (Đ_{11})^{x_1} (Đ_{22})^{x_2}$ interpolation formulae for C1-C2, and C1-C3 diffusion in all-silica FAU, NaX, and NaY zeolites. We note the excellent agreement of the Vignes interpolation formulae with the MD simulated values of $Đ_{12}$ in all cases. Generally speaking, the Darken interpolation scheme is performs less well than the Vignes scheme.

7. Even though the cations were allowed to move, the MD simulations show these to be practically immobile, and tightly anchored to the zeolite framewok.


**MFI, Na-MFI**

**Figures 19, 20, 21, and 22** present snapshots of the location of C1 and Na+ ions in MFI with 2 $Na^+$, 4 $Na^+$, 6 $Na^+$, and 8 $Na^+$, respectively. The nearly-immobile Na+ ions constrict the movement of C1 molecules within the intersecting channel structure of MFI. This is in sharp contrast to the effect of

cations on diffusion in NaX and NaY, where the constriction effects are negligibly small because of the open structure. **Figure 29** compares the methane diffusivity data for all-silica MFI with MFI with 2 $Na^+$, 4 $Na^+$, 6 $Na^+$, and 8 $Na^+$. The presence of cations has the effect of (a) increasing the adsorption strength, and (b) decreasing the accessible pore volume; see pore volume fraction data in Table 3. More importantly, the channels of MFI are more constricted and obstructed by the nearly-immobile $Na^+$, and the degree of confinement is significantly increased. As a result the self- and M-S diffusivities are significantly lowered due to the presence of cations; this effect has also been reported by Leroy and Jobic [58] in QENS experiments. These authors attribute the lowering of diffusivities to "steric hindrance" by the cations. Furthermore, the self- exchange coefficient $Đ_{ii}$ is also significantly reduced with increased number of cations.


### LTA (all-silica), LTA-5A, LTA-4A

**Figure 46** presents snapshots of the location of C1, $Na^+$ and $Ca^{++}$ ions in LTA, LTA-5A, and LTA-4A. The MD data on the influence of cations on diffusion of methane in all-silica LTA, LTA-5A (96 Si, 96 Al, 32 $Na^+$, 32 $Ca^{++}$; Si/Al = 1), and LTA-4A (96 Si, 96 Al, 96 $Na^+$; Si/Al = 1) are presented in **Figures 51 and 52**. First, let us consider the data at a constant temperature; see **Figure 51**. The adsorption strength increases with the number of cations present, and the hierarchy of adsorption strengths is LTA-4A > LTA-5A > LTA (all-silica). This trend is similar to that for FAU and MFI zeolites.

For both LTA-5A and LTA-4A the self- and M-S diffusivities are practically identical, and only the data on self-diffusivities are presented and compared. At any given loading the hierarchy of diffusivities is all-silica LTA (all-silica) > LTA-5A; the presence of cations decreases diffusivities by a few orders of magnitude. The lowest diffusivity is for LTA-4A that contains the maximum number of cations, 96 $Na^+$ ions; these ions occupy sites that essentially block the 8-membered ring window [59-61]; this causes a significant reduction in the diffusivity to values that are too low to be determined from

MD. LTA-5A has fewer total number of cations: 32 $Na^+$ and 32 $Ca^{++}$. The window openings are blocked to a lesser extent than LTA-4A and therefore the diffusivity is higher than LTA-4A.

For LTA-5A and LTA-4A the $Đ_{ii}$ are not determinable, and the assumption of uncoupled flux relations, as proposed by Habgood [62], is a good engineering approximation.

**Figure 52** presents MD data for self-diffusivities in LTA (all-silica), and LTA-5A at a variety of temperatures. The data for LTA (all-silica) at various *T* is taken from our earlier published work [12]. At a loading of 0.5 molecules per cage, the hierarchy of activation energies is LTA-5A > LTA (all-silica), and reflects the higher adsorption strength of C1 in LTA-5A due to the presence of cations (cf. **Figure 51**). This hierarchy is in line with experimental data [63].

There is some experimental evidence to confirm the trends in the influence of cations on diffusivities of alkanes in LTA, MFI, and FAU obtained from MD simulations[64].

**LTL, ISV,  ERI**

**Figures 58 − 63** present the results for these three zeolites that are not discussed in the main text of this paper. One-dimensional diffusion in LTL is similar to that within AFI. ISV has an intersecting channel structure and the results are similar to that of MFI. ERI has cages separated by narrow windows; diffusion in these structures are similar to that for CHA, DDR and LTA. In this context we note that for mixtures containing $CO_2$ segregation effects are experience because of preferential location of $CO_2$ at the window regions [9-11].

## 18.    Simulation results for MOFs

The pore landscapes, along with the simulation data in graphical form for IRMOF-1, CuBTC, MIL-47, Zn(bdc)dabco, Co(bdc)dabco, Co-FA, Mn-FA, Zn(tbip), and MIL-53 are presented in **Figures 64 − 101**. It must be remarked here that the simulations for diffusion of methane in Co-FA and Mn-FA that were reported in earlier work, cited in the main text of this paper [65] were only carried out to 4 molecules per unit cell. In the present work the loadings were varied to values that exceed 4 molecules

per unit cell, and this leads to the inflection behaviour for adsorption and diffusion in both these materials.

# 19. Simulation results for COFs

The pore landscapes, along with the simulation data in graphical form for COF-102, COF-103, and COF-108 are presented in **Figures 102 – 109**.

# 20. Simulation results for cylindrical silica pores

The pore landscapes, along with the simulation data in graphical form for cylindrical silica pores of 0.6, 0.75, 1, 1.5, 2, 3, 4, 5.8, 7.6, 10, 20, and 30 nm are presented in **Figures 109 – 138**. The data for the 1, 1.5, 2, 3, 4, 5.8, 7.6, and 10 nm pores are from our earlier publication, re-analysed for current purposes [41]. The sensitivity studies for the 1.5, 2 and 3 nm pores are new simulation data. The sensitivity analysis shows that the self-exchange coefficient $Đ_{ii}$ for the 2 nm and 3 nm pores equals the corresponding fluid phase diffusivity value $Đ_{ii,fl}$ obtained with the corresponding force field parameters in Table 11. For the 1.5 nm pore the factor $F_i = \dfrac{Đ_{ii}}{Đ_{ii,fl}}$ equals 0.9, irrespective of the Lennard-Jones energy interaction factor, suggesting that this factor is predominantly dictated by the degree of confinement within the pore.

Additionally, for the 2 and 3 nm pores, the temperature was varied over a wide range and the zero-loading diffusivities $Đ_i(0)$ compared with the Knudsen diffusivity calculated from

$$D_{i,Kn} = \frac{d_{p,eff}}{3} \sqrt{\frac{8RT}{\pi M_i}} \tag{54}$$

Following Bhatia and Nicholson [66] we define the effective pore diameter, $d_{p,eff}$ by

$$d_{p,eff} = d_p - 0.92(\sigma_i + \sigma_O) \tag{55}$$

where $d_p$ is the centre-to-centre distance between the O atoms on the surface of the pore, $\sigma_i$ is the Lennard-Jones size parameter for molecule-molecule interaction, and $\sigma_O$ is the Lennard-Jones size

23

parameter for O atoms in the silica structure (the Lennard-Jones parameters are tabulated in the Supplementary material); see also our earlier work [41]. The correction to the pore diameter is especially relevant for pores smaller than about 3 nm.

The varying $T$ studies demonstrate that the ratio $Đ_i(0)/D_{i,Kn}$ is dictated by $\varepsilon_{i-O}/k_B T$ and at low high $T$, $Đ_i(0) \approx D_{i,Kn}$. Furthermore, we note from the Arrhenius plots that the $Đ_i(0)$ does not vary as $\sqrt{T}$ anticipated by the Knudsen formula, except at very high $T$. The activation energies are significantly increased due to adsorption effects.

# 21. Acknowledgements

The calculation of the accessible pore volume using the Widom insertion of He probe atoms is implemented within the BIGMAC code.

# 22. Notation

| | |
|---|---|
| $[B]$ | matrix of inverse Maxwell-Stefan coefficients, $m^{-2}$ s |
| $c_i$ | concentration of species $i$, mol $m^{-3}$ |
| $c_t$ | total concentration in mixture, mol $m^{-3}$ |
| $d_p$ | pore diameter, m |
| $d_{p,eff}$ | effective pore diameter defined by equation (55), m |
| $D_{i,self}$ | self-diffusivity of species $i$ within pore, $m^2$ $s^{-1}$ |
| $Đ_{ii,fl}$ | self-diffusivity of species $i$ in fluid phase, $m^2$ $s^{-1}$ |
| $Đ_i$ | Maxwell-Stefan diffusivity for species-pore wall interaction, $m^2$ $s^{-1}$ |
| $Đ_i(0)$ | zero-loading M-S diffusivity for species-pore wall interaction, $m^2$ $s^{-1}$ |
| $Đ_{12}$ | M-S exchange coefficient defined by equation (2), $m^2$ $s^{-1}$ |
| $Đ_{12}^{*}$ | M-S exchange coefficient defined by equation (46), $m^2$ $s^{-1}$ |
| $Đ_{12,fl}$ | Maxwell-Stefan diffusivity for fluid phase mixture, $m^2$ $s^{-1}$ |
| $D_{i,Kn}$ | Knudsen diffusivity of species i, $m^2$ $s^{-1}$ |
| $k_B$ | Boltzmann constant, $1.38 \times 10^{-23}$ J molecule$^{-1}$ K$^{-1}$ |
| $M_i$ | molar mass of species $i$, kg mol$^{-1}$ |
| $N_i$ | mol flux of species $i$, mol $m^{-2}$ $s^{-1}$ |
| $n_i$ | number of molecules of species $i$ in simulation box, dimensionless |
| $n$ | number of species in mixture, dimensionless |
| $\mathbf{r}_{l,i}(t)$ | position vector for molecule $l$ of species $i$ at any time $t$, m |
| $R$ | gas constant, 8.314 J mol$^{-1}$ K$^{-1}$ |
| $x_i$ | mole fraction of species $i$ based on loading within pore, dimensionless |
| $t$ | time, s |
| $T$ | absolute temperature, K |

### Greek letters

| | |
|---|---|
| $[\Delta]$ | matrix of Maxwell-Stefan diffusivities, $m^2\ s^{-1}$ |
| $\varepsilon$ | Lennard-Jones interaction energy parameter, J molecule$^{-1}$ |
| $\phi$ | fractional pore volume, dimensionless |
| $[\Gamma]$ | matrix of thermodynamic factors, dimensionless |
| $\eta_i$ | viscosity of species $i$, Pa s |
| $\theta_i$ | fractional occupancy of species $i$, dimensionless |
| $\mu_i$ | molar chemical potential, J mol$^{-1}$ |
| $\rho$ | framework density, kg m$^{-3}$ |
| $\sigma$ | Lennard-Jones size parameter, m |

### Subscripts

| | |
|---|---|
| eff | effective pore diameter |
| fl | referring to fluid phase |
| i | referring to component $i$ |
| Kn | referring to Knudsen |
| O | referring to O atoms in silica |
| p | referring to pore |
| s | referring to surface, or wall of pore |
| t | referring to total mixture |

### Vector and Matrix Notation

| | |
|---|---|
| $\nabla$ | gradient operator |
| ( ) | vector |
| [ ] | square matrix |

Table 1. Characteristic sizes of channels or windows for zeolite structures, pore volume expressed in mL/g, and fractional pore volume. The characteristic dimension is used in the determination of the "degree of confinement", *F*, in the main text.

| Zeolite | Channel or window size/ Å | Pore volume, mL/(g framework) | Fractional pore volume | Characteristic dimension, nm |
|---|---|---|---|---|
| MFI | 10-ring intersecting channels of 5.1 – 5.6 Å size | 0.165 | 0.297 | 0.56 nm |
| AFI | 12-ring 1D channels of 7.3 Å size | 0.159 | 0.274 | 0.73 nm |
| FAU | Cages separated by 7.4 Å size windows | 0.328 | 0.44 | 0.74 nm |
| CHA | Cages separated by 3.8 Å size windows | 0.264 | 0.38 | 0.38 nm |
| LTA | Cages separated by 4.1 Å size windows | 0.310 | 0.4 | 0.41 nm |
| DDR | Cages separated by 3.6 Å $\times$ 4.4 Å size windows | 0.139 | 0.245 | 0.36 nm |
| BEA | Intersecting channels of two sizes: 12-ring of 7.1 Å and 10-ring of 5.6 Å | 0.271 | 0.41 | 0.63 nm |
| LTL | 12-ring 1D channels of 7.1 Å size | 0.17 | 0.276 | 0.71 nm |
| ISV | Intersecting channels of two sizes: 12-ring of 6.1×6.5 Å and 12-ring of 5.9 Å $\times$ 6.6 Å | 0.278 | 0.425 | 0.62 nm |
| ERI | Cages separated by 3.6 Å $\times$ 5.1 Å size windows | 0.228 | 0.36 | 0.36 nm |

Table 2. Summary of force field used for zeolite structures. The interaction between adsorbates was calculated using Lennard-Jones potentials and electrostatic interactions using an Ewald summation method. For adsorbate-adsorbate interactions, Lorentz-Berthelot mixing rules were applied for $\sigma$ and $\varepsilon/k_B$. Leonard-Jones interaction with the zeolite was only taken $\sigma$ and $\varepsilon/k_B$ and epsilon for the adsorbates and for the interaction with the adsorbates and with the zeolites. The charges are also shown for the pseudo atoms.

| (pseudo-) atom | Atom-atom $\sigma$ / Å | Atom-atom $\varepsilon/k_B$ / K | Atom - O in zeolite $\sigma$ / Å | Atom - O in zeolite $\varepsilon/k_B$ / K |
|---|---|---|---|---|
| CH$_4$ | 3.72 | 158.5 | 3.47 | 115 |
| Ar | 3.42 | 124.07 | 3.17 | 95.61 |
| Ne | 2.789 | 35.7 | 2.798 | 56.87 |
| Kr | 3.636 | 166.4 | 3.45 | 109.6 |

Table 3. Data on zeolite structures with cations (data on all-silica structures also included for comparison purposes). The number of atoms per unit cell of these structures are specified, along with the pore volume data.

| Zeolite | Si | Al | Si/Al | Na++ | Ca++ | Fractional pore volume |
|---------|-----|-----|---------|------|------|----------|
| LTA | 192 | 0 | ∞ | 0 | 0 | 0.4 |
| LTA-5A | 96 | 96 | 1 | 32 | 32 | 0.38 |
| LTA-4A | 96 | 96 | 1 | 96 | 0 | |
| | | | | | | |
| FAU | 192 | 0 | ∞ | 0 | 0 | 0.44 |
| NaX | 106 | 86 | 1.23 | 86 | 0 | 0.40 |
| NaY | 144 | 48 | 3 | 48 | 0 | 0.408 |
| | | | | | | |
| MFI | 96 | 0 | ∞ | 0 | 0 | 0.297 |
| MFI-2Na | 94 | 2 | 47 | 2 | 0 | 0.286 |
| MFI-4Na | 92 | 4 | 23 | 4 | 0 | 0.274 |
| MFI-6Na | 90 | 6 | 15 | 6 | 0 | 0.267 |
| MFI-8Na | 88 | 8 | 11 | 8 | 0 | 0.257 |

Table 4. Lennard-Jones paarameters used to determine the pore volume in zeolites in which cations $Na^+$ and $Ca^{++}$ are present. The $Na^+$ - $Na^+$ parameters are from Calero et al. [14-16]. The $Ca^{++}$- $Ca^{++}$ parameters are are taken from DREIDING [37]. The He-He parameters are from Table 1 of the paper.by Talu and Myers [46]. The interaction parameters for interaction of He with the O atoms of zeolite frameworks is from Table 1 of Talu and Myers [46]

| (pseudo-) atom | Atom-atom $\sigma$ / Å | Atom-atom $\varepsilon/k_B$ / K |
|---|---|---|
| He-He | 2.64 | 10.9 |
| He-$Na^+$ | 2.4 | 36.8 |
| He - O | 2.952 | 28 |
| He - $Ca^{++}$ | 2.7 | 52.4 |
| $Na^+$ - $Na^+$ | 2.16 | 124.4 |
| $Ca^{++}$- $Ca^{++}$ | 2.8 | 251.58 |

Table 5. Structural information on MOFs. Dimensions of unit cell, pore volume expressed in mL/g, and fractional pore volume. The data on pore volume fraction is obtained using the helium probe insertion technique [43, 46].

| MOF | $a$ / Å | $b$ / Å | $c$ / Å | Pore volume, mL/(g framework) | Fractional pore volume |
|------|---------|---------|---------|-------------------------------|------------------------|
| IRMOF-1 | 25.832 | 25.832 | 25.832 | 1.369 | 0.81 |
| CuBTC | 26.343 | 26.343 | 26.343 | 0.848 | 0.75 |
| MIL-47 | 6.808 | 16.12 | 13.917 | 0.606 | 0.61 |
| MIL-53 | 16.64500826 | 11.34 | 27.596 | 0.465 | 0.56 |
| Zn(bdc)dabco | 10.9288 | 10.9288 | 9.6084 | 0.801 | 0.66 |
| Co(bdc)dabco | 10.963 | 10.963 | 9.469 | 0.796 | 0.65 |
| Co-FA | 11.3834 | 9.9292 | 14.4324 | 0.139 | 0.25 |
| Mn-FA | 11.715 | 10.248 | 15.159 | 0.190 | 0.3 |
| Zn(tbip) | 28.863 | 49.992 | 7.977 | 0.118 | 0.175 |

Table 6. Channel dimensions of MOFs.  The characteristic dimension is used in the determination of the "degree of confinement", $F$, in the main text.

| MOF | Channel dimensions | Characteristic dimension, nm |
|---|---|---|
| IRMOF-1 | Two alternating, inter-connected, cavities of 10.9 Å and 14.3 Å with window size of 8 Å. | 0.8 nm |
| CuBTC | The CuBTC structure consists of two types of "cages" and two types of "windows" separating these cages. Large cages are inter-connected by 9 Å windows of square cross-section. The large cages are also connected to tetrahedral-shaped pockets of ca. 6 Å size through triangular-shaped windows of ca. 4.6 Å size | 0.9 nm |
| MIL-47 | One-dimensional diamond-shaped channels with free internal diameter of ca 8.5 Å | 0.85 nm |
| MIL-53 | One-dimensional lozenge-shaped channels with free internal diameter of ca 8.5 Å | 0.85 nm |
| Zn(bdc)dabco | There exist two types of intersecting channels of about 7.5 Å × 7.5 Å along the $x$-axis and channels of 3.8 Å × 4.7 Å along $y$ and $z$ axes. | 0.57 nm |
| Co(bdc)dabco | There exist two types of intersecting channels of about 7.6 Å × 7.6 Å along the $x$-axis and channels of 3.7 Å × 5.1 Å along $y$ and $z$ axes. | 0.57 nm |
| Co-FA | The metal network exhibits diamondoid connectivity and the overall framework gives rise to zig-zag channels along the $y$ axis where guest dimethyl-formamide molecules reside. The effective pore size of these one-dimensional channels is 5 – 6 Å. | 0.55 nm |
| Mn-FA | Adamantane-like cages of 5.5 Å diameter are connected to each other via a small window of approximately 4.5 Å to form a 1D zig-zag channel along the $y$ axis | 0.45 nm |
| Zn(tbip) | One-dimensional channels of 4.5 Å | 0.45 nm |

Table 7. Lennard-Jones parameters for atoms in MOFs and COFs. For the atoms in the guest organic framework, the generic UFF [36] was used. The DREIDING [37] force fields was used for the organic linker atoms.

| (pseudo-) atom | $\sigma$ / Å | $\varepsilon/k_B$ / K |
|---|---|---|
| Cu | 3.114 | 2.518 |
| V | 2.8 | 8.05 |
| Zn | 2.69 | 0.41 |
| Fe | 4.04 | 27.7 |
| Co | 2.56 | 7.046 |
| Mn | 2.64 | 6.54 |
| B | 3.58 | 47.8 |
| Si | 3.80 | 156 |
| O (organic) | 3.03 | 48.2 |
| O (inorganic) | 2.98 | 700 |
| C | 3.47 | 47.9 |
| N | 3.26 | 38.95 |
| H | 2.85 | 7.65 |

Table 8. Structural information on COFs. Dimensions of unit cell, pore volume expressed in mL/g, and fractional pore volume. The data on pore volume fraction is obtained using the helium probe insertion technique [43, 46]

| COF | $a$ / Å | $b$ / Å | $c$ / Å | Pore volume, mL/g | Fractional pore volume |
|---|---|---|---|---|---|
| COF-102 | 27.1771 | 27.1771 | 27.1771 | 1.875 | 0.8 |
| COF-103 | 28.2477 | 28.2477 | 28.2477 | 2.040 | 0.82 |
| COF-108 | 28.401 | 28.401 | 28.401 | 5.467 | 0.93 |

Table 9. Channel dimensions of COFs. The characteristic dimension is used in the determination of the "degree of confinement", $F$, in the main text.

| MOF | Channel dimensions | Characteristic dimension, nm |
|---|---|---|
| COF-102 | Cavity of size 8.9 Å | 0.89 nm |
| COF-103 | Cavity of size 9.6 Å | 0.96 nm |
| COF-108 | Two cavities, of sizes 15.2 Å and 29.6 Å | 1.52 nm |

Table 10. Lennard-Jones parameters for guest molecules $CH_4$ and Ar in silica pores. The interaction between adsorbates was calculated using Lennard-Jones potentials. For adsorbate-adsorbate interactions, Lorentz-Berthelot mixing rules were applied for $\sigma$ and $\varepsilon/k_B$. Leonard-Jones interaction with the silica was considered to be dominated by interactions with the O atoms

| (pseudo-) atom | Atom-atom $\sigma$ / Å | Atom-atom $\varepsilon/k_B$ / K | Atom - O in silica $\sigma$ / Å | Atom - O in silica $\varepsilon/k_B$ / K |
|---|---|---|---|---|
| $CH_4$ | 3.72 | 158.5 | 3.47 | 115 |
| Ar | 3.42 | 124.07 | 3.17 | 95.61 |

Table 11. Lennard-Jones parameters for guest molecule $CH_4$ in the sensitivity analysis carried out for the 1.5, 2 and 3 nm pores.

| (pseudo-) atom | C1-C1 $\sigma$/ Å | C1-C1 $\varepsilon/k_B$ / K | C1 - O in silica $\sigma$/ Å | C1 – O atoms in silica $\varepsilon/k_B$ / K |
|---|---|---|---|---|
| Base case | 3.72 | 158.5 | 3.47 | 115 |
| Case 1 | 3.72 | 50 | 3.47 | 64.6 |
| Case 2 | 3.72 | 100 | 3.47 | 91.4 |
| Case 3 | 3.72 | 200 | 3.47 | 129 |
| Case 4 | 3.72 | 300 | 3.47 | 158 |

# 23. References

[1]     C. Baerlocher, L.B. McCusker, Database of Zeolite Structures, International Zeolite Association, http://www.iza-structure.org/databases/, 26 June 2001.

[2]     J.P. Ryckaert, A. Bellemans, Molecular dynamics of liquid alkanes, Faraday Discuss. Chem. Soc. 66 (1978) 95-106.

[3]     D. Dubbeldam, S. Calero, T.J.H. Vlugt, R. Krishna, T.L.M. Maesen, B. Smit, United Atom Forcefield for Alkanes in Nanoporous Materials, J. Phys. Chem. B 108 (2004) 12301-12313.

[4]     A.I. Skoulidas, D.S. Sholl, Transport diffusivities of $CH_4$, $CF_4$, He, Ne, Ar, Xe, and $SF_6$ in silicalite from atomistic simulations, J. Phys. Chem. B 106 (2002) 5058-5067.

[5]     O. Talu, A.L. Myers, Reference potentials for adsorption of helium, argon, methane and krypton in high-silica zeolites, Colloids Surf., A 187-188 (2001) 83-93.

[6]     A.I. Skoulidas, D.S. Sholl, Molecular Dynamics Simulations of Self, Corrected, and Transport Diffusivities of Light Gases in Four Silica Zeolites to Assess Influences of Pore Shape and Connectivity, J. Phys. Chem. A 107 (2003) 10132-10141.

[7]     R. Krishna, J.M. van Baten, Using molecular simulations for screening of zeolites for separation of $CO_2$/$CH_4$ mixtures, Chem. Eng. J. 133 (2007) 121-131.

[8]     R. Krishna, J.M. van Baten, Insights into diffusion of gases in zeolites gained from molecular dynamics simulations, Microporous Mesoporous Mater. 109 (2008) 91-108.

[9]     R. Krishna, J.M. van Baten, Onsager coefficients for binary mixture diffusion in nanopores, Chem. Eng. Sci. 63 (2008) 3120-3140.

[10]    R. Krishna, J.M. van Baten, Influence of segregated adsorption on mixture diffusion in DDR zeolite, Chem. Phys. Lett. 446 (2007) 344-349.

[11]    R. Krishna, J.M. van Baten, Segregation effects in adsorption of $CO_2$ containing mixtures and their consequences for separation selectivities in cage-type zeolites, Sep. Purif. Technol. 61 (2008) 414-423.

[12]    R. Krishna, J.M. van Baten, A molecular dynamics investigation of a variety of influences of temperature on diffusion in zeolites, Microporous Mesoporous Mater. XX (2009) XXX-XXX. (http://dx.doi.org/10.1016/j.micromeso.2009.01.015)

[13]    E. García-Pérez, J.B. Parra, C.O. Ania, A. García-Sánchez, J.M. Van Baten, R. Krishna, D. Dubbeldam, S. Calero, A computational study of $CO_2$, $N_2$ and $CH_4$ adsorption in zeolites, Adsorption 13 (2007) 469-476.

[14]    S. Calero, D. Dubbeldam, R. Krishna, B. Smit, T.J.H. Vlugt, J.F.M. Denayer, J.A. Martens, T.L.M. Maesen, Understanding the role of sodium during adsorption. A force field for alkanes in sodium exchanged faujasites, J. Am. Chem. Soc. 126 (2004) 11377-11386.

[15]    E. García-Pérez, D. Dubbeldam, T.L.M. Maesen, S. Calero, Influence of cation Na/Ca ratio on adsorption in LTA 5A: A systematic molecular simulations study of alkane chain length, J. Phys. Chem. B 110 (2006) 23968-23976.

[16]    A. García-Sánchez, E. García-Pérez, D. Dubbeldam, R. Krishna, S. Calero, A Simulation Study of Alkanes in Linde Type A Zeolites, Adsorpt. Sci. Technol. 25 (2007) 417-427.

[17]    R. Krishna, J.M. van Baten, E. García-Pérez, S. Calero, Incorporating the loading dependence of the Maxwell-Stefan diffusivity in the modeling of $CH_4$ and $CO_2$ permeation across zeolite membranes, Ind. Eng. Chem. Res. 46 (2007) 2974-2986.

[18]    R. Krishna, J.M. van Baten, Diffusion of hydrocarbon mixtures in MFI zeolite: Influence of intersection blocking, Chem. Eng. J. 140 (2008) 614-620.

[19] C. Chmelik, L. Heinke, J. Kärger, D.B. Shah, W. Schmidt, J.M. van Baten, R. Krishna, Inflection in the loading dependence of the Maxwell-Stefan diffusivity of iso-butane in MFI zeolite, Chem. Phys. Lett. 459 (2008) 141-145.

[20] K. Li, D.H. Olson, J.Y. Lee, W. Bi, K. Wu, T. Yuen, Q. Xu, J. Li, Multifunctional Microporous MOFs Exhibiting Gas/Hydrocarbon Adsorption Selectivity, Separation Capability and Three-Dimensional Magnetic Ordering, Adv. Funct. Mater. 18 (2008) 2205-2214.

[21] D.N. Dybtsev, H. Chun, S.H. Yoon, D. Kim, K. Kim, Microporous Manganese Formate: A Simple Metal-Organic Porous Material with High Framework Stability and Highly Selective Gas Sorption Properties, J. Am. Chem. Soc. 126 (2004) 32-33.

[22] P.S. Bárcia, F. Zapata, J.A.C. Silva, A.E. Rodrigues, B. Chen, Kinetic Separation of Hexane Isomers by Fixed-Bed Adsorption with a Microporous Metal-Organic Framework, J. Phys. Chem. B 111 (2008) 6101-6103.

[23] J.Y. Lee, D.H. Olson, L. Pan, T.J. Emge, J. Li, Microporous Metal–Organic Frameworks with High Gas Sorption and Separation Capacity, Adv. Funct. Mater. 17 (2007) 1255-1262.

[24] H. Wang, J. Getzschmann, I. Senkovska, S. Kaskel, Structural Transformation and High Pressure Methane Adsorption of $Co_2(1,4-bdc)_2 dabco$, Microporous Mesoporous Mater. 116 (2008) 653-657.

[25] L. Alaerts, C.E.A. Kirschhock, M. Maes, M. van der Veen, V. Finsy, A. Depla, J.A. Martens, G.V. Baron, P.A. Jacobs, J.F.M. Denayer, D. De Vos, Selective Adsorption and Separation of Xylene Isomers and Ethylbenzene with the Microporous Vanadium(IV) Terephthalate MIL-47, Angew. Chem. Int. Ed. 46 (2007) 4293-4297.

[26] V. Finsy, H. Verelst, L. Alaerts, D. De Vos, P.A. Jacobs, G.V. Baron, J.F.M. Denayer, Pore-Filling-Dependent Selectivity Effects in the Vapor-Phase Separation of Xylene Isomers on the Metal-Organic Framework MIL-47, J. Am. Chem. Soc. 130 (2008) 7110-7118.

[27] K. Barthelet, J. Marrot, D. Riou, G. Férey, A Breathing Hybrid Organic - Inorganic Solid with Very Large Pores and High Magnetic Characteristics, Angew. Chem. Int. Ed. 41 (2007) 281-284.

[28] P. Horcajada, C. Serre, G. Maurin, N.A. Ramsahye, F. Balas, M. Vallet-Regí, M. Sebban, F. Taulelle, G. Férey, Flexible Porous Metal-Organic Frameworks for a Controlled Drug Delivery, J. Am. Chem. Soc. 130 (2008) 6774-6780.

[29] L. Pan, B. Parker, X. Huang, D.H. Olson, J.Y. Lee, J. Li, Zn(tbip) ($H_2$ tbip)=5-*tert*-Butyl Isophthalic Acid): A Highly Stable Guest-Free Microporous Metal Organic Framework with Unique Gas Separation Capability, J. Am. Chem. Soc. 128 (2006) 4180-4181.

[30] L. Pan, D.H. Olson, L.R. Ciemnolonski, R. Heddy, J. Li, Separation of Hydrocarbons with a Microporous Metal–Organic Framework, Angew. Chem. Int. Ed. 45 (2006) 616-619.

[31] D. Dubbeldam, K.S. Walton, D.E. Ellis, R.Q. Snurr, Exceptional Negative Thermal Expansion in Isoreticular Metal–Organic Frameworks, Angew. Chem. Int. Ed. 46 (2007) 4496-4499.

[32] D. Dubbeldam, H. Frost, K.S. Walton, R.Q. Snurr, Molecular simulation of adsorption sites of light gases in the metal-organic framework IRMOF-1, Fluid Phase Equilib. 261 (2007) 152-161.

[33] S.S.Y. Chui, S.M.F. Lo, J.P.H. Charmant, A.G. Orpen, I.D. Williams, A chemically functionalizable nanoporous material $[Cu_3(TMA)_2(H2O)_3]_n$, Science 283 (1999) 1148-1150.

[34] Q. Yang, C. Zhong, Electrostatic-Field-Induced Enhancement of Gas Mixture Separation in Metal-OrganicFrameworks: A Computational Study, ChemPhysChem 7 (2006) 1417-1421.

[35] J.M. van Baten, R. Krishna, MD animations of diffusion in nanoporous materials, University of Amsterdam, Amsterdam, http://www.science.uva.nl/research/cr/animateMD/, 7 April 2009.

[36] A.K. Rappé, C.J. Casewit, K.S. Colwel, W.A. Goddard, W.M. Skiff, UFF, a Full Periodic Table Force Field for Molecular Mechanics and Molecular Dynamics Simulations, J. Am. Chem. Soc. 114 (1992) 10024-10035.

[37] S.L. Mayo, B.D. Olafson, W.A. Goddard, DREIDING: A Generic Force Field for Molecular Simulations, J. Phys. Chem. 94 (1990) 8897-8909.

[38]  I. Senkovska, S. Kaskel, High pressure methane adsorption in the metal-organic frameworks $Cu_3(btc)_2$, $Zn_2(bdc)_2dabco$, and $Cr_3F(H_2O)_2O(bdc)_3$, Microporous Mesoporous Mater. 112 (2008) 108-115.

[39]  H.M. El-Kaderi, J.R. Hunt, J.L. Mendoza-Cortés, A.P. Adrien P. Côté, R.E. Robert E. Taylor, M. O'Keeffe, O.M. Yaghi, Designed Synthesis of 3D Covalent Organic Frameworks, Science 316 (2007) 268-272.

[40]  R. Babarao, J. Jiang, Exceptionally high $CO_2$ storage in covalent-organic frameworks: Atomistic simulation study, Energy Environ. Sci. 1 (2008) 139-143.

[41]  R. Krishna, J.M. van Baten, An investigation of the characteristics of Maxwell-Stefan diffusivities of binary mixtures in silica nanopores, Chem. Eng. Sci. 64 (2009) 870-882.

[42]  B. Coasne, F. Di Renzo, A. Galarneau, R.J.M. Pellenq, Adsorption of Simple Fluid on Silica Surface and Nanopore: Effect of Surface Chemistry and Pore Shape, Langmuir 24 (2008) 7285-7293.

[43]  A.L. Myers, P.A. Monson, Adsorption in Porous Materials at High Pressure: Theory and Experiment, Langmuir 18 (2002) 10261-10273.

[44]  R. Babarao, Z. Hu, J. Jiang, S. Chempath, S.I. Sandler, Storage and separation of $CO_2$ and $CH_4$ in silicalite, $C_{168}$ schwarzite, and IRMOF-1: A comparative study from Monte Carlo simulation, Langmuir 23 (2007) 659-666.

[45]  D. Frenkel, B. Smit, Understanding molecular simulations: from algorithms to applications, Academic Press, 2nd Edition, San Diego, 2002.

[46]  O. Talu, A.L. Myers, Molecular Simulation of Adsorption: Gibbs Dividing Surface and Comparison with Experiment, A.I.Ch.E.J. 47 (2001) 1160-1168.

[47]  W. Smith, T.R. Forester, I.T. Todorov, The DL_POLY Molecular Simulation Package, Warrington, England, http://www.cse.clrc.ac.uk/msi/software/DL_POLY/index.shtml, March 2006.

[48]  SARA, Computing & Networking Services, Amsterdam, https://subtrac.sara.nl/userdoc/wiki/lisa/description, 16 January 2008.

[49]  R. Krishna, J.M. van Baten, Diffusion of alkane mixtures in zeolites. Validating the Maxwell-Stefan formulation using MD simulations, J. Phys. Chem. B 109 (2005) 6386-6396.

[50]  J.M. van Baten, R. Krishna, Entropy effects in adsorption and diffusion of alkane isomers in mordenite: An investigation using CBMC and MD simulations, Microporous Mesoporous Mater. 84 (2005) 179-191.

[51]  R. Krishna, J.M. van Baten, Describing binary mixture diffusion in carbon nanotubes with the Maxwell-Stefan equations. An investigation using molecular dynamics simulations, Ind. Eng. Chem. Res. 45 (2006) 2084-2093.

[52]  R. Krishna, J.M. van Baten, The Darken relation for multicomponent diffusion in liquid mixtures of linear alkanes. An investigation using Molecular Dynamics (MD) simulations, Ind. Eng. Chem. Res. 44 (2005) 6939-6947.

[53]  R. Krishna, J.M. van Baten, Validating the Darken relation for diffusivities in fluid mixtures of varying densities by use of MD simulations, Chem Eng Technol 29 (2006) 761-765.

[54]  L.S. Darken, Diffusion, Mobility and Their Interrelation through Free Energy in Binary Metallic Systems, Trans. Inst. Min. Metall. Engrs 175 (1948) 184-201.

[55]  A.I. Skoulidas, D.S. Sholl, R. Krishna, Correlation effects in diffusion of $CH_4/CF_4$ mixtures in MFI zeolite. A study linking MD simulations with the Maxwell-Stefan formulation, Langmuir 19 (2003) 7977-7988.

[56]  S. Chempath, R. Krishna, R.Q. Snurr, Nonequilibrium MD simulations of difusion of binary mixtures containing short n-alkanes in faujasite, J. Phys. Chem. B 108 (2004) 13481-13491.

[57]  R. Krishna, Multicomponent surface diffusion of adsorbed species - A description based on the generalized Maxwell-Stefan equations, Chem. Eng. Sci. 45 (1990) 1779-1791.

[58]  F. Leroy, H. Jobic, Influence of extra-framework cations on the diffusion of alkanes in silicalite: Comparison between quasi-elastic neutron scattering and molecular simulations, Chem. Phys. Lett. 406 (2005) 375-380.

[59] N. Hedin, G.J. DeMartin, W.J. Roth, K.G. Strohmaier, S.C. Reyes, PFG NMR self-diffusion of small hydrocarbons in high silica DDR, CHA and LTA structures, Microporous Mesoporous Mater. 109 (2008) 327-334.

[60] N. Hedin, G.J. DeMartin, K.G. Strohmaier, S.C. Reyes, PFG NMR self-diffusion of propylene in ITQ-29, CaA and NaCaA: Window size and cation effects, Microporous Mesoporous Mater. 98 (2007) 182-188.

[61] S. Fritzsche, R. Haberlandt, J. Kärger, H. Pfeifer, K. Heinzinger, M. Wolfsberg, Influence of Exchangeable Cations on the Diffusion of Neutral Diffusants in Zeolites of Type LTA - an MD Study, Chem. Phys. Lett. 242 (1995) 361-366.

[62] H.W. Habgood, The kinetics of molecular sieve action.  Sorption of nitrogen-methane mixtures by Linde molecular sieve 4A, Canad. J. Chem. 36 (1958) 1384-1397.

[63] J. Kärger, D.M. Ruthven, Diffusion in zeolites and other microporous solids, John Wiley, New York, 1992.

[64] R. Krishna, J.M. van Baten, Loading dependence of self-diffusivities of gases in zeolites, Chem. Eng. Technol. 30 (2007) 1235-1241.

[65] R. Krishna, J.M. van Baten, A molecular simulation study of commensurate – incommensurate adsorption of n-alkanes in cobalt formate frameworks, Mol. Simulation XX (2009) XXX-XXX. (http://dx.doi.org/10.1080/08927020902744672)

[66] S.K. Bhatia, D. Nicholson, Transport of Simple Fluids in Nanopores: Theory and Simulation, A.I.Ch.E.J. 52 (2006) 29-38.

Figure 1

# Potential for molecules

**H$_2$O**

$\theta_0$

q$^-$

r$_0$

q$^-$

q$^+$

$\theta_0$

q$^-$

q$^+$

q$^-$

**CO$_2$**

r$_0$
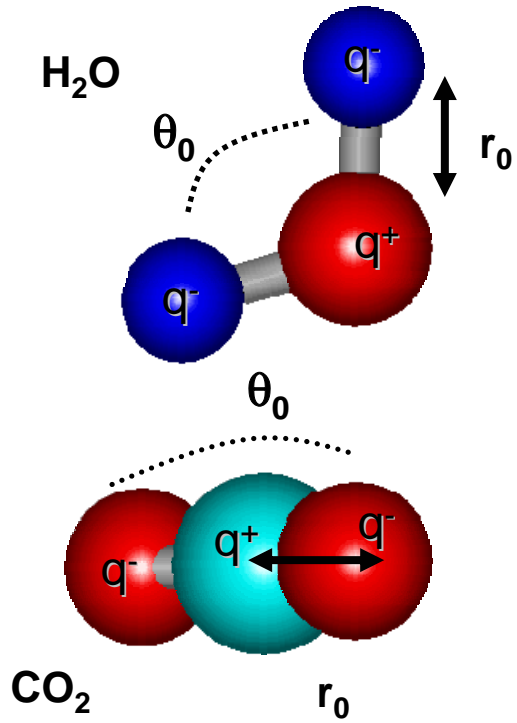
$$U = \sum_{\substack{bond \\ stretching}} \frac{1}{2}(r - r_0)^2 +$$

$$+ \sum_{\substack{bond \\ bending}} \frac{1}{2}k_\theta(\theta - \theta_0)^2 +$$

$$+ \sum_{torsions} \sum_{n=0}^{5} \eta_n \cos^n \phi +$$

$$+ \sum_{Coulombic} \frac{q_i q_j}{r_{ij}} +$$

$$+ \sum_{\substack{Lennard- \\ Jones}} \left[ \frac{A_{ij}}{r_{ij}^{12}} - \frac{B_{ij}}{r_{ij}^6} \right]$$

**The Coulombic term is relevant for molecules such as CO$_2$ and H$_2$O**

**United atom model (CH3, CH2… are single interaction centers)**

**Linear alkane**

r$_0$

$\theta_0$
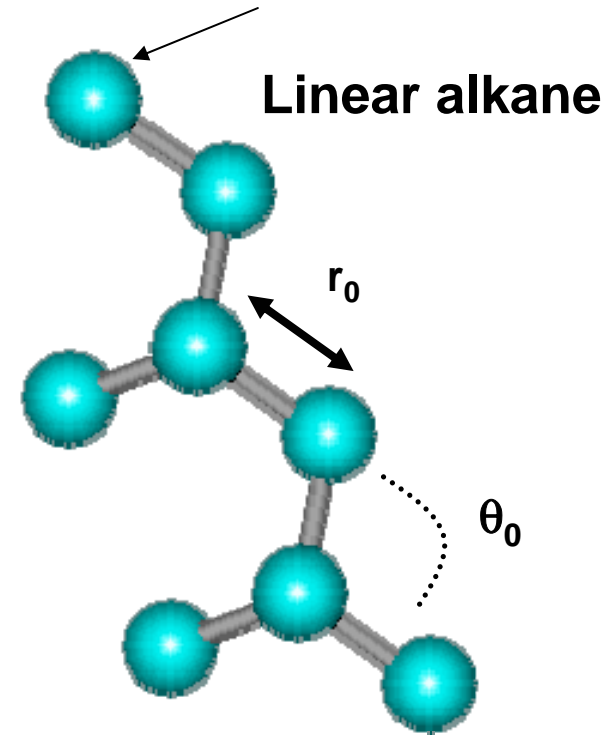
Figure 2

**Guest-host interactions**

Na$^+$

Ca$^{++}$

O

O

O

$q = -$

Si

$q = +$

Al

$q = +$

O

O

CH$_4$

**L-J and Coulomb interactions**

**Linear alkane**

q$^-$ q$^+$ q$^-$

CO$_2$
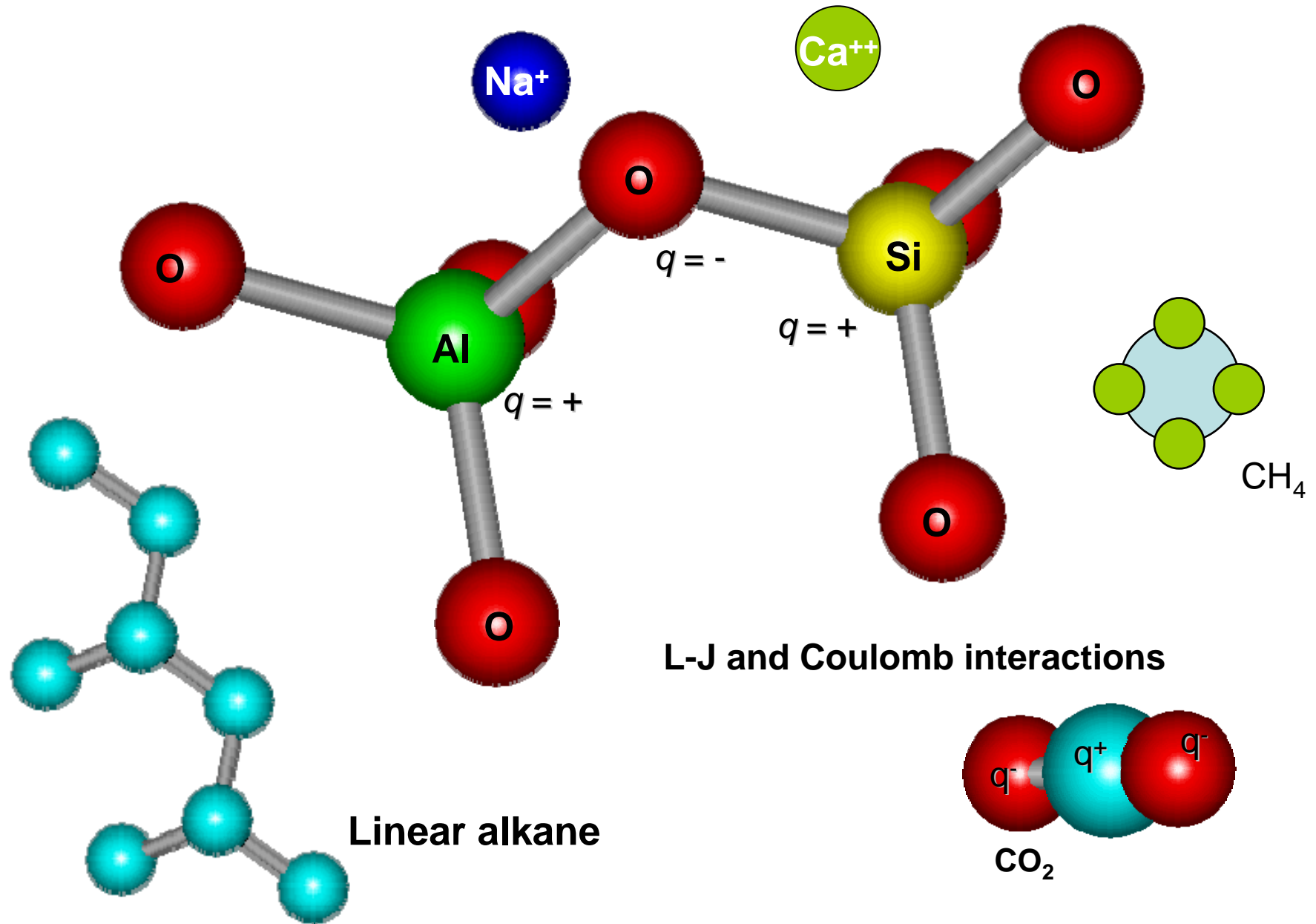
# Self-diffusivities in pure fluids, 300 K

Figure 3
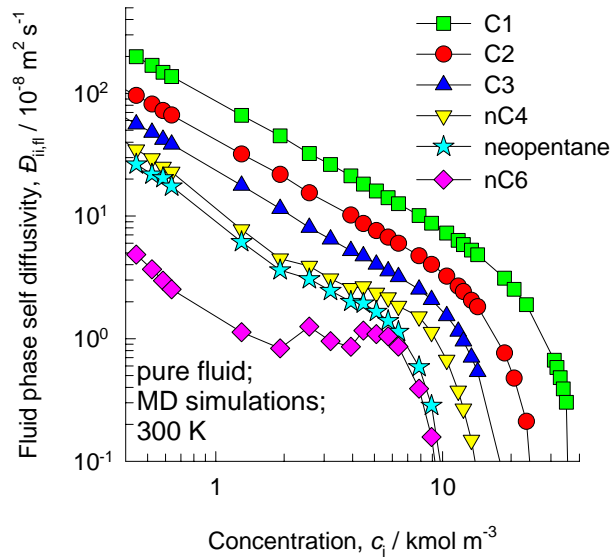
These data are for comparison with corresponding exchange coefficients in micro- and meso- porous materials
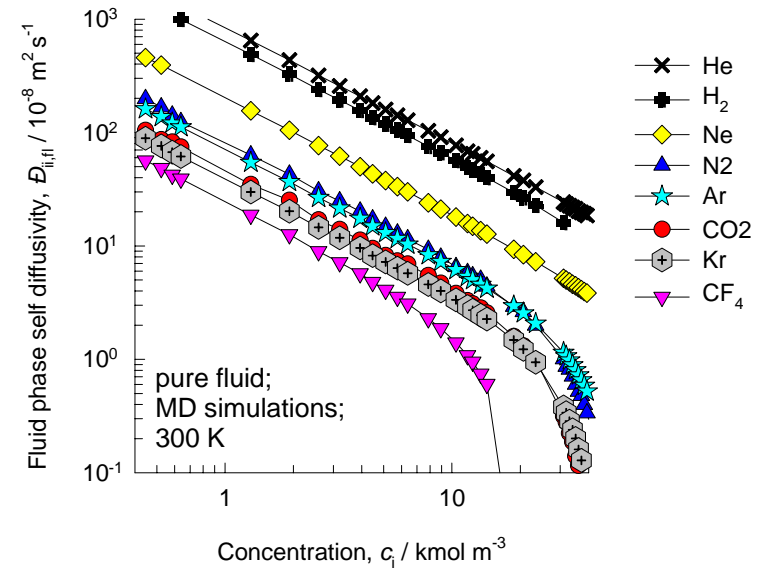
The sensitivity to the value of $\varepsilon/k_B$, for C1-C1 interactions is presented below. This data is used for analysing the sensitivity in the diffusion data for C1 in pores of 1.5, 2, and 3 nm.
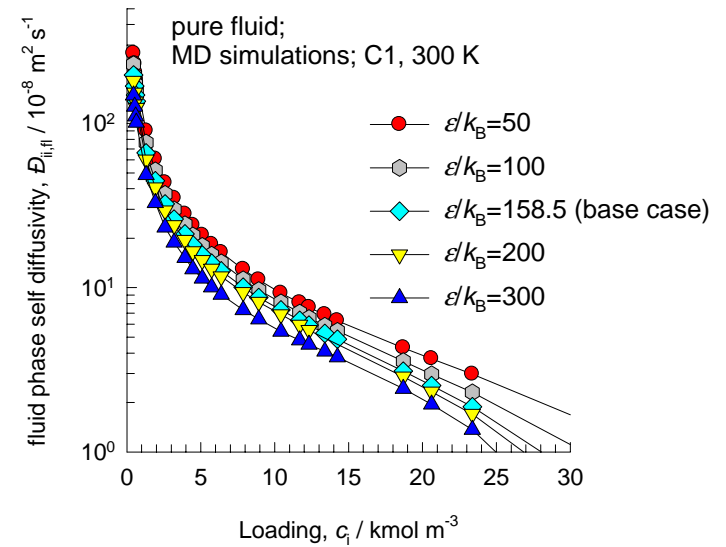
Figure 4
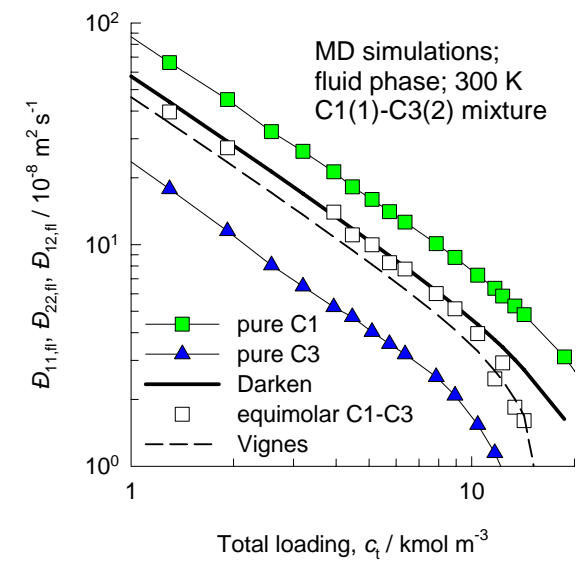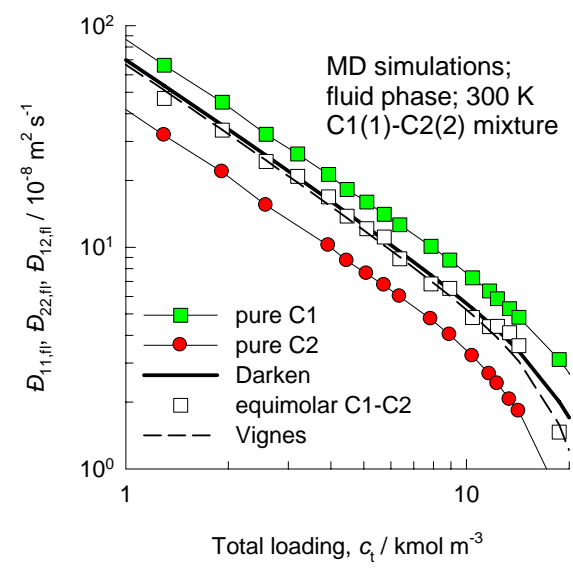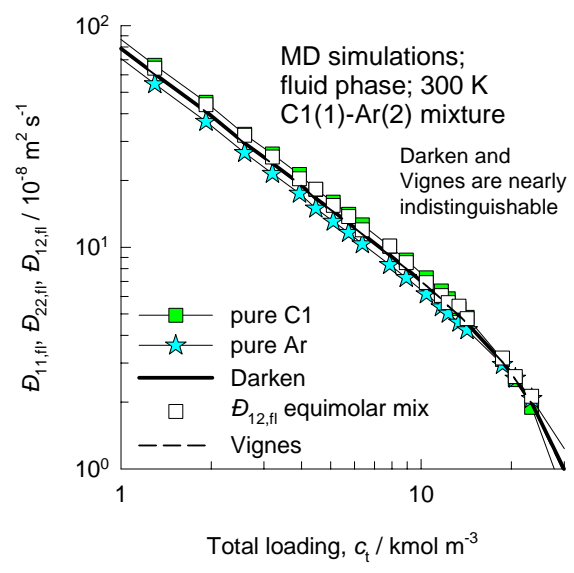
Test of Darken and Vignes interpolation formulae for fluid mixtures
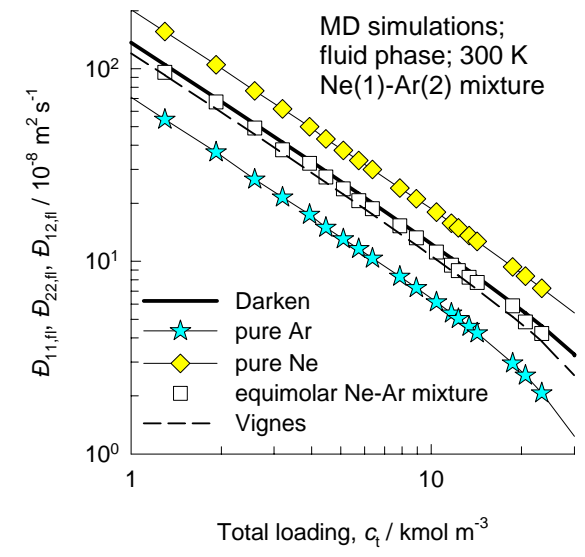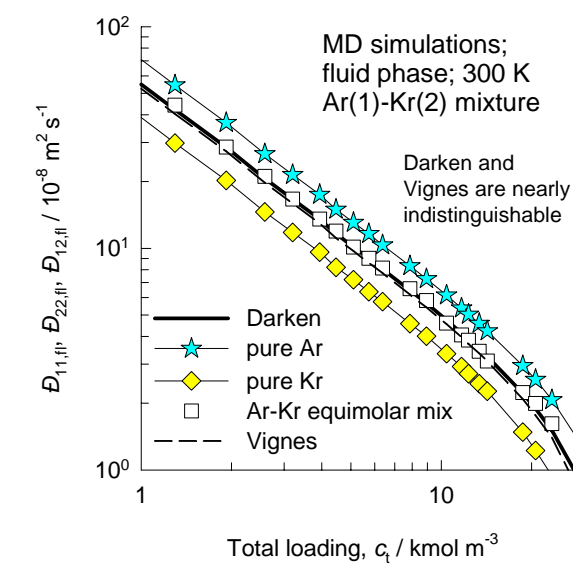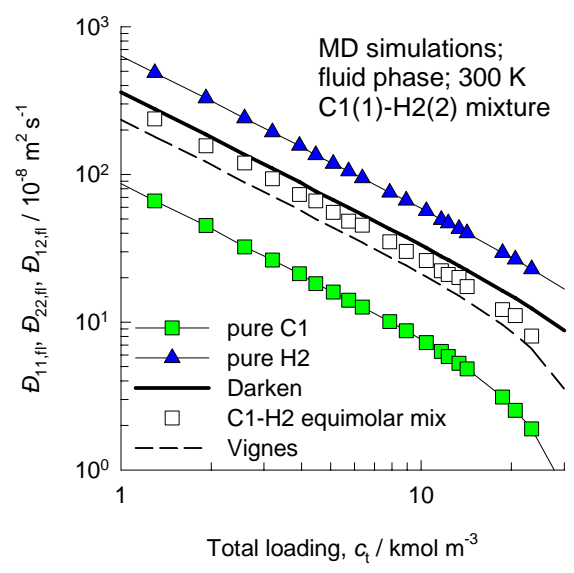
Figure 5
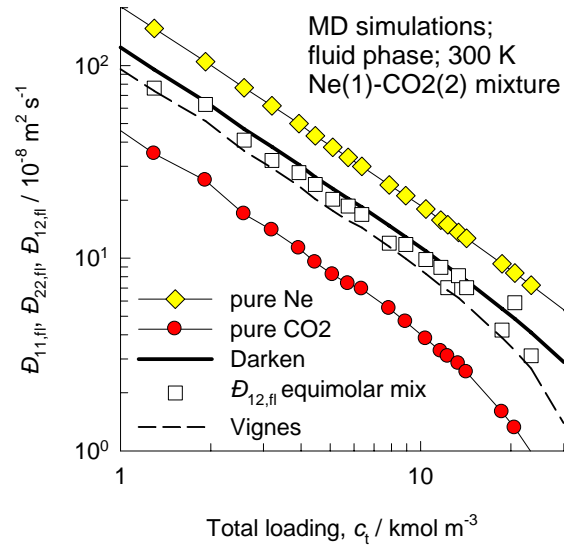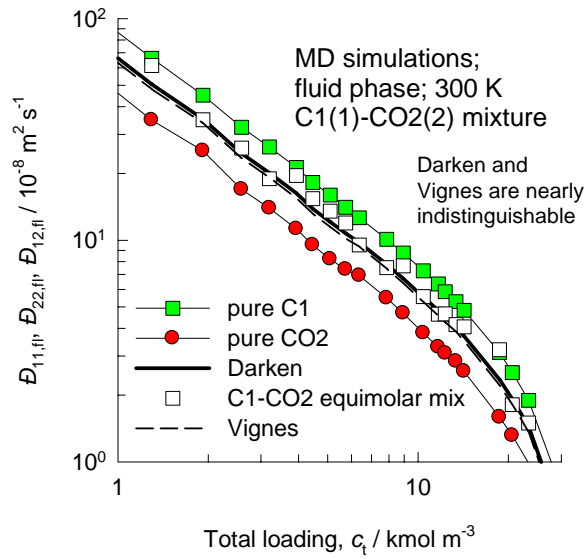
Test of Darken and Vignes interpolation formulae for fluid mixtures
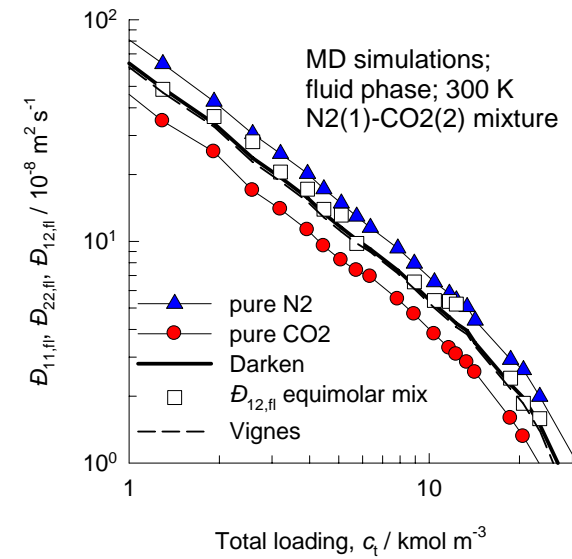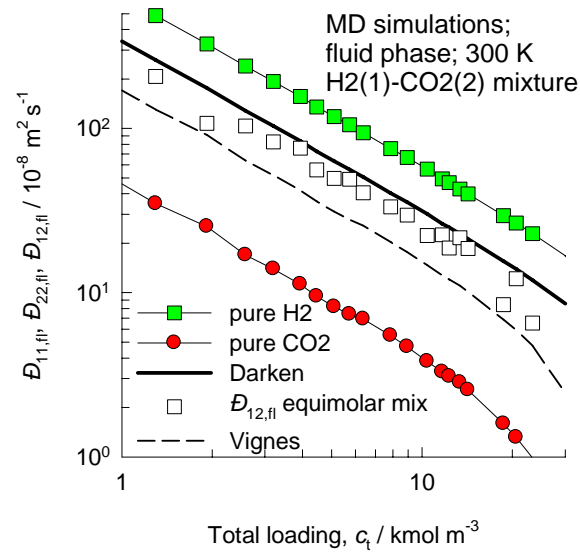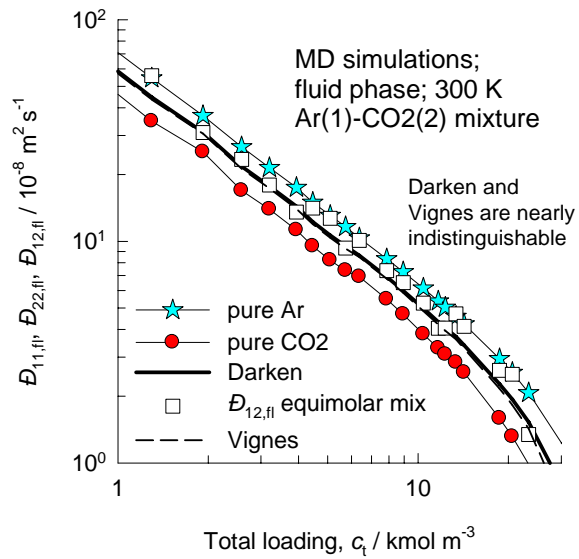
# Shear viscosity of pure fluids, 300 K

Figure 6



pure fluid;
MD simulations;
300 K

H2
Ar
C1
Kr
C2
C3
nC4
nC6

viscosity, $\eta_i$ / $10^{-6}$ Pa s

Concentration, $c_i$ / kmol m$^{-3}$
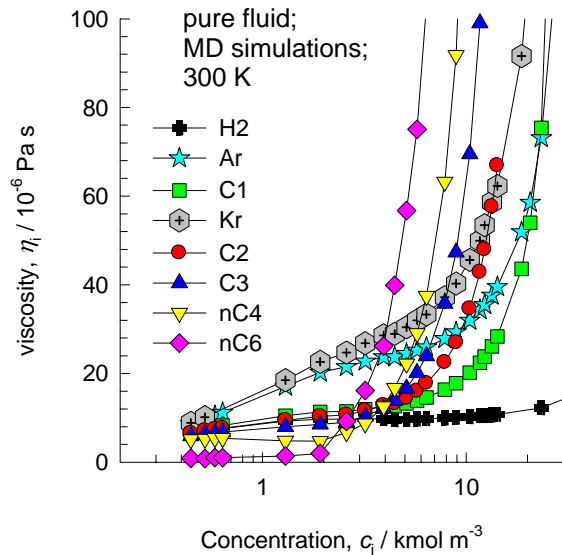
The data on viscosity is required for calculation of the viscous flow contribution in silica mesopores.

The sensitivity to the value of $\varepsilon/k_B$, for C1-C1 interactions is presented below.



viscosity, $\eta_i$ / $10^{-6}$ Pa s

$\varepsilon/k_B$=50
$\varepsilon/k_B$=100
$\varepsilon/k_B$=158.5 (base case)
$\varepsilon/k_B$=200
$\varepsilon/k_B$=300

pure fluid;
MD simulations; C1, 300 K

Loading, $c_i$ / kmol m$^{-3}$



viscosity, $\eta_i$ / $10^{-6}$ Pa s

$\varepsilon/k_B$=50
$\varepsilon/k_B$=100
$\varepsilon/k_B$=158.5 (base case)
$\varepsilon/k_B$=200
$\varepsilon/k_B$=300

pure fluid;
MD simulations; C1, 300 K

Loading, $c_i$ / kmol m$^{-3}$

# FAU

Figure 7

12-ring
window of FAU

7.4 Å  7.4 Å
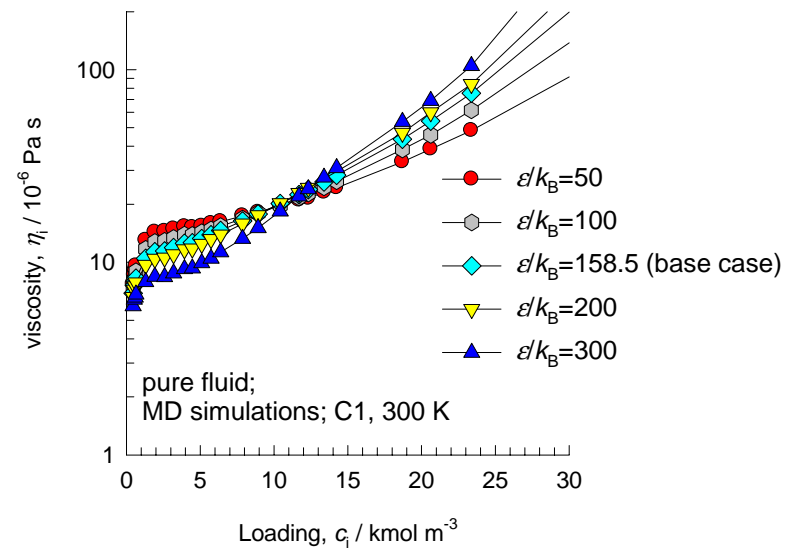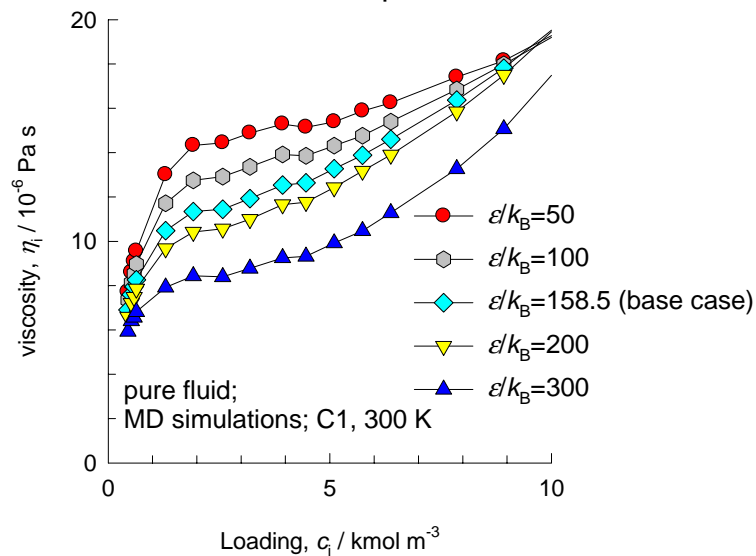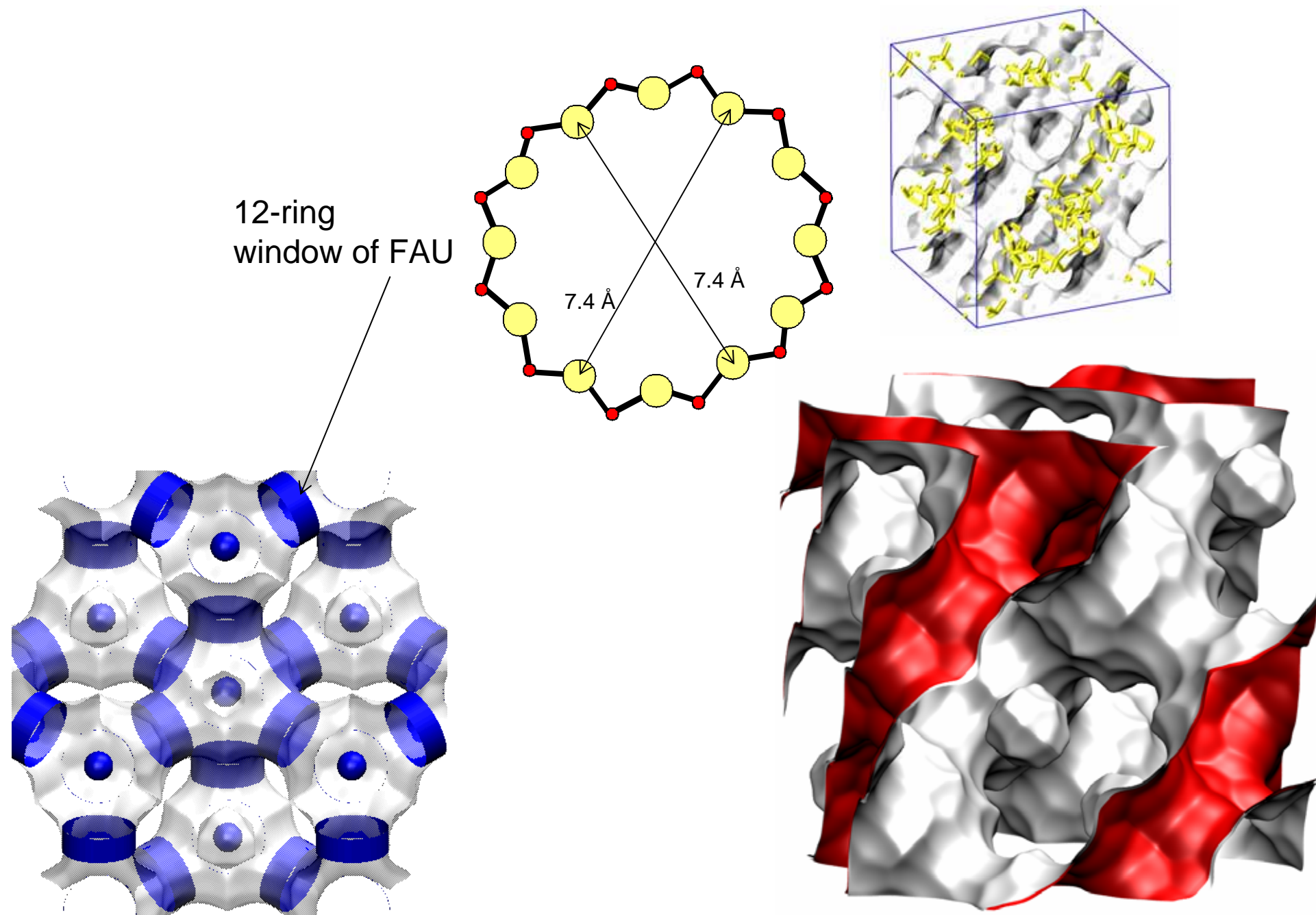
# NaY (148 Si, 48 Al, 48 Na+, Si/Al=3)

Figure 8
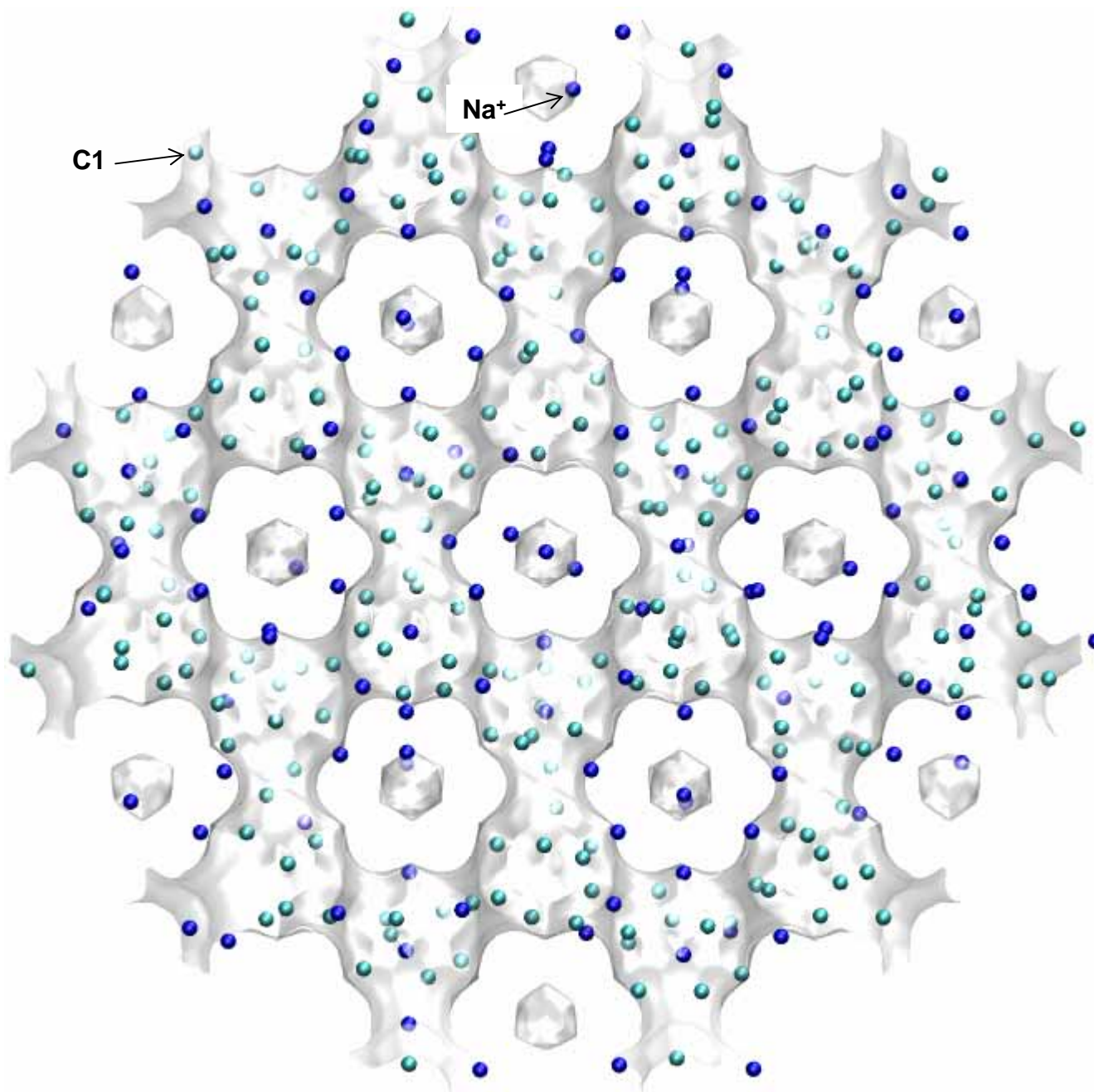
**NaX (106 Si, 86 Al, 86 Na+, Si/Al=1.23)**

Figure 9
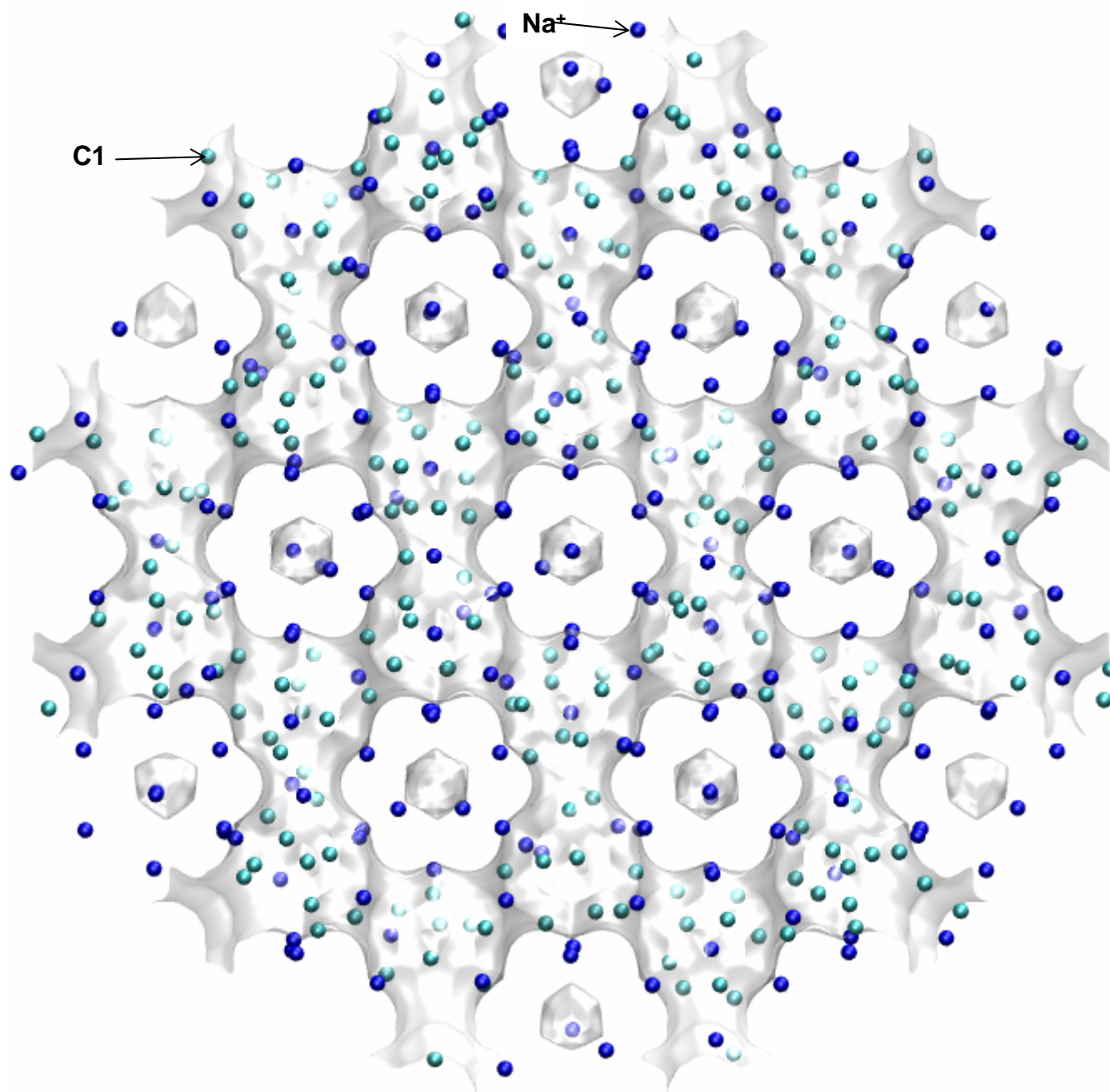
Figure 10
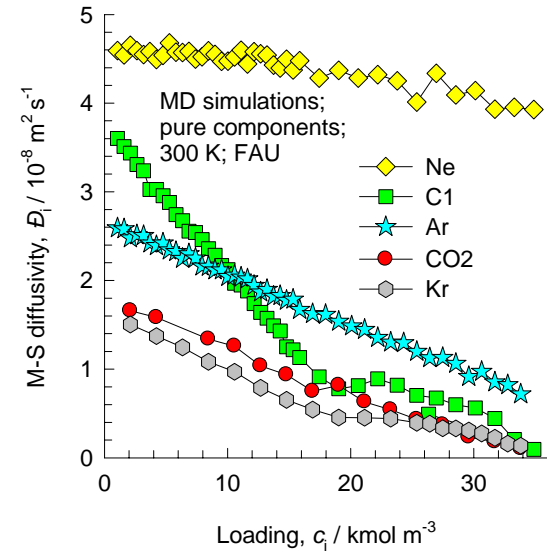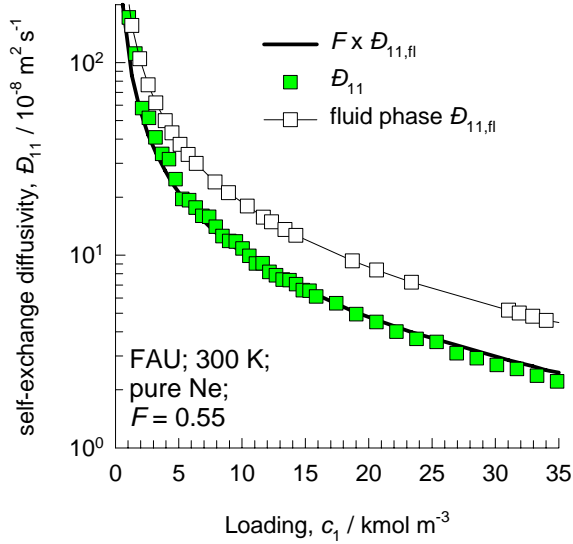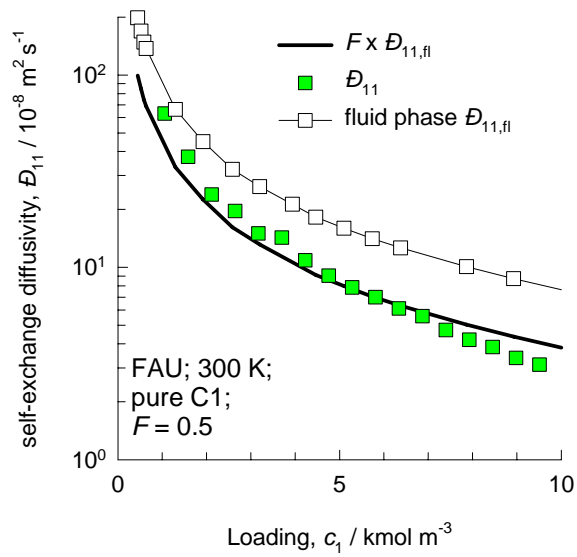
Data for all-silica FAU for unary diffusion
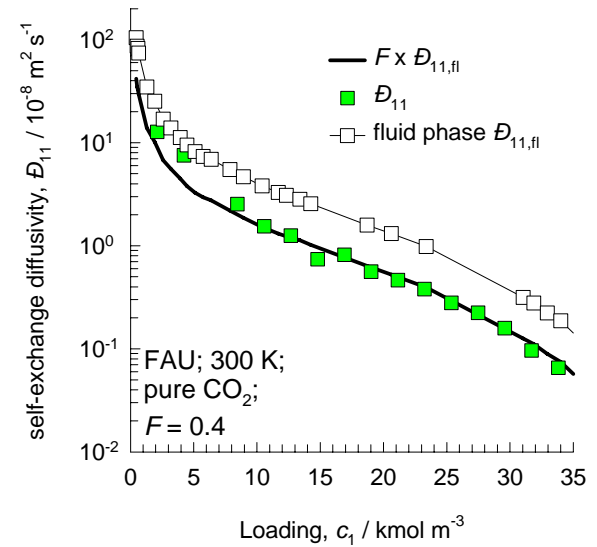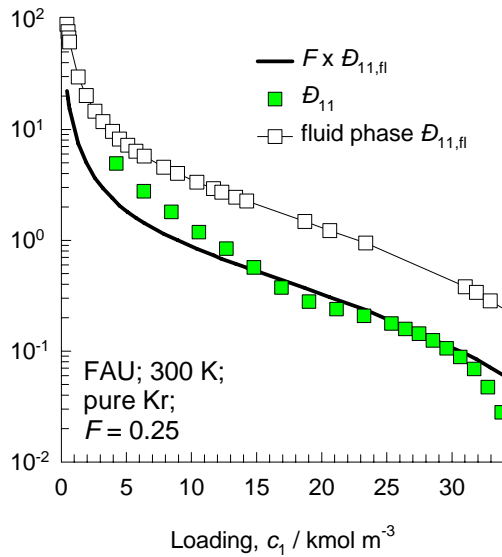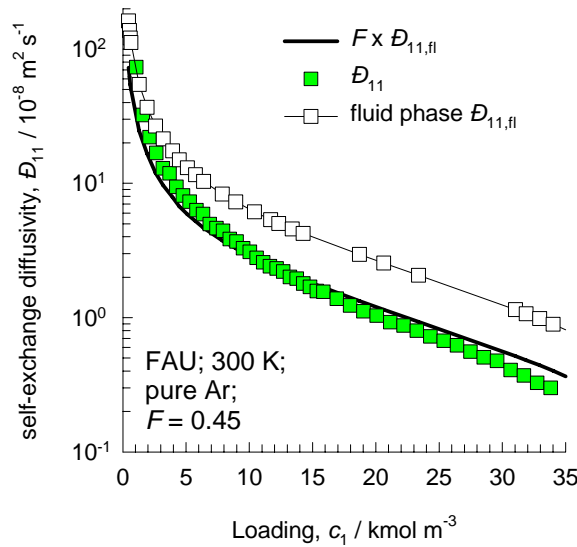
Figure 11
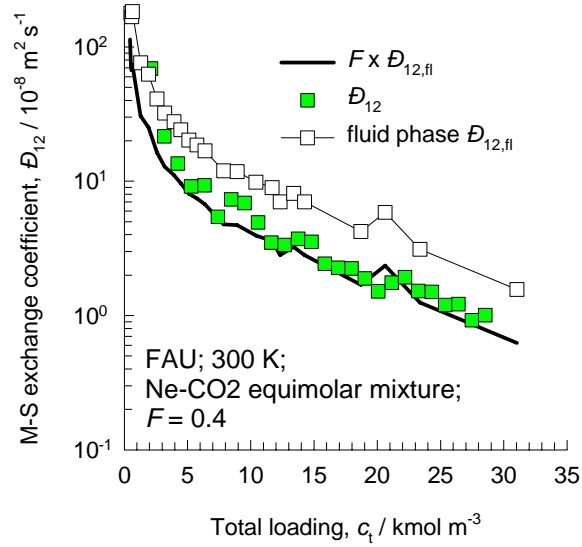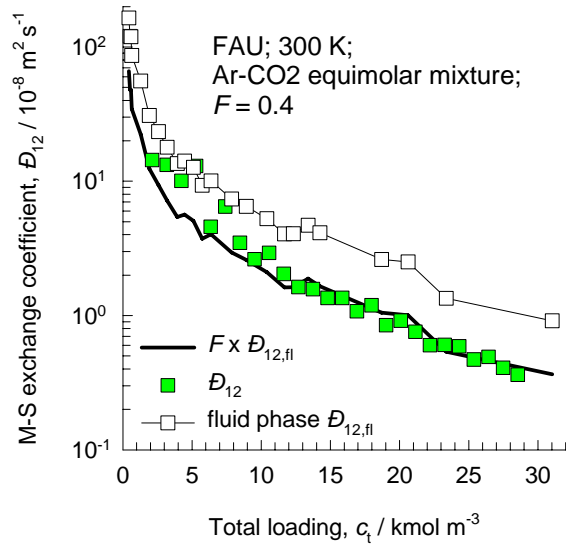
Data for all-silica FAU for binary mixtures
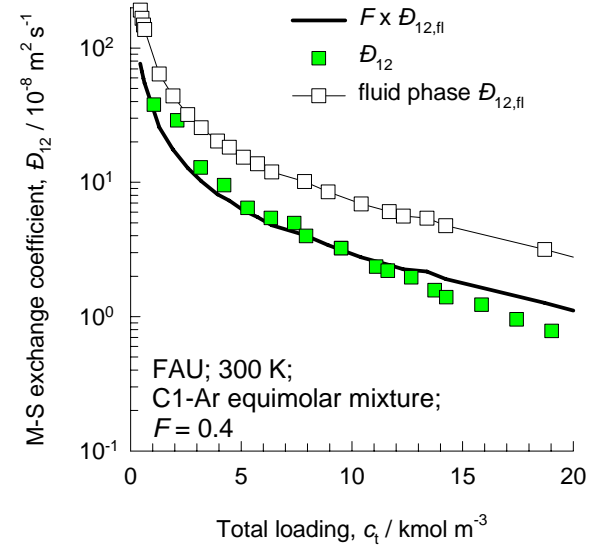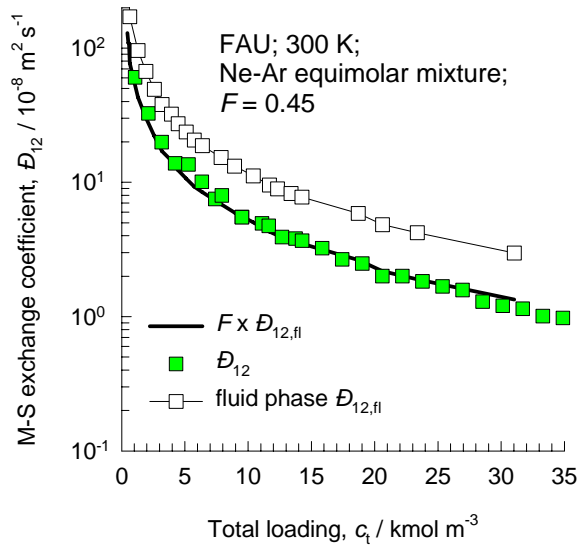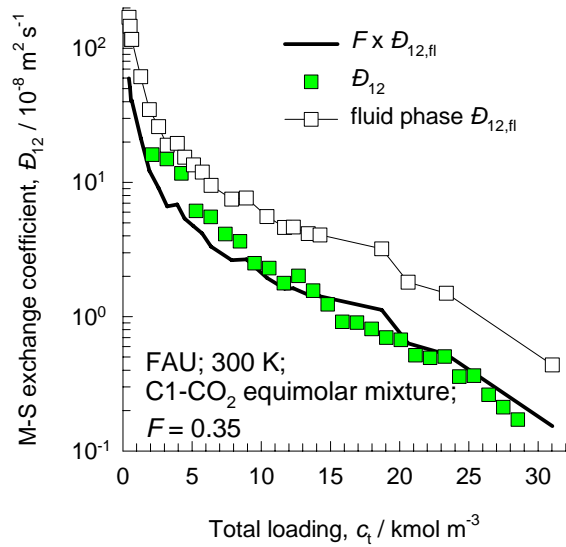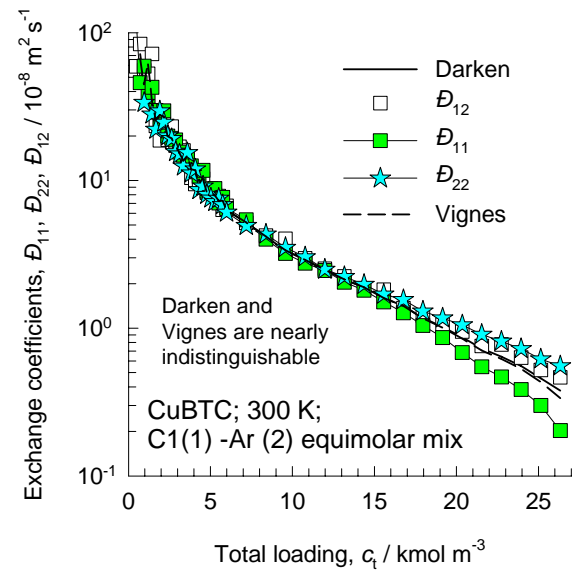
Figure 12
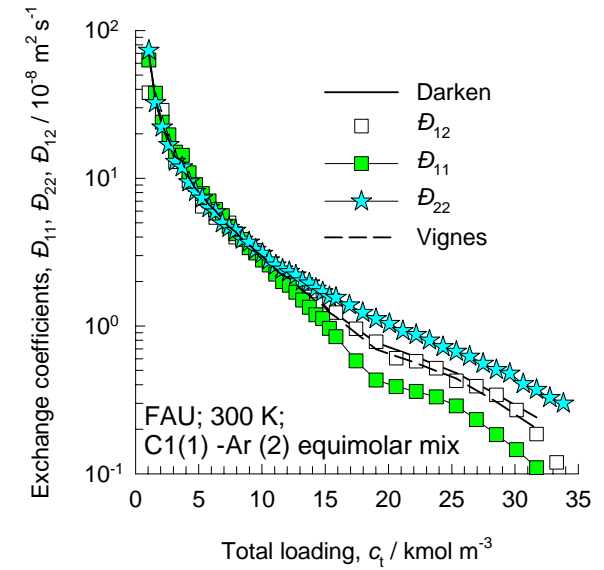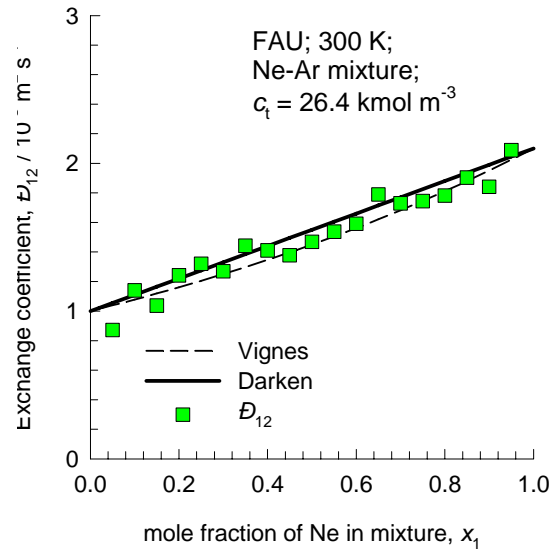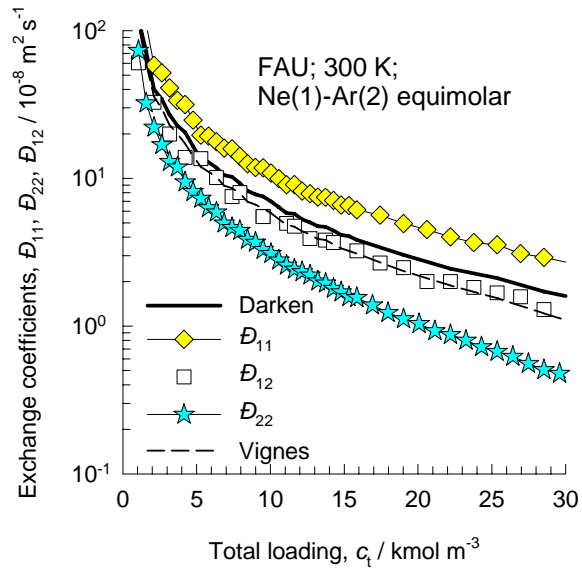
Test of Darken and Vignes interpolation formulae for FAU
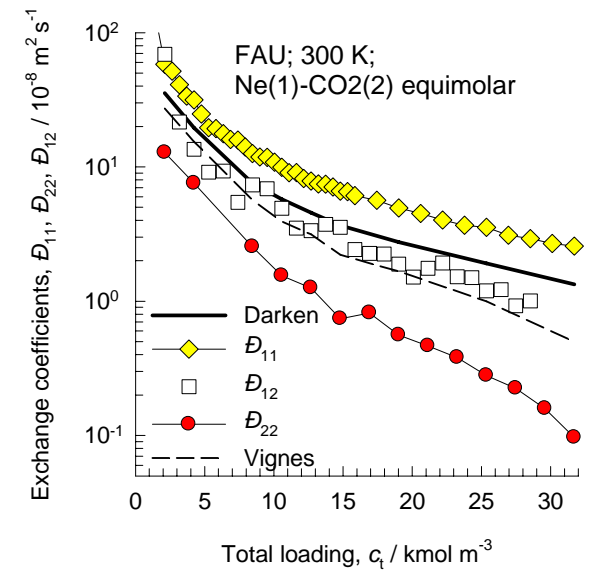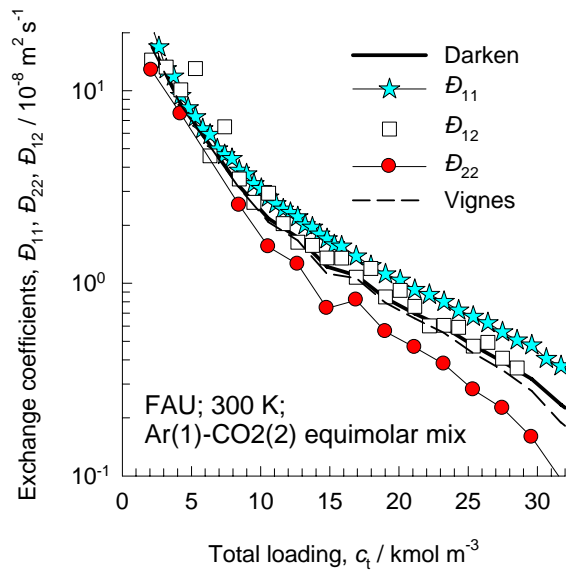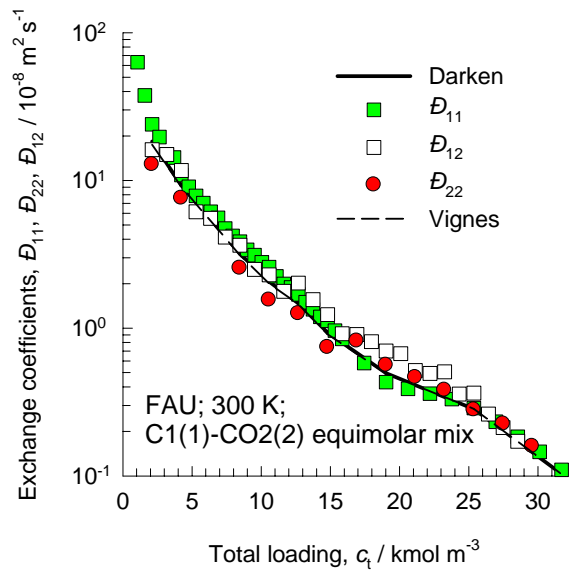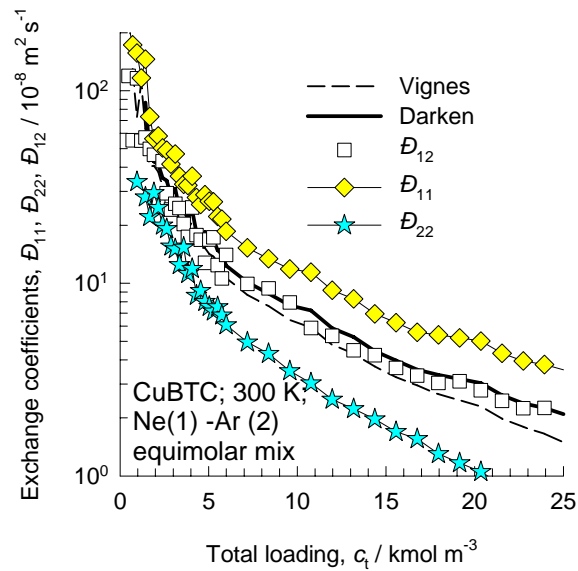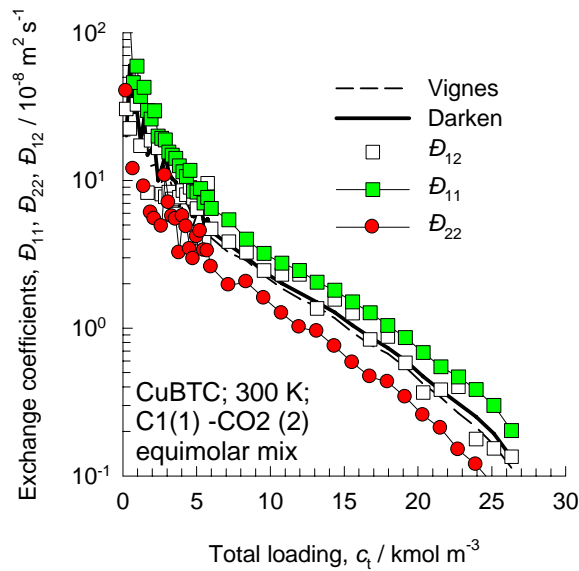
Figure 13

# Prediction of $D_{i,self}$ and $\Delta_{ij}$ in binary mixtures in FAU using Vignes interpolation and M-S model
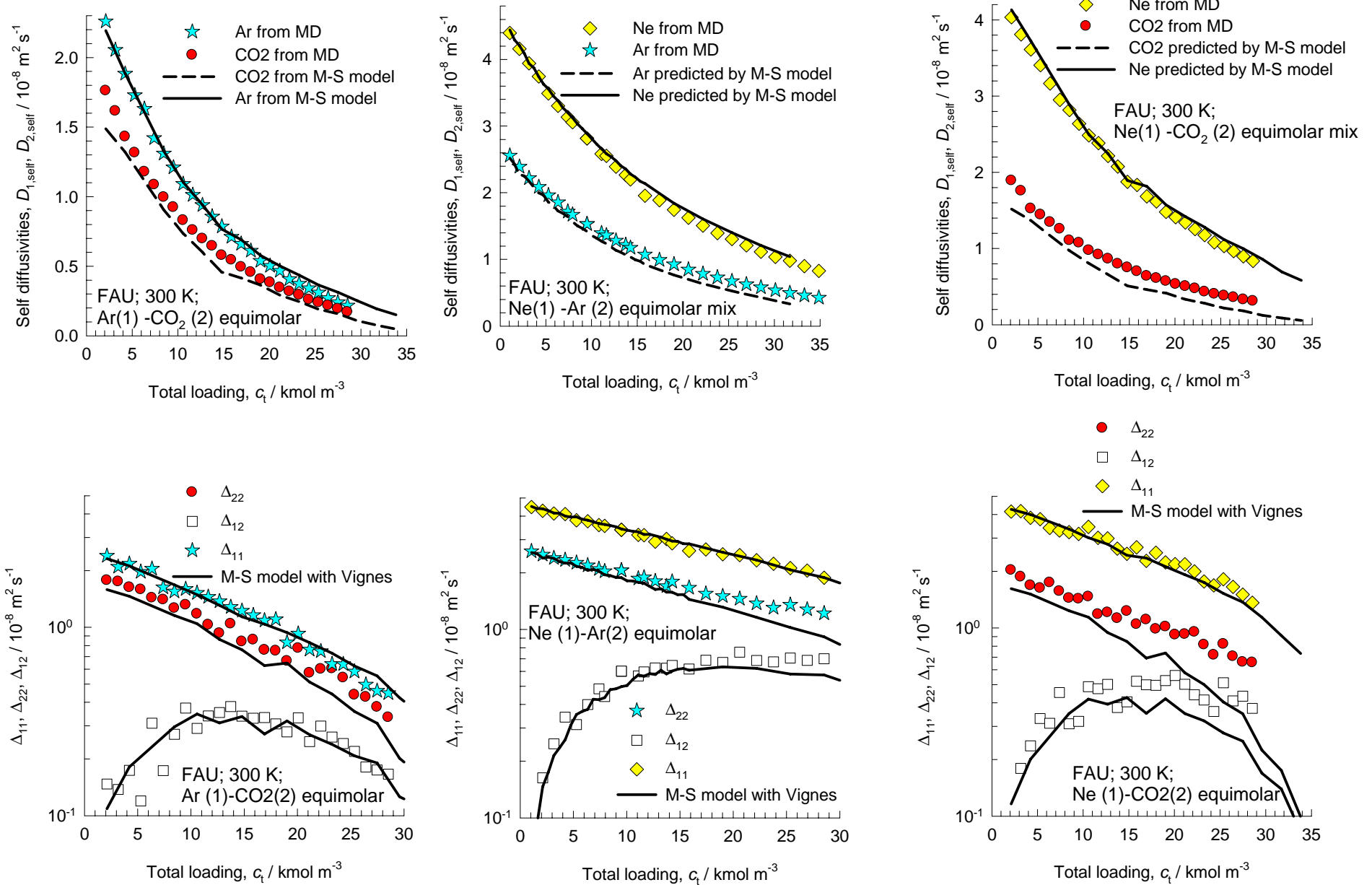
Figure 14
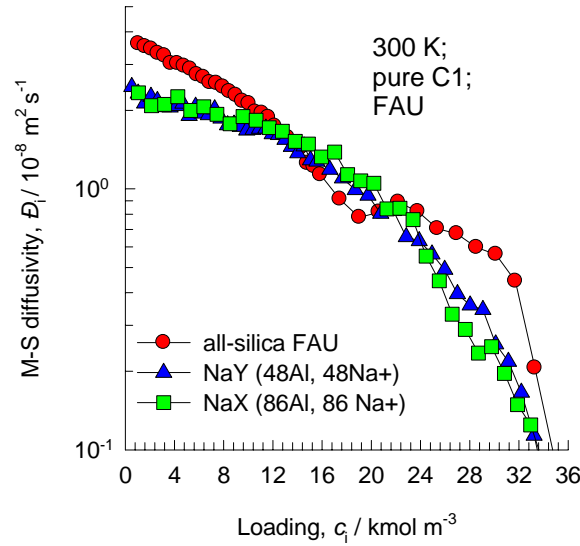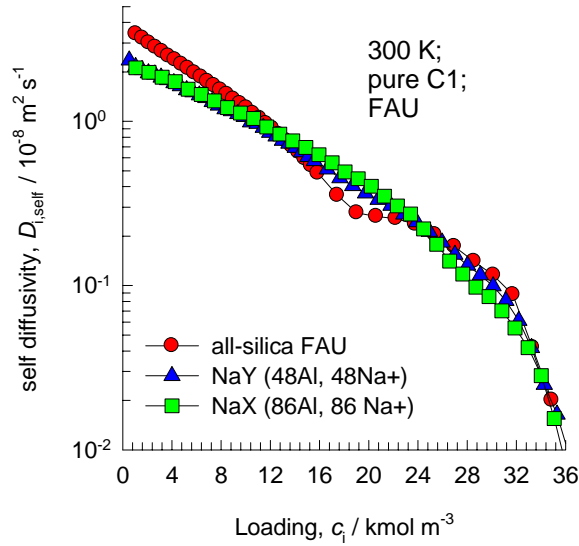


The presence of Na+ ions increases the adsorption strength; the more the number of Na+ ions, the higher the adsorption strength

GCMC simulations; pure component C1; 300 K; FAU
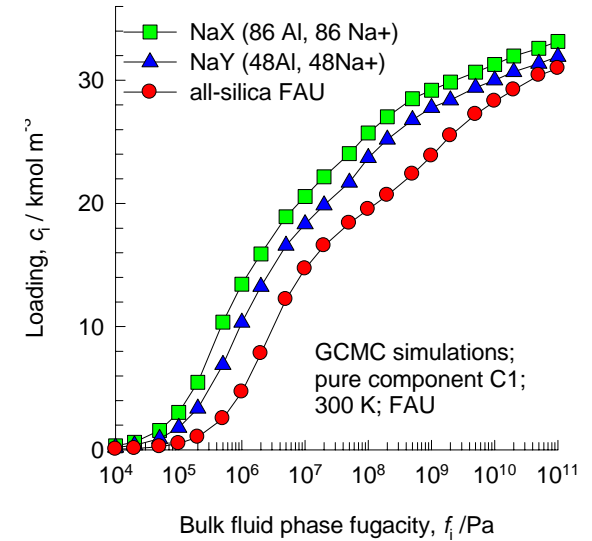
Comparison of all-silica FAU with Na+ exchanged FAU; Data for methane (C1) at 300 K
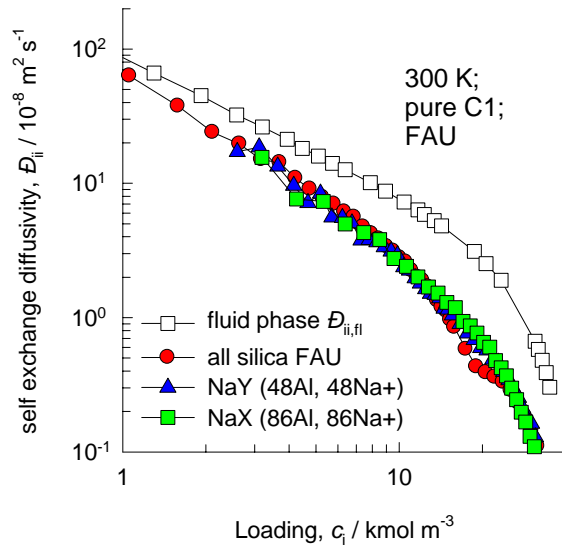
The exchange coefficient is independent of the number of Na+ present. The $F_i$ factor remains the same.
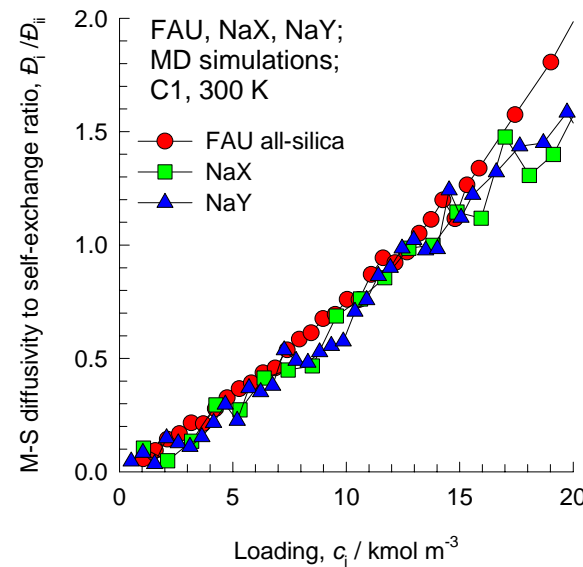
Figure 15
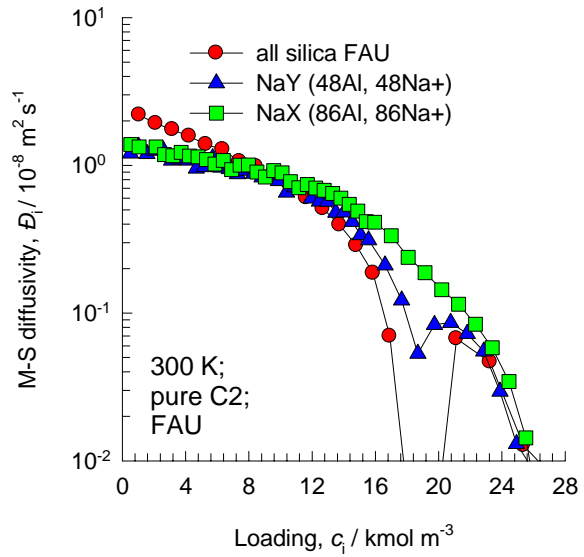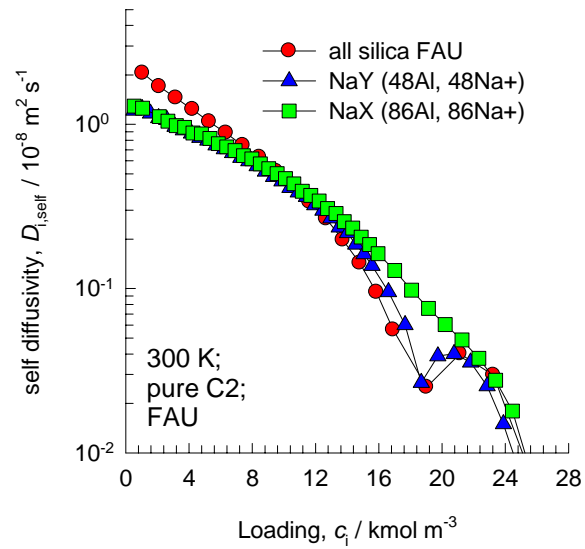
The presence of Na+ ions increases the adsorption strength.
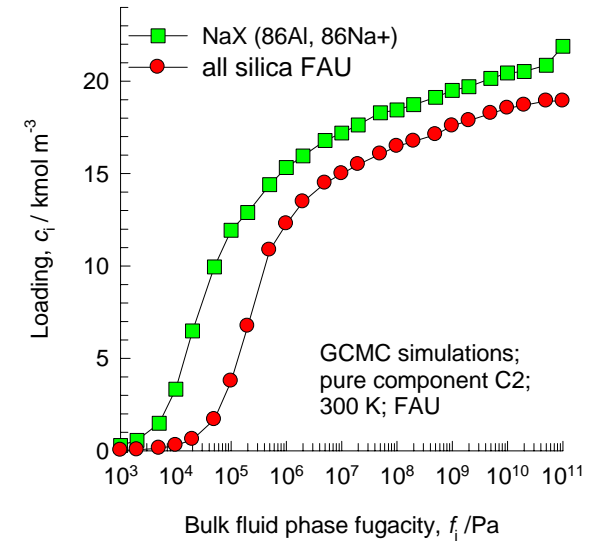
Comparison of all-silica FAU with Na+ exchanged FAU; Data for ethane (C2) at 300 K
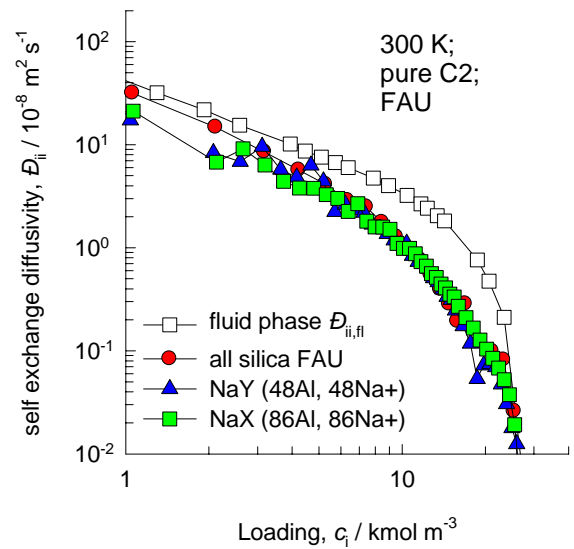
The exchange coefficient is independent of the number of Na+ present. The $F_i$ factor remains the same.
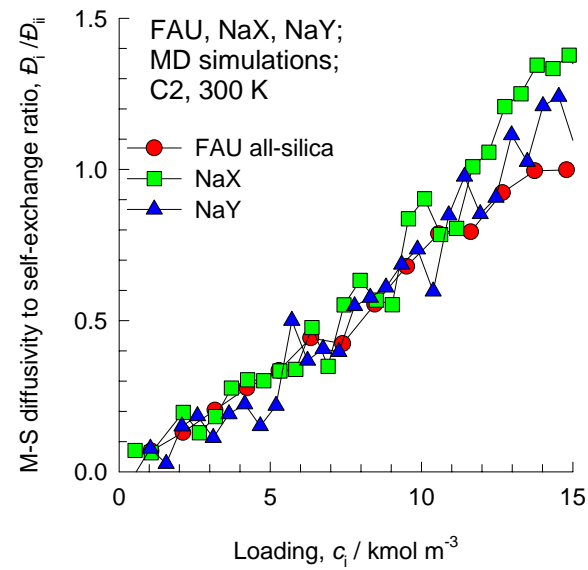
Figure 16
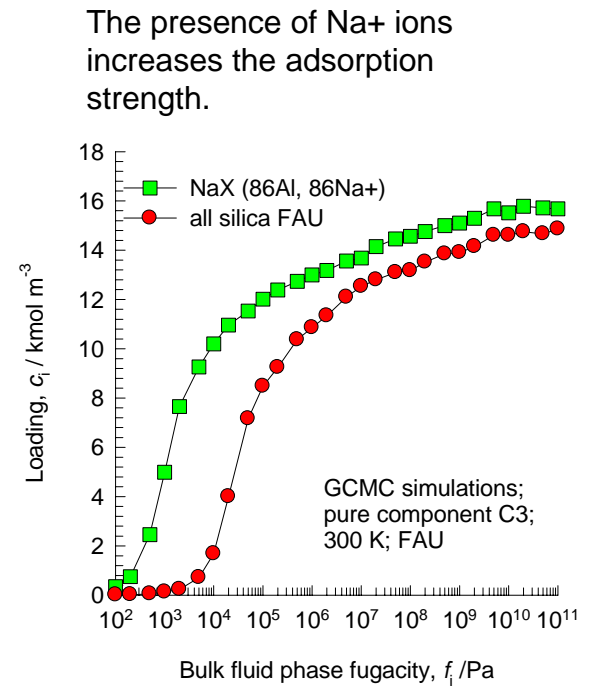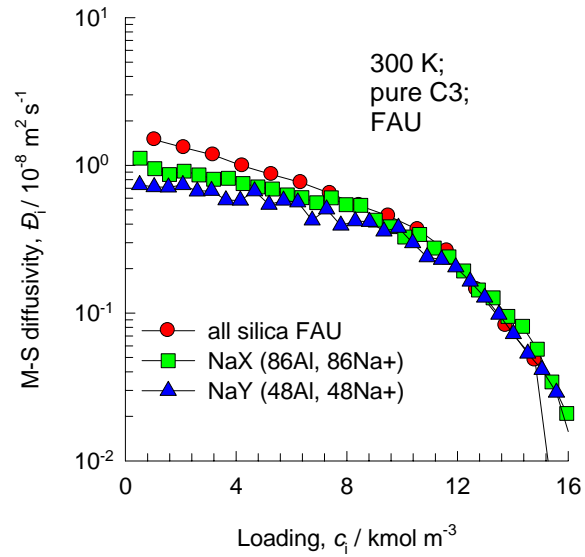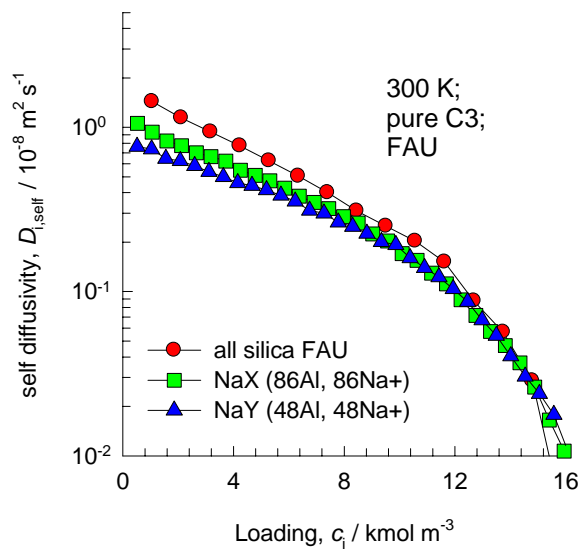
Comparison of all-silica FAU with Na+ exchanged FAU;
Data for propane (C3) at 300 K

The presence of Na+ ions increases the adsorption strength.
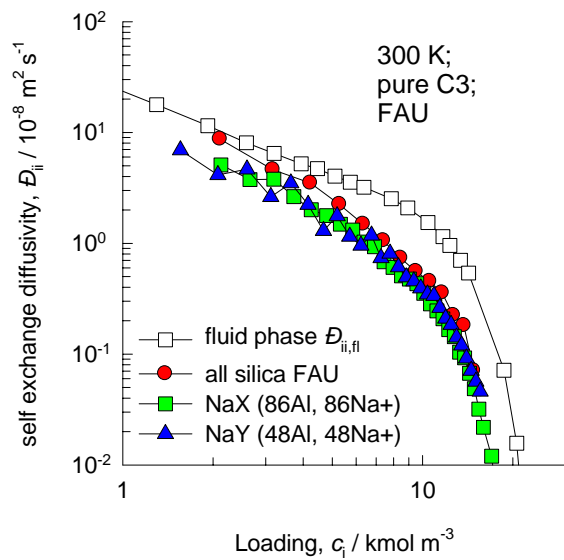
The exchange coefficient is nearly independent of the number of Na+ present.
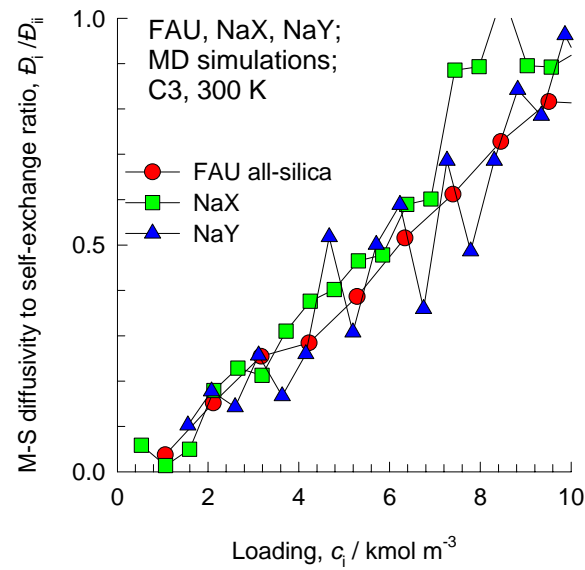
Figure 17

# Test of Darken and Vignes interpolation formulae for mixture diffusion in FAU (all silica), NaX, and NaY
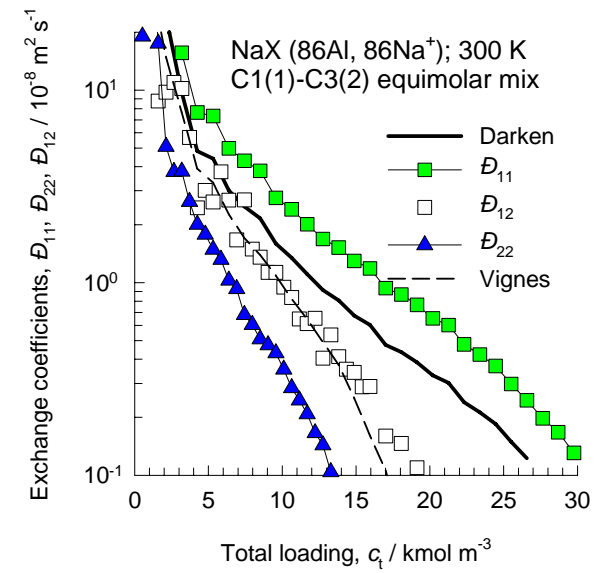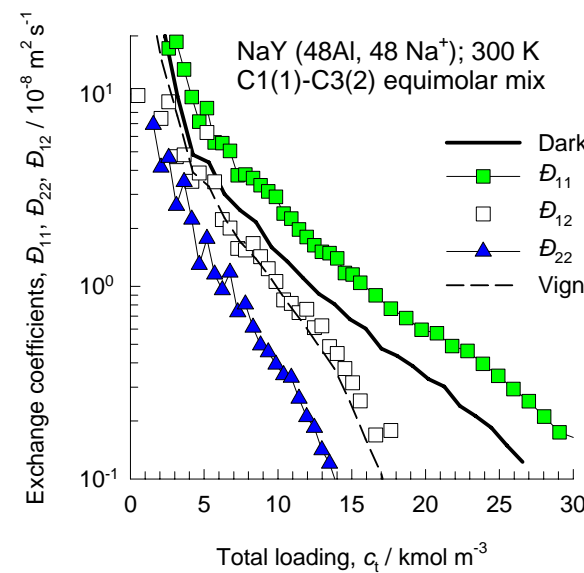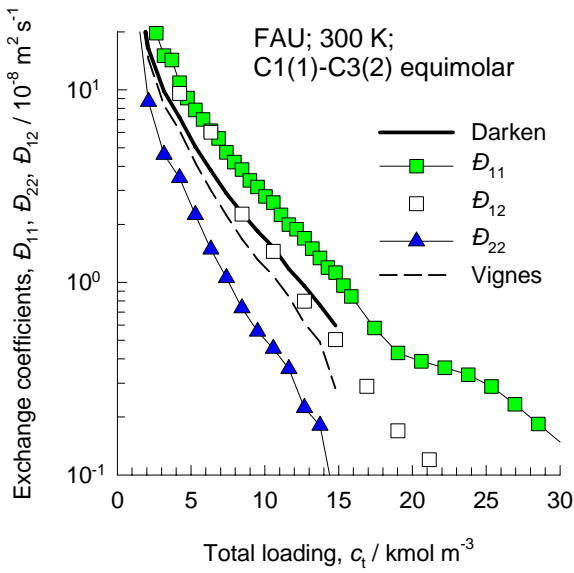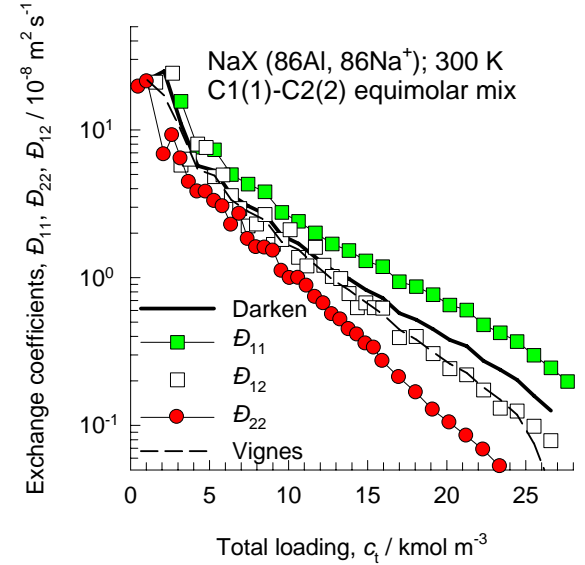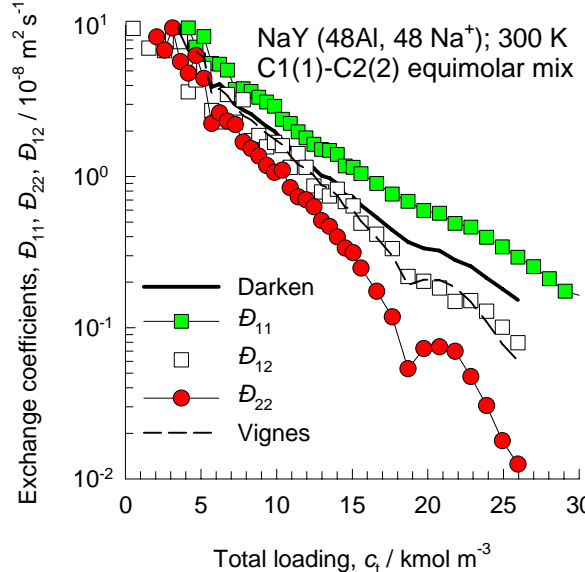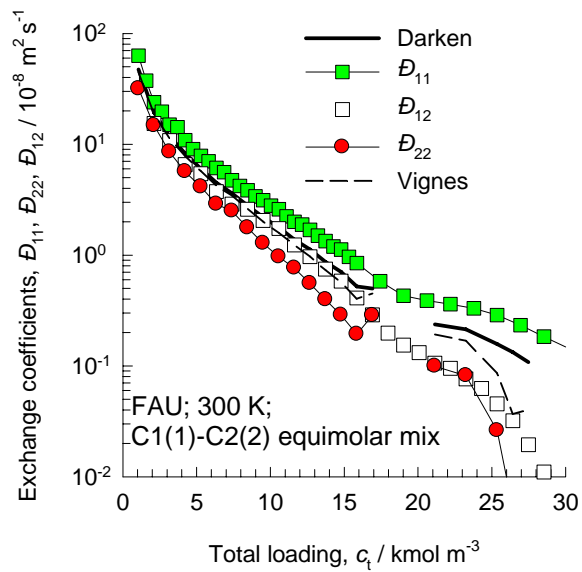
# MFI

Figure 18

10 ring channel
of MFI viewed along [100]
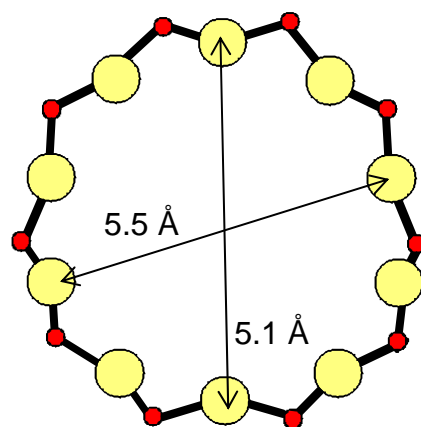
10 ring channel
of MFI viewed along [010]
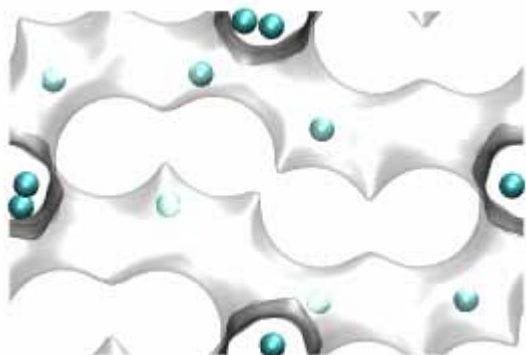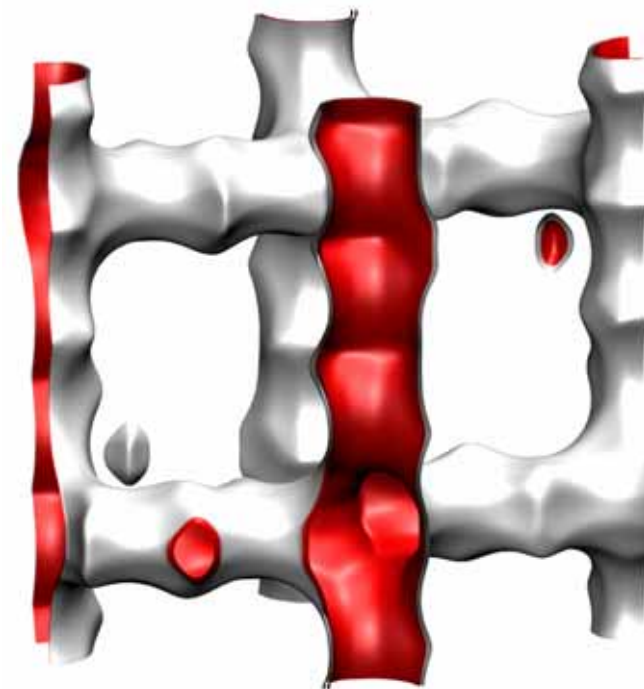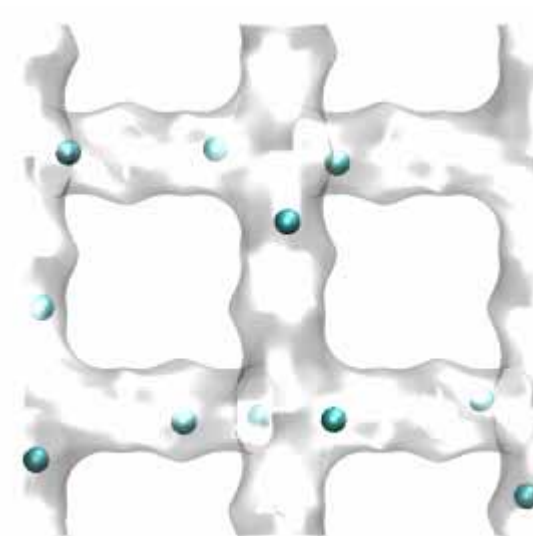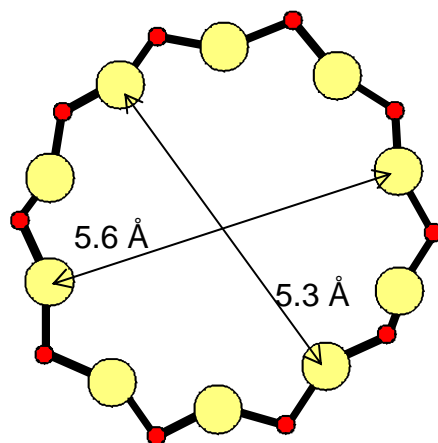
# MFI (94 Si, 2 Al, 2 Na⁺)

Figure 19
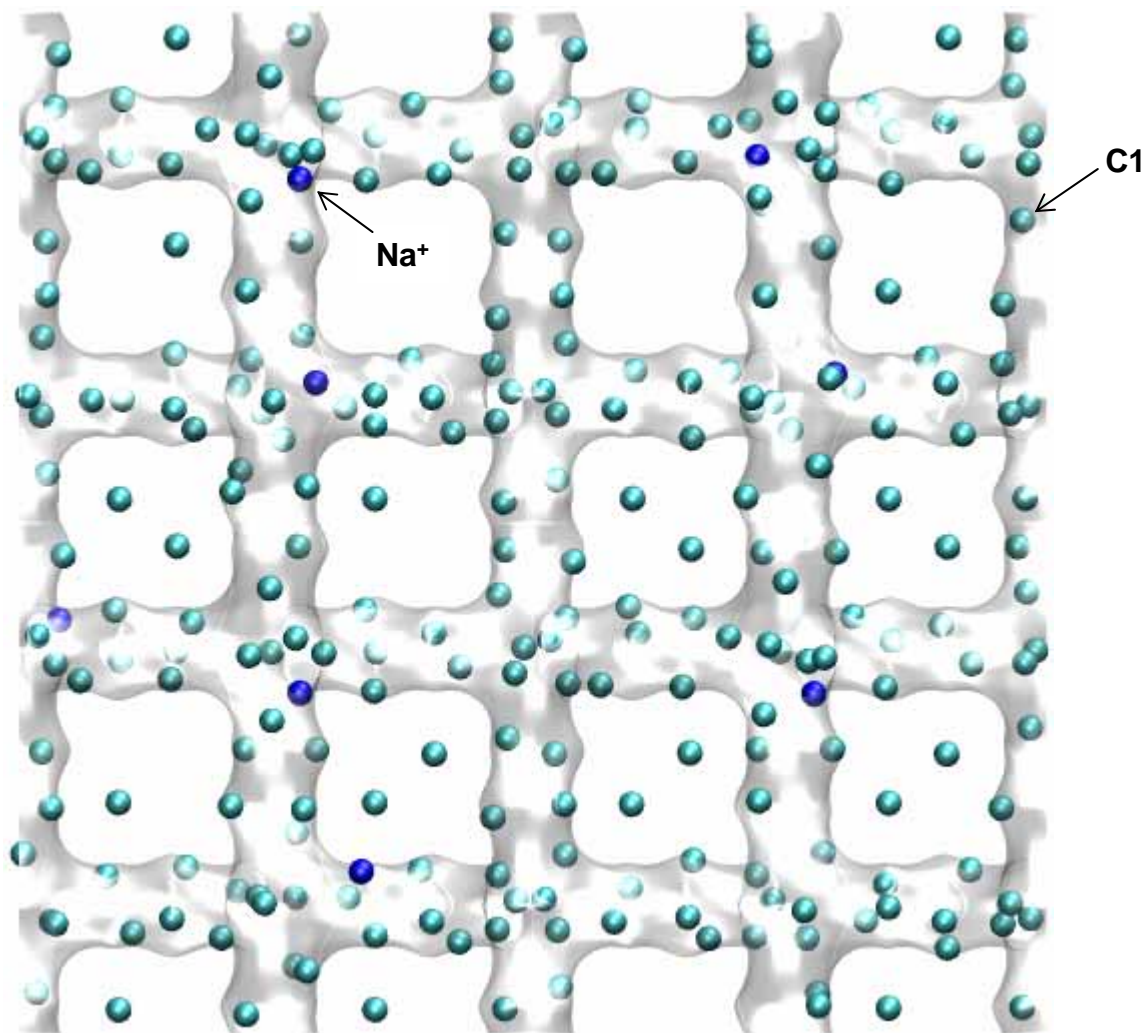
# MFI (92 Si, 4 Al, 4 Na⁺)

Figure 20
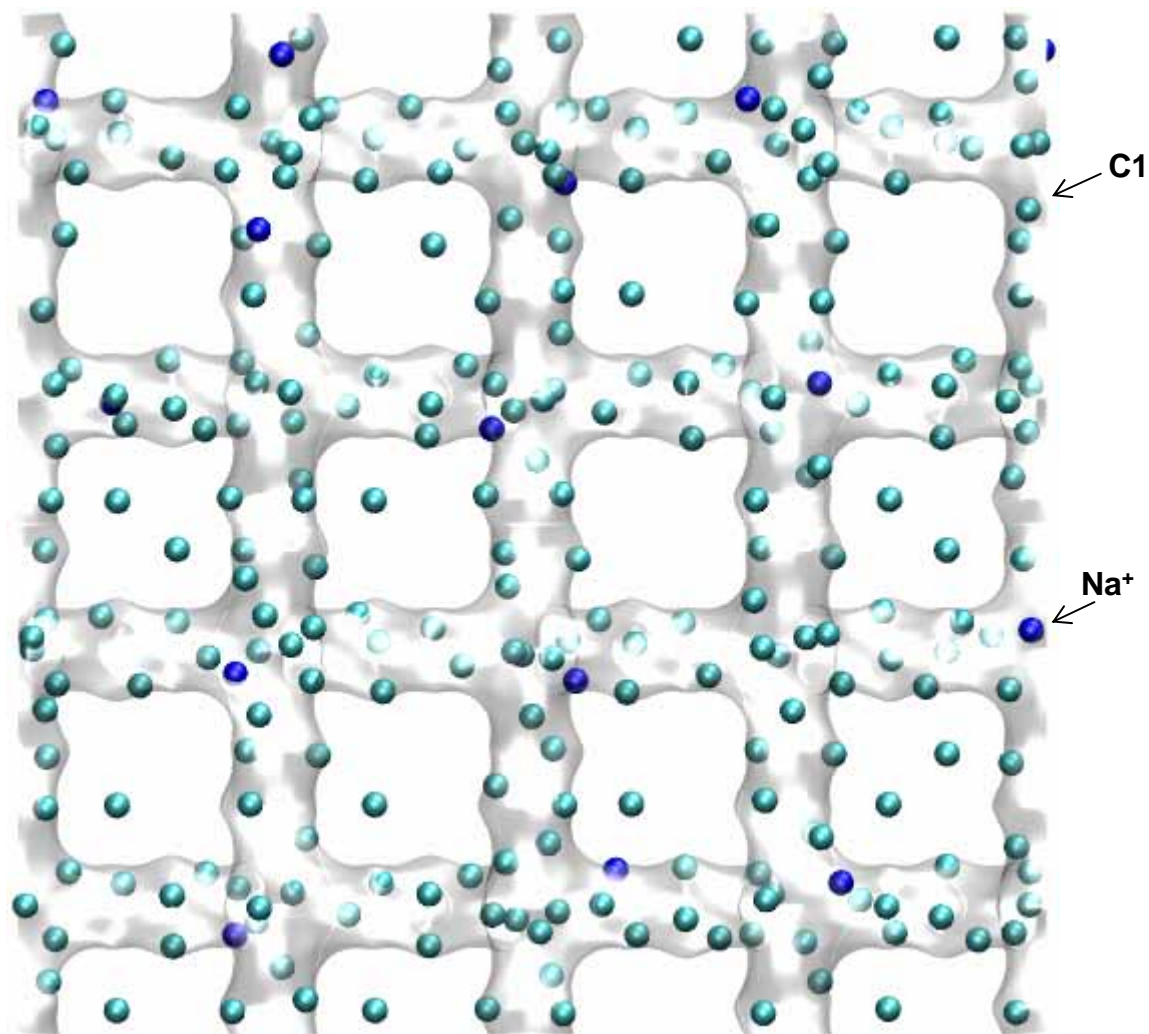
# MFI (90 Si, 6 Al, 6 Na⁺)

Figure 21
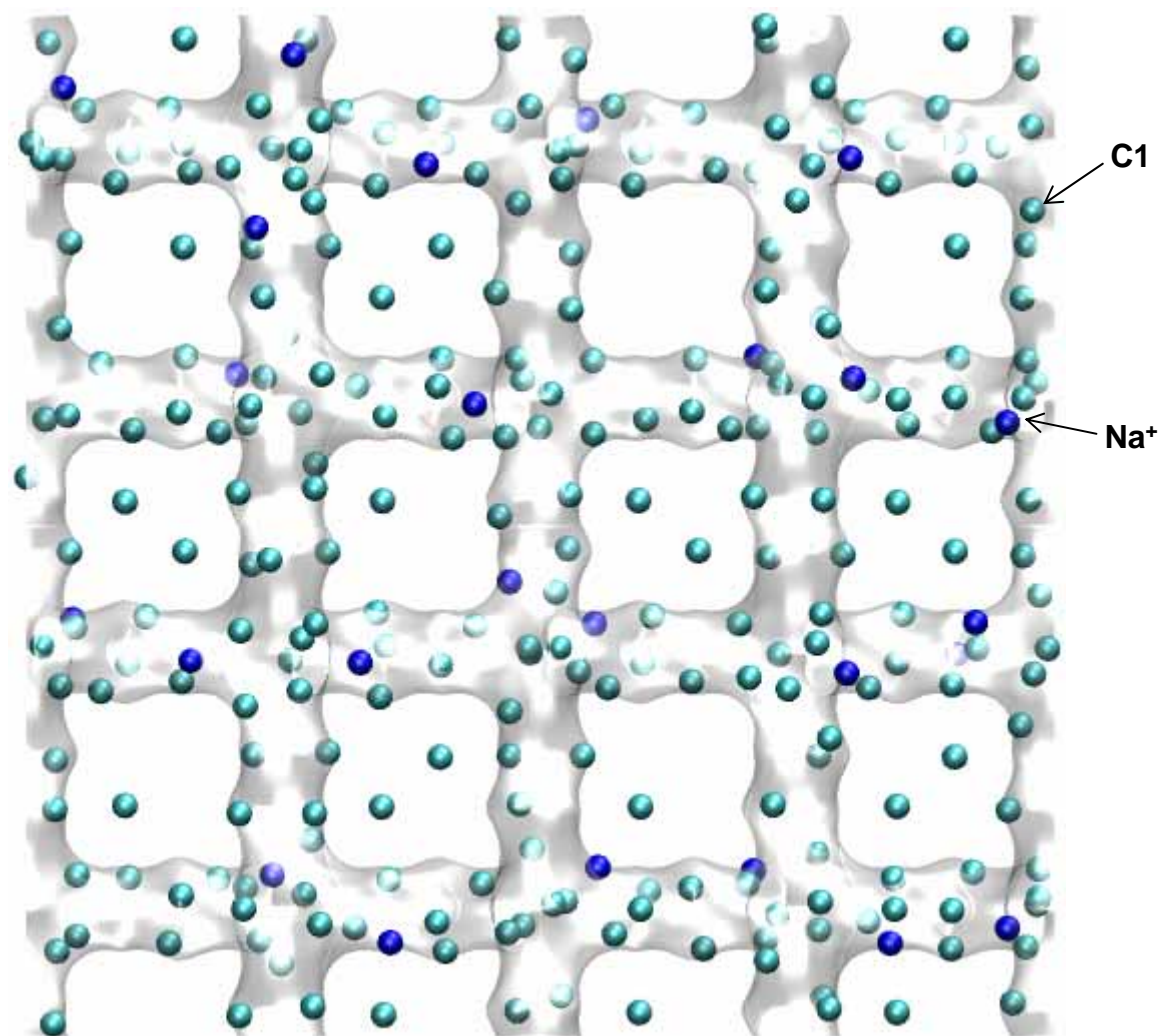
# MFI (88 Si, 8 Al, 8 Na⁺)

Figure 22



C1

Na⁺
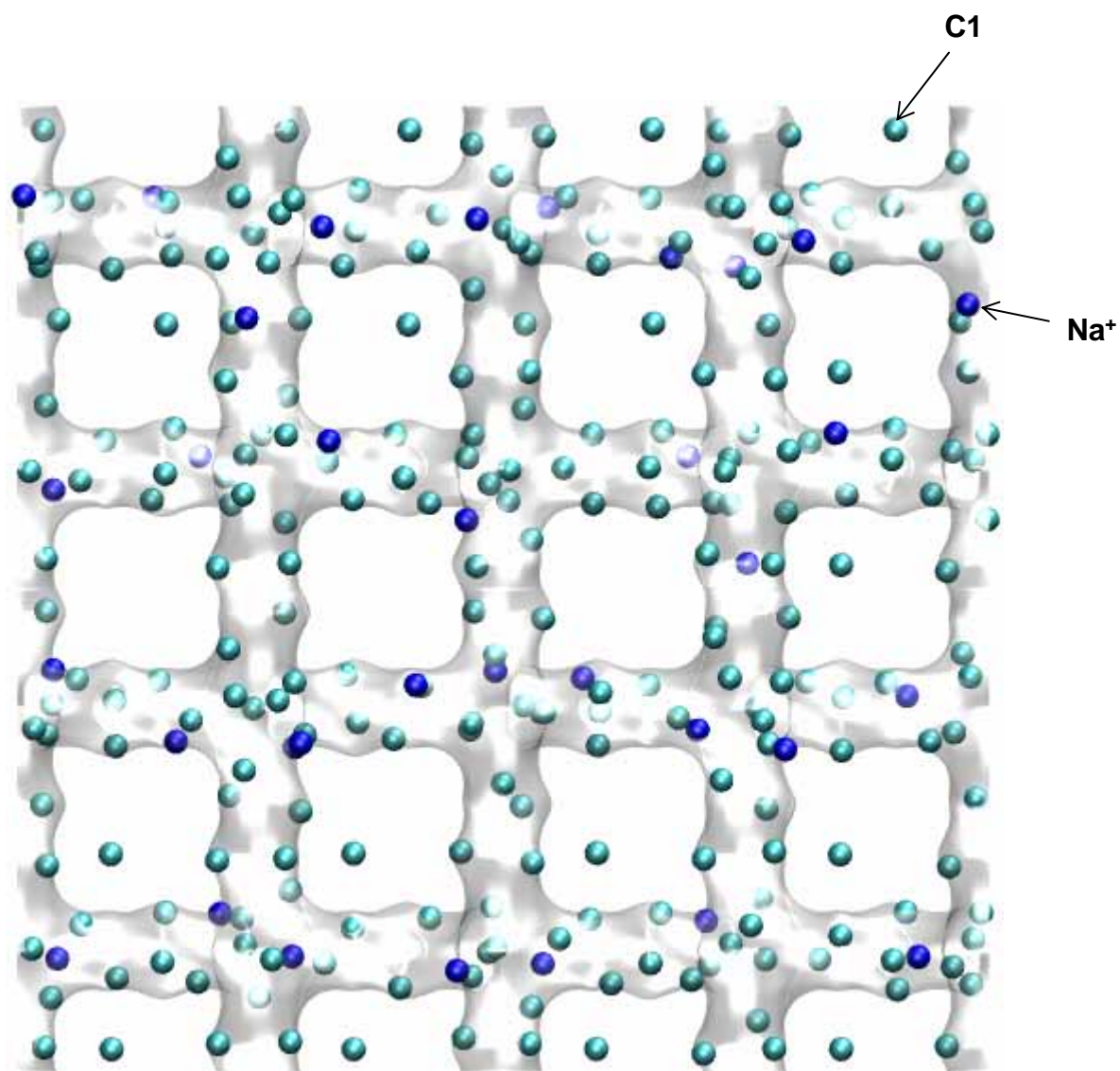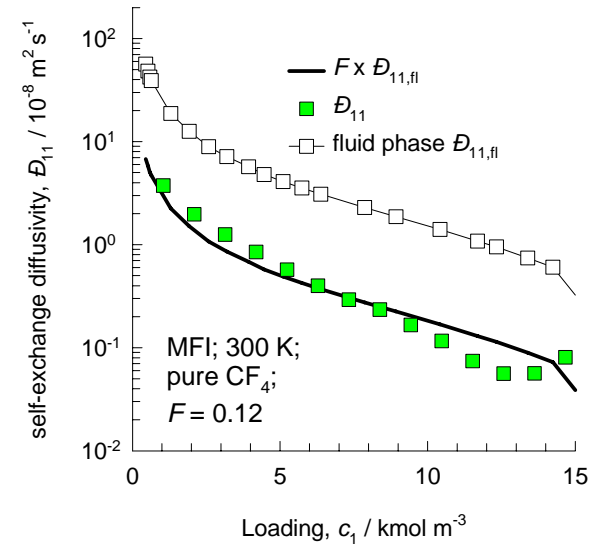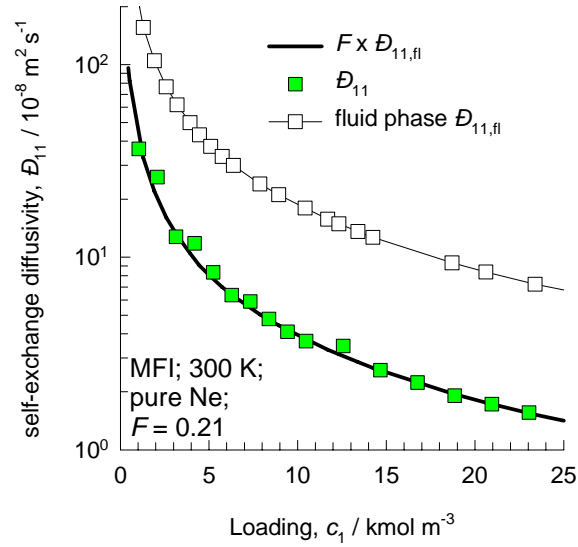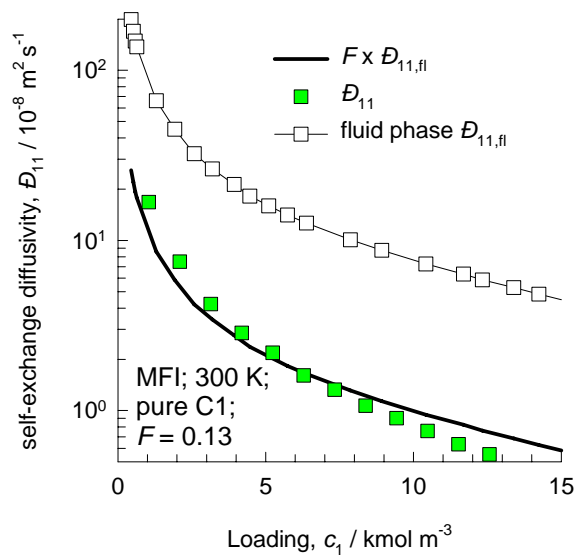
Figure 23

Data for all-silica MFI for unary diffusion
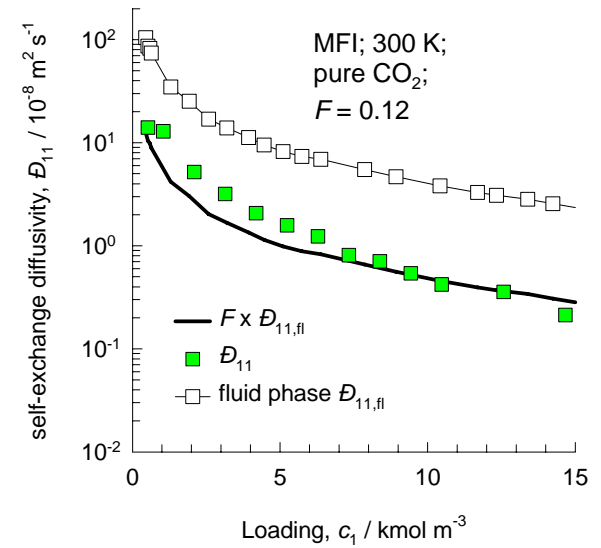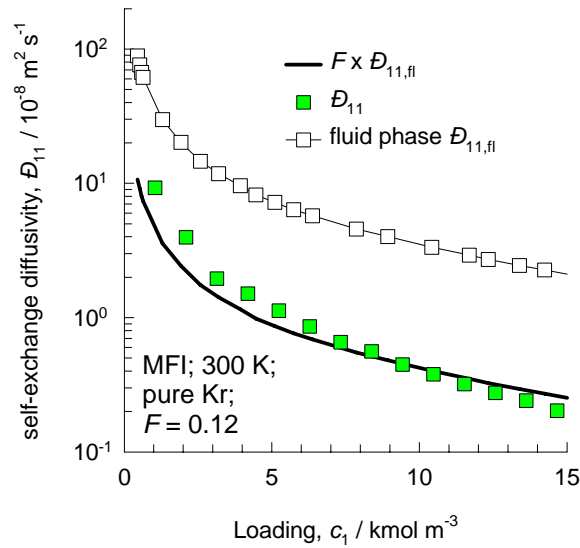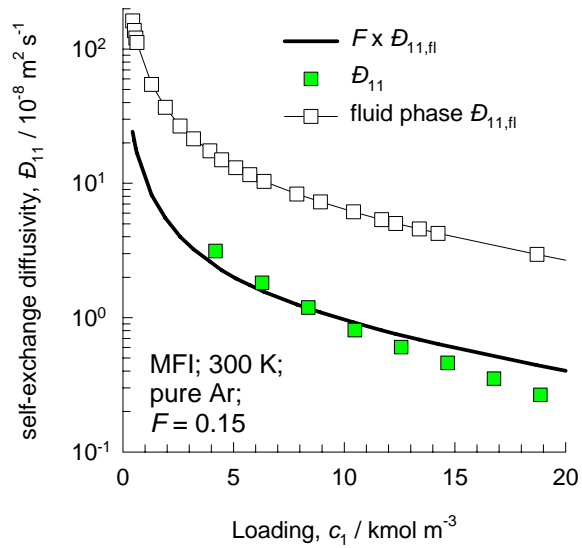
Figure 24
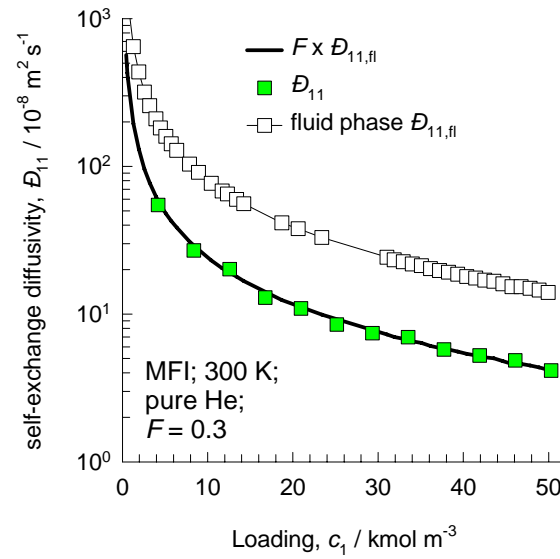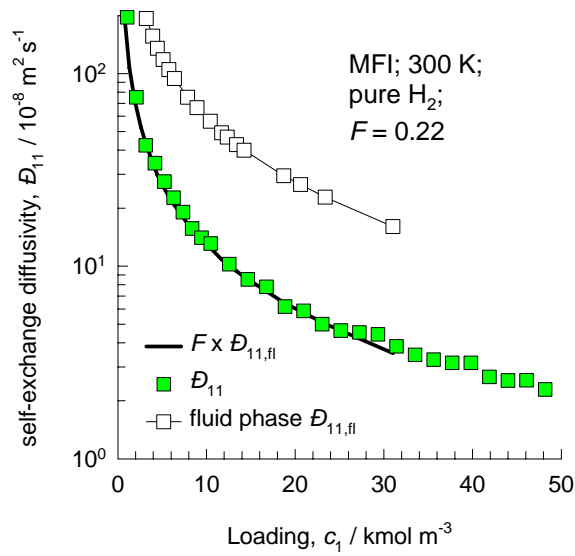
Data for all-silica MFI for unary diffusion
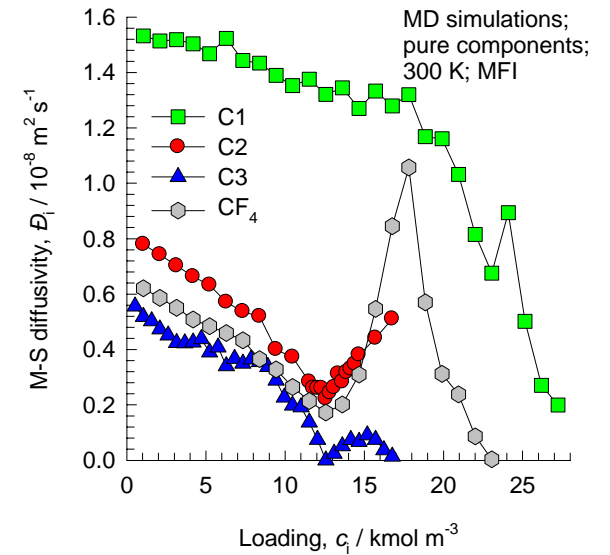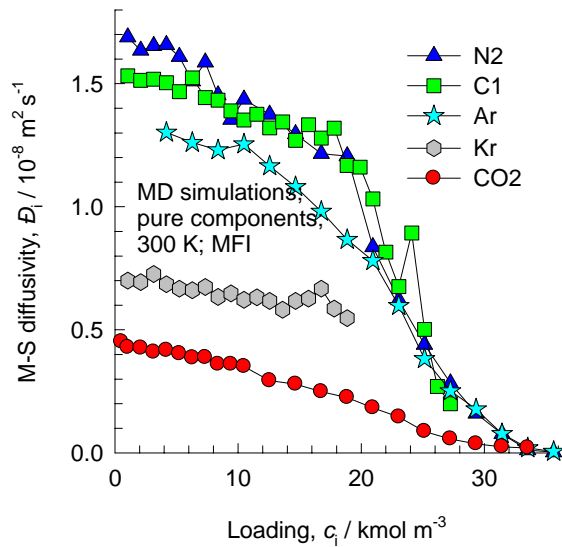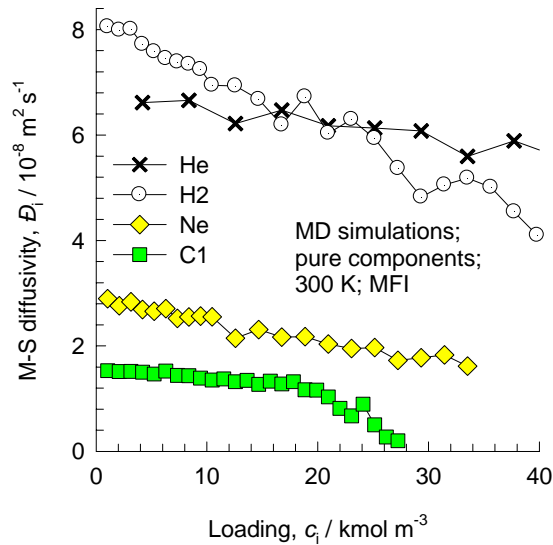
Figure 25
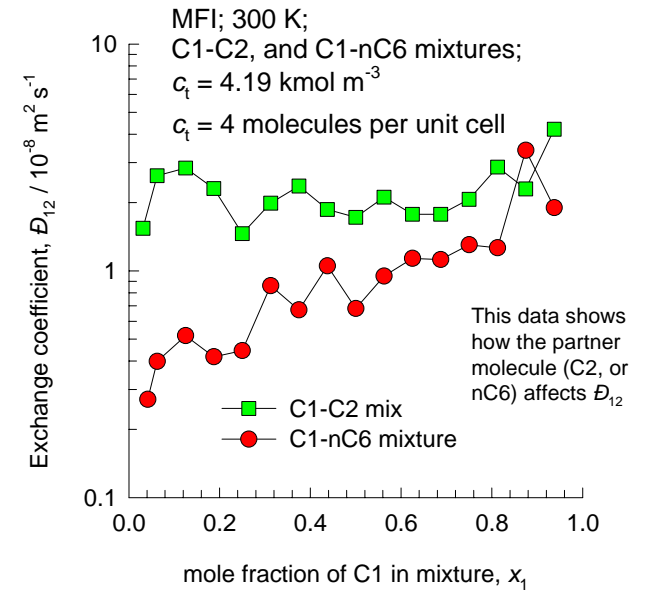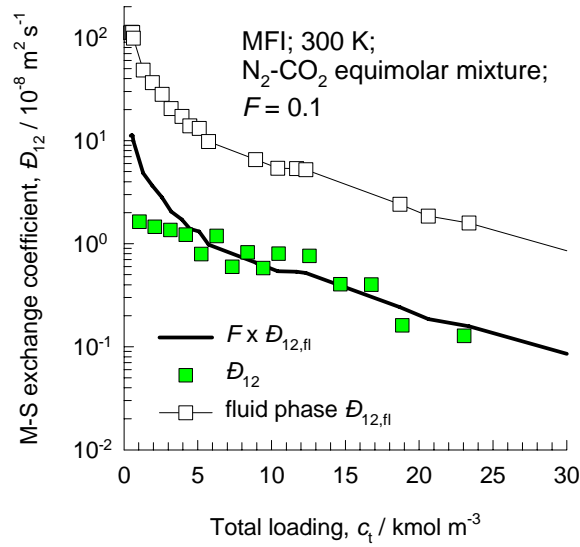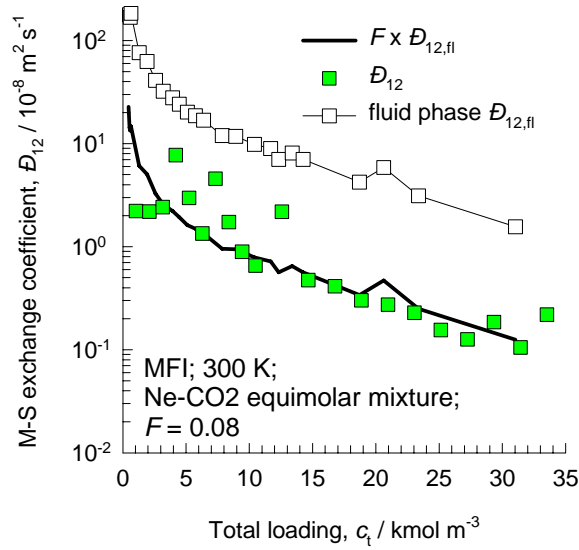
Data for all-silica MFI for binary mixtures
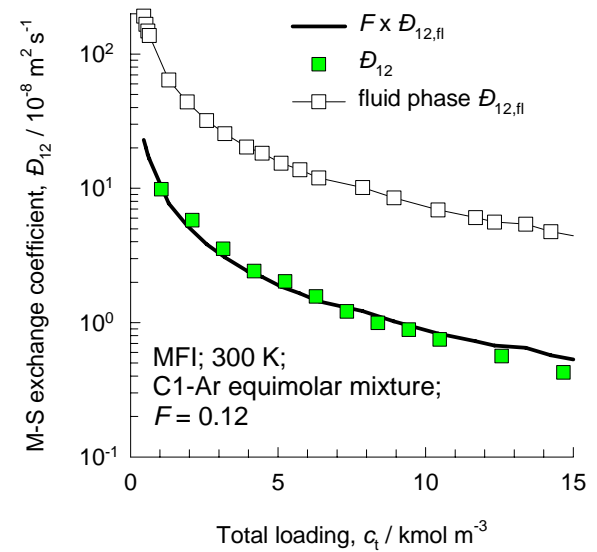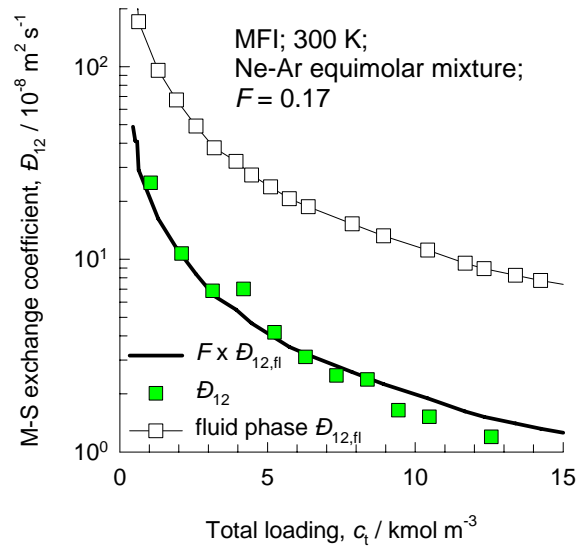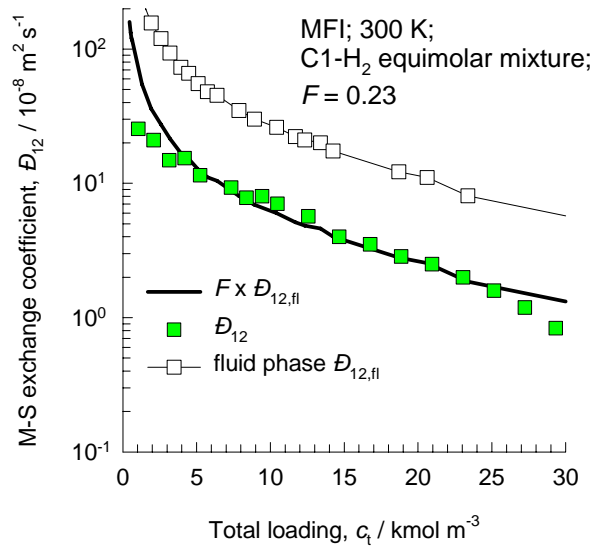
Figure 26
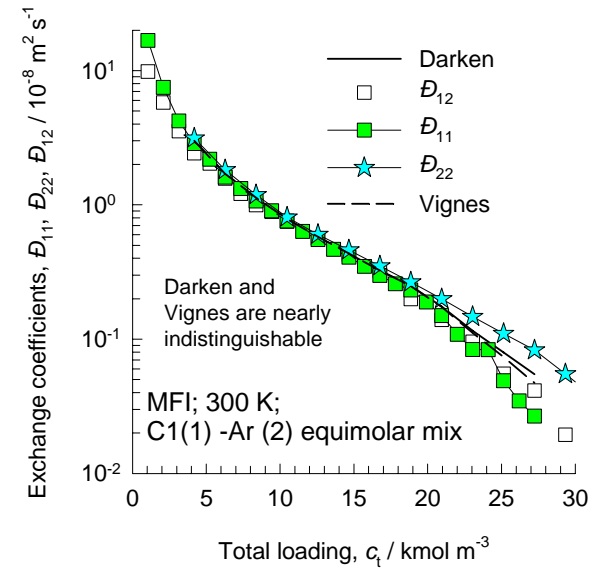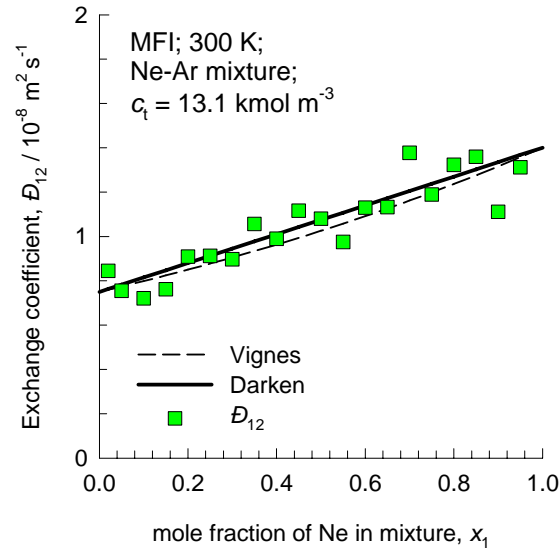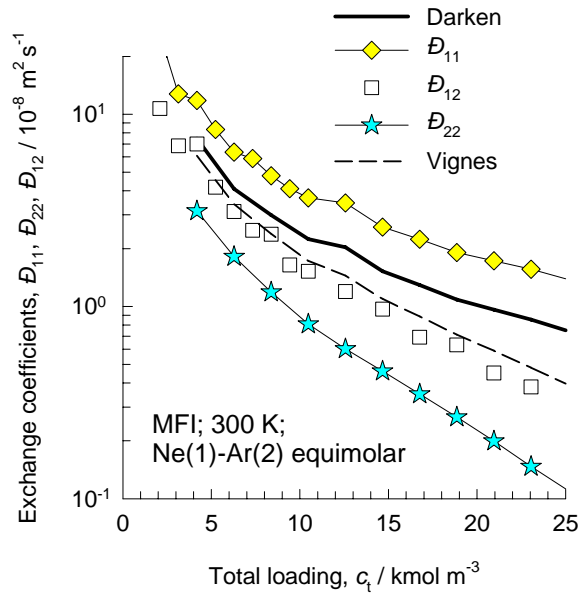
Test of Darken and Vignes interpolation formulae for MFI
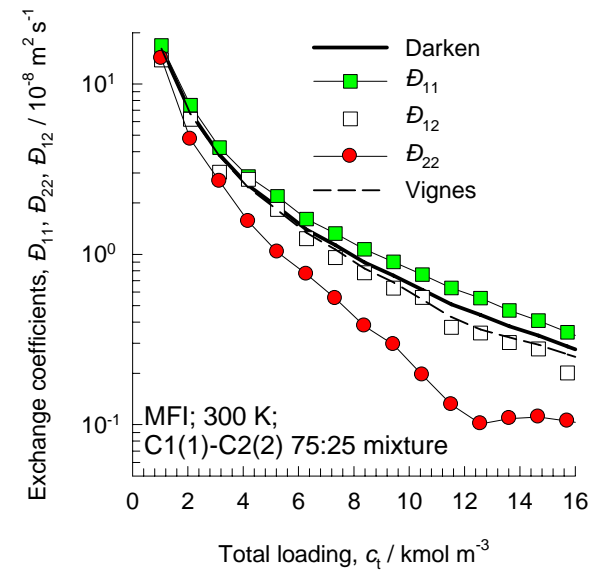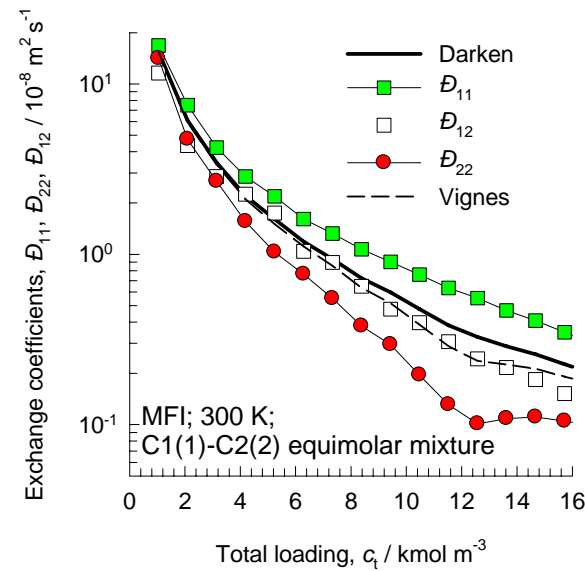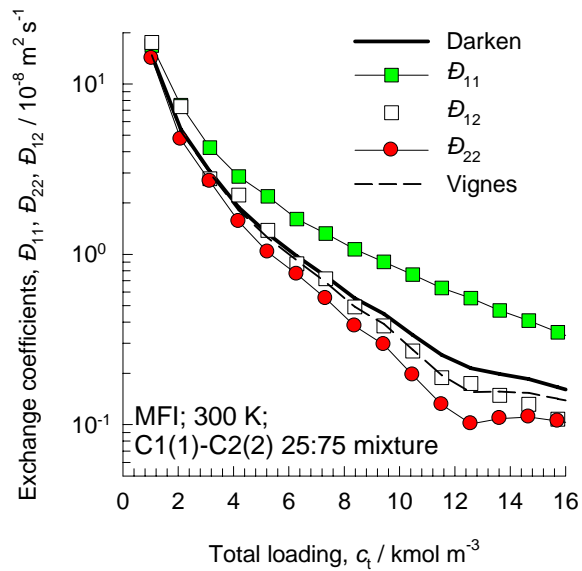
Figure 27
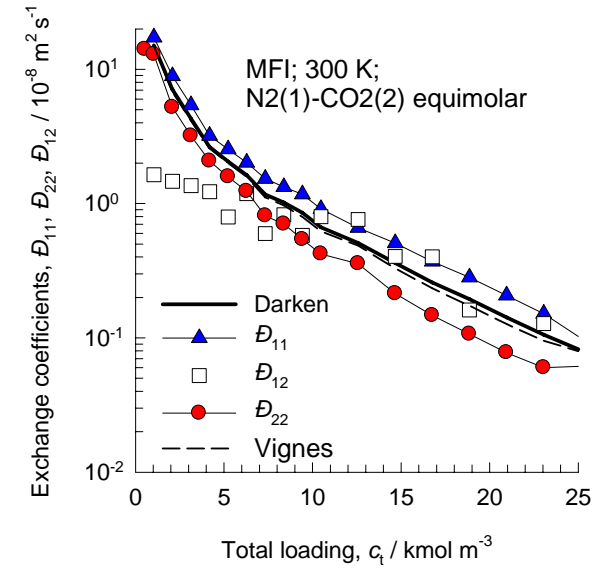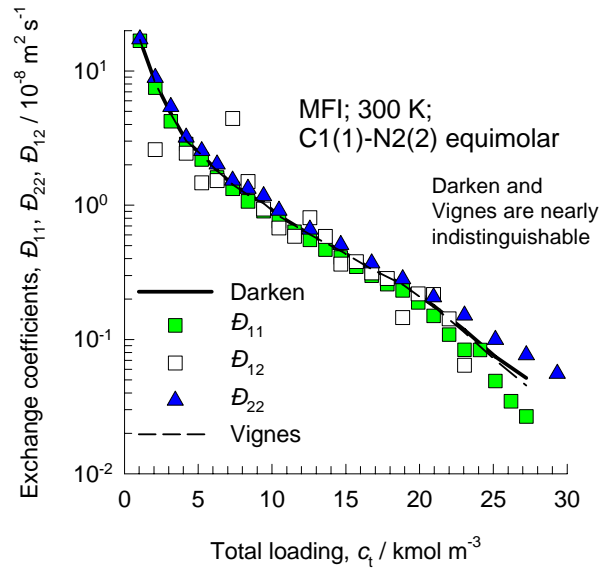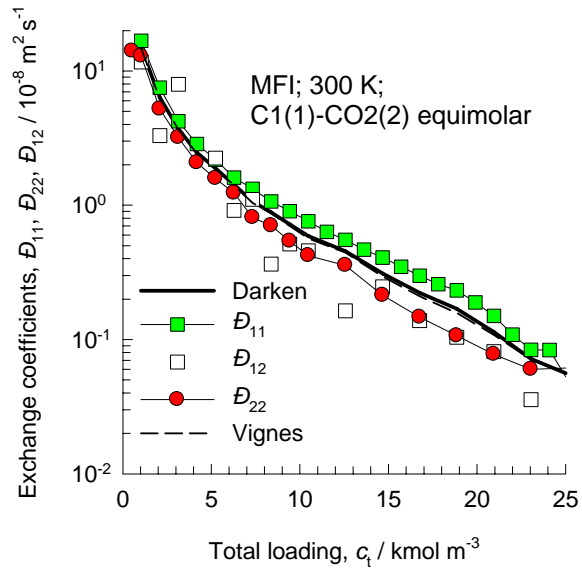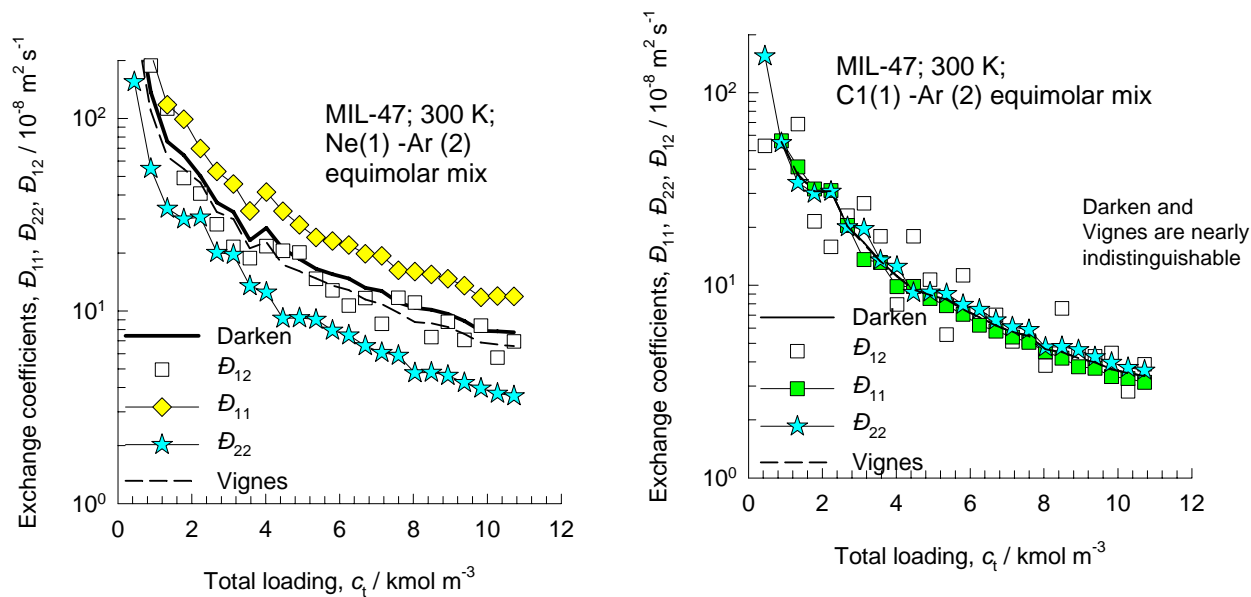
Test of Darken and Vignes interpolation formulae for MFI
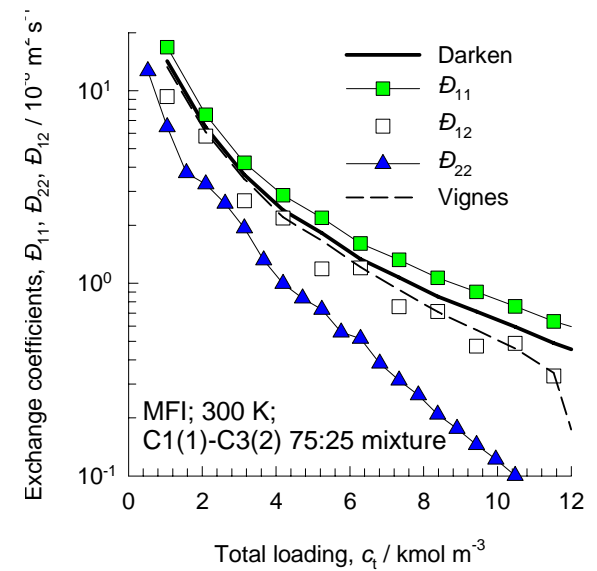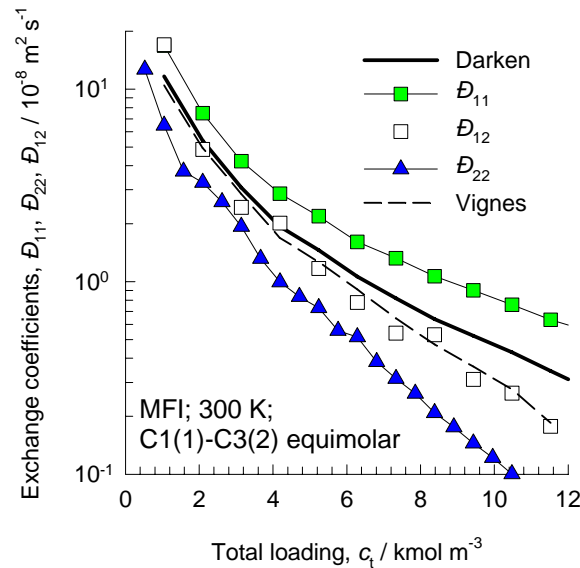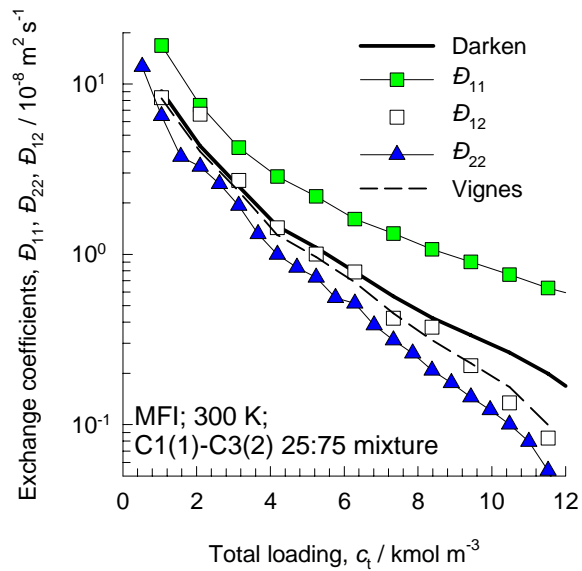
Figure 28

Prediction of $D_{i,self}$ and $\Delta_{ij}$ in binary mixtures in MFI using Vignes interpolation and M-S model

$$[\Delta] = \begin{bmatrix} \dfrac{1}{Ð_1} + \dfrac{x_2}{Ð_{12}} & -\dfrac{x_1}{Ð_{12}} \\[2ex] -\dfrac{x_2}{Ð_{12}} & \dfrac{1}{Ð_2} + \dfrac{x_1}{Ð_{12}} \end{bmatrix}^{-1}$$

Unary diffusion data

Vignes interpolation

$$\frac{1}{D_{1,self}} = \frac{1}{Ð_1} + \frac{x_1}{Ð_{11}} + \frac{x_2}{Ð_{12}}$$

$$\frac{1}{D_{2,self}} = \frac{1}{Ð_2} + \frac{x_2}{Ð_{22}} + \frac{x_1}{Ð_{12}}$$

Vignes interpolation
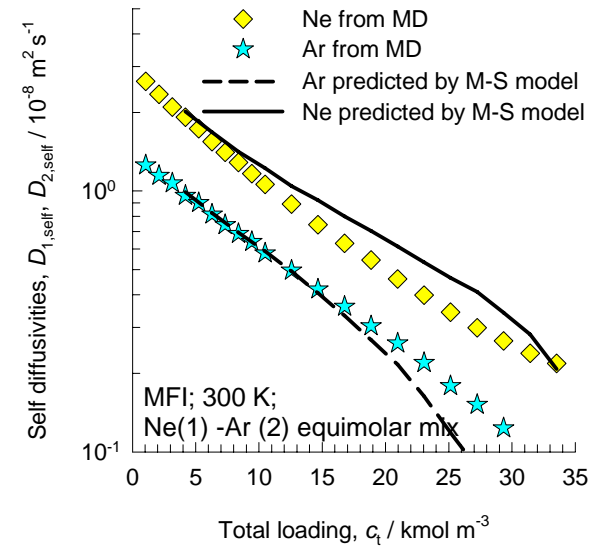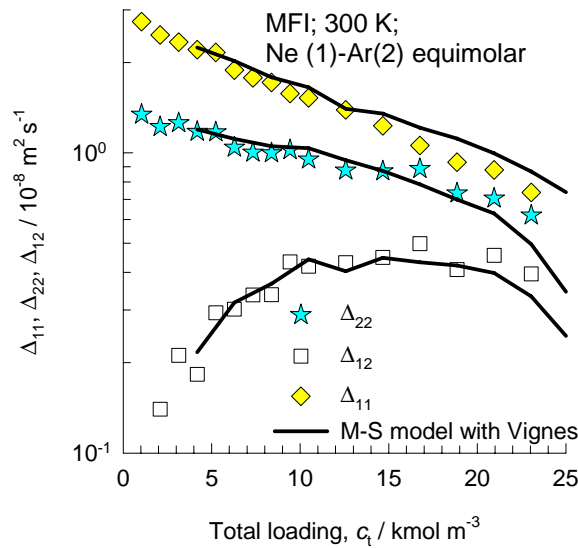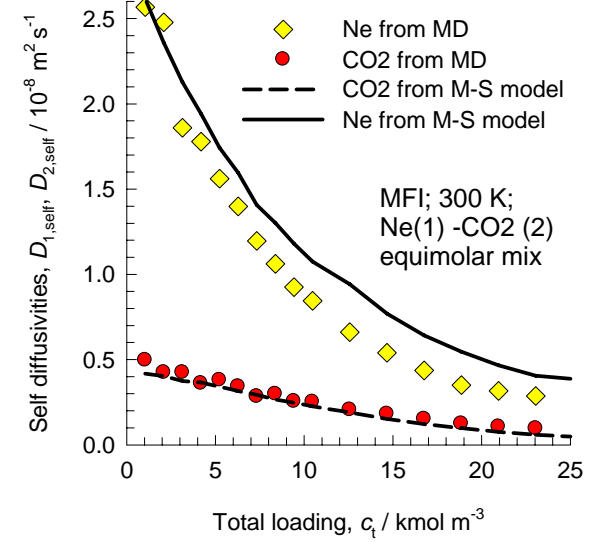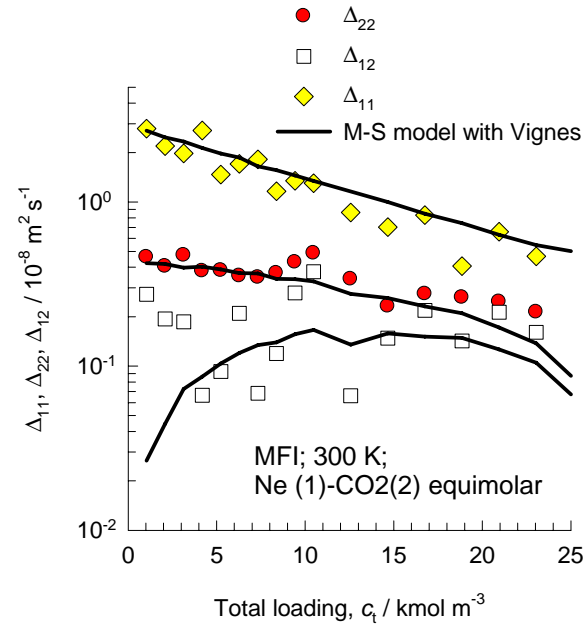
Figure 29
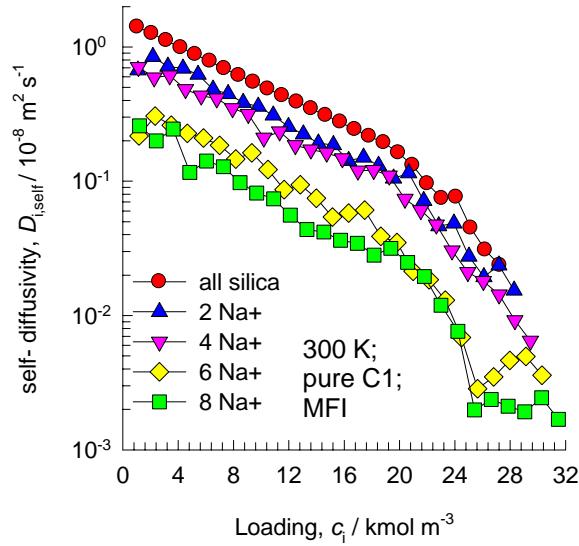
The presence of Na+
ions increases the
degree of confinement
and reduces the self-
diffusivities
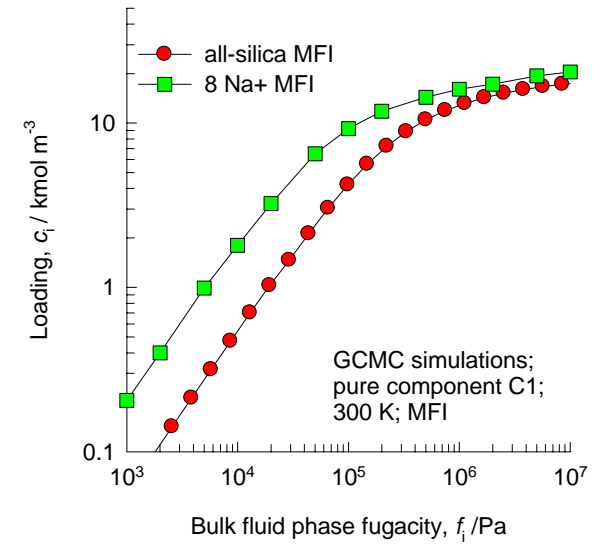
The presence of Na+
ions increases the
adsorption strength

Comparison of all-silica MFI with Na+ exchanged MFI;
Data for methane (C1) at 300 K
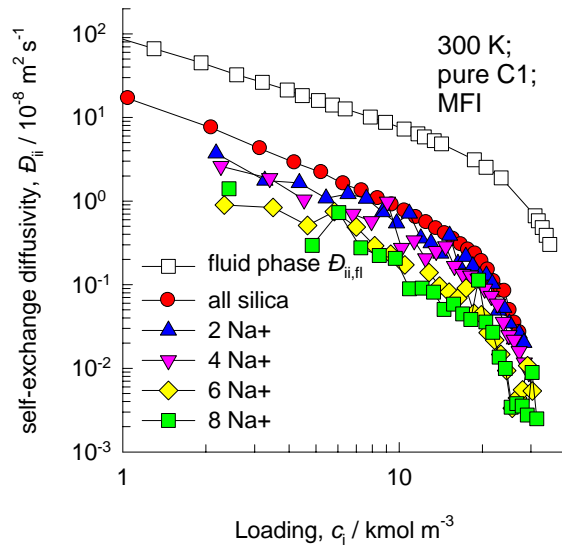
The presence of Na+
ions increases the
degree of confinement
and reduces the self-
exchange coefficients

Figure 30

# AFI
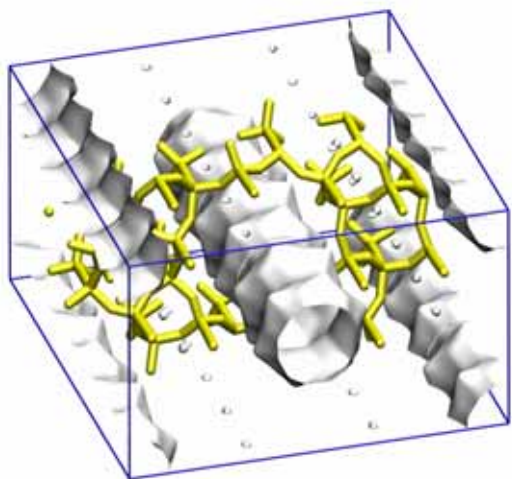
12-ring
channel of AFI

7.3 Å

7.3 Å
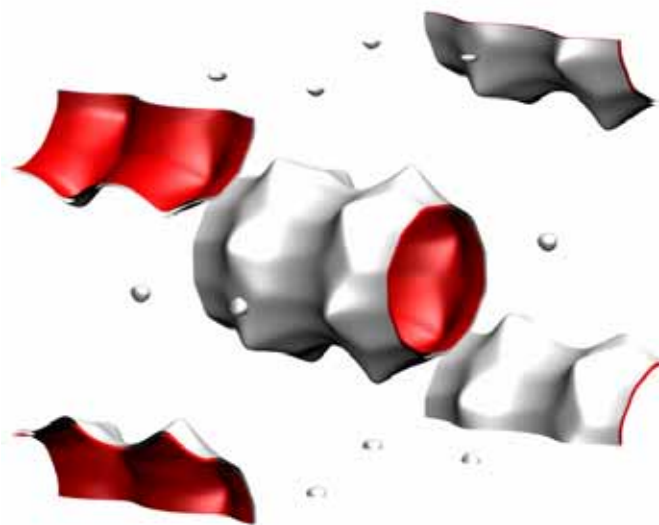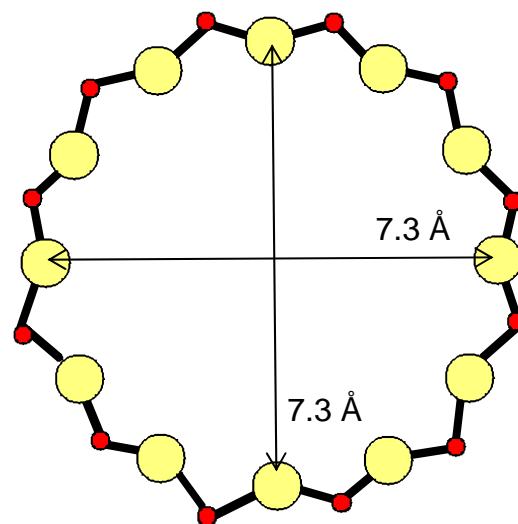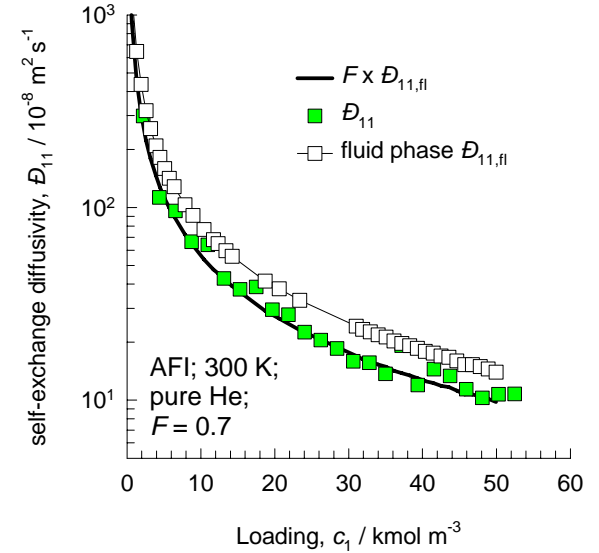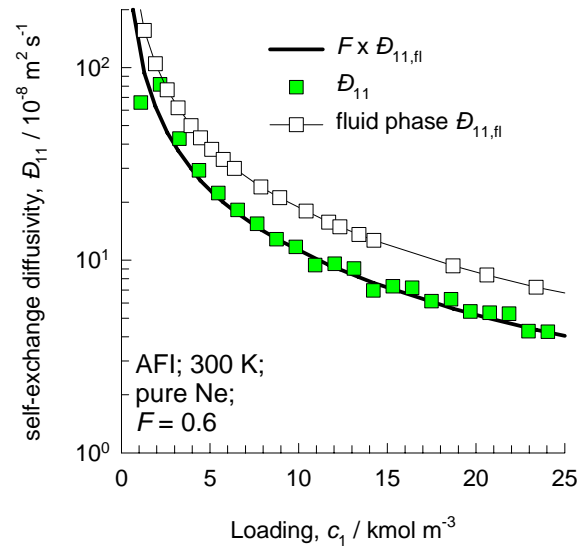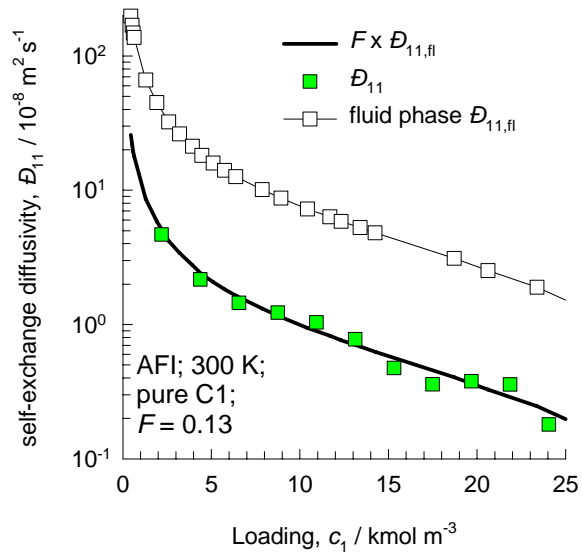
Figure 31

Data for all-silica AFI for unary diffusion
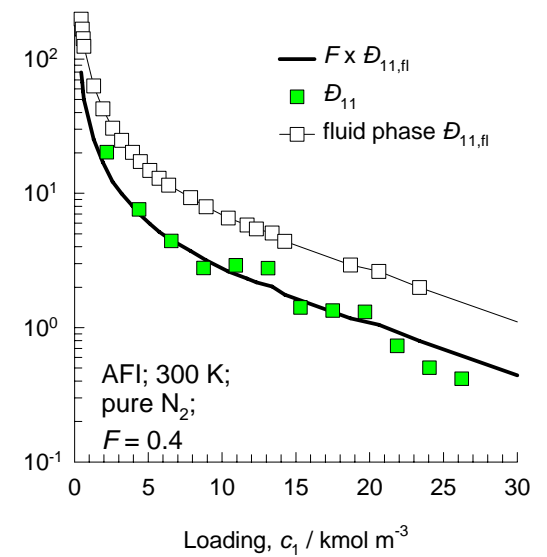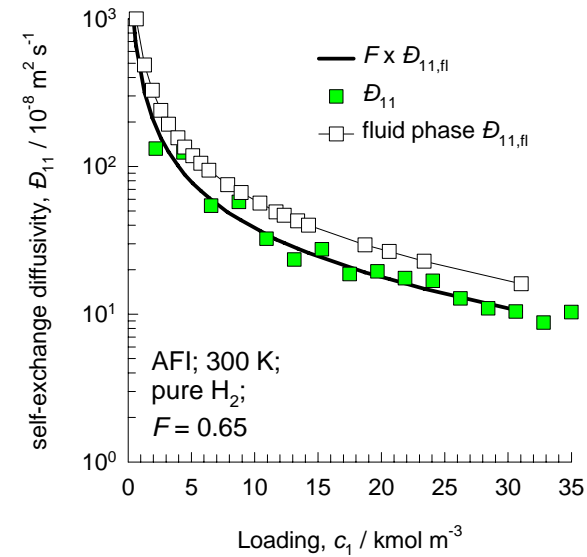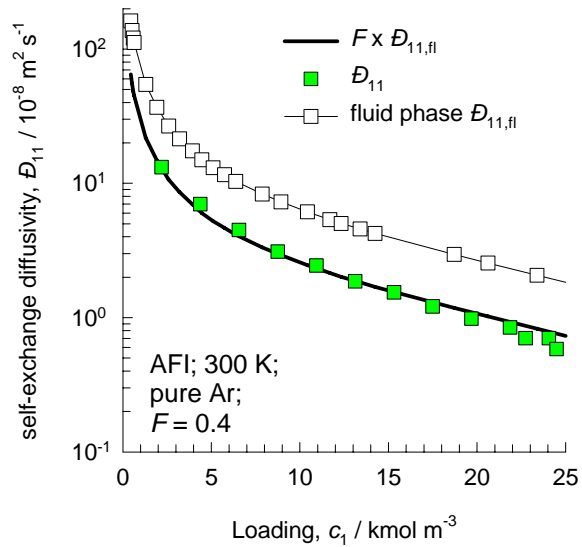
Figure 32

# Unary M-S diffusivities



## Data for all-silica AFI for binary mixtures

Figure 33
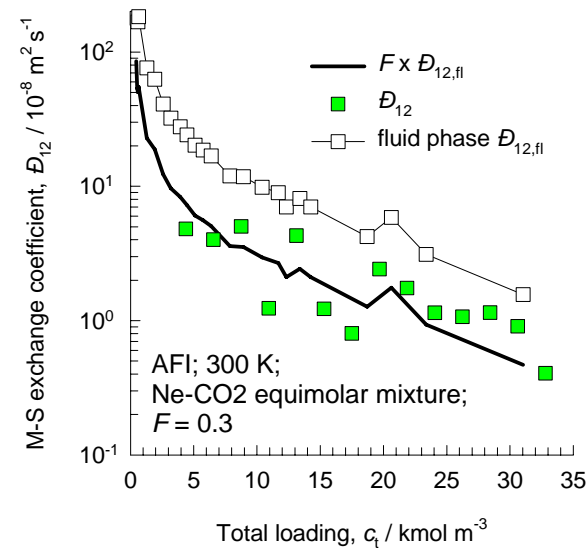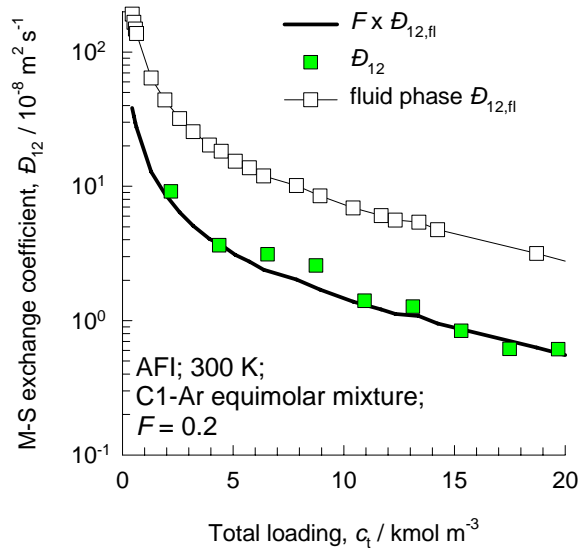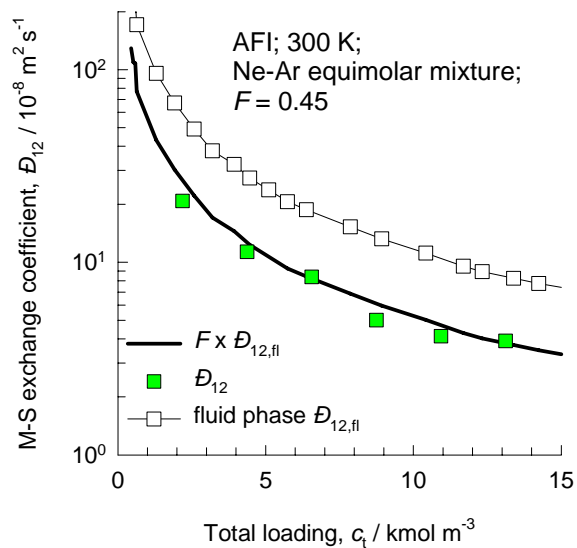
Test of Darken and Vignes interpolation formulae for AFI

Figure 34
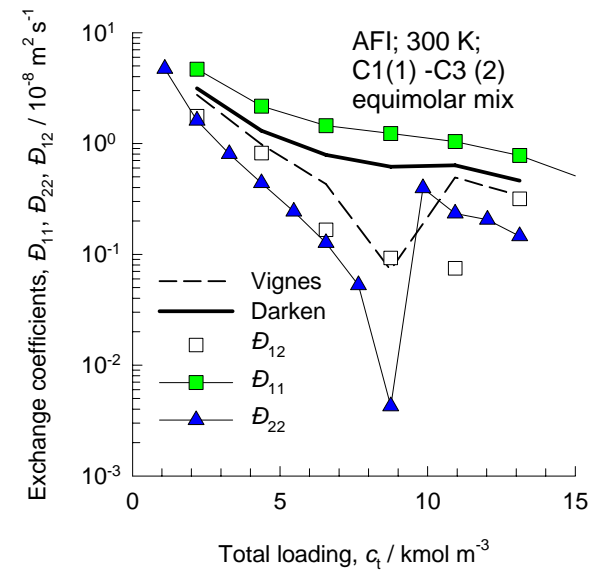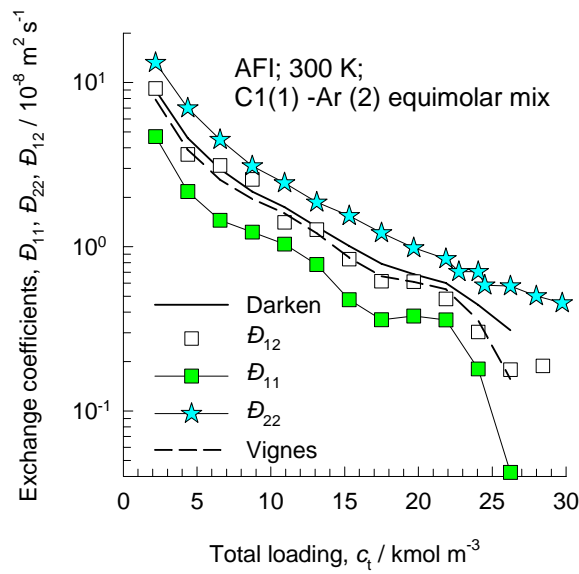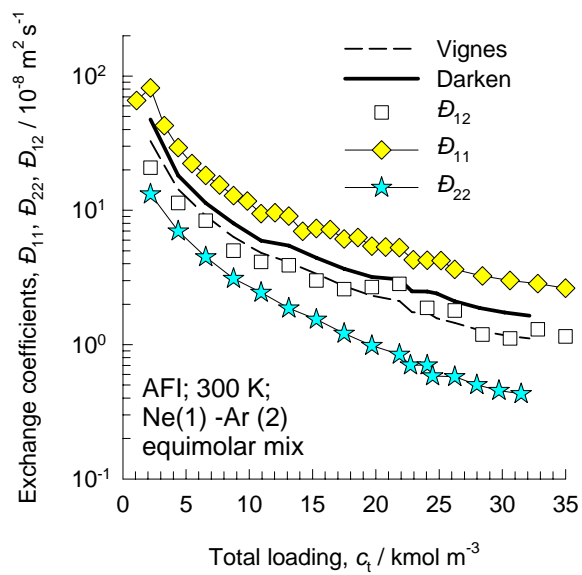
Prediction of $D_{i,self}$ and $\Delta_{ij}$ in binary mixtures in AFI using Vignes interpolation and M-S model

$$[\Delta] = \begin{bmatrix} \dfrac{1}{Ð_1} + \dfrac{x_2}{Ð_{12}} & -\dfrac{x_1}{Ð_{12}} \\[2ex] -\dfrac{x_2}{Ð_{12}} & \dfrac{1}{Ð_2} + \dfrac{x_1}{Ð_{12}} \end{bmatrix}^{-1}$$

Unary diffusion data

Vignes interpolation

$$\frac{1}{D_{1,self}} = \frac{1}{Ð_1} + \frac{x_1}{Ð_{11}} + \frac{x_2}{Ð_{12}}$$

$$\frac{1}{D_{2,self}} = \frac{1}{Ð_2} + \frac{x_2}{Ð_{22}} + \frac{x_1}{Ð_{12}}$$

Vignes interpolation

# BEA

12 ring channel
viewed along [100]

7.1 Å

7.3 Å

12 ring channel
viewed along [001]

5.6 Å

5.6 Å
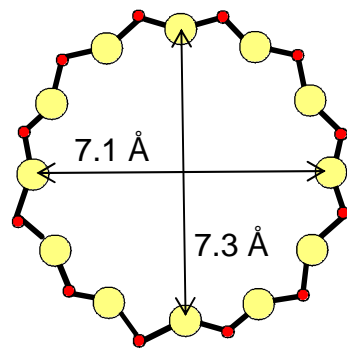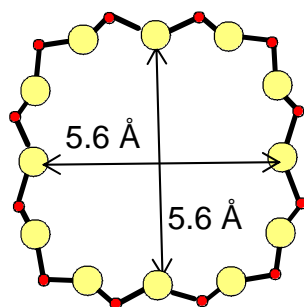
Figure 36

# BEA: snapshots of location of molecules
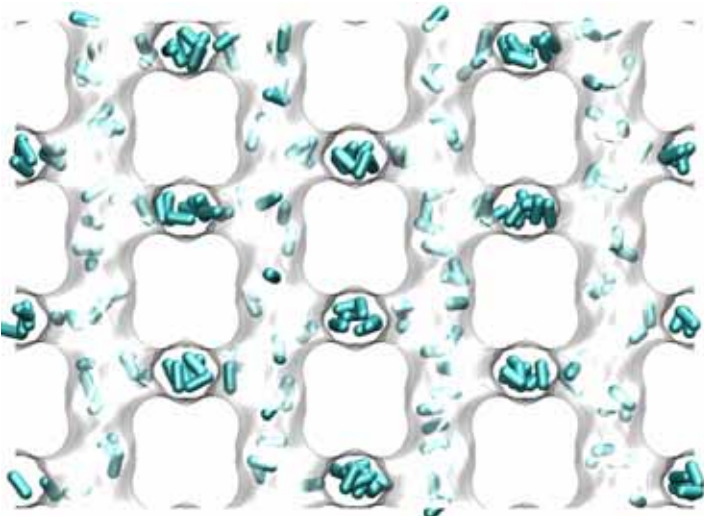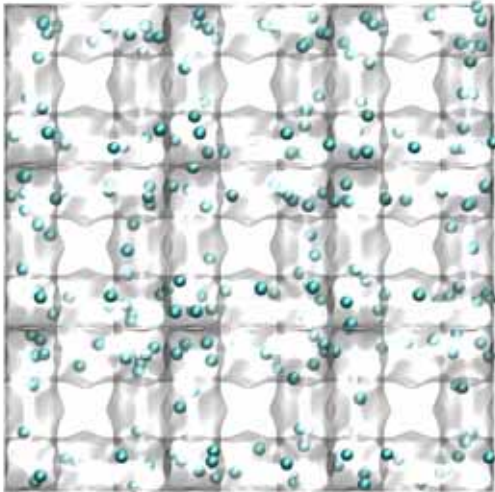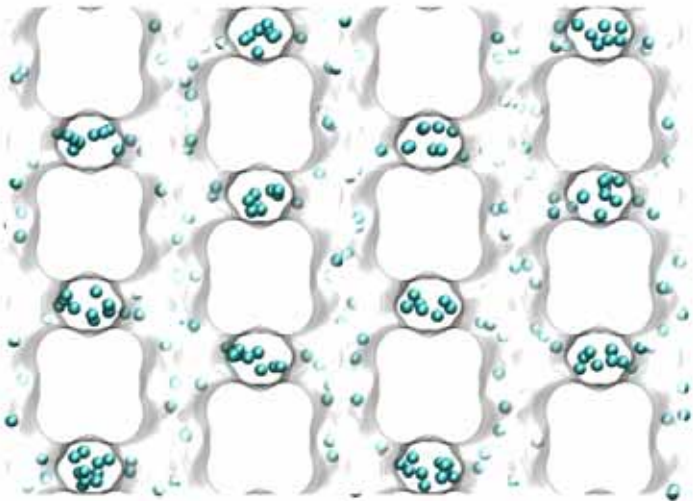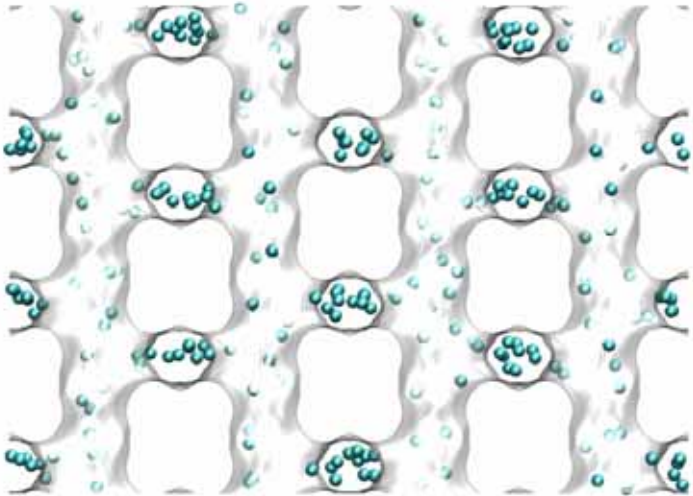
Figure 37
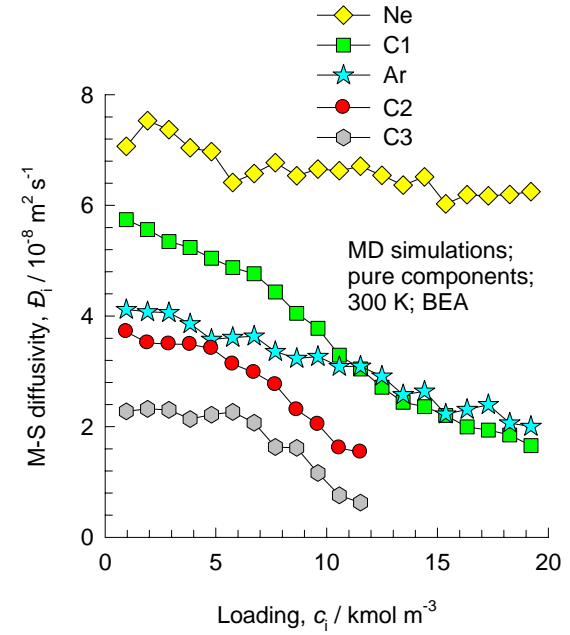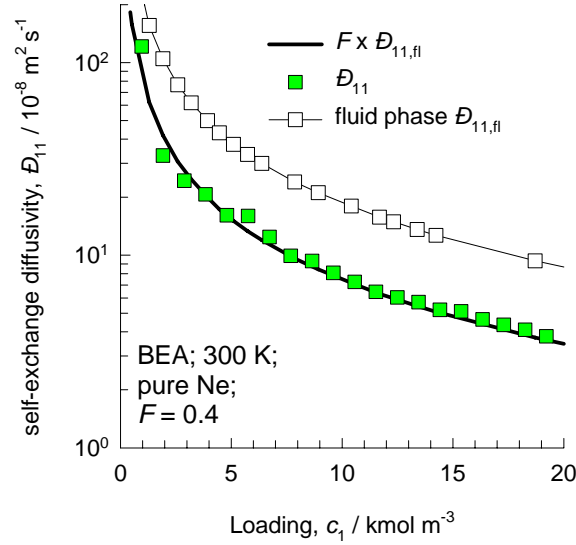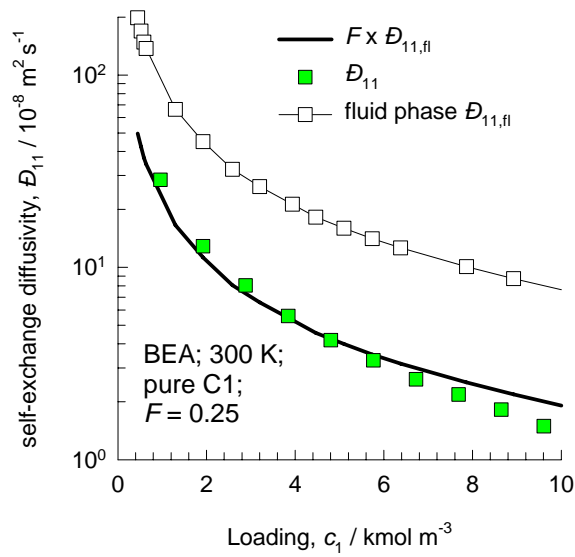
Data for BEA for unary diffusion
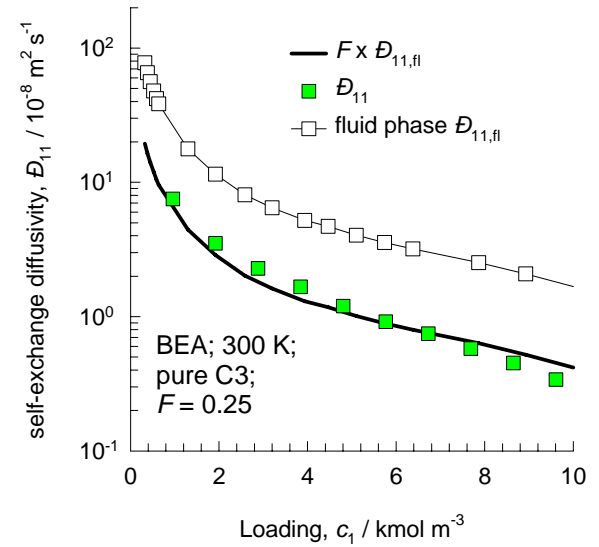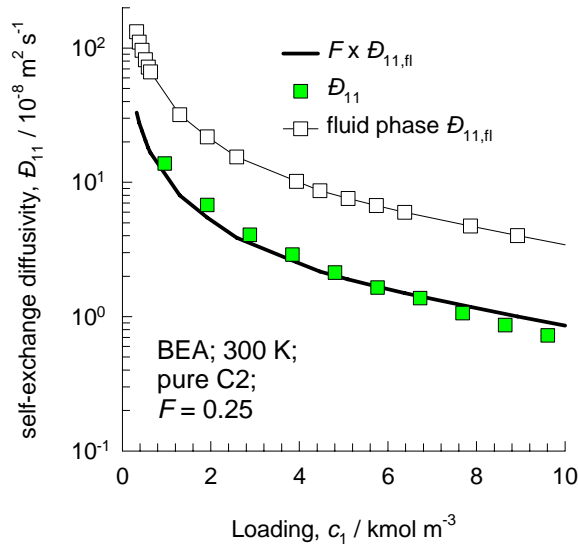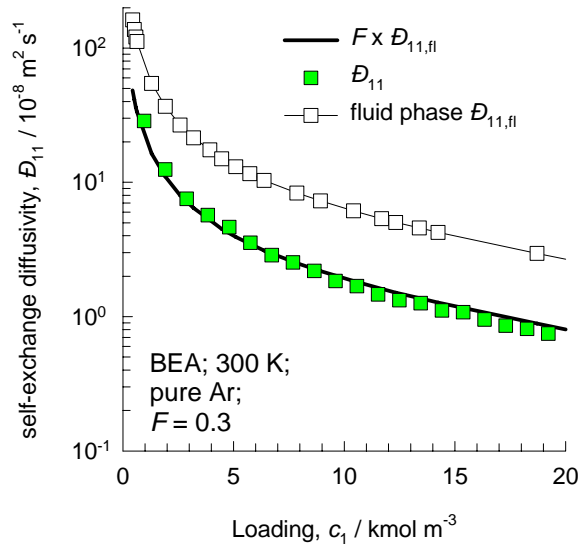
# Data for all-silica BEA for binary mixtures

Figure 38
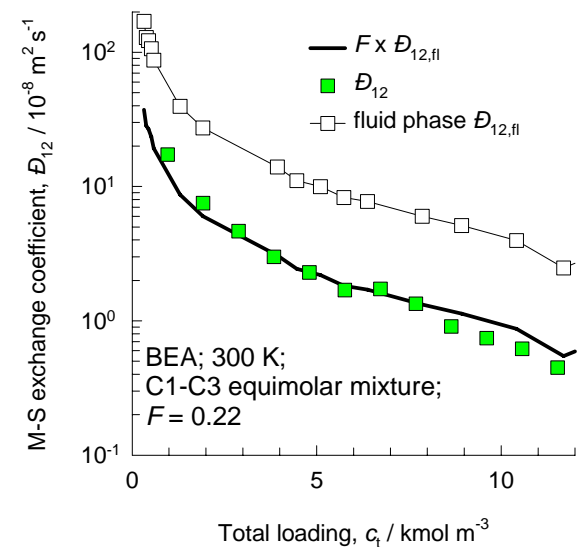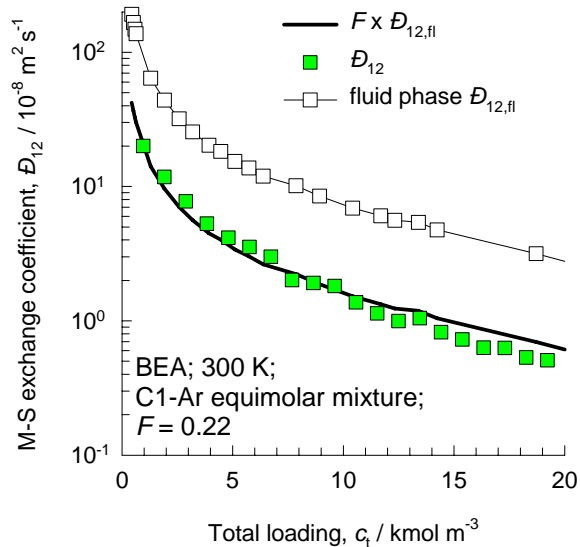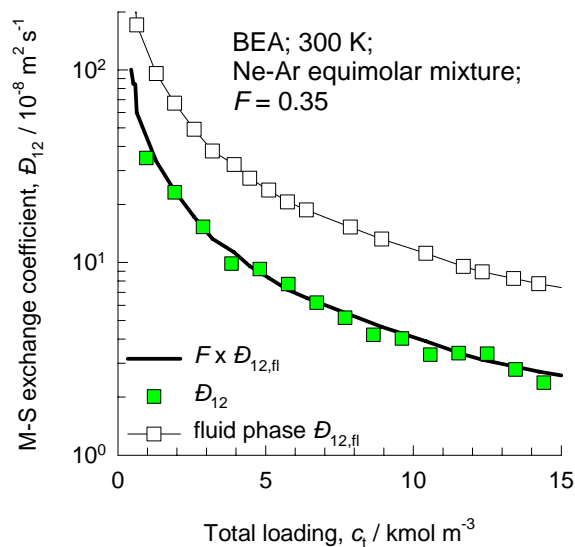


BEA; 300 K;
Ne-Ar equimolar mixture;
$F = 0.35$

BEA; 300 K;
C1-Ar equimolar mixture;
$F = 0.22$

BEA; 300 K;
C1-C3 equimolar mixture;
$F = 0.22$

# Test of Darken and Vignes interpolation formulae for BEA

BEA; 300 K;
Ne(1)-Ar(2) equimolar mixture

BEA; 300 K;
C1(1) -Ar (2) equimolar mix

Darken and
Vignes are nearly
indistinguishable

BEA; 300 K;
C1(1)-C3(2) equimolar mixture

Figure 39
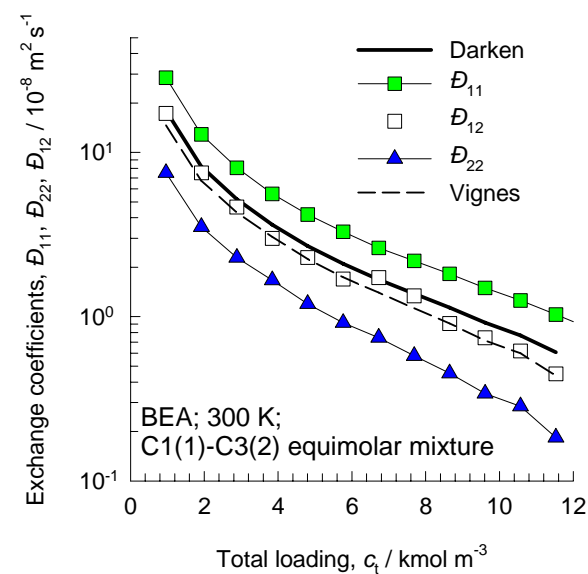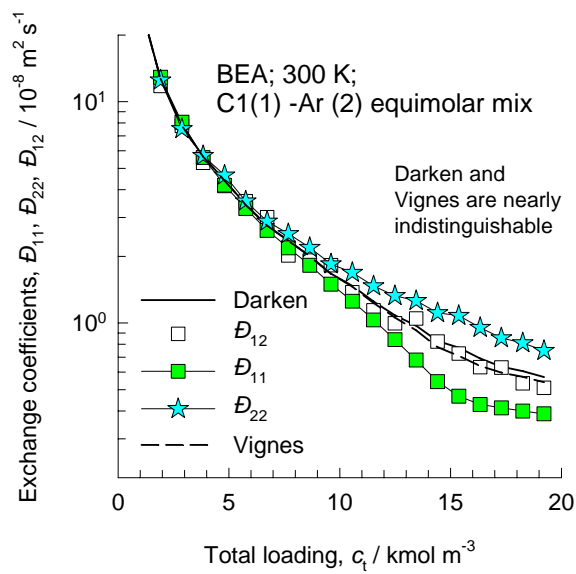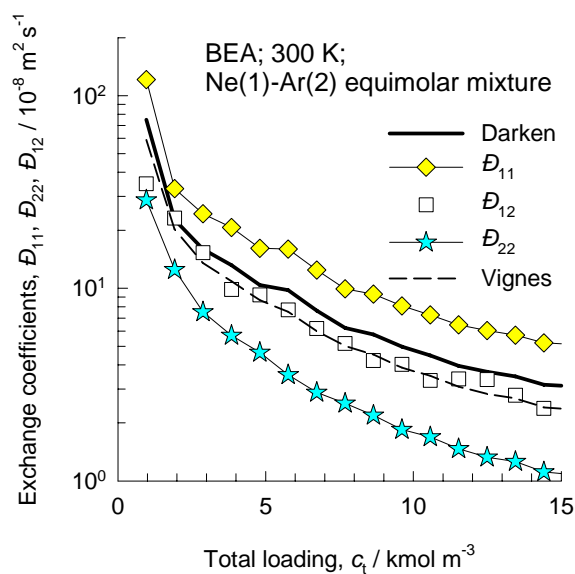
Prediction of $D_{i,self}$ and $\Delta_{ij}$ in binary mixtures in BEA using Vignes interpolation and M-S model

$$[\Delta] = \begin{bmatrix} \dfrac{1}{\DJ_1} + \dfrac{x_2}{\DJ_{12}} & -\dfrac{x_1}{\DJ_{12}} \\[2ex] -\dfrac{x_2}{\DJ_{12}} & \dfrac{1}{\DJ_2} + \dfrac{x_1}{\DJ_{12}} \end{bmatrix}^{-1}$$

Unary diffusion data

Vignes interpolation

$$\frac{1}{D_{1,self}} = \frac{1}{\DJ_1} + \frac{x_1}{\DJ_{11}} + \frac{x_2}{\DJ_{12}}$$

$$\frac{1}{D_{2,self}} = \frac{1}{\DJ_2} + \frac{x_2}{\DJ_{22}} + \frac{x_1}{\DJ_{12}}$$

Vignes interpolation

# CHA (all silica)

Figure 40

8-ring window of CHA

3.8 Å

3.8 Å
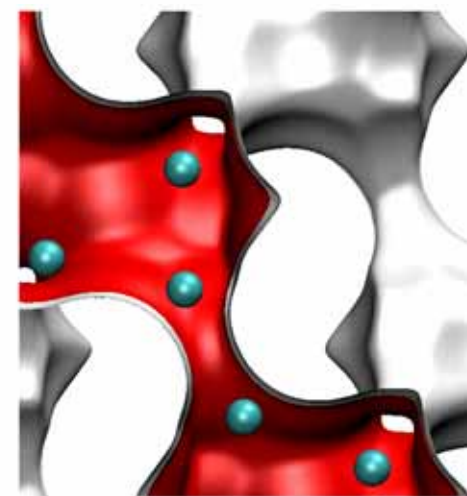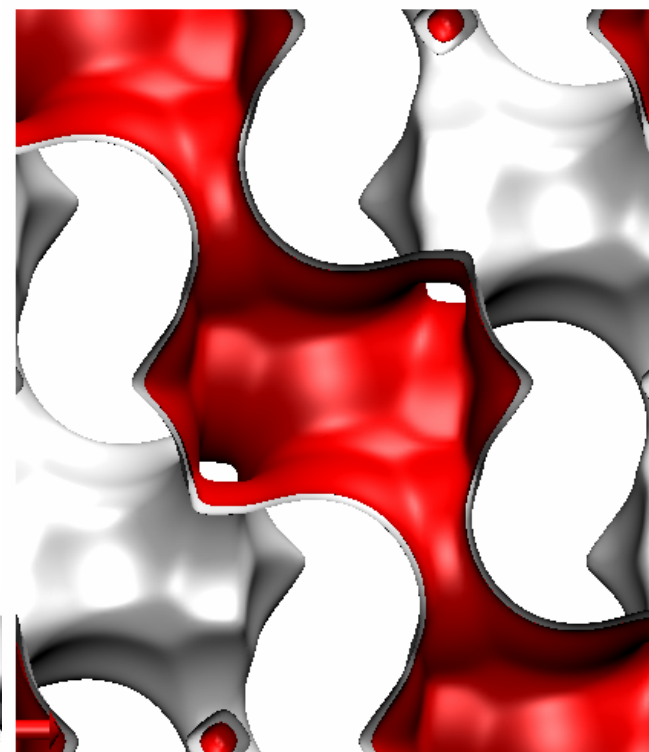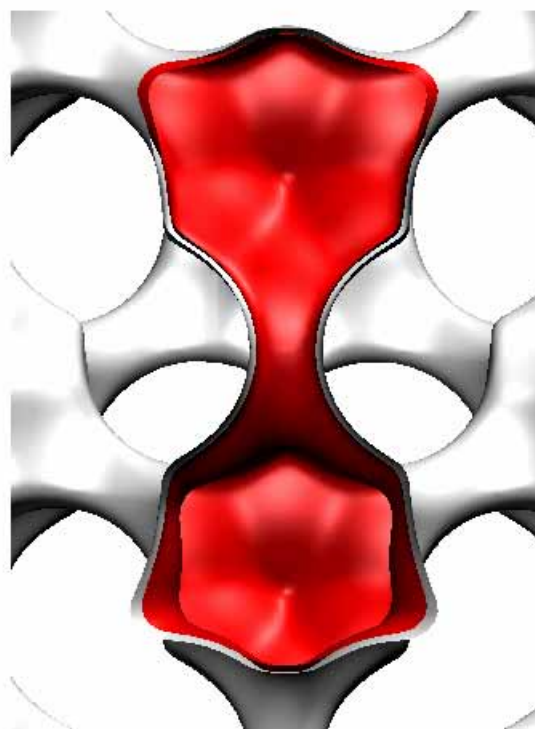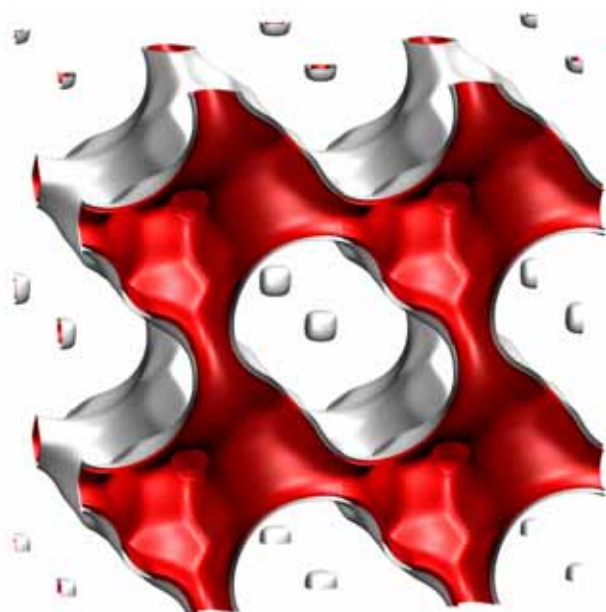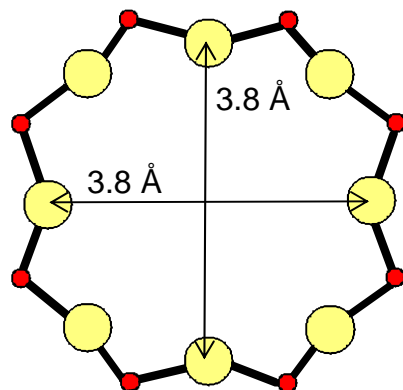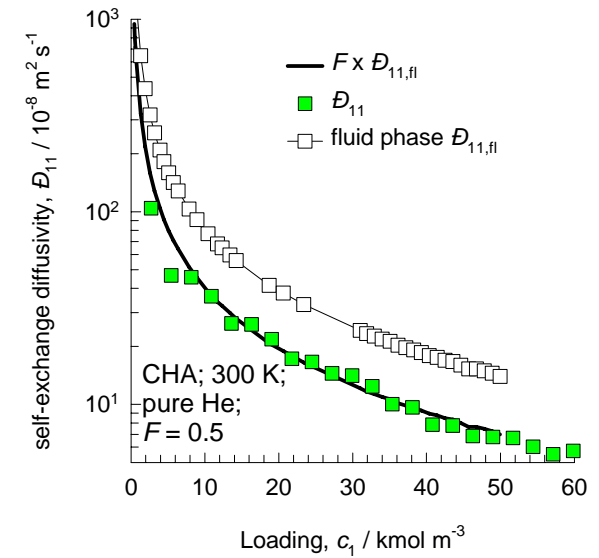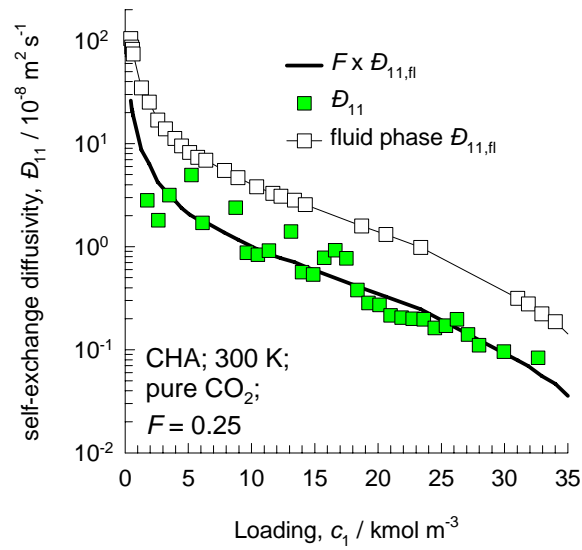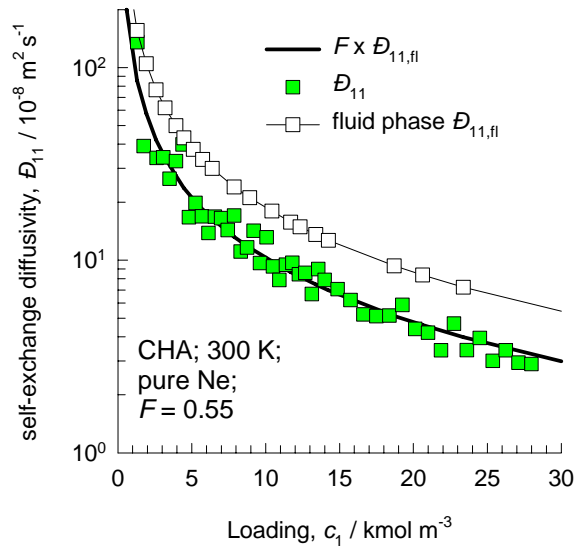
Figure 41

Data for all-silica CHA for unary diffusion
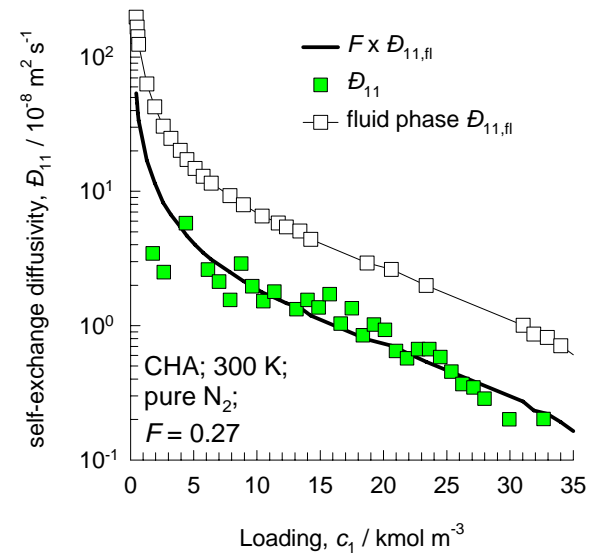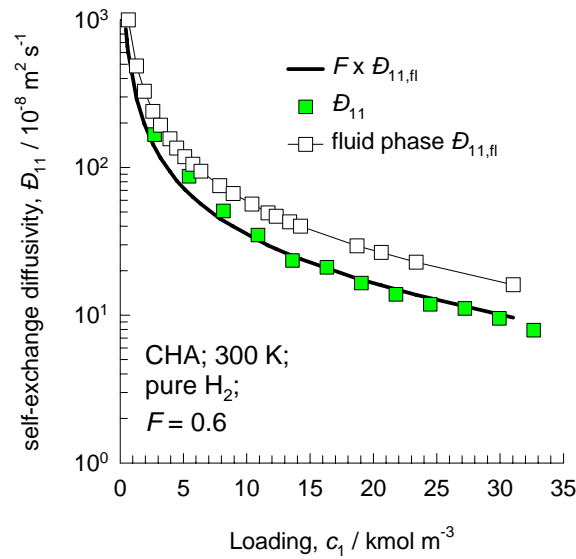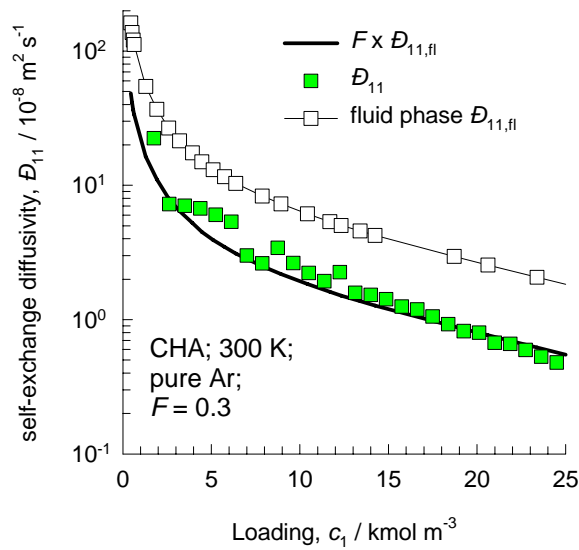
# Unary self diffusivities
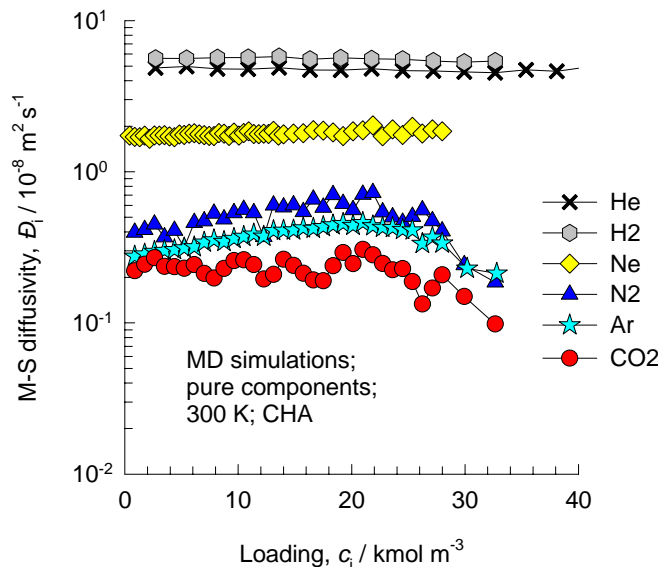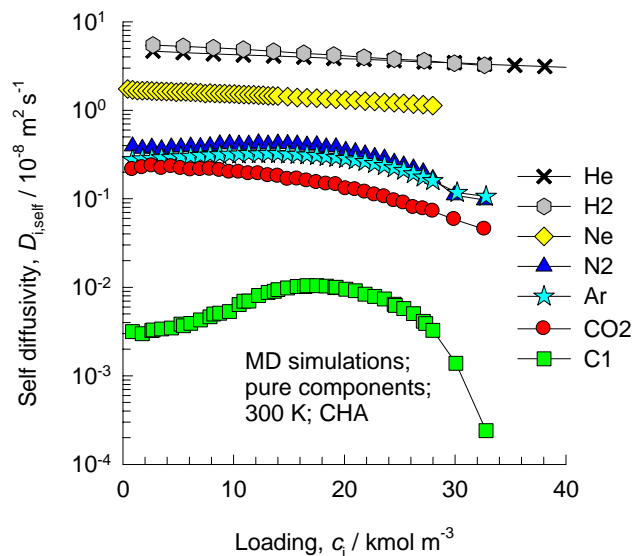


Figure 42
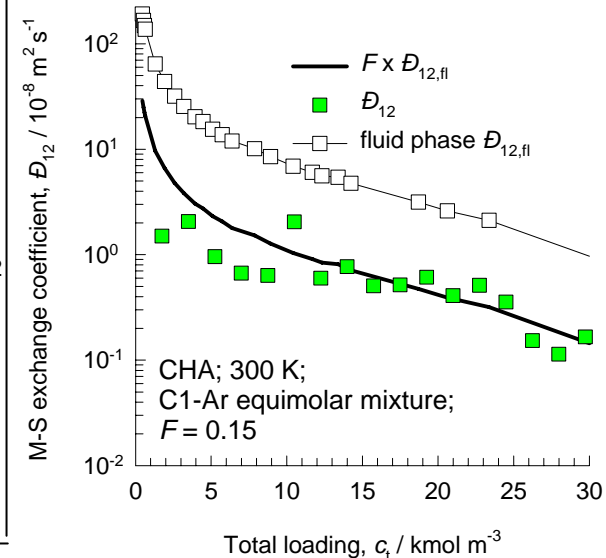
## Data for all-silica CHA for binary mixtures
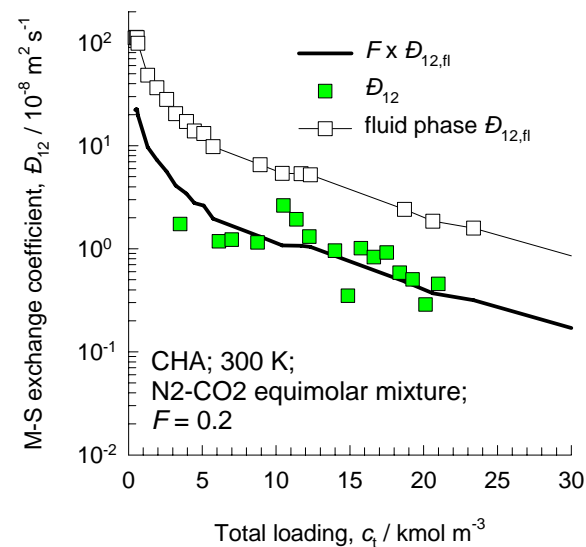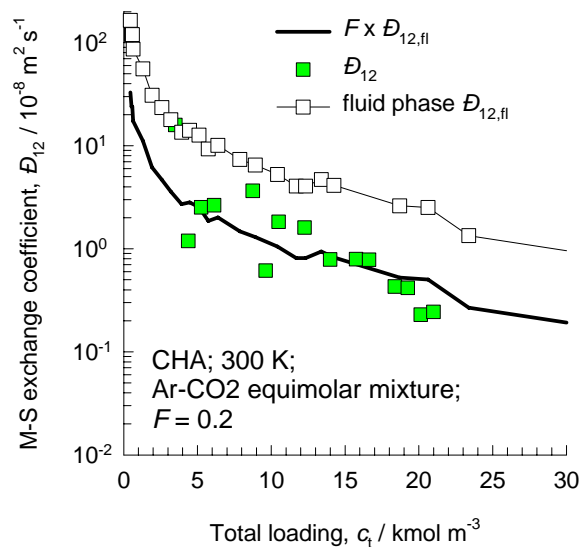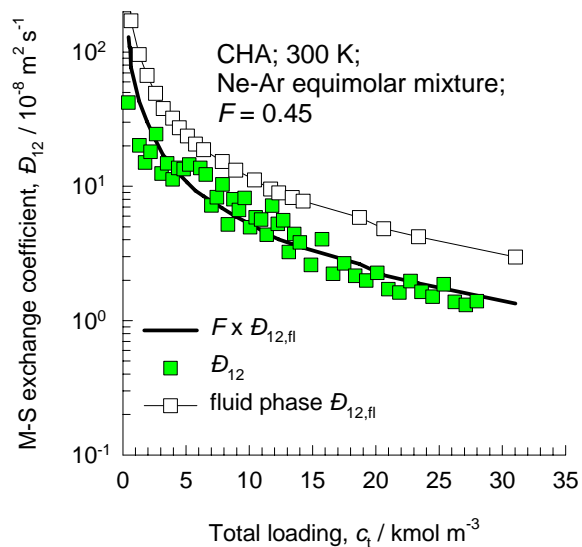
Figure 43
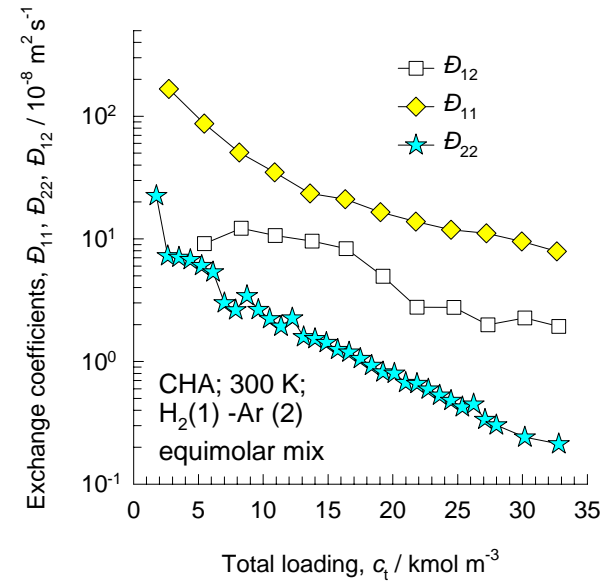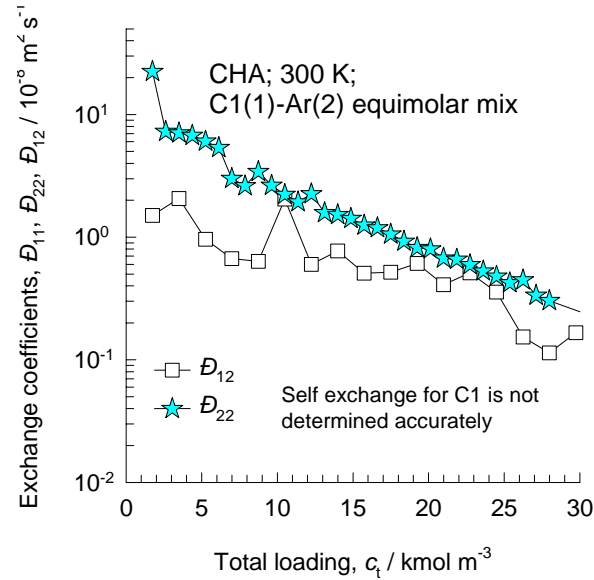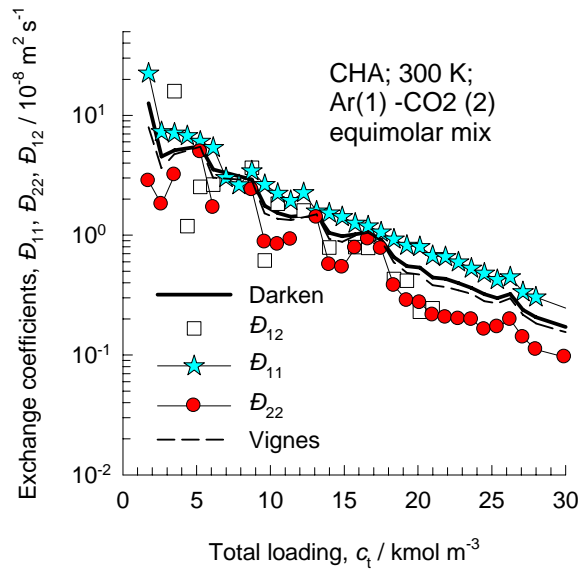
Test of Darken and Vignes interpolation formulae for CHA
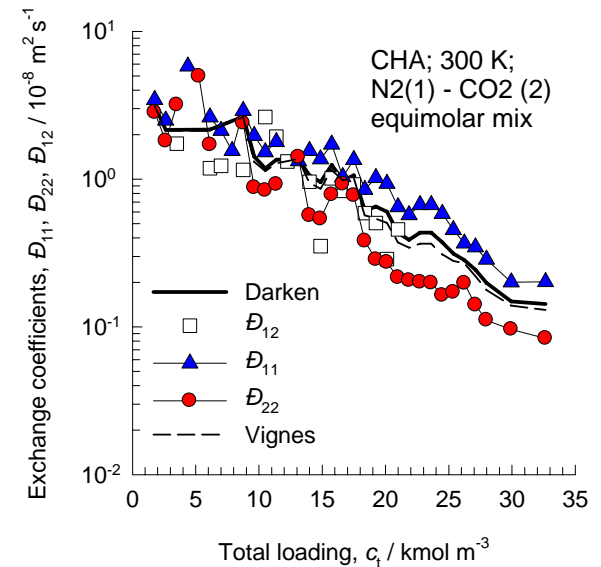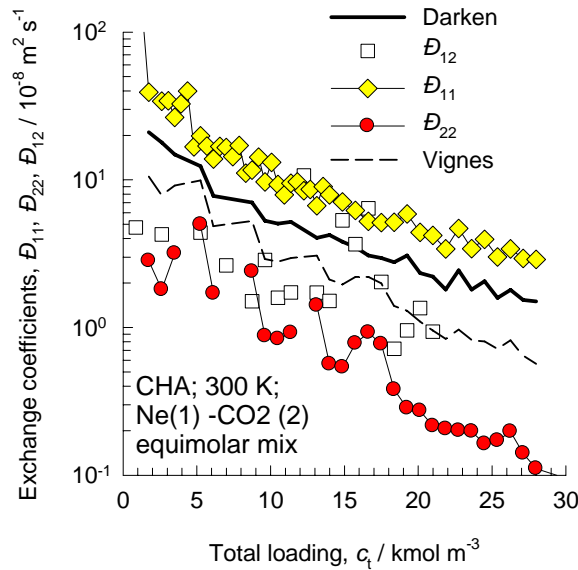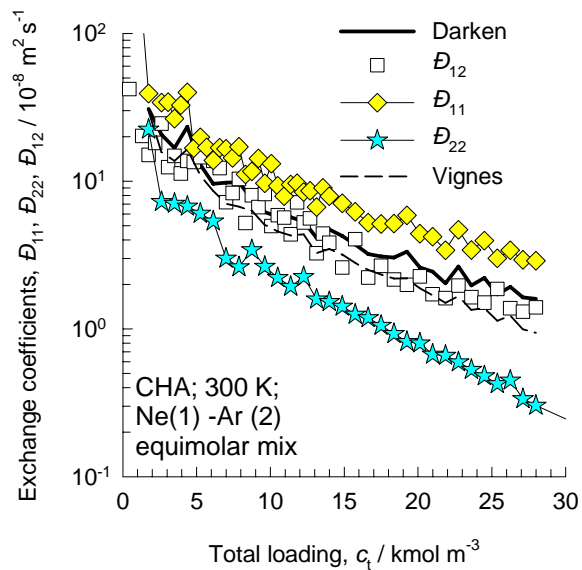
Figure 44

Prediction of $D_{i,self}$ and $\Delta_{ij}$ in binary mixtures in CHA using Vignes interpolation and M-S model

$$[\Delta] = \begin{bmatrix} \dfrac{1}{D_1} + \dfrac{x_2}{D_{12}} & -\dfrac{x_1}{D_{12}} \\[2ex] -\dfrac{x_2}{D_{12}} & \dfrac{1}{D_2} + \dfrac{x_1}{D_{12}} \end{bmatrix}^{-1}$$

Unary diffusion data

Vignes interpolation

$$\frac{1}{D_{1,self}} = \frac{1}{D_1} + \frac{x_1}{D_{11}} + \frac{x_2}{D_{12}}$$

$$\frac{1}{D_{2,self}} = \frac{1}{D_2} + \frac{x_2}{D_{22}} + \frac{x_1}{D_{12}}$$

Vignes interpolation
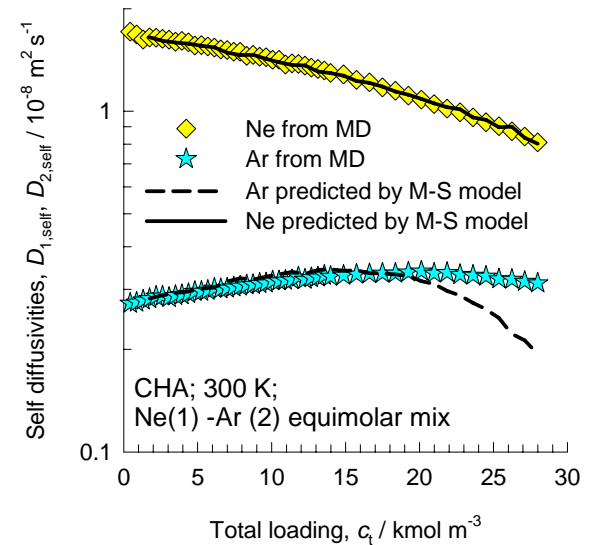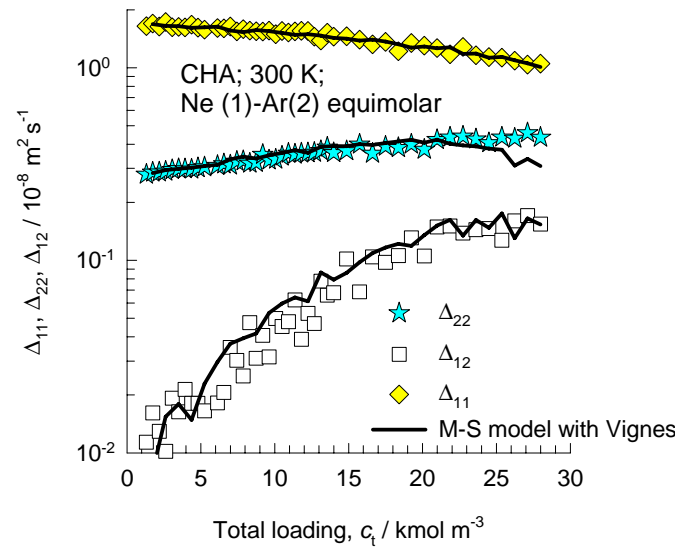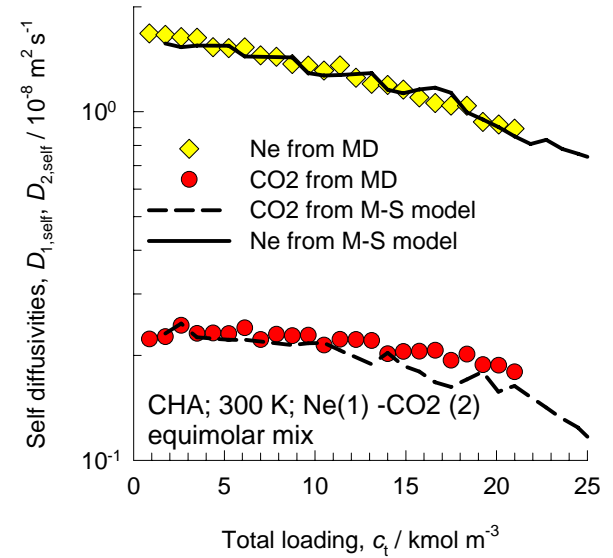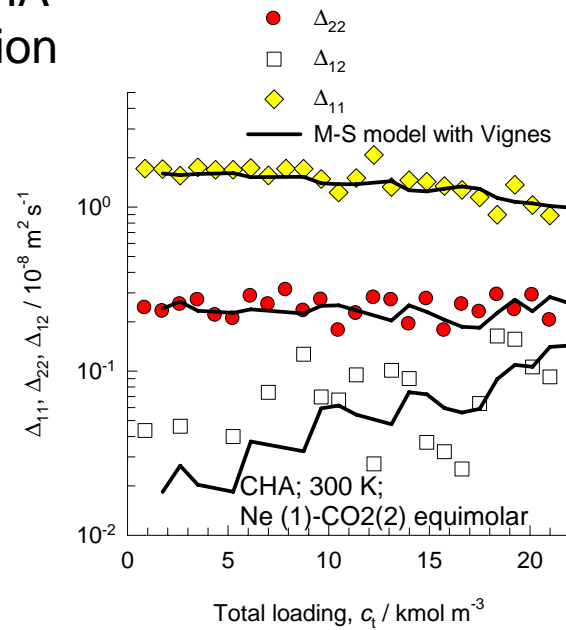
# LTA

Figure 45

8-ring
window
of LTA

4.1 Å

4.1 Å

LTA
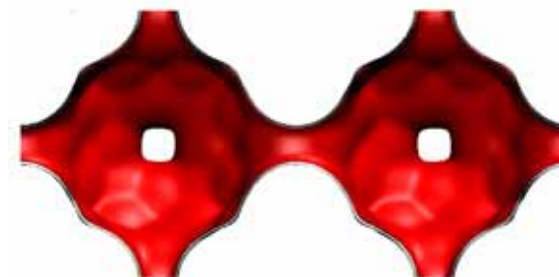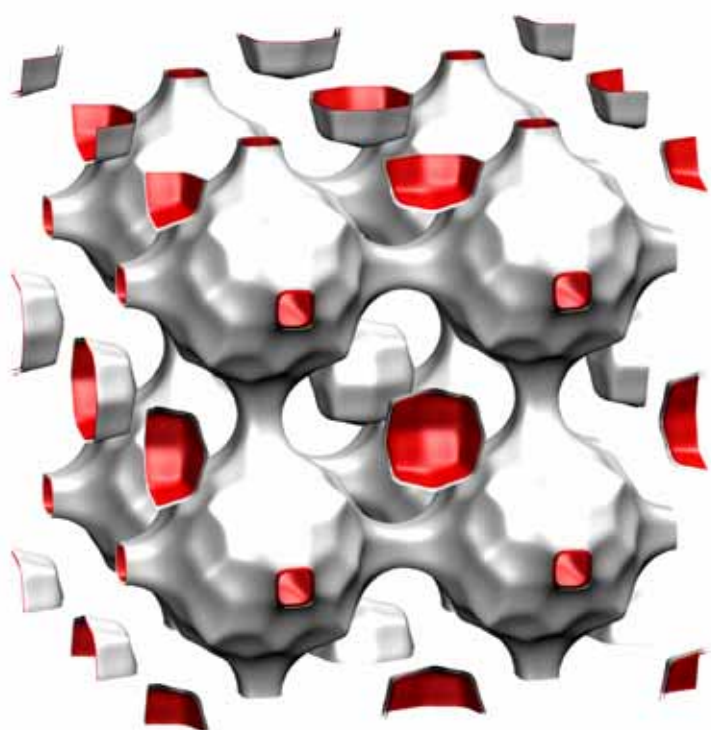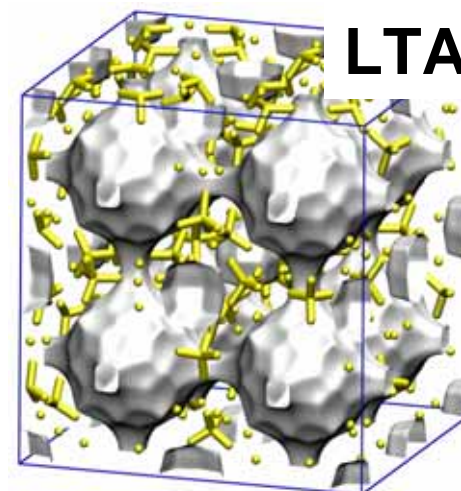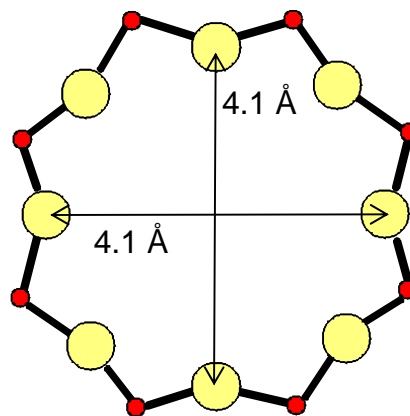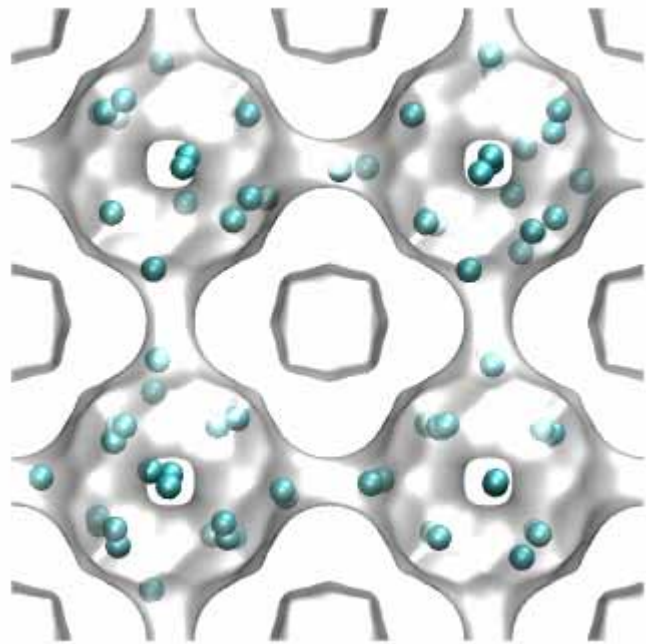
Figure 46

LTA (all silica)

**Snapshots of methane**

LTA-5A (32 Na+, 32 Ca++)

LTA-4A (96 Na+)

Na+

Na+

Ca++

C1

C1
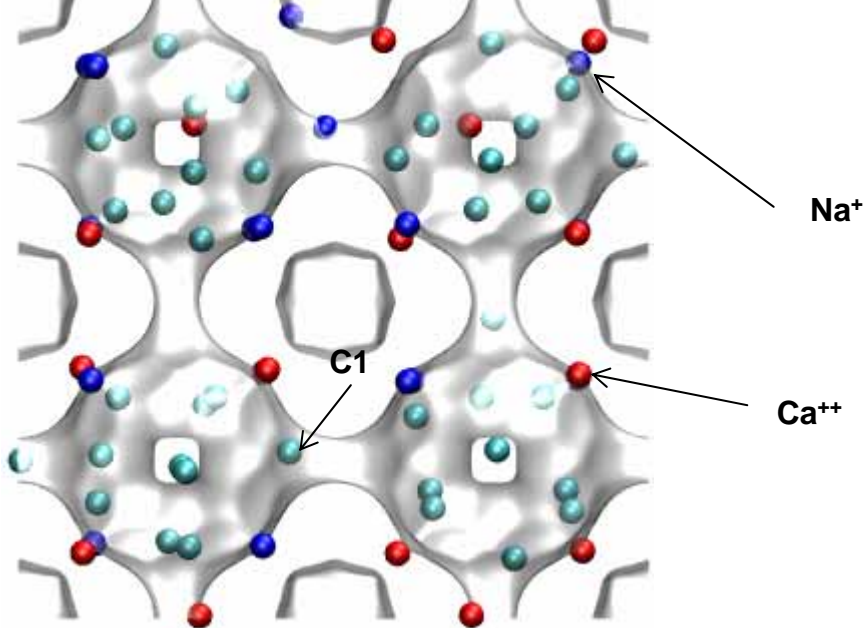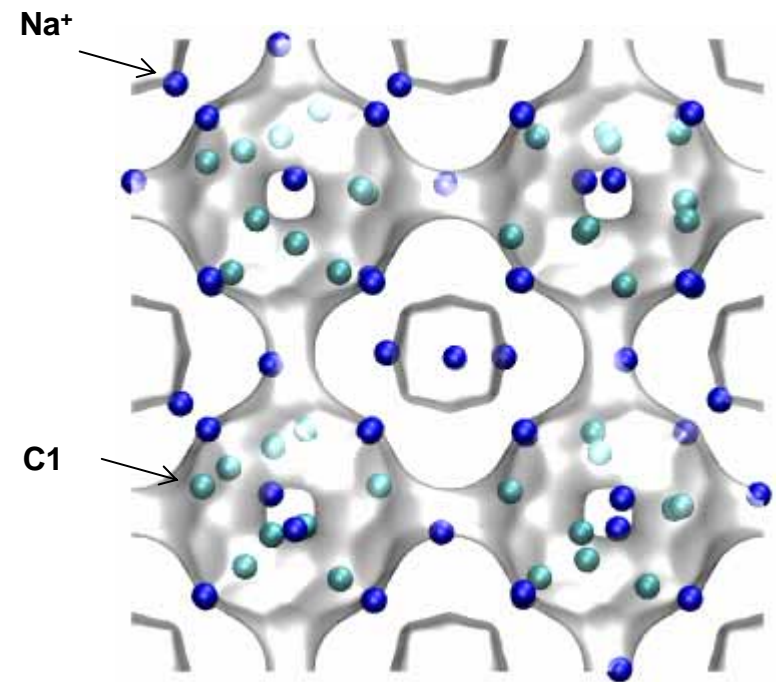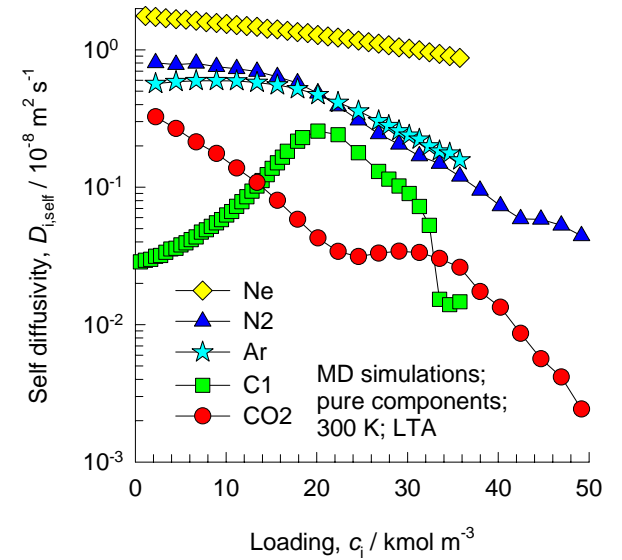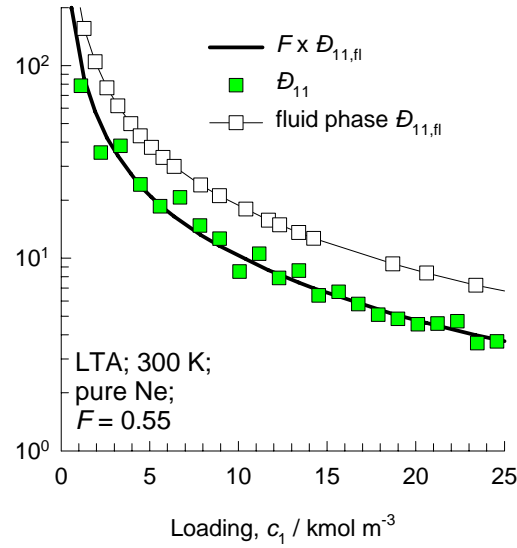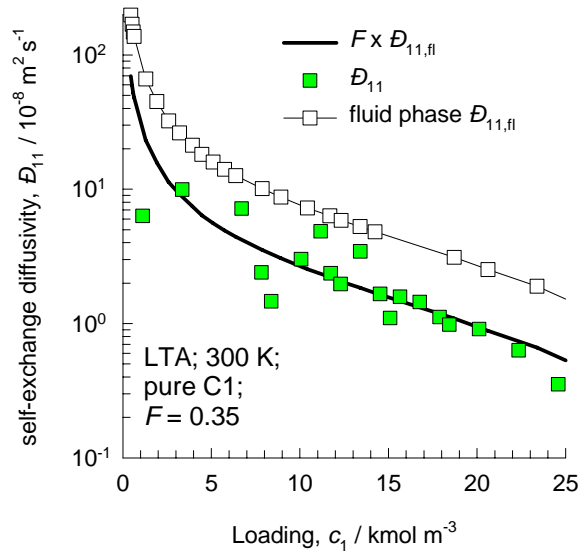
Figure 47

Data for all-silica LTA for unary diffusion
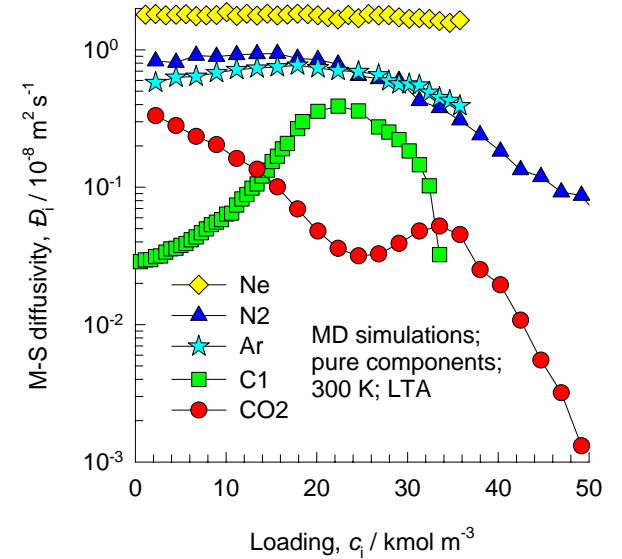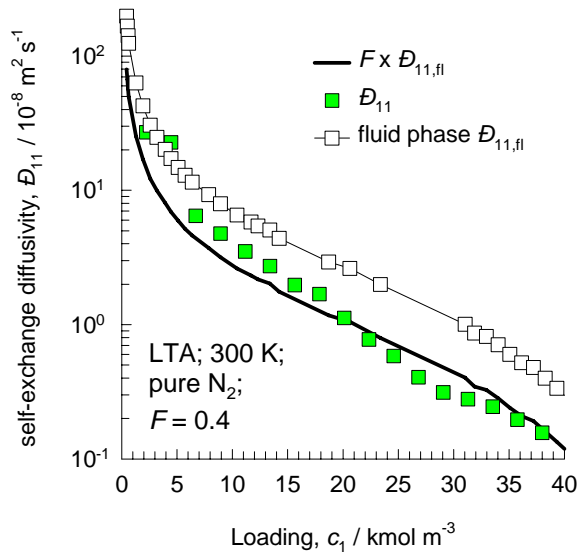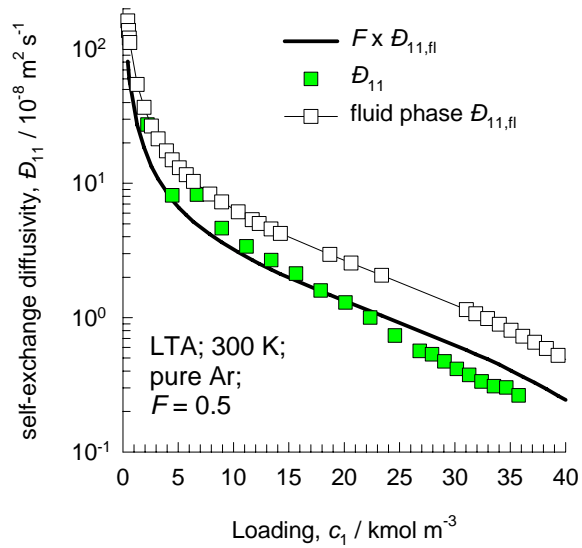
Figure 48
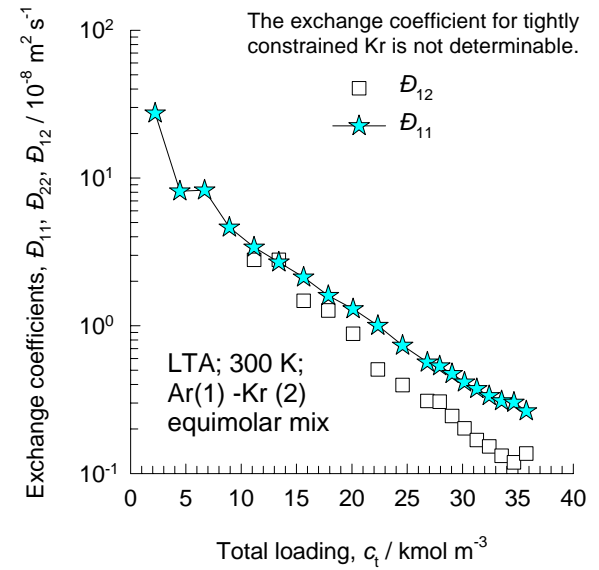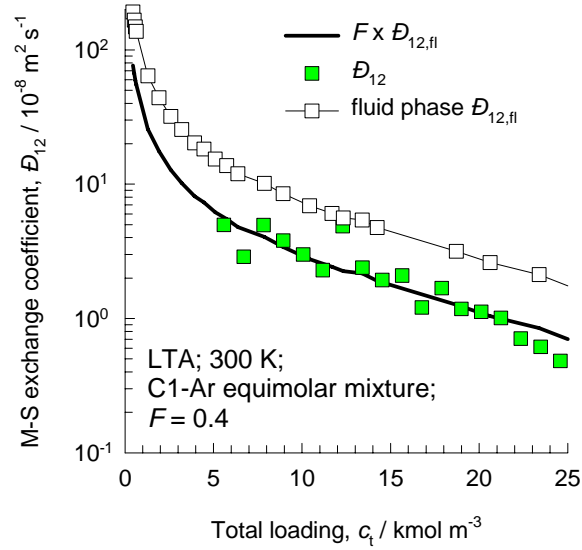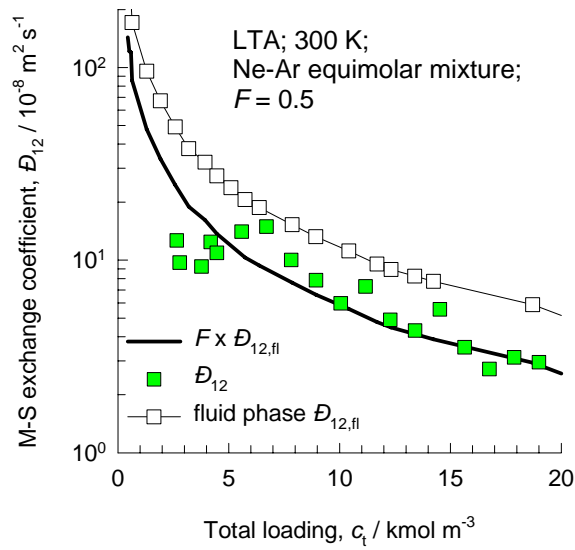


Data for all-silica LTA for binary mixtures
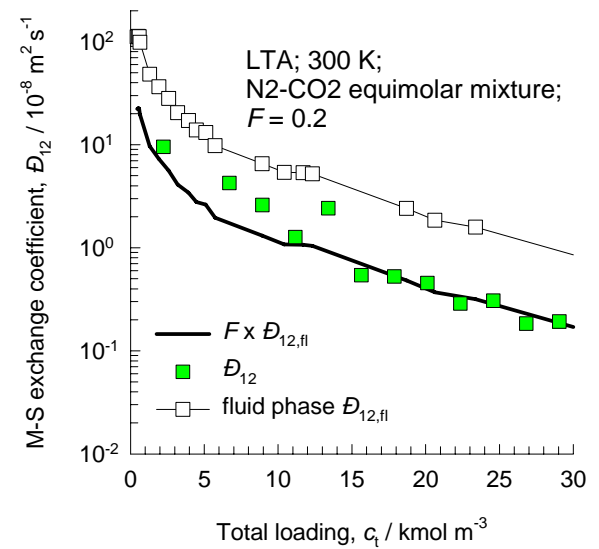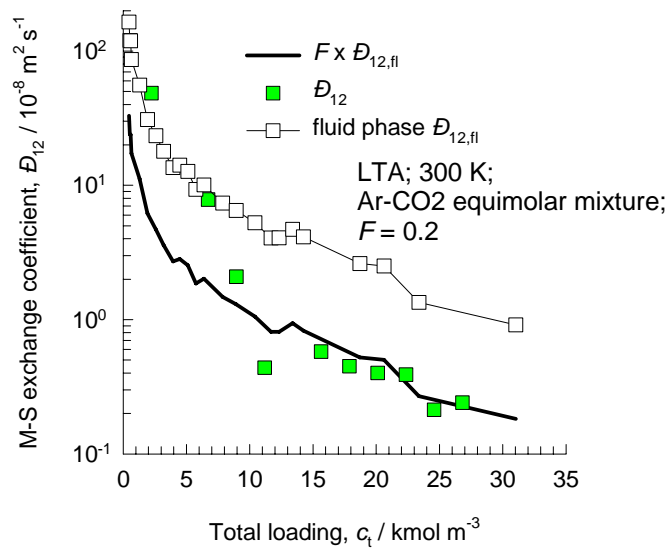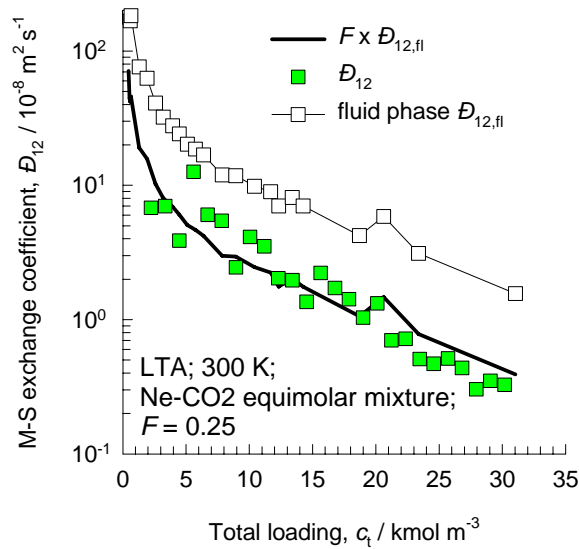
Figure 49
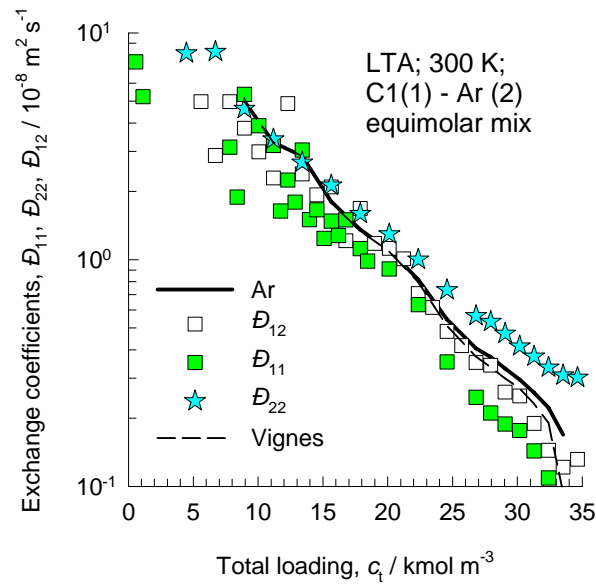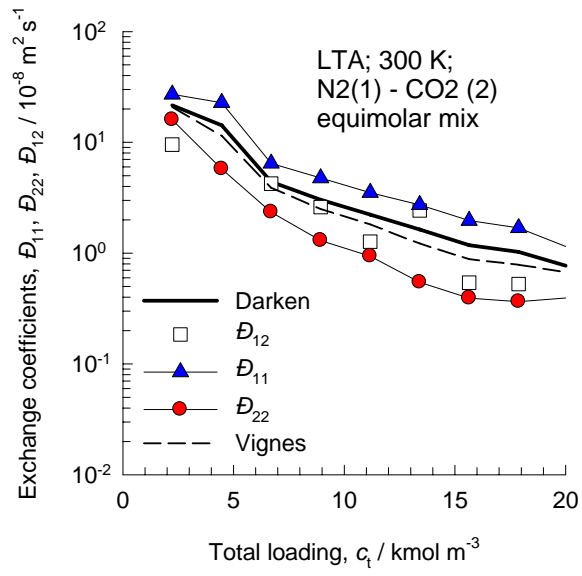
Test of Darken and Vignes interpolation formulae for LTA
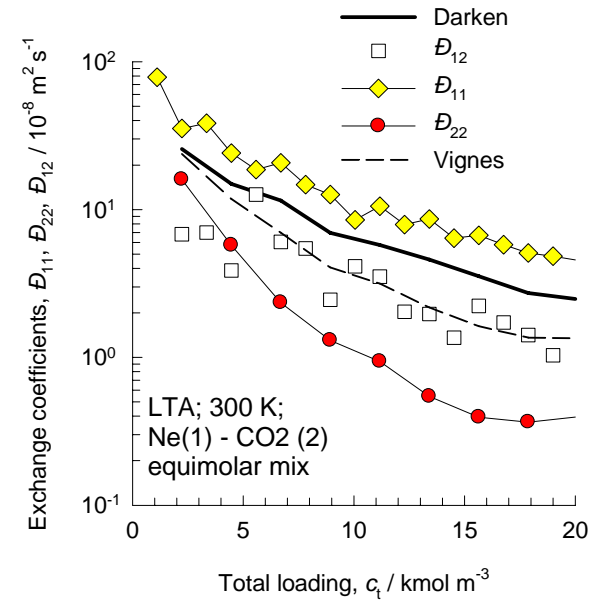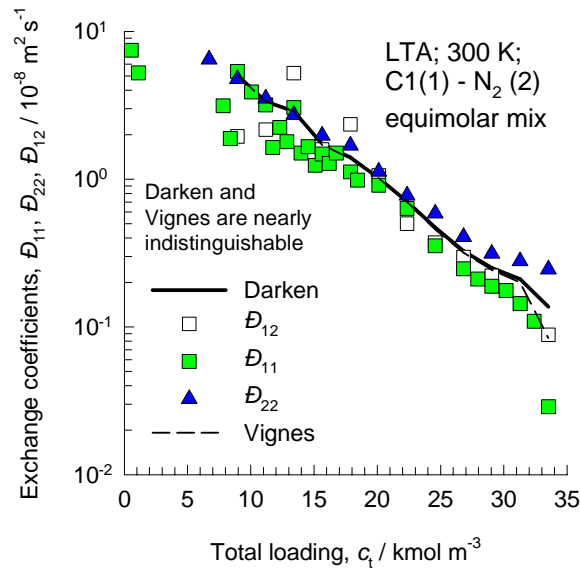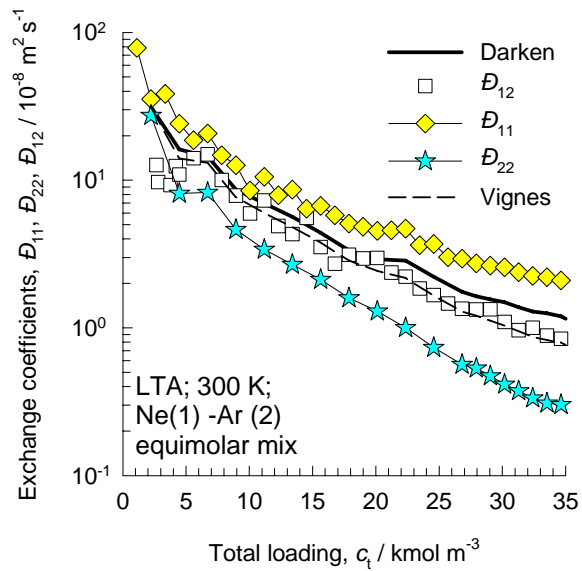
# Prediction of $D_{i,self}$ and $\Delta_{ij}$ in binary mixtures in LTA using Vignes interpolation and M-S model

The predictions for Ne in Ne-CO2 mixtures are poor because of the blockage of the window regions by CO2.  See R. Krishna and J.M. van Baten, Segregation effects in adsorption of CO2 containing mixtures and their consequences for separation selectivities in cage-type zeolites, Separation and Purification Technology, 61, 414-423 (2008)

Figure 50

$$[\Delta] = \begin{bmatrix} \dfrac{1}{D_1} + \dfrac{x_2}{D_{12}} & -\dfrac{x_1}{D_{12}} \\[2mm] -\dfrac{x_2}{D_{12}} & \dfrac{1}{D_2} + \dfrac{x_1}{D_{12}} \end{bmatrix}^{-1}$$

Unary diffusion data

Vignes interpolation

$$\frac{1}{D_{1,self}} = \frac{1}{D_1} + \frac{x_1}{D_{11}} + \frac{x_2}{D_{12}}$$

$$\frac{1}{D_{2,self}} = \frac{1}{D_2} + \frac{x_2}{D_{22}} + \frac{x_1}{D_{12}}$$

Vignes interpolation



LTA; 300 K; Ne (1)-CO2(2) equimolar

- $\Delta_{22}$
- $\Delta_{12}$
- $\Delta_{11}$
- M-S model with Vignes



LTA; 300 K; Ne(1) -CO2 (2) equimolar mix

- Ne from MD
- CO2 from MD
- CO2 from M-S model
- Ne from M-S model



LTA; 300 K; Ne (1)-Ar(2) equimolar

- $\Delta_{22}$
- $\Delta_{12}$
- $\Delta_{11}$
- M-S model with Vignes



LTA; 300 K; Ne(1) -Ar (2) equimolar mix

- Ne from MD
- Ar from MD
- Ar predicted by M-S model
- Ne predicted by M-S model
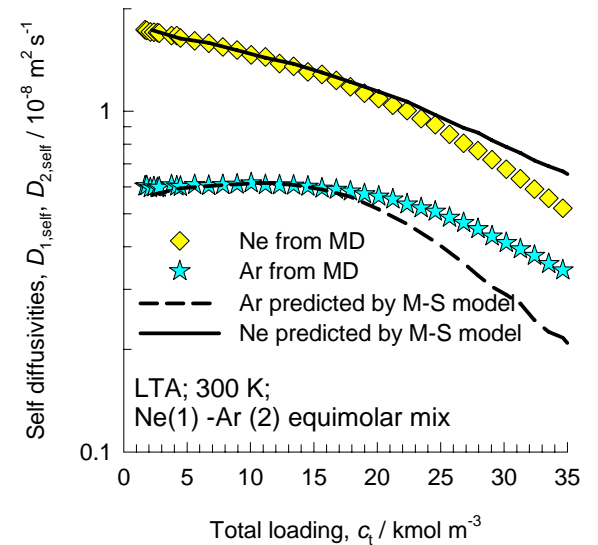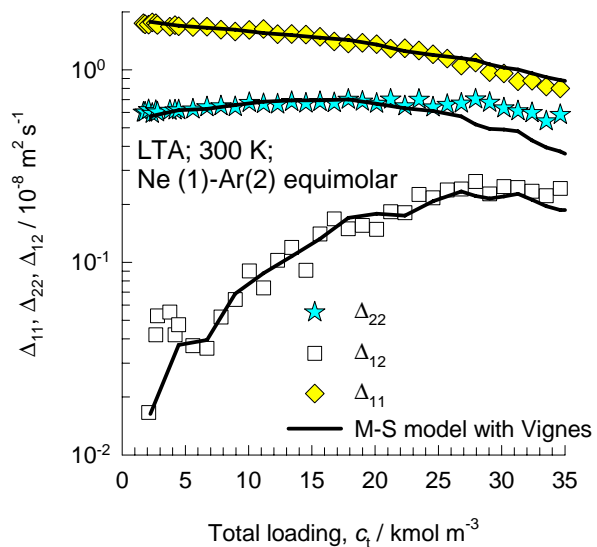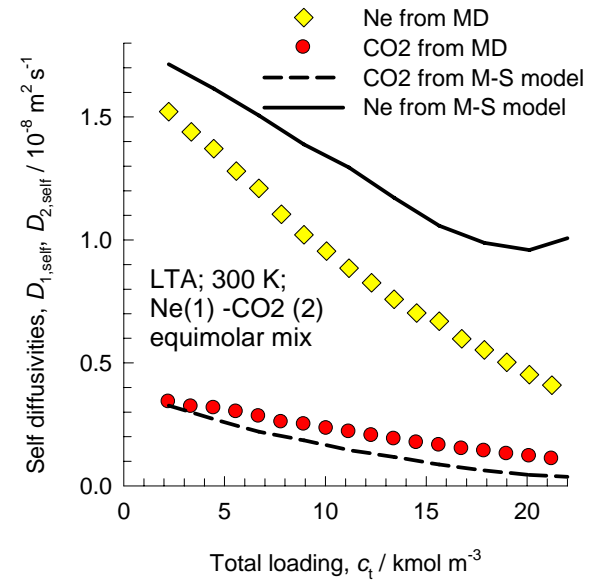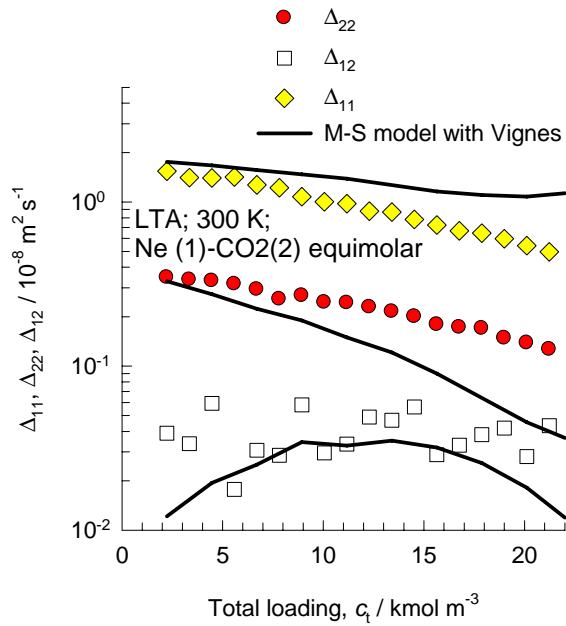
Figure 51
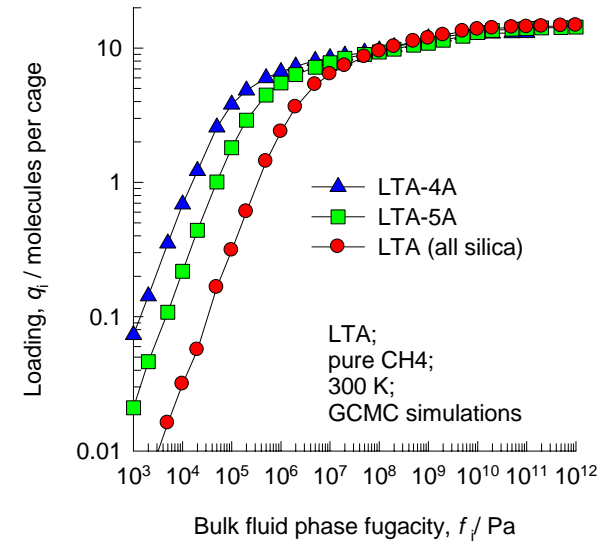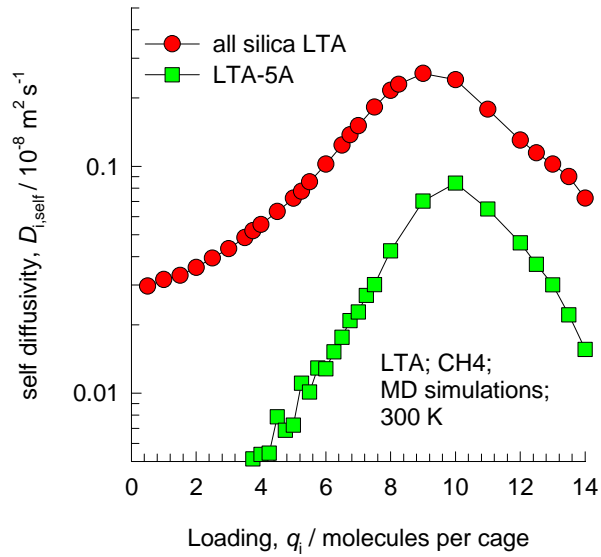


Comparison of all-silica LTA with LTA-5A, and LTA-4A;
Data for methane (C1) for 300 K, and 800 K

The presence of Na+
and Ca++ ions increases
the adsorption strength.

The cations cause the window region to be more constricted, and
consequently the inter-cage hopping of C1 is practically un-correlated.
The self- and M-S diffusivities are nearly identical.  The self-diffusivities
are only reported here. The exchange coefficient is indeterminate, and is
not relevant for LTA-4A, and LTA-5A; for these structures the Habgood
approximation is a good one.

Figure 52
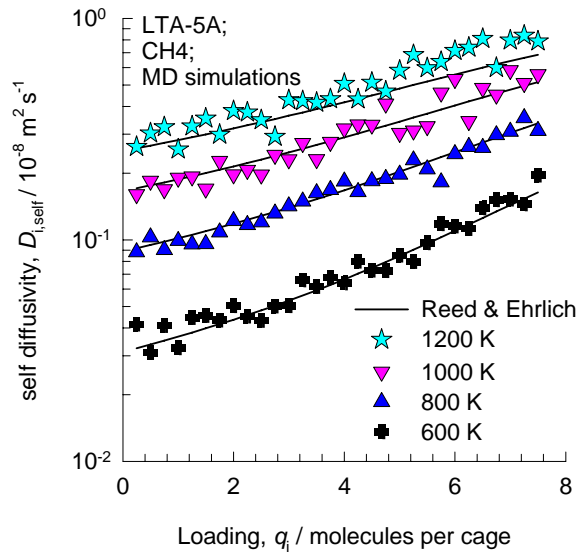


For LTA-5A the cations cause the window region to be more constricted, and consequently the inter-cage hopping of C1 is practically un-correlated. The self- and M-S diffusivities are nearly identical. The self-diffusivities are only reported here.

## Comparison of all-silica LTA with LTA-5A; Activation energy

The all-silica LTA data presented here is from our earlier publication
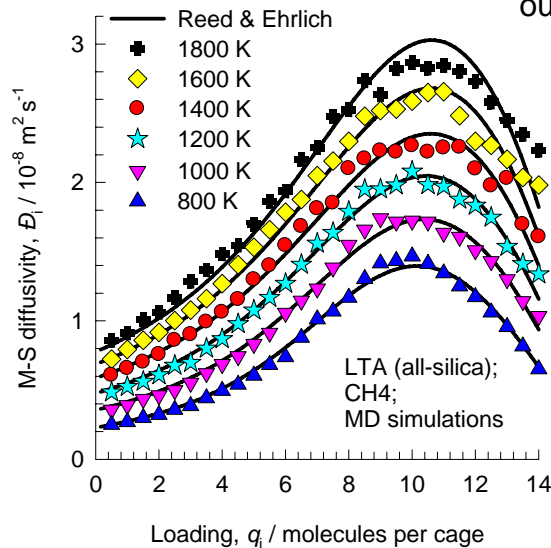


The activation energy is increased significantly for LTA-5A with cations present.
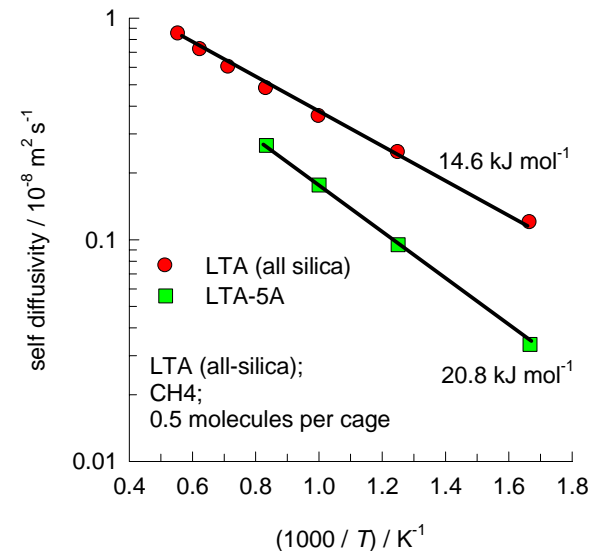
# DDR

8-ring window of DDR

4.4 Å

3.6 Å
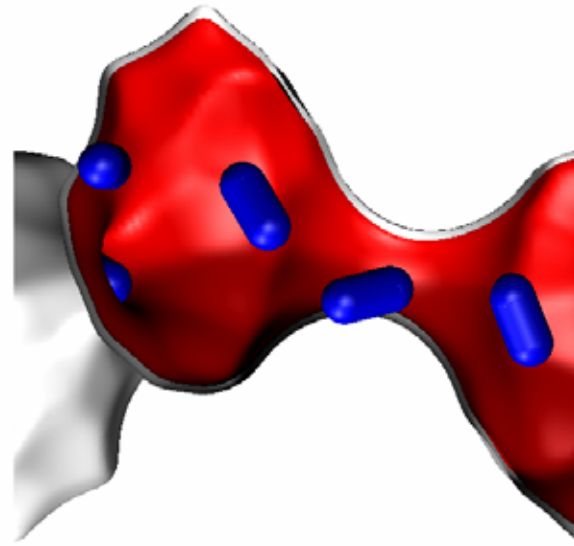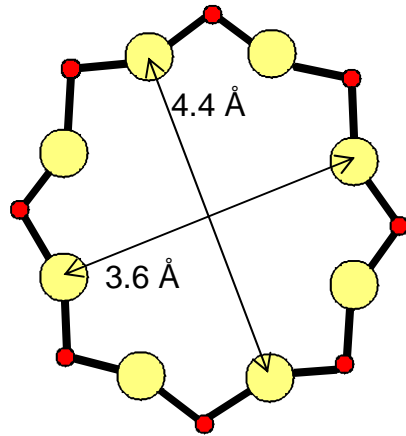
Figure 53

Data for all-silica DDR for unary diffusion; we consider the average of diffusivities in the x- and y-directions

DDR; 300 K;
pure $CO_2$;
$F = 0.06$

DDR; 300 K;
pure Ne;
$F = 0.35$

DDR; 300 K;
pure $N_2$;
$F = 0.17$
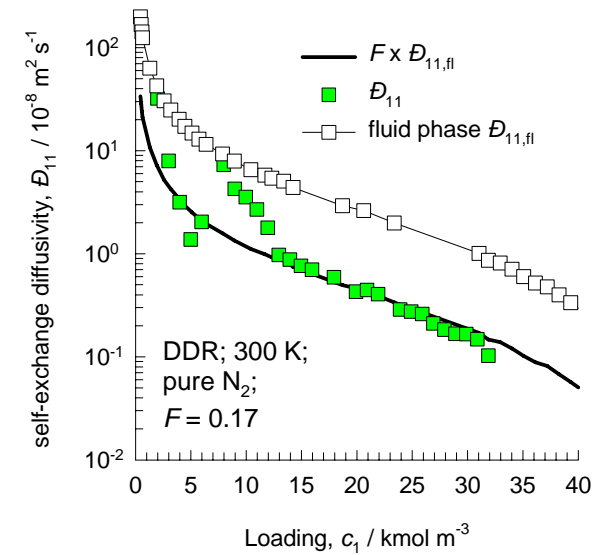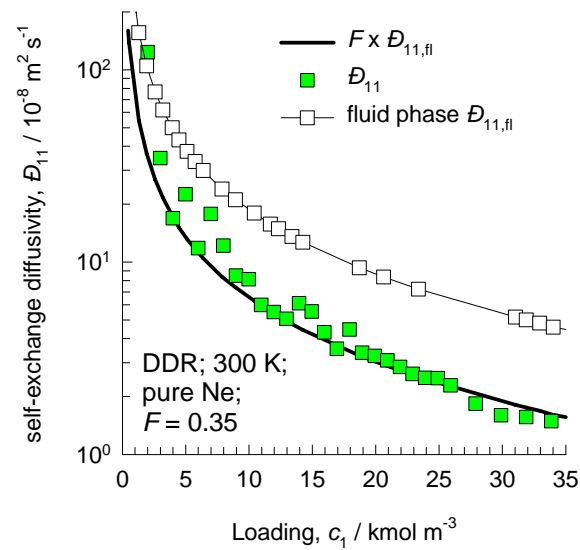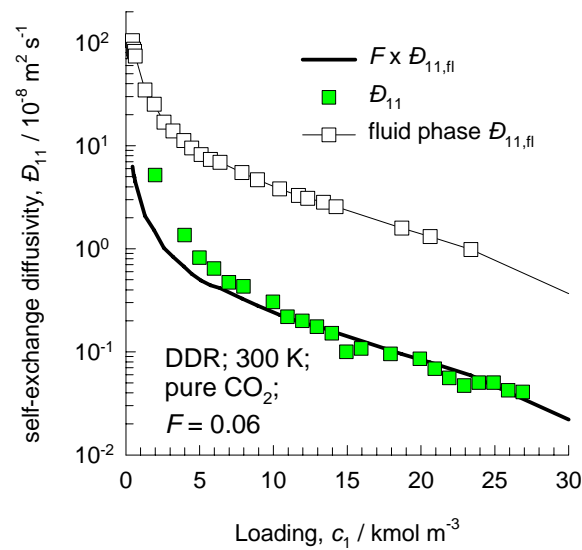
# Unary diffusion data for DDR
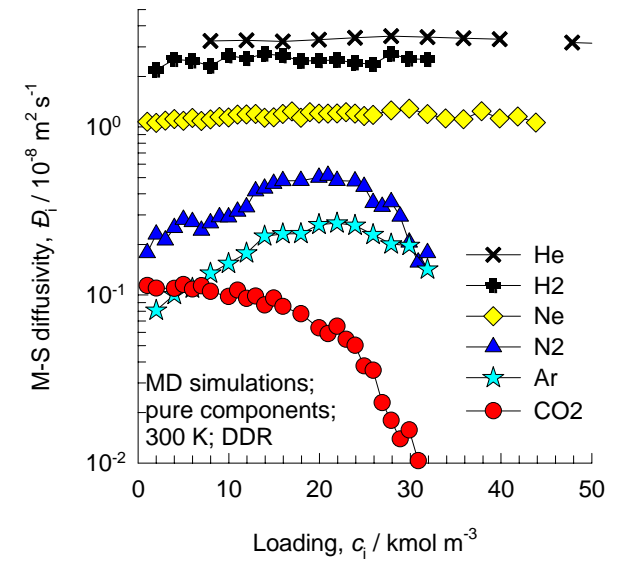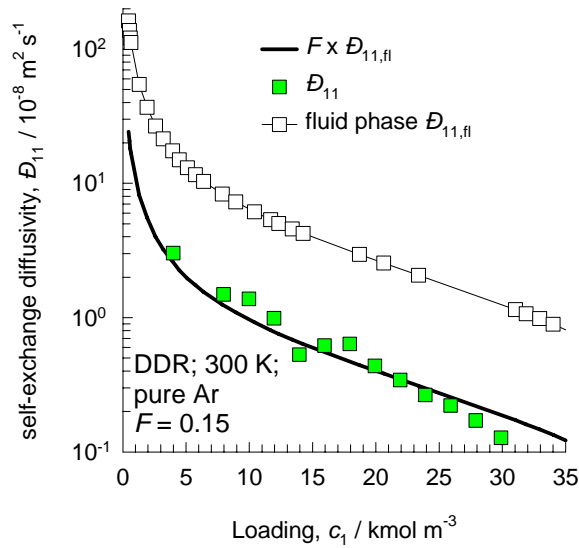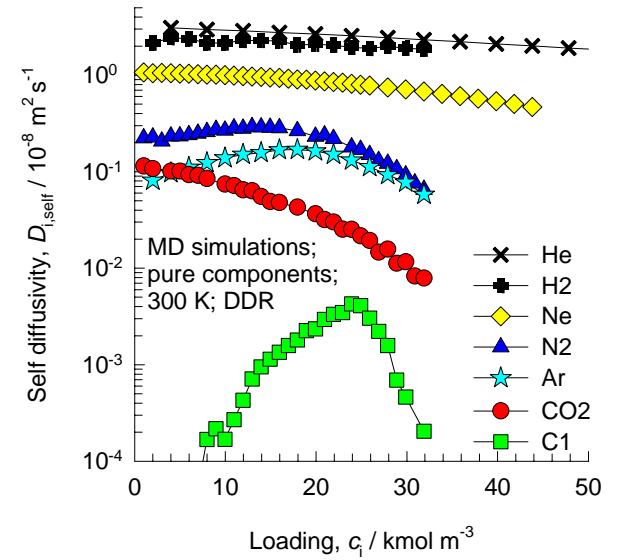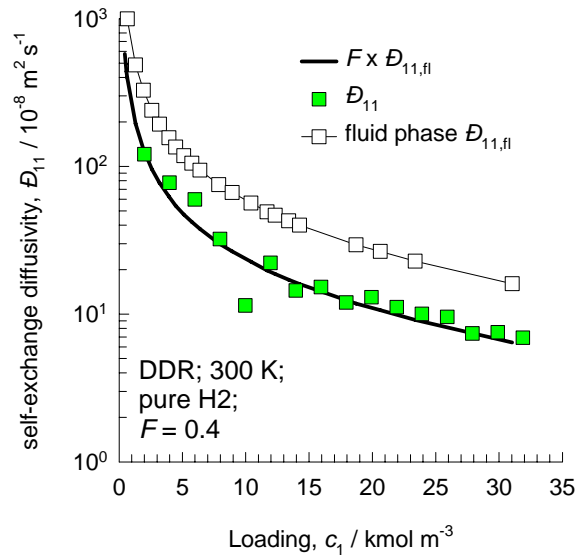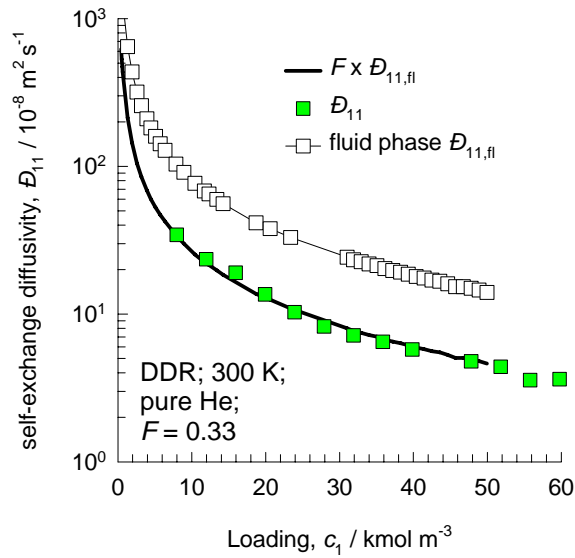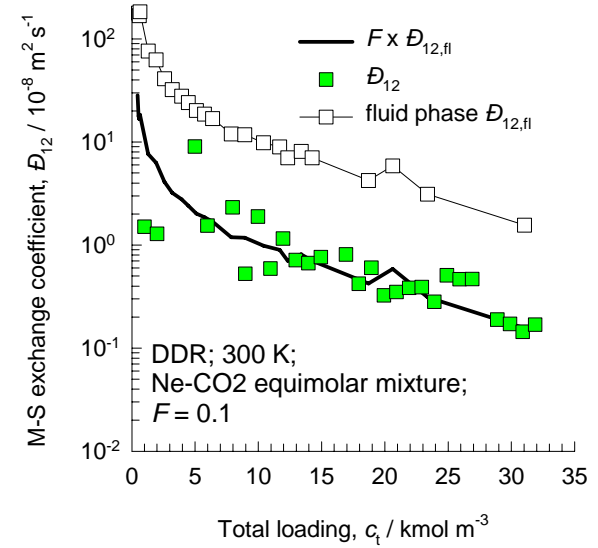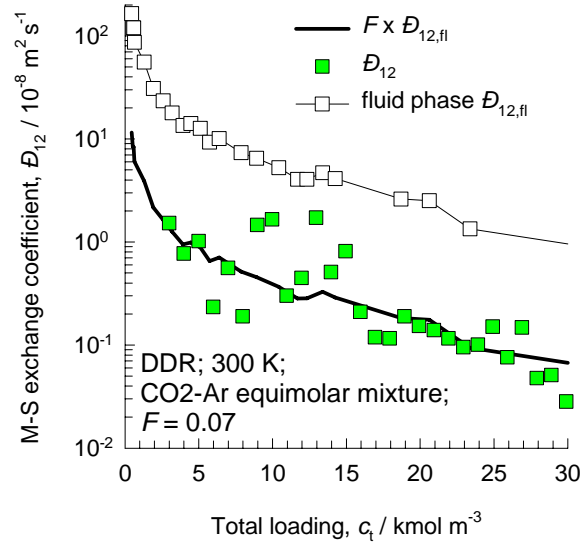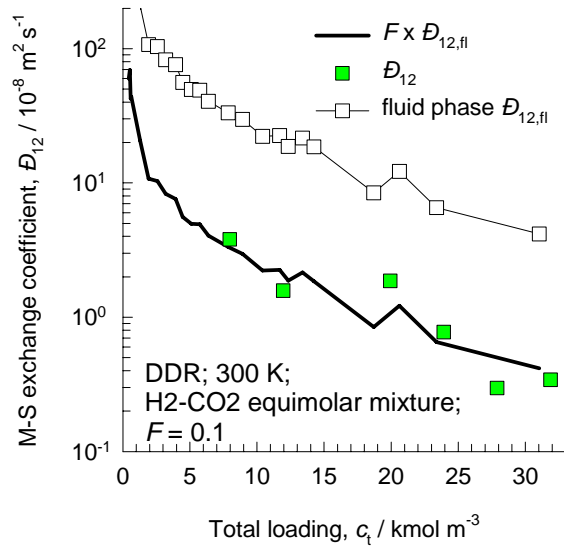
Figure 54

Figure 55



Binary diffusion data for DDR
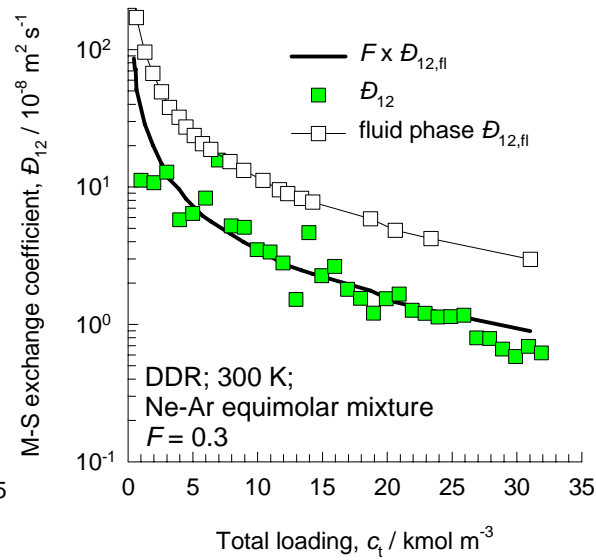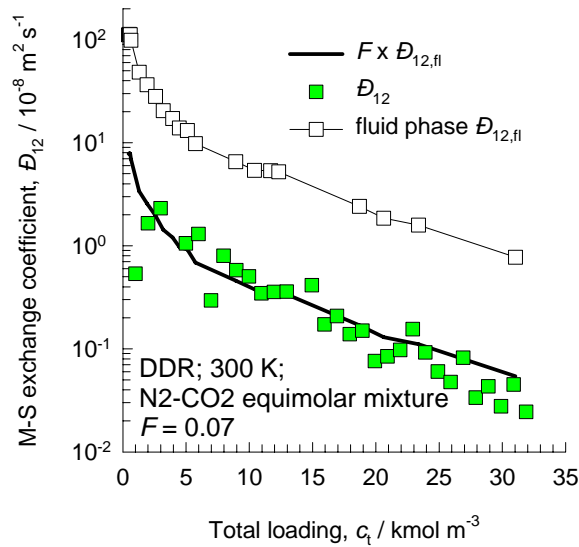
Figure 56
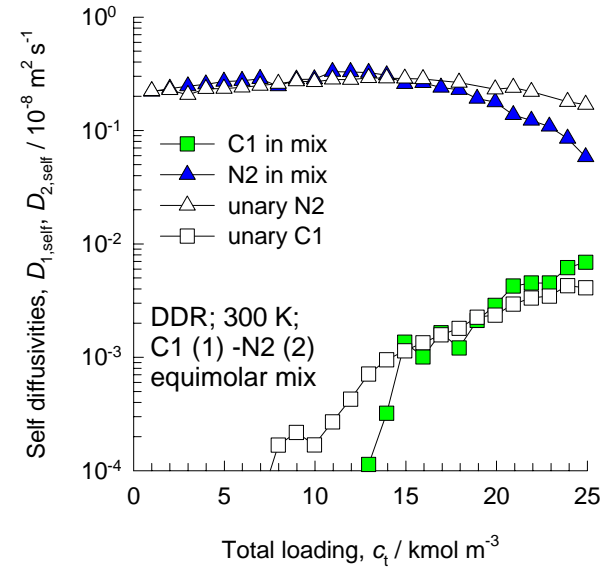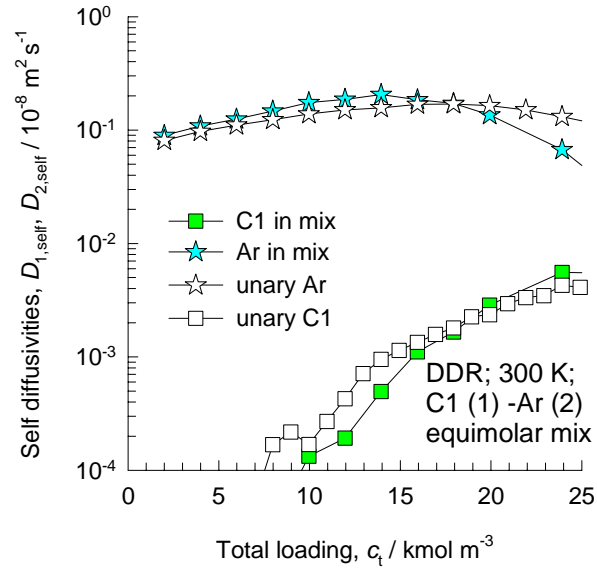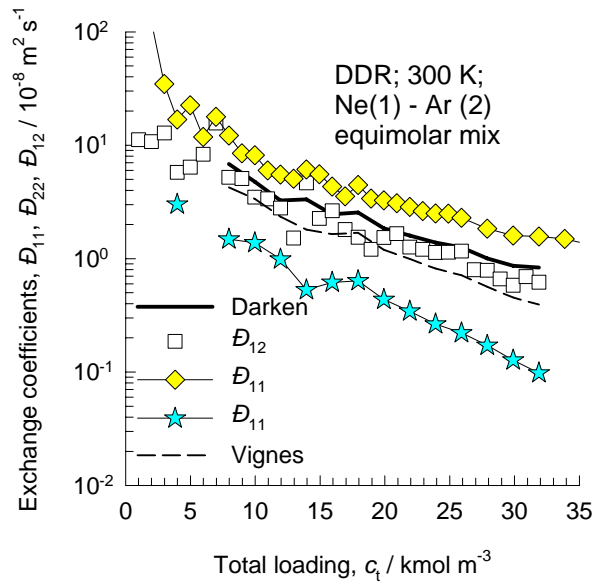
Test of Darken and Vignes interpolation formulae for DDR
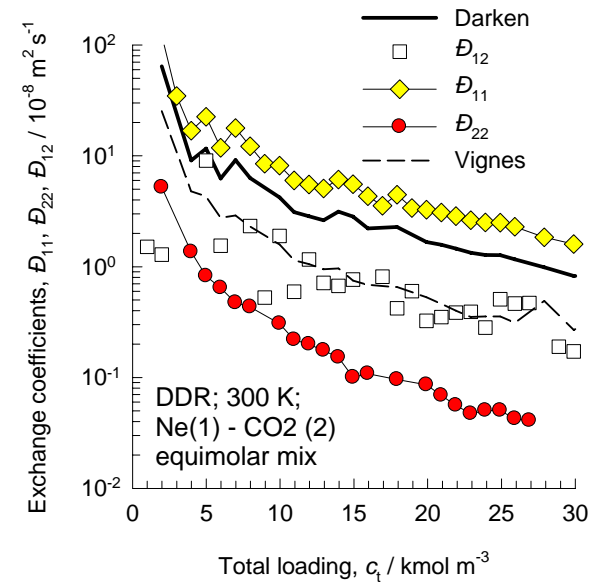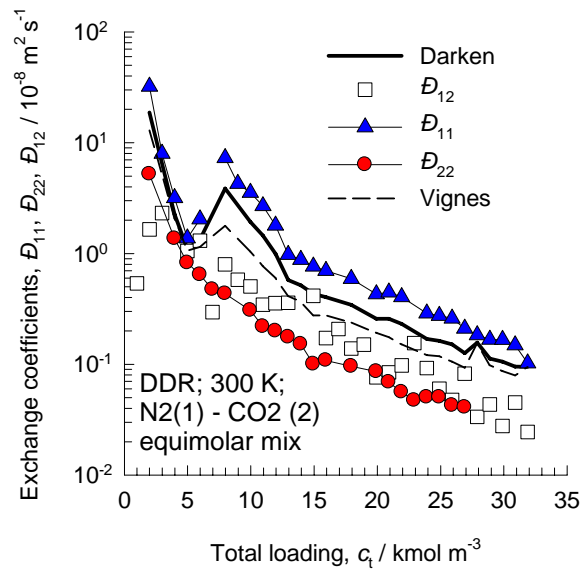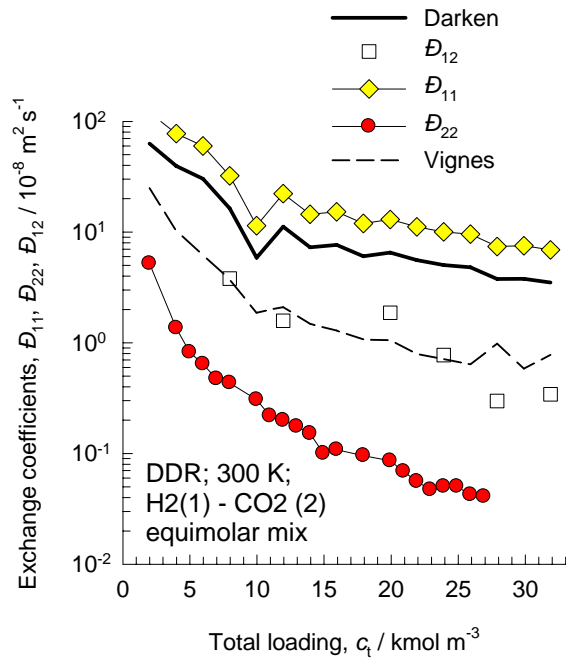
# Figure 57

Prediction of $D_{i,self}$ and $\Delta_{ij}$ in binary mixtures in DDR using Vignes interpolation and M-S model
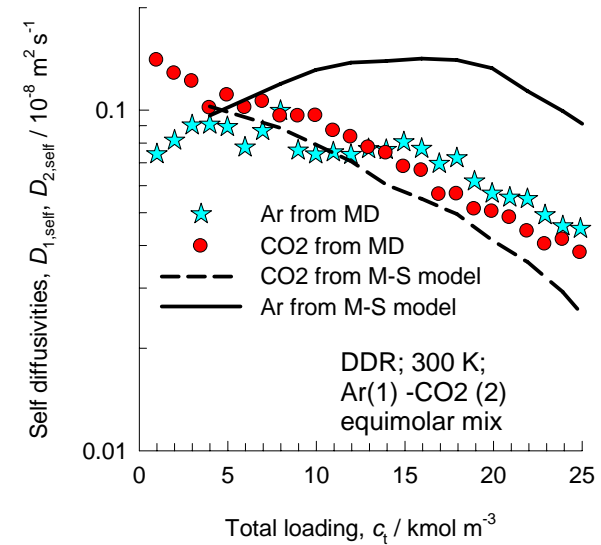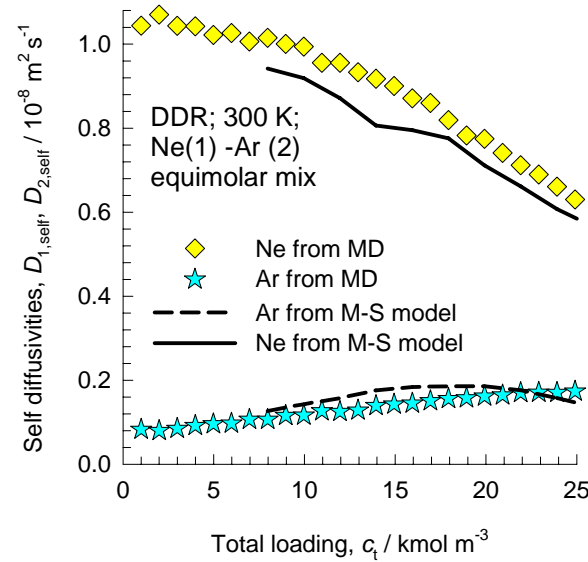


DDR; 300 K;
Ne(1) -Ar (2)
equimolar mix

◆ Ne from MD
★ Ar from MD
- - - Ar from M-S model
—— Ne from M-S model

DDR; 300 K;
Ar(1) -CO2 (2)
equimolar mix

★ Ar from MD
● CO2 from MD
- - - CO2 from M-S model
—— Ar from M-S model

The predictions for Ne in Ne-CO2 and Ar in Ar-CO2 mixtures are poor because of the blockage of the window regions by CO2. See R. Krishna and J.M. van Baten, Segregation effects in adsorption of CO2 containing mixtures and their consequences for separation selectivities in cage-type zeolites, Separation and Purification Technology, 61, 414-423 (2008)

$$[\Delta] = \begin{bmatrix} \dfrac{1}{Đ_1} + \dfrac{x_2}{Đ_{12}} & -\dfrac{x_1}{Đ_{12}} \\[2ex] -\dfrac{x_2}{Đ_{12}} & \dfrac{1}{Đ_2} + \dfrac{x_1}{Đ_{12}} \end{bmatrix}^{-1}$$

Unary diffusion data

Vignes interpolation
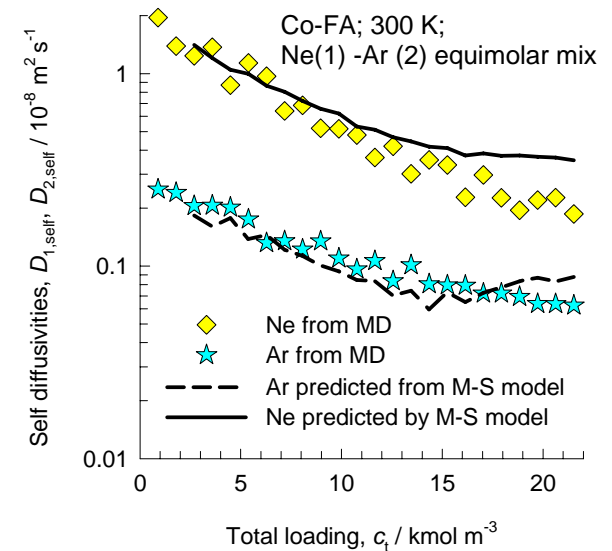
$$\frac{1}{D_{1,self}} = \frac{1}{Đ_1} + \frac{x_1}{Đ_{11}} + \frac{x_2}{Đ_{12}}$$

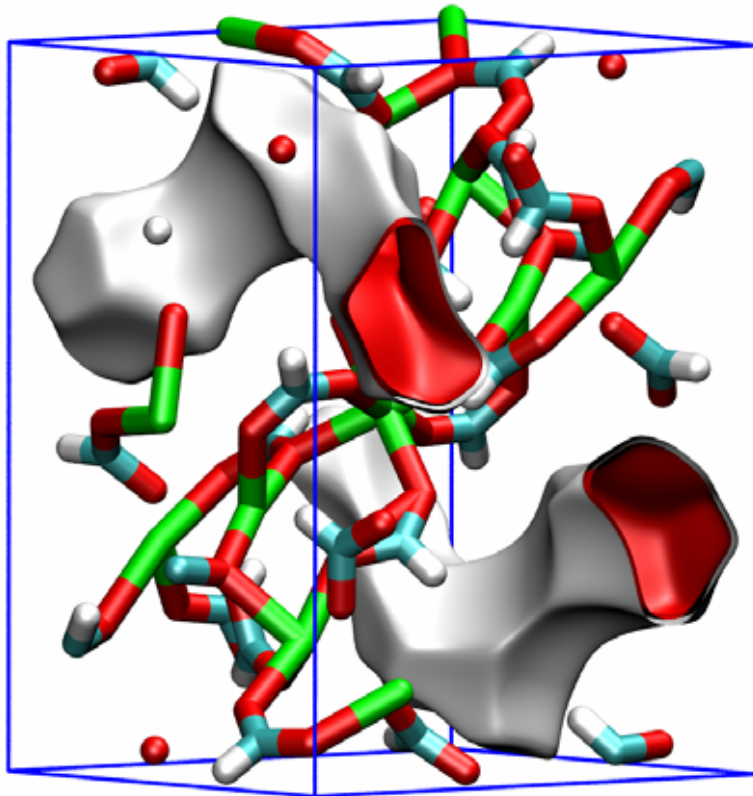$$\frac{1}{D_{2,self}} = \frac{1}{Đ_2} + \frac{x_2}{Đ_{22}} + \frac{x_1}{Đ_{12}}$$

Vignes interpolation

● $\Delta_{22}$
□ $\Delta_{12}$
◆ $\Delta_{11}$
—— M-S model with Vignes

DDR; 300 K;
Ne (1)-CO2(2) equimolar

◆ Ne from MD
● CO2 from MD
- - - CO2 from M-S model
—— Ne from M-S model

DDR; 300 K;
Ne(1) -CO2 (2)
equimolar mix
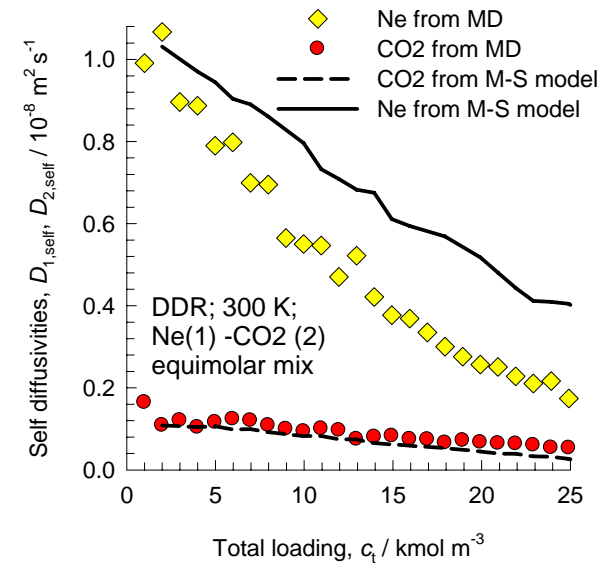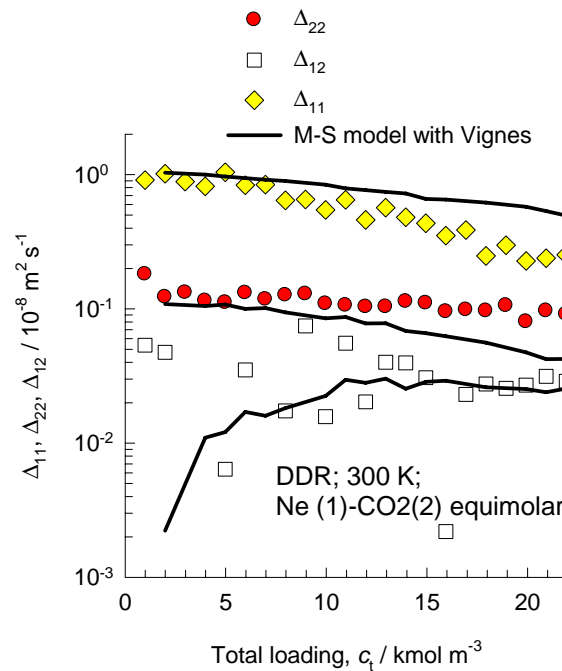
LTL
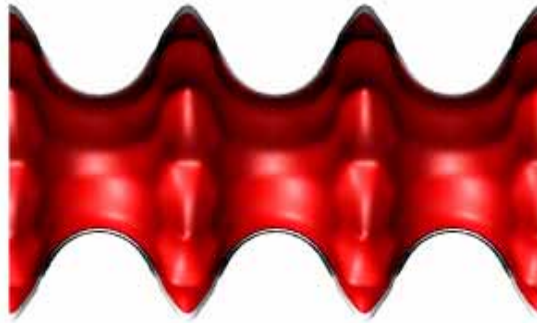
Figure 58

12 ring channel viewed along [100]

7.1 Å

7.1 Å

MD simulations; pure components; 300 K; ISV

C1
CO2
C2

M-S diffusivity, $Đ_i$ / $10^{-8}$ m$^2$ s$^{-1}$

Loading, $c_i$ / kmol m$^{-3}$
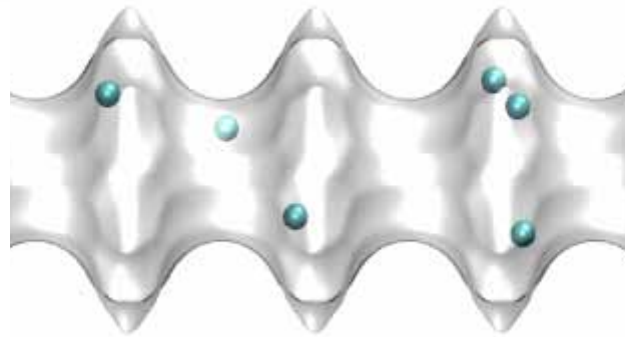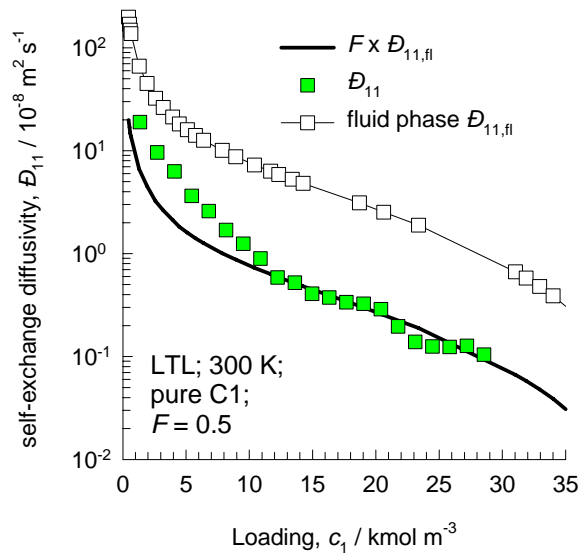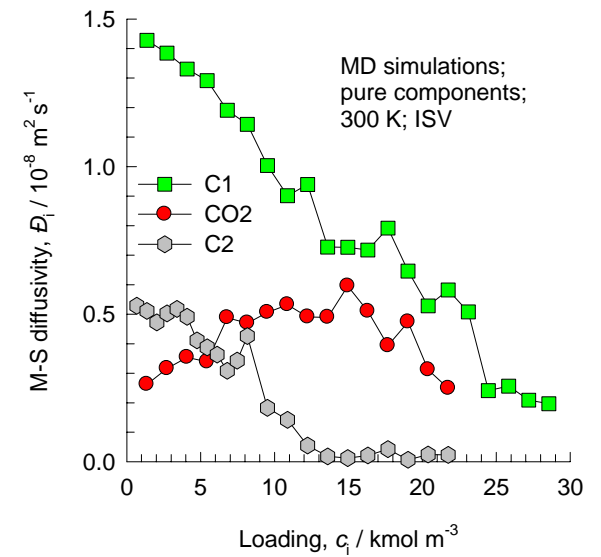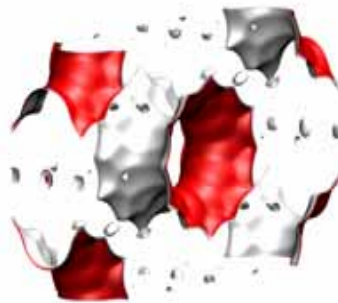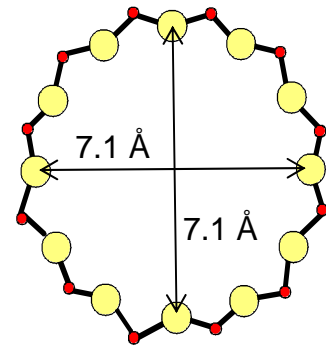
LTL has a 1D channel system
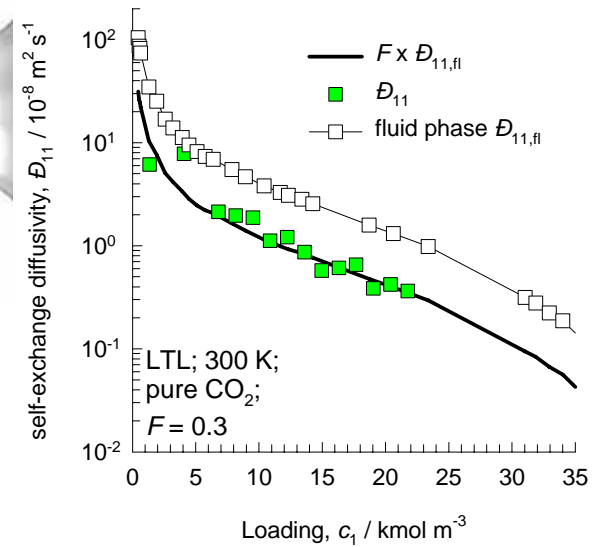
$F \times Đ_{11,fl}$
$Đ_{11}$
fluid phase $Đ_{11,fl}$

LTL; 300 K; pure C1; $F$ = 0.5

self-exchange diffusivity, $Đ_{11}$ / $10^{-8}$ m$^2$ s$^{-1}$

Loading, $c_1$ / kmol m$^{-3}$

$F \times Đ_{11,fl}$
$Đ_{11}$
fluid phase $Đ_{11,fl}$

LTL; 300 K; pure CO$_2$; $F$ = 0.3

self-exchange diffusivity, $Đ_{11}$ / $10^{-8}$ m$^2$ s$^{-1}$

Loading, $c_1$ / kmol m$^{-3}$

# ISV

Figure 59

12 ring channel
viewed along [100]

6.5 Å

6.1 Å

12 ring channel
viewed along [001]

5.9 Å

6.6 Å



ISV has an intersecting channel system





ISV; 300 K;
pure C1;
$F = 0.17$

- $F \times Ð_{11,fl}$
- $Ð_{11}$
- fluid phase $Ð_{11,fl}$

self-exchange diffusivity, $Ð_{11}$ / $10^{-8}$ m$^2$ s$^{-1}$

Loading, $c_1$ / kmol m$^{-3}$



MD simulations;
pure components;
300 K; ISV

M-S diffusivity, $Ð_i$ / $10^{-8}$ m$^2$ s$^{-1}$

- C1
- C2

Loading, $c_i$ / kmol m$^{-3}$
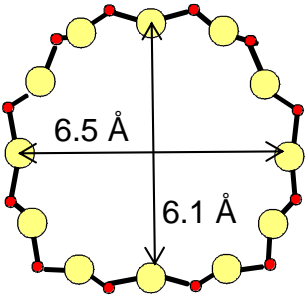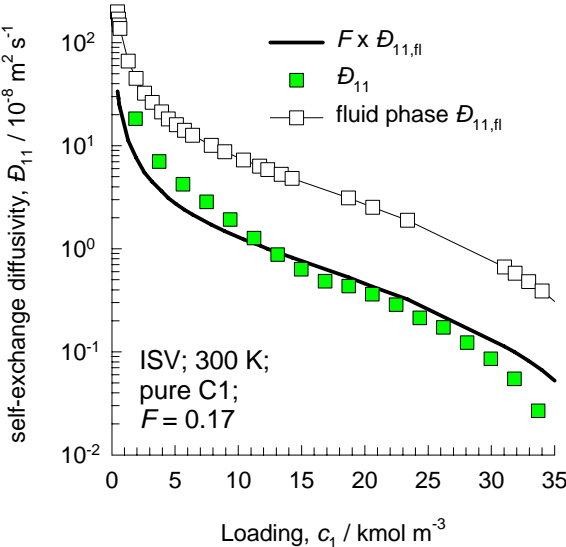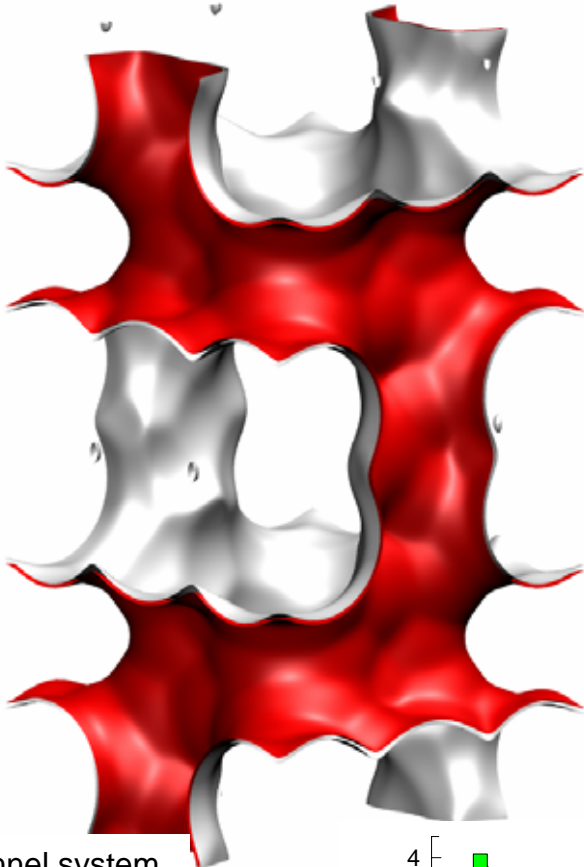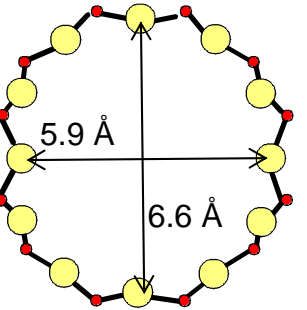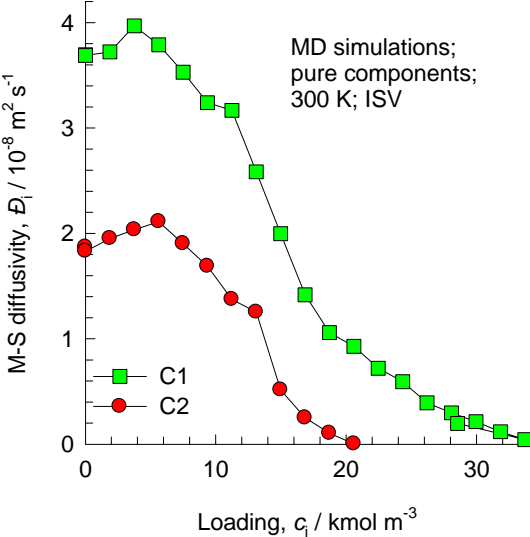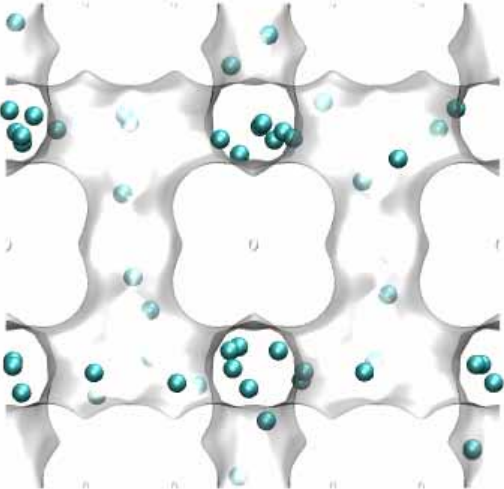
Figure 60

## Test of Darken and Vignes interpolation formulae for ISV



ISV; 300 K;
C1(1)-C2(2) equimolar mix

Legend:
— Darken
■ $Đ_{11}$
□ $Đ_{12}$
● $Đ_{22}$
— — Vignes

Exchange coefficients, $Đ_{11}$, $Đ_{22}$, $Đ_{12}$ / $10^{-8}$ $m^2$ $s^{-1}$

Total loading, $c_t$ / kmol $m^{-3}$
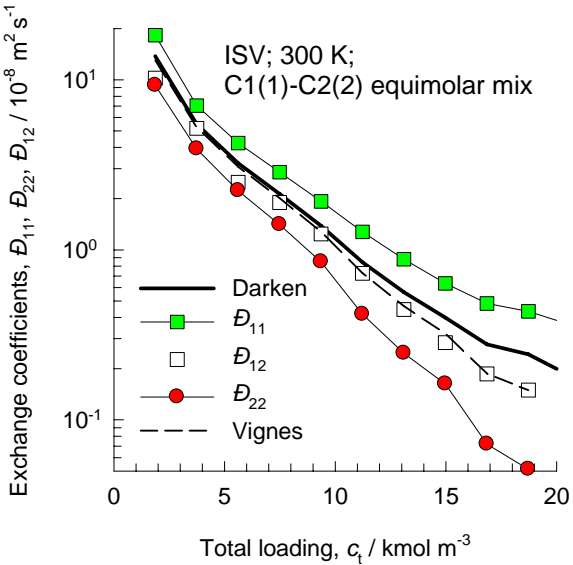
## Prediction of self diffusivities in C1-C2 mixture in ISV using Vignes interpolation and M-S model
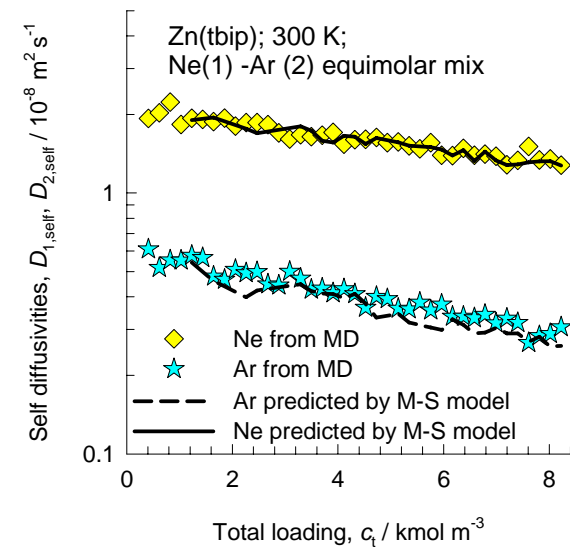
Unary diffusion data

$$\frac{1}{D_{1,self}} = \frac{1}{Đ_1} + \frac{x_1}{Đ_{11}} + \frac{x_2}{Đ_{12}}$$

$$\frac{1}{D_{2,self}} = \frac{1}{Đ_2} + \frac{x_2}{Đ_{22}} + \frac{x_1}{Đ_{12}}$$

Vignes interpolation



Legend:
■ C1 from MD
● C2 from MD
— — C2 from M-S model
— C1 from M-S model

ISV; 300 K;
C1(1) -C2 (2) equimolar mix

Self diffusivities, $D_{1,self}$, $D_{2,self}$ / $10^{-8}$ $m^2$ $s^{-1}$

Total loading, $c_t$ / kmol $m^{-3}$

# ERI

Figure 61



Window of ERI

5.1 Å

3.6 Å
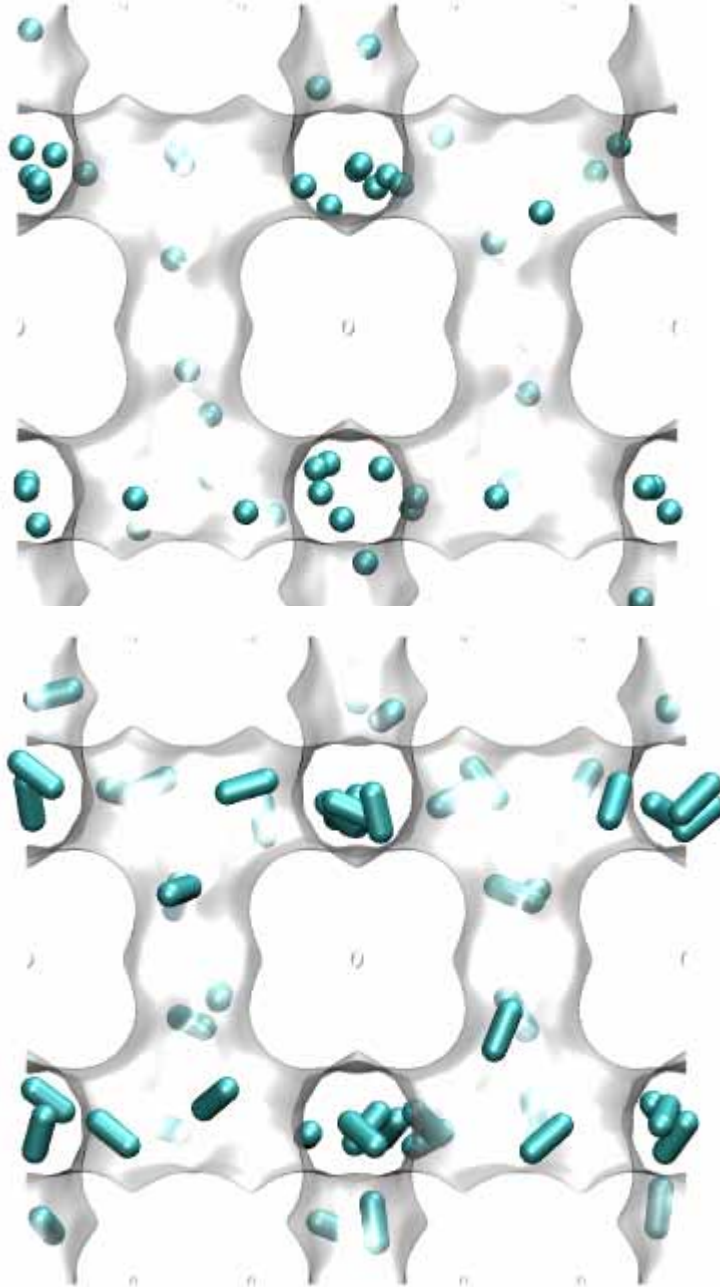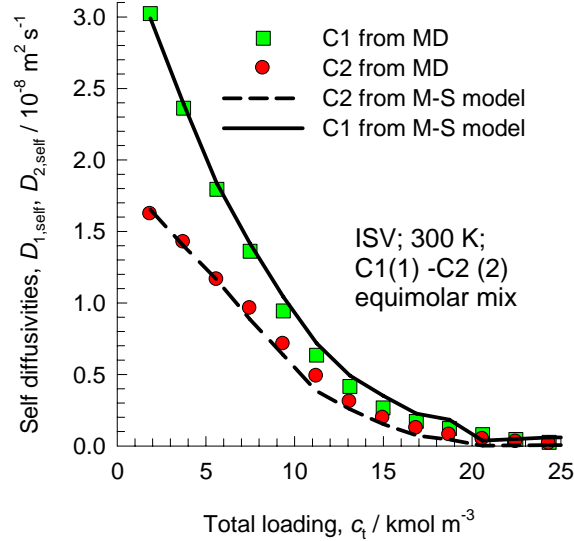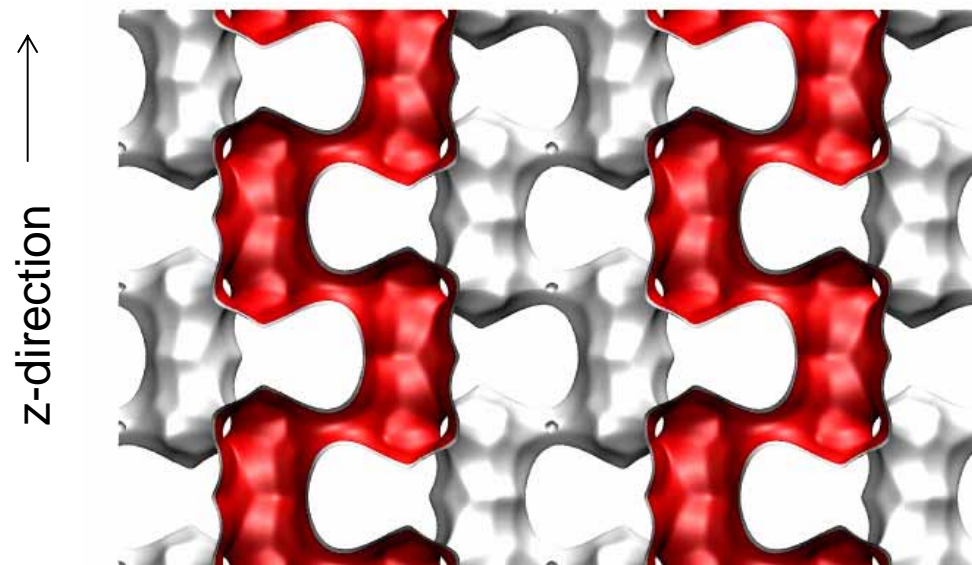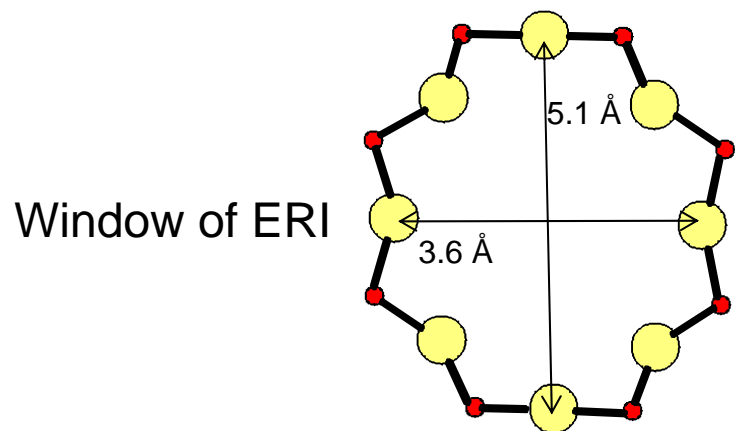
z-direction

x-y projection

x-y projection
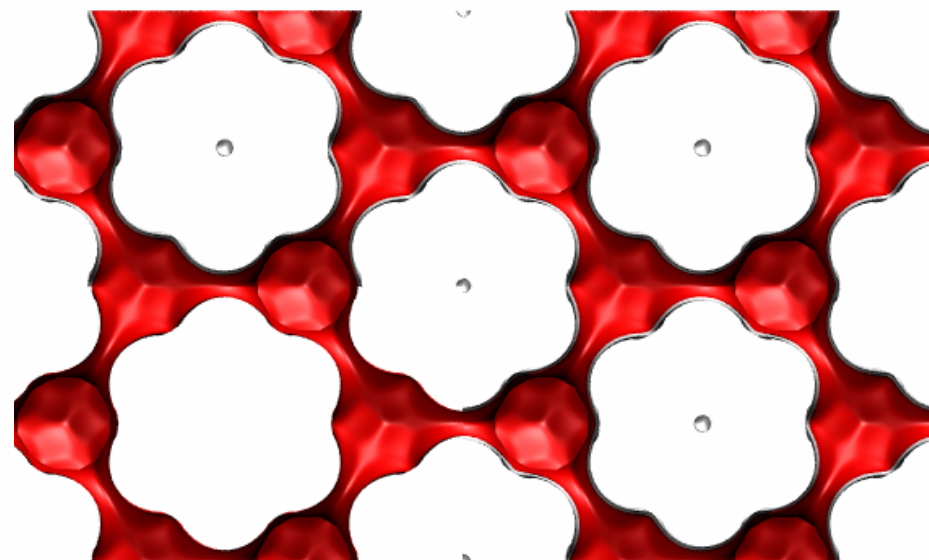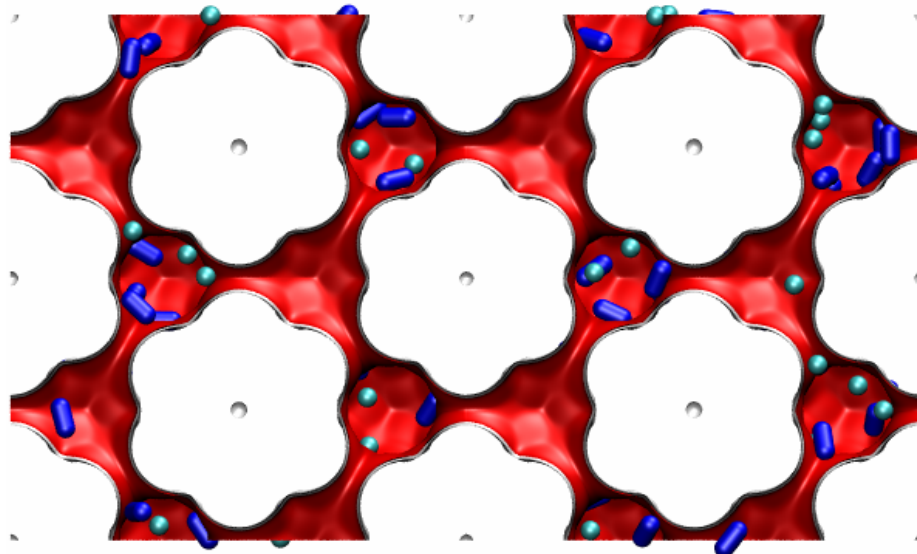
Figure 62
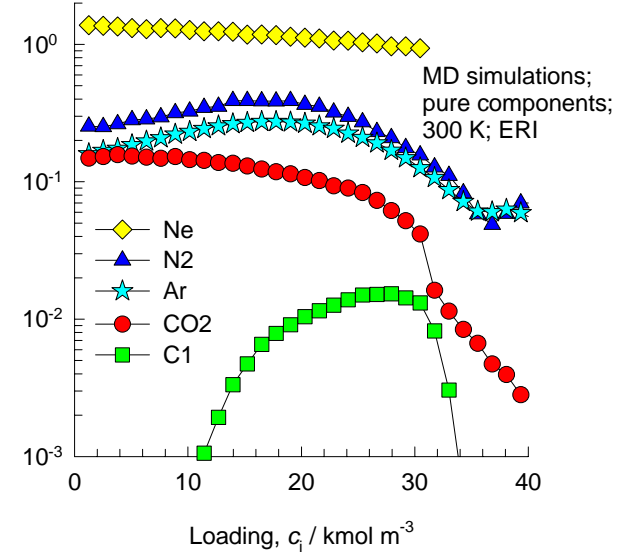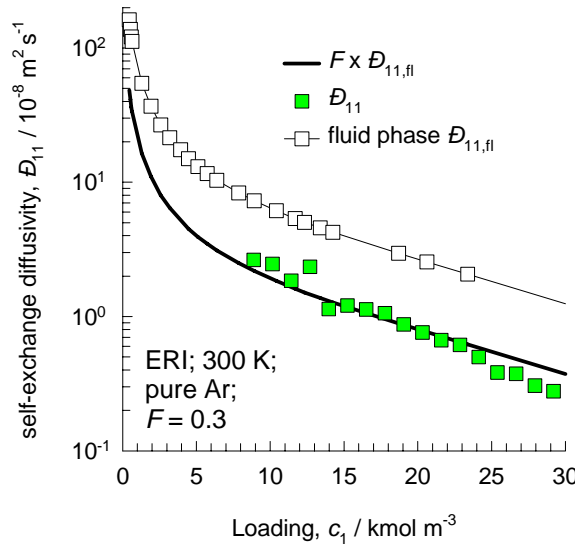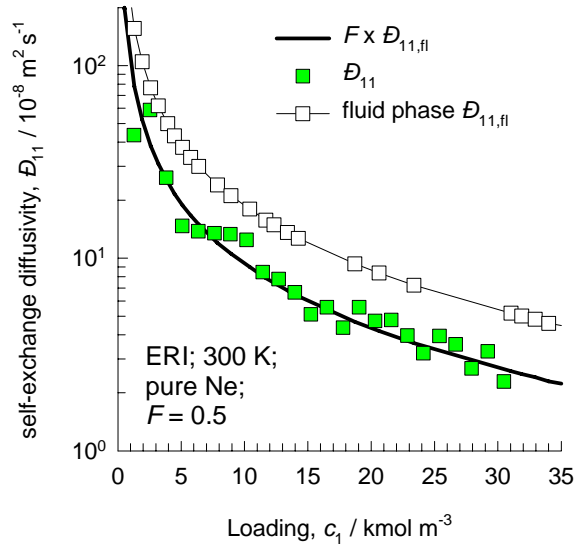
Data for all-silica ERI for unary diffusion; we consider the average
of diffusivities in the x- and y-directions

Figure 63

# Data for all-silica ERI for binary mixture diffusion



ERI; 300 K;
N2-CO2 equimolar mixture
$F = 0.15$

ERI; 300 K;
N2(1) - CO2 (2)
equimolar mix

ERI; 300 K;
C1(1) -CO2 (2)
equimolar mix
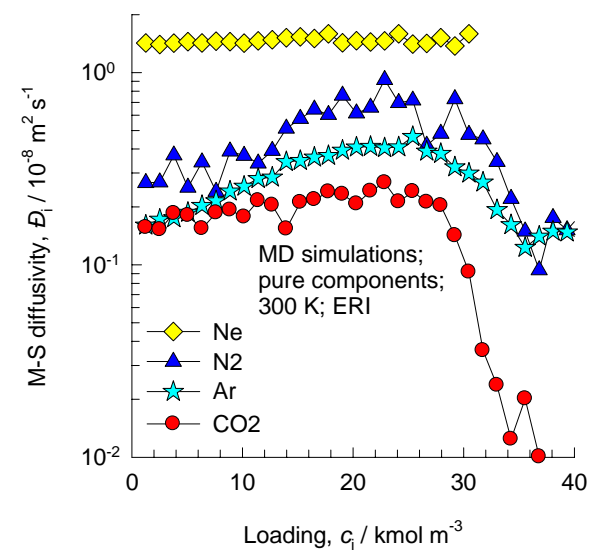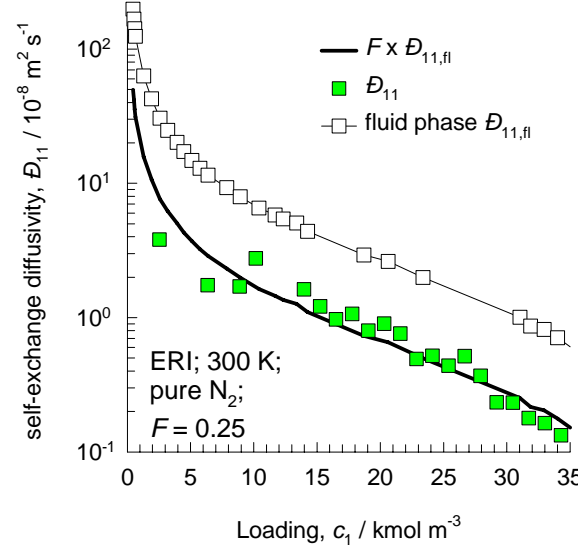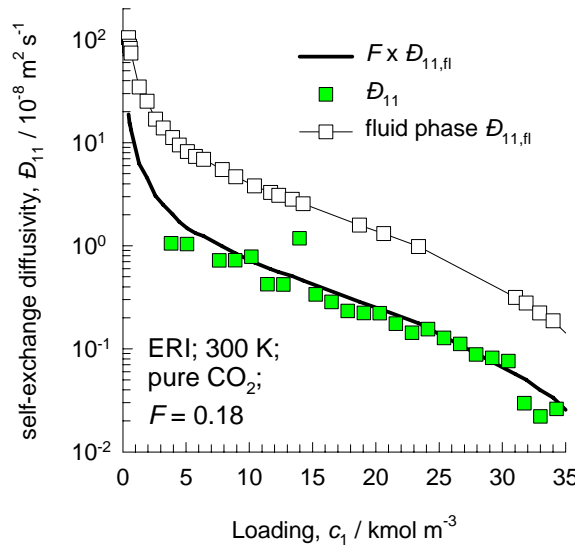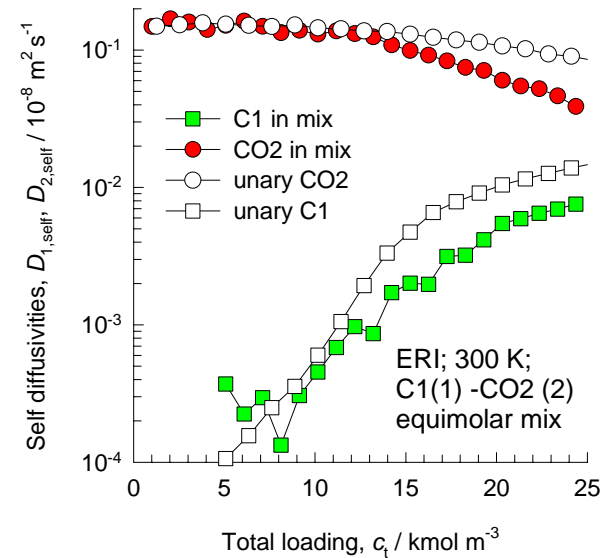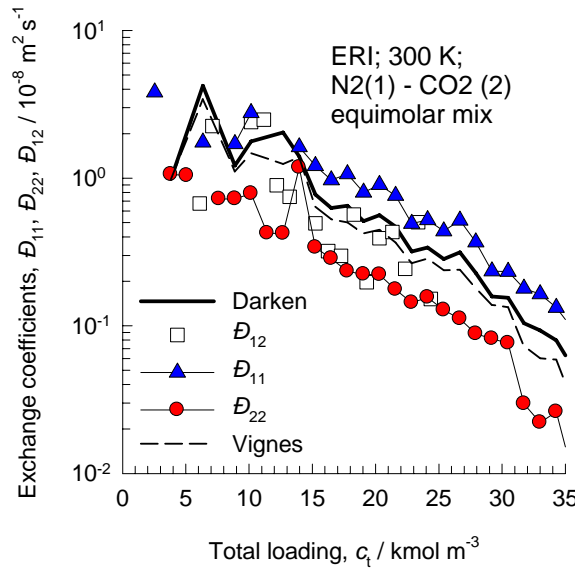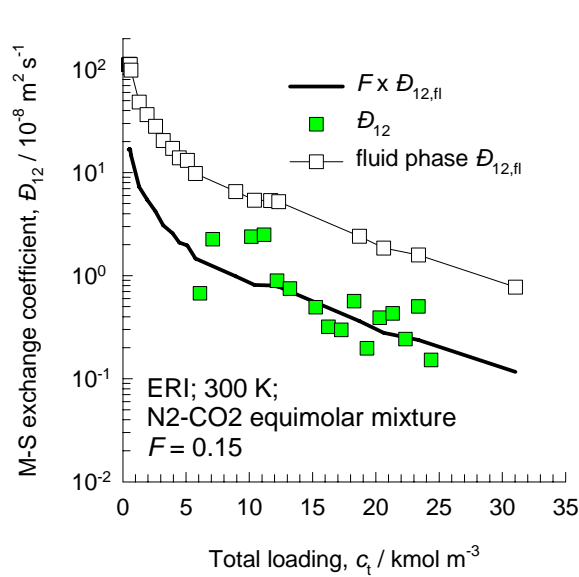
# Prediction of self diffusivities in binary mixture in ERI using Vignes interpolation and M-S model



Unary diffusion data

$$\frac{1}{D_{1,self}} = \frac{1}{Đ_1} + \frac{x_1}{Đ_{11}} + \frac{x_2}{Đ_{12}}$$

$$\frac{1}{D_{2,self}} = \frac{1}{Đ_2} + \frac{x_2}{Đ_{22}} + \frac{x_1}{Đ_{12}}$$

Vignes interpolation

Predictions ( lines) are compared with MD (symbols)

The predictions for Ar are poor because of the blockage of the window regions by CO2. See R. Krishna and J.M. van Baten, Segregation effects in adsorption of CO2 containing mixtures and their consequences for separation selectivities in cage-type zeolites, Separation and Purification Technology, 61, 414-423 (2008)

ERI; 300 K;
Ar(1) -CO2 (2)
equimolar mix
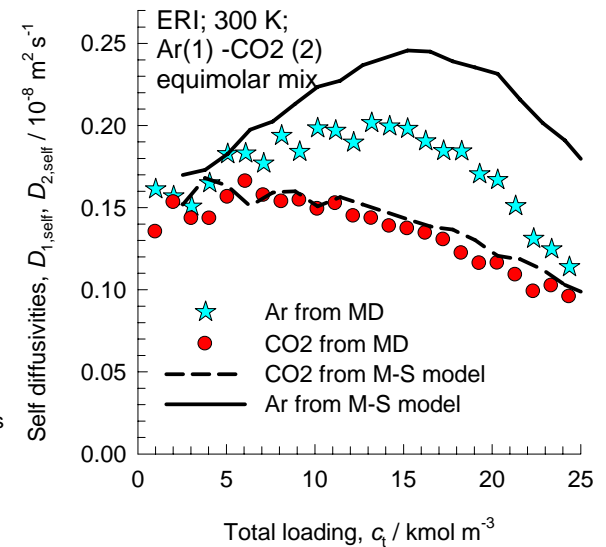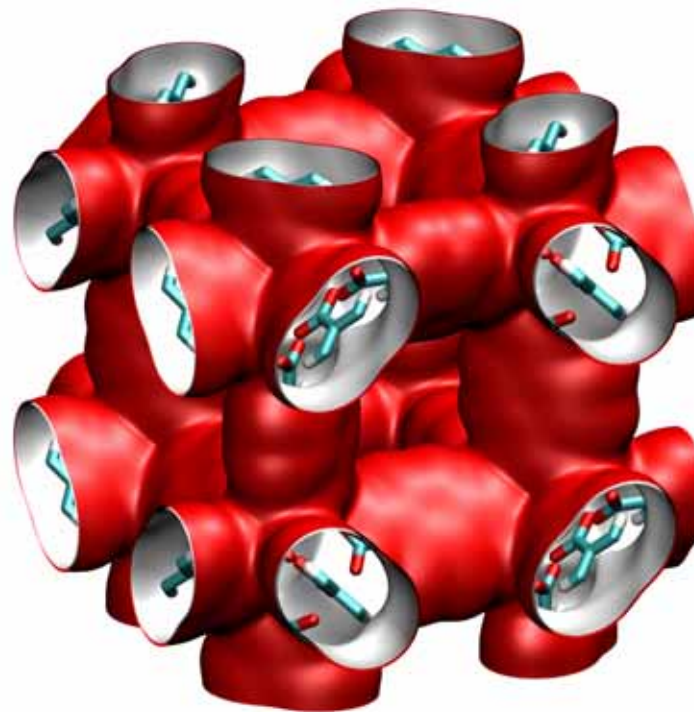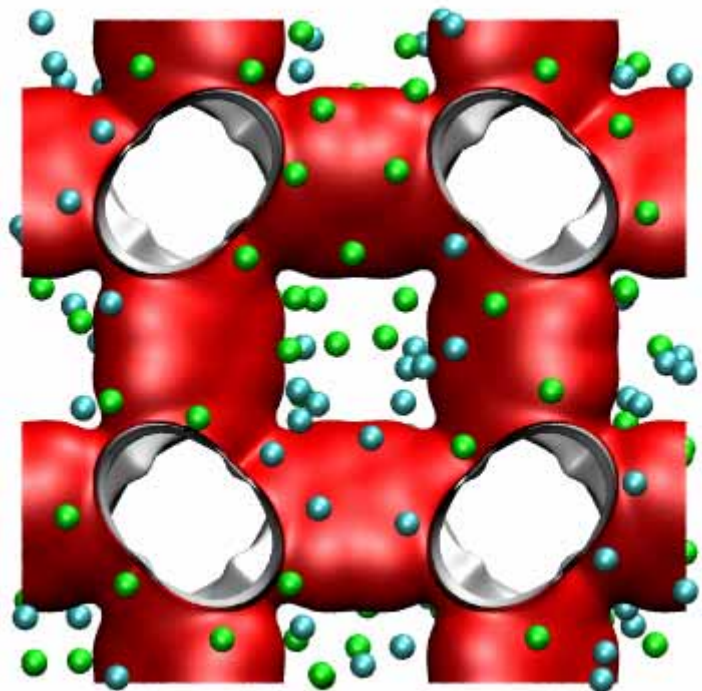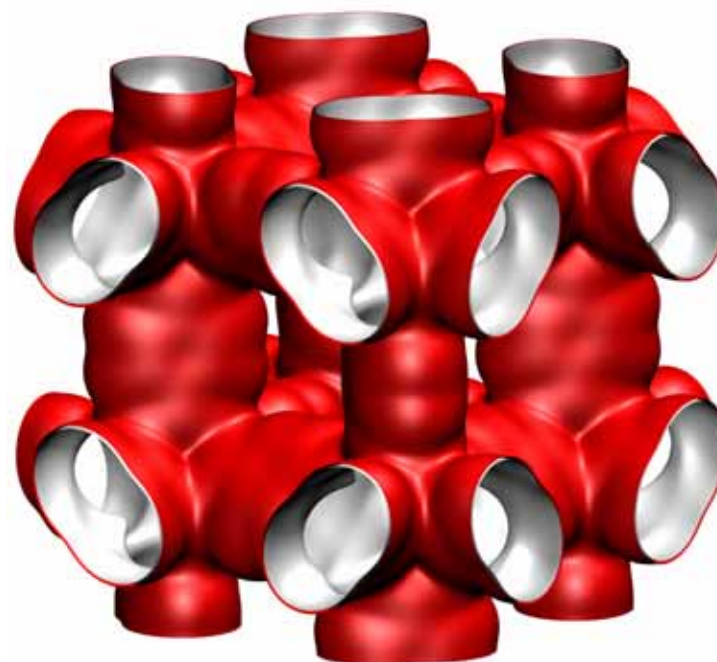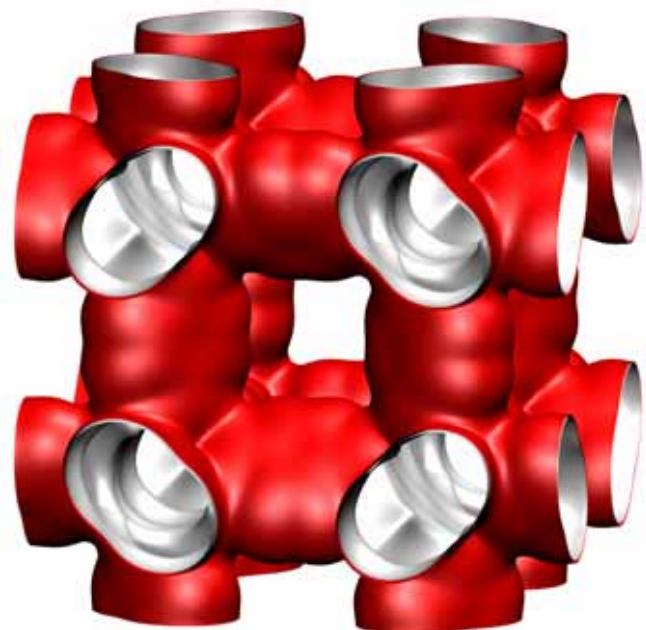
Figure 64

IRMOF-1

Figure 65
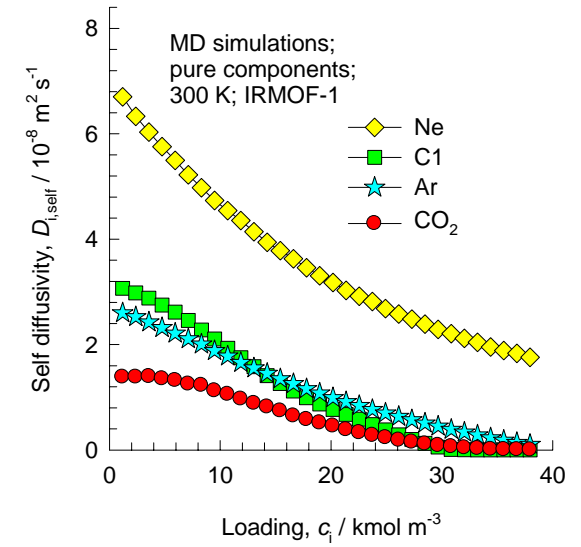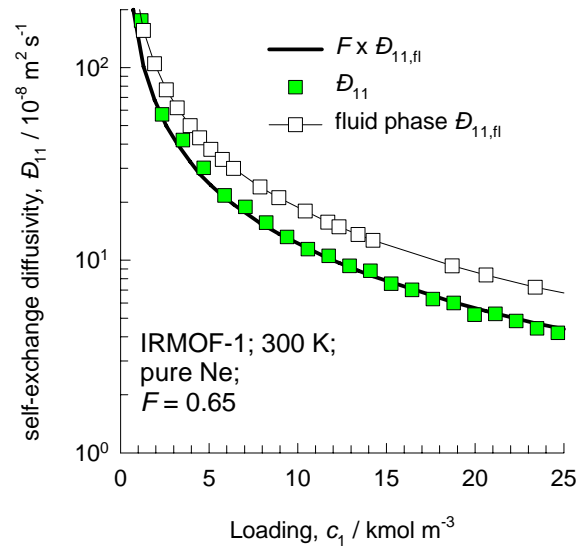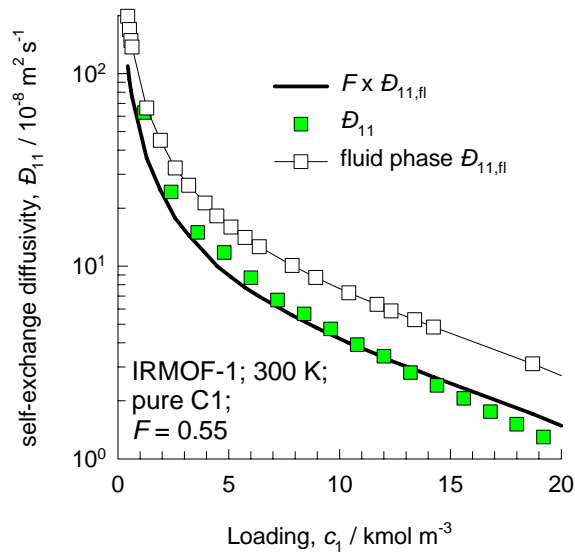
Data for IRMOF-1 for pure components
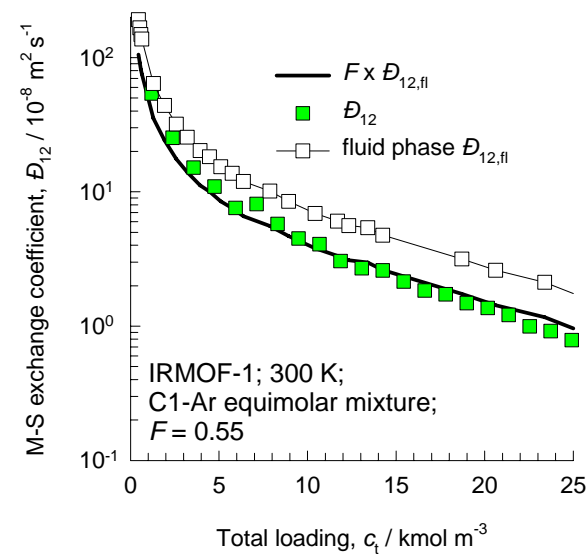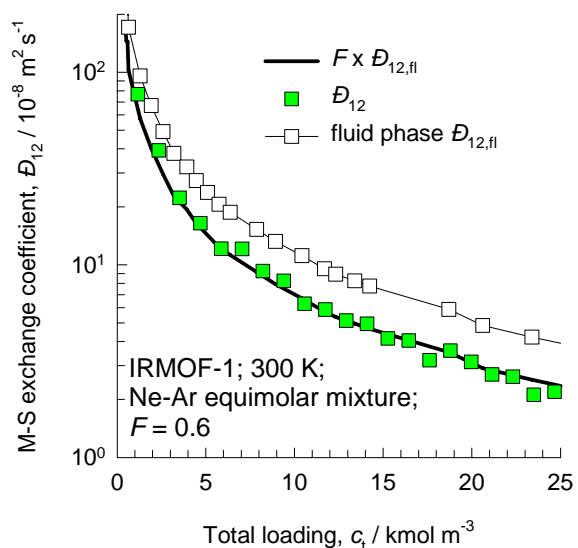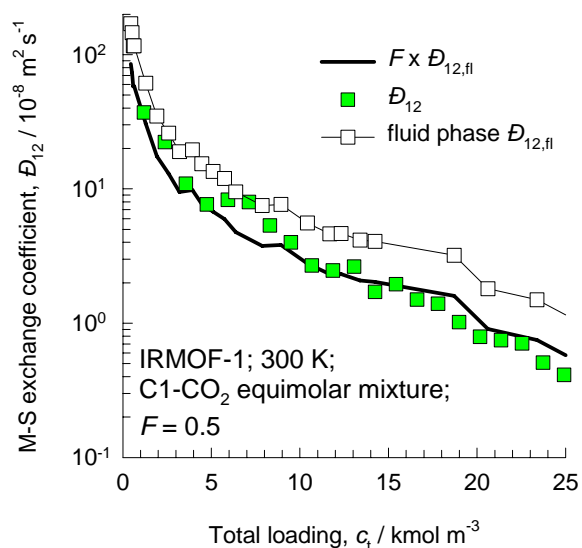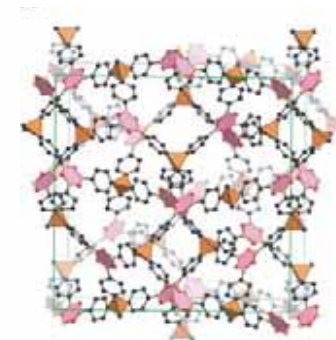
## Test of Darken and Vignes interpolation formulae for IRMOF-1
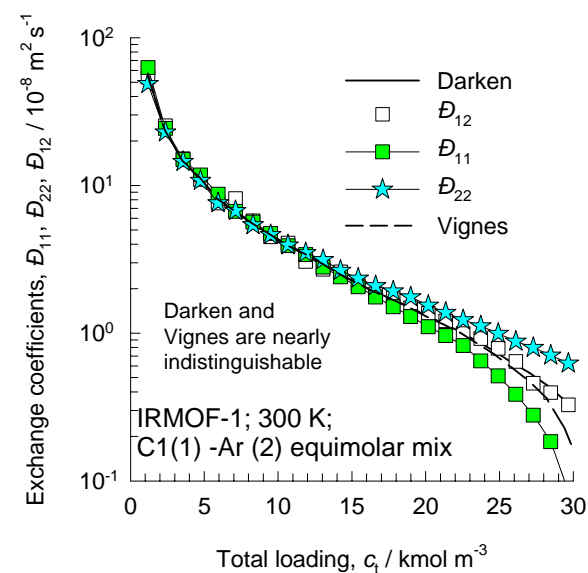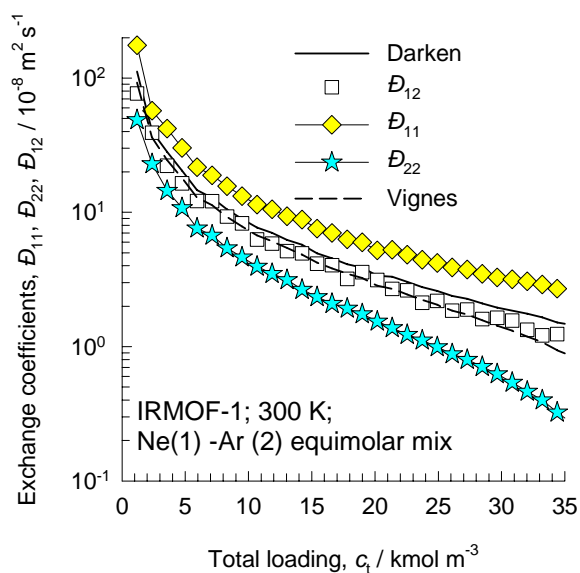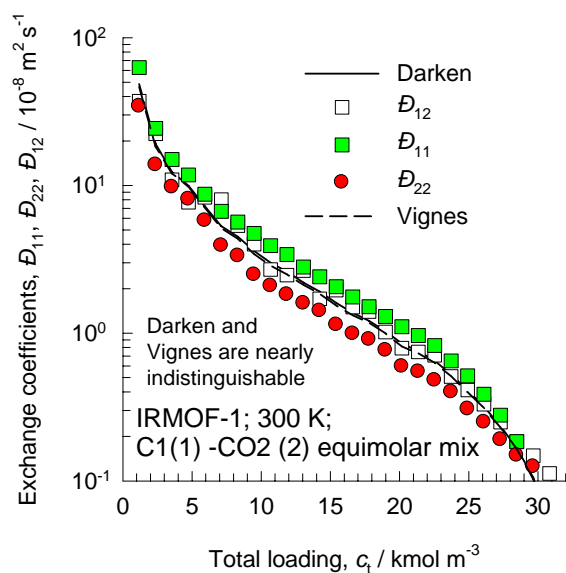
# Prediction of $D_{i,self}$ and $\Delta_{ij}$ in binary mixtures in IRMOF-1 using Vignes interpolation and M-S model

Figure 67
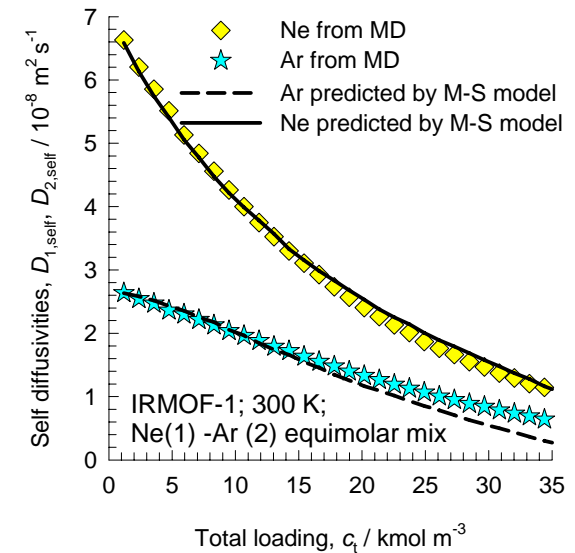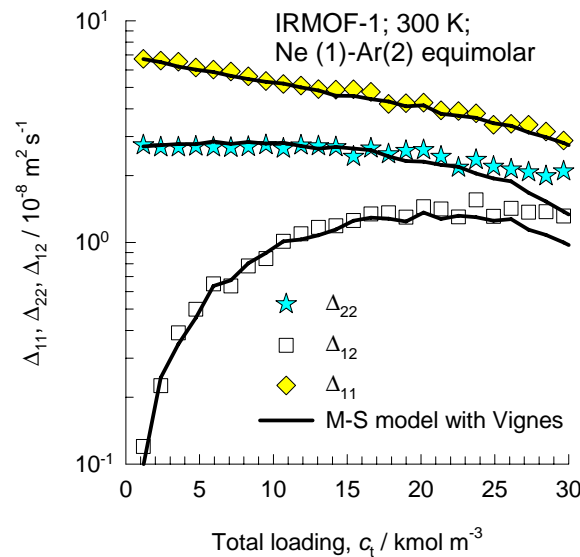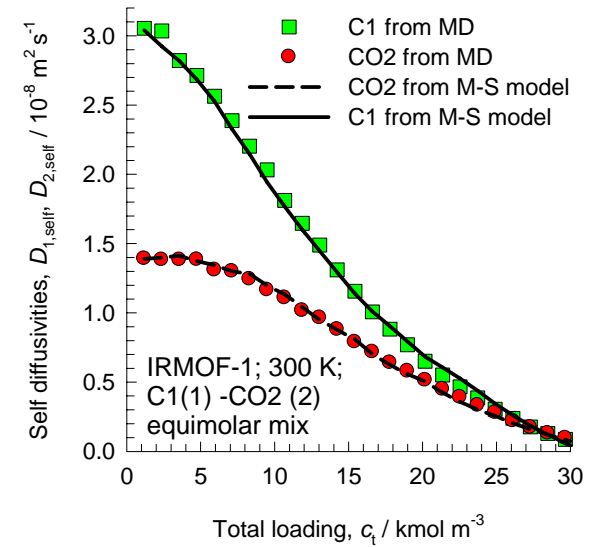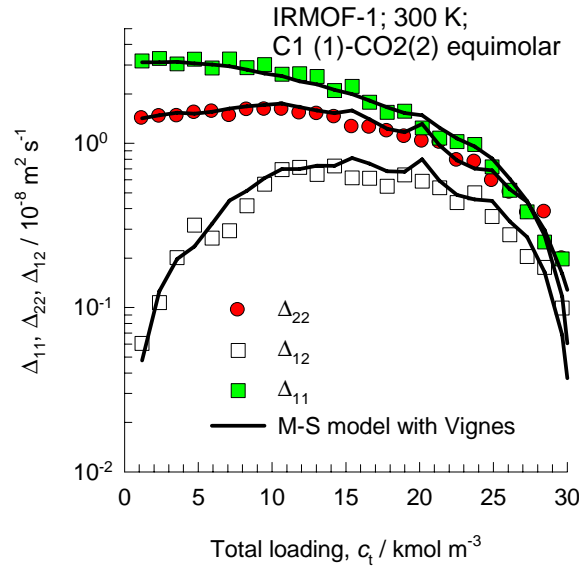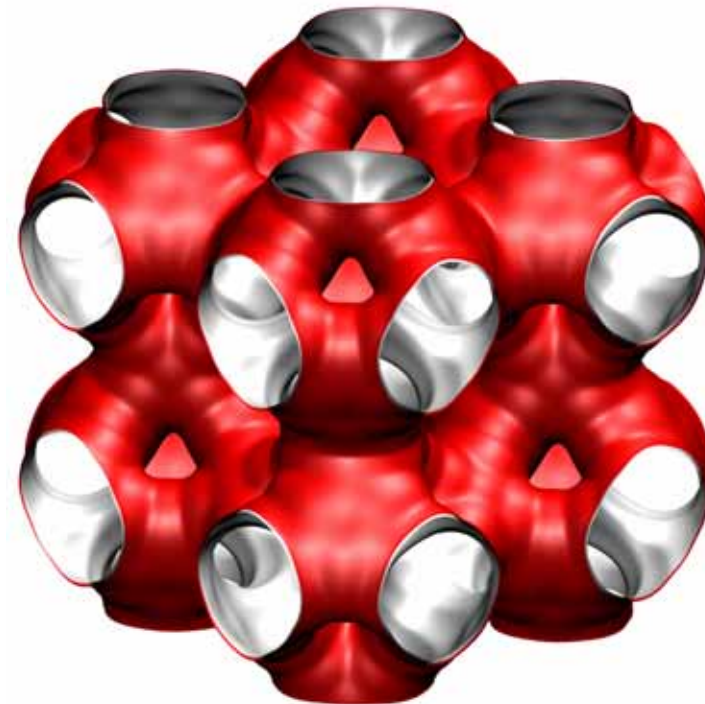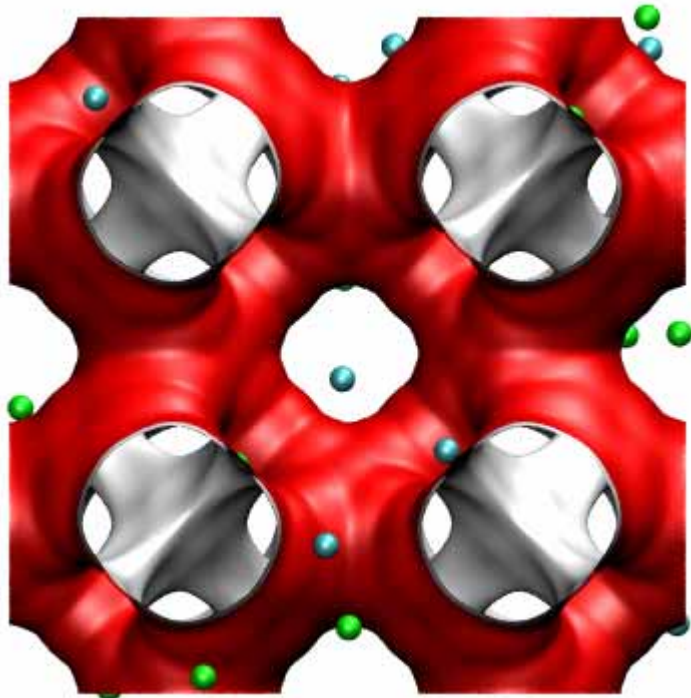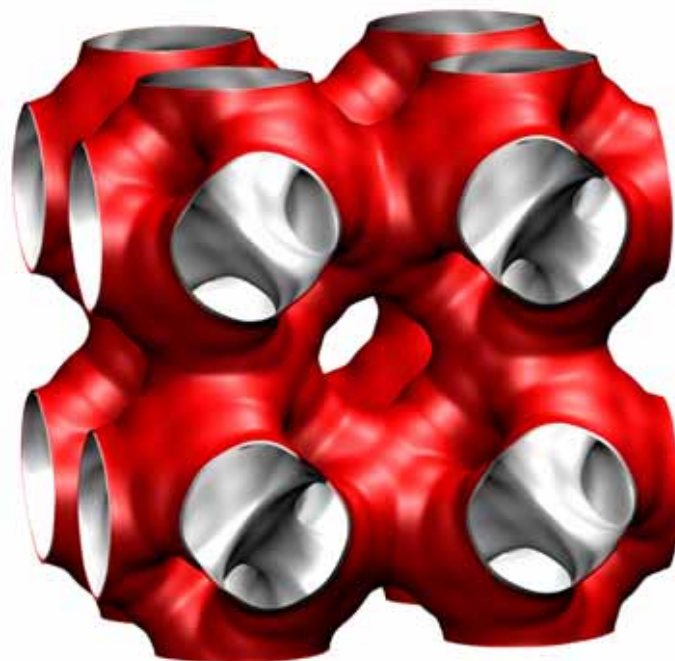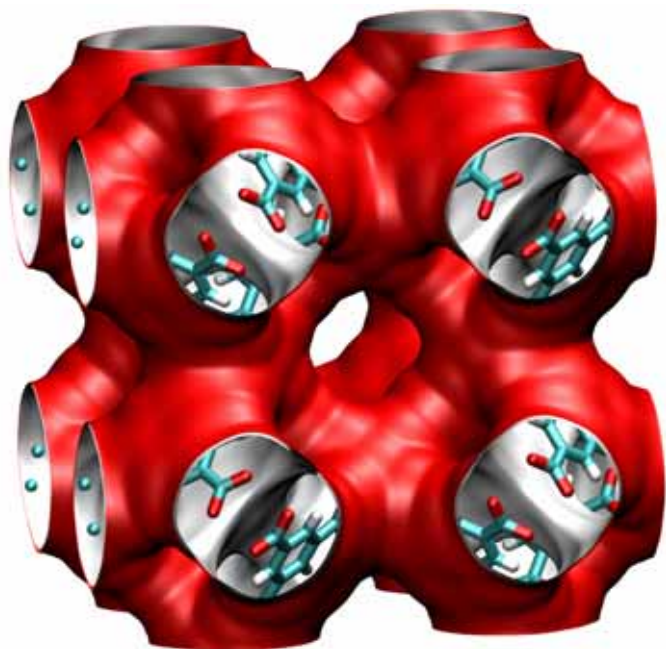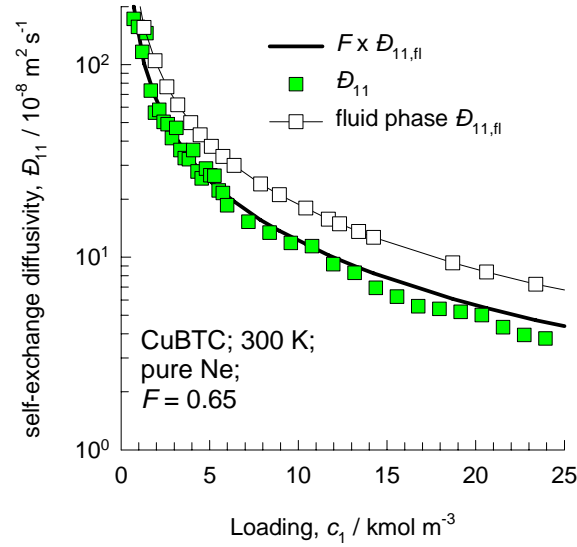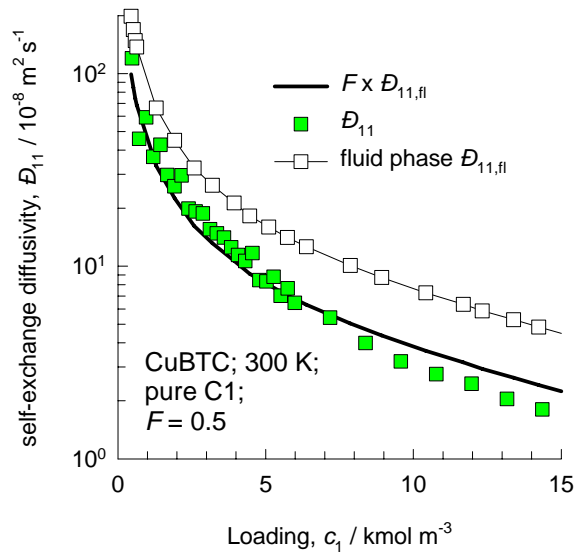
**CuBTC**

Figure 69

Data for CuBTC for pure components
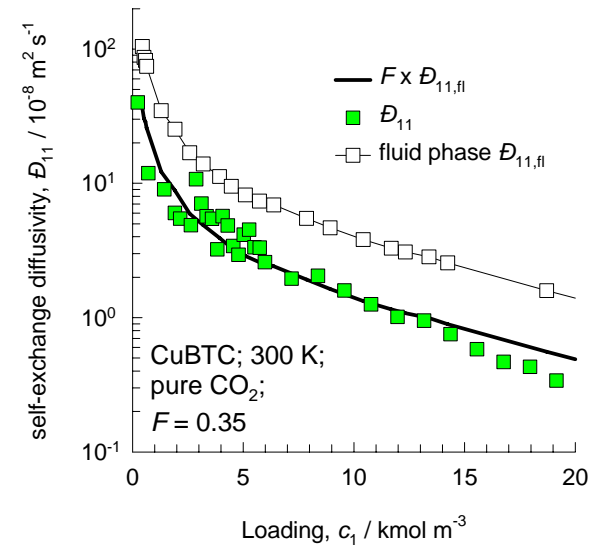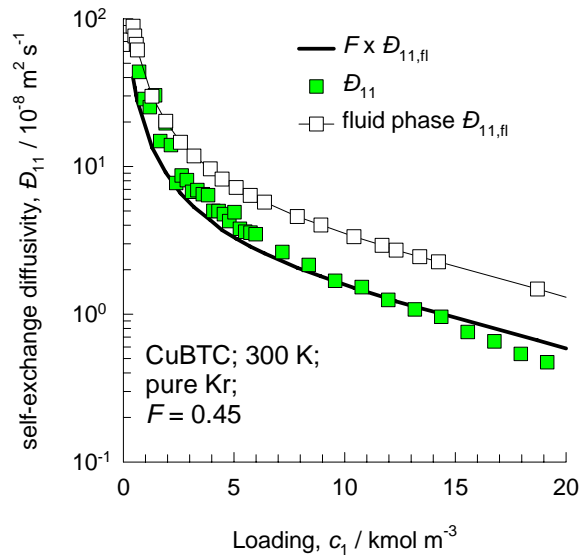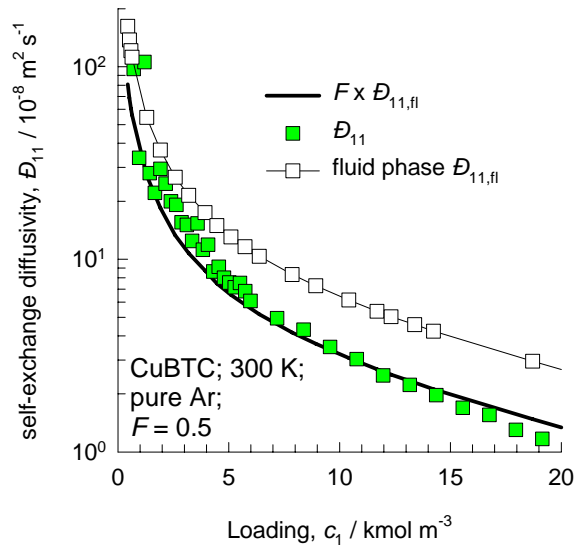
Figure 70
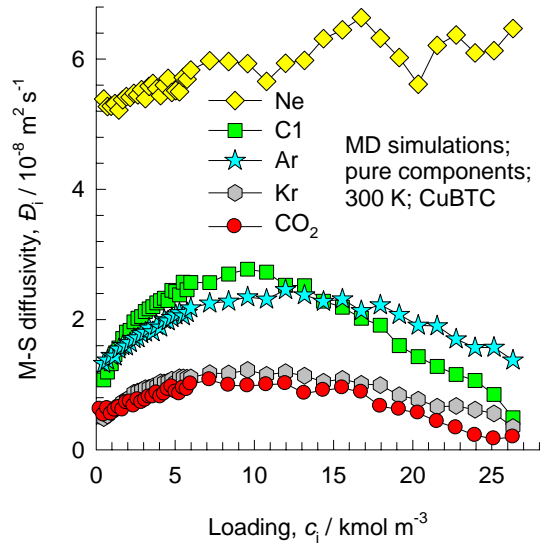
Data for CuBTC for pure components
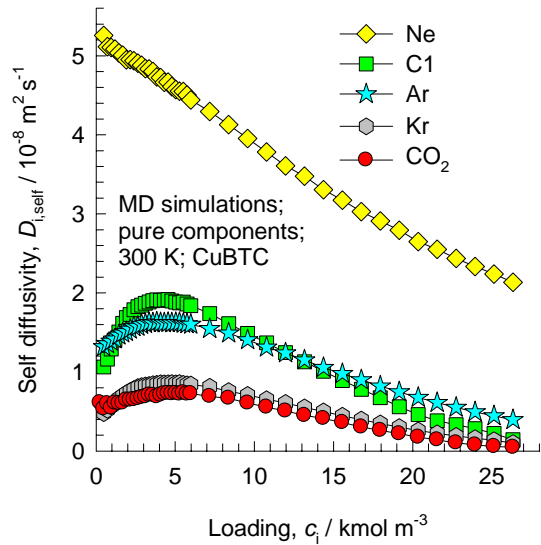
Comparison of simulated isotherm for C1 with experimental data of Senkovska and Kaskel, *Micro. Mesopor. Mat.*, 112, 108-115 (2008)
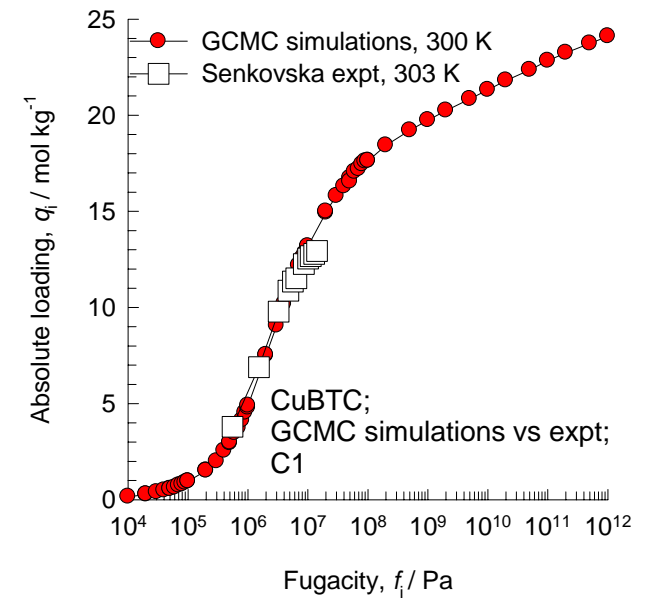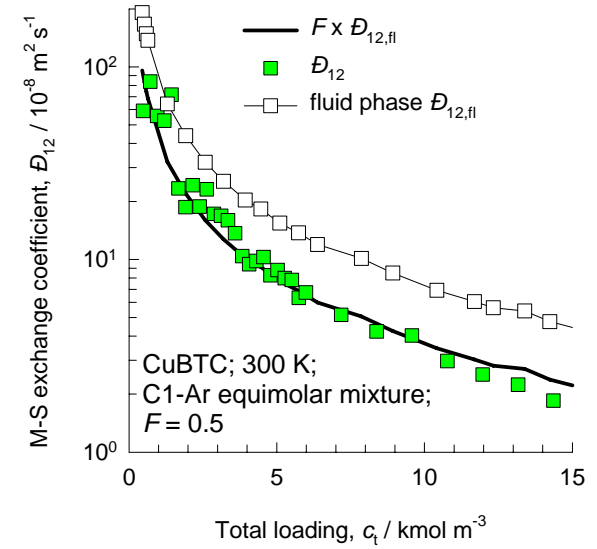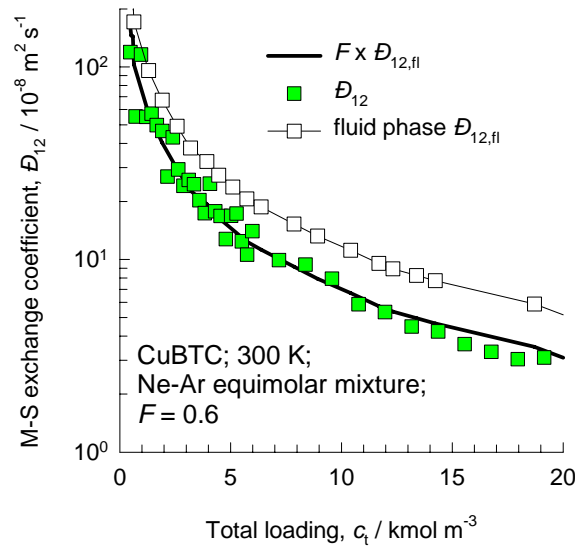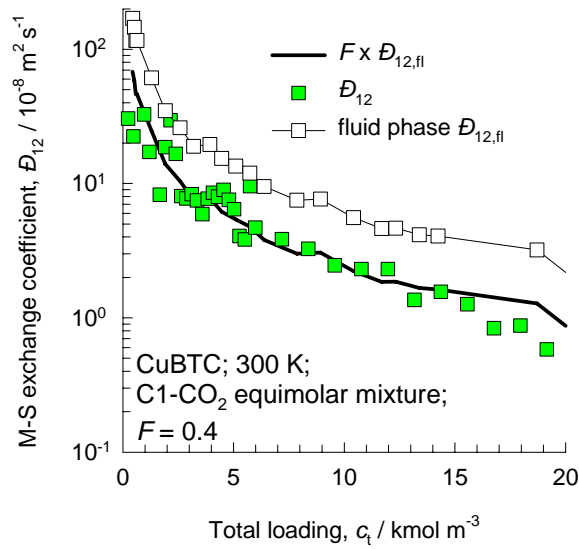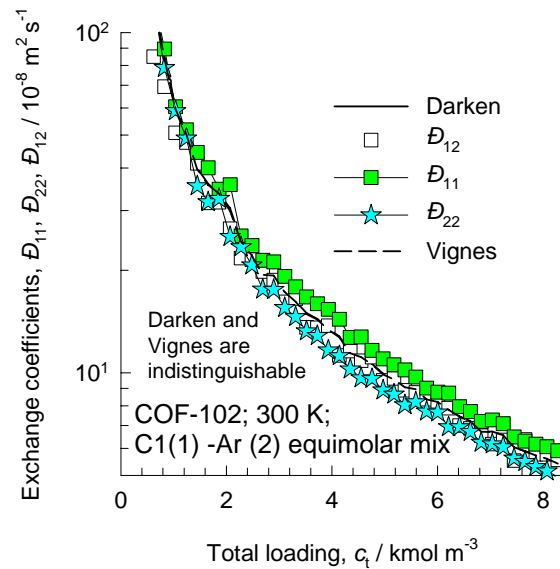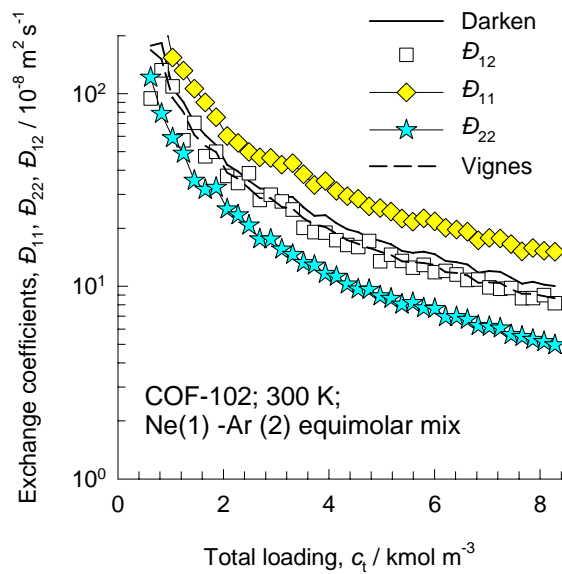
Figure 71

Figure 72

# Prediction of $D_{i,self}$ and $\Delta_{ij}$ in binary mixtures in CuBTC using Vignes interpolation and M-S model

$$[\Delta] = \begin{bmatrix} \dfrac{1}{Đ_1} + \dfrac{x_2}{Đ_{12}} & -\dfrac{x_1}{Đ_{12}} \\ -\dfrac{x_2}{Đ_{12}} & \dfrac{1}{Đ_2} + \dfrac{x_1}{Đ_{12}} \end{bmatrix}^{-1}$$

Unary diffusion data

Vignes interpolation

$$\frac{1}{D_{1,self}} = \frac{1}{Đ_1} + \frac{x_1}{Đ_{11}} + \frac{x_2}{Đ_{12}}$$

$$\frac{1}{D_{2,self}} = \frac{1}{Đ_2} + \frac{x_2}{Đ_{22}} + \frac{x_1}{Đ_{12}}$$

Vignes interpolation
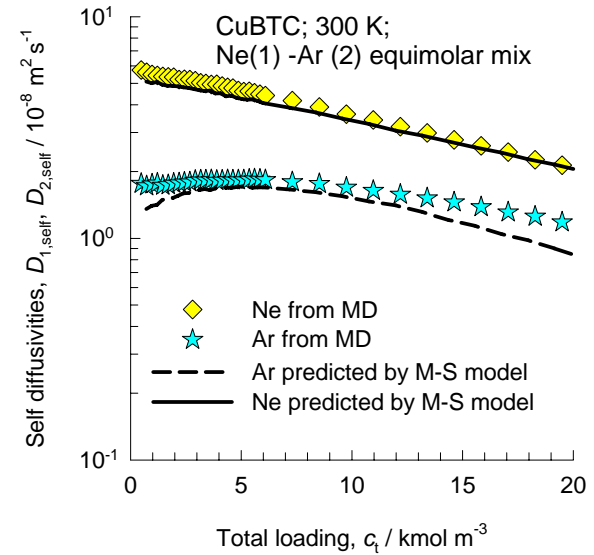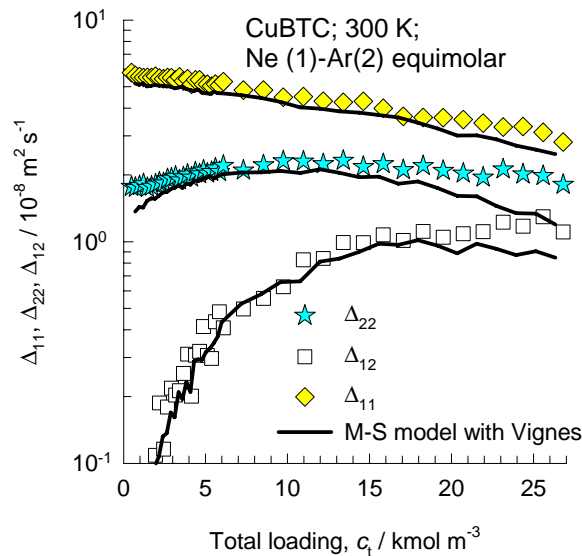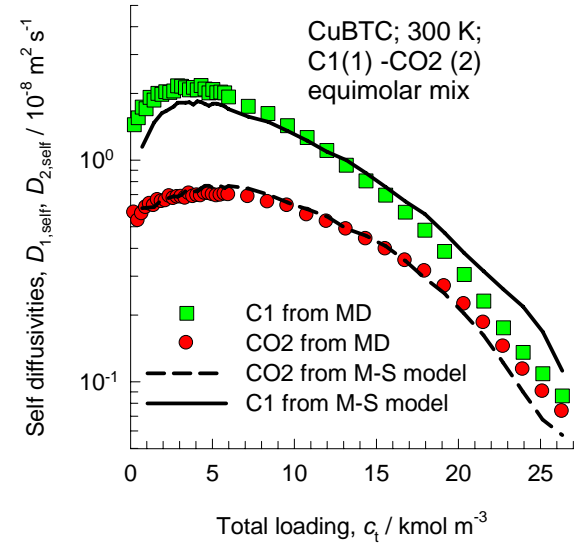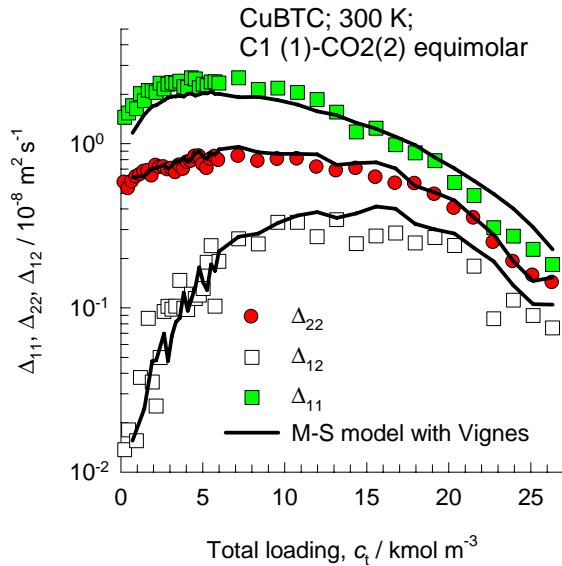
# MIL – 47 structure
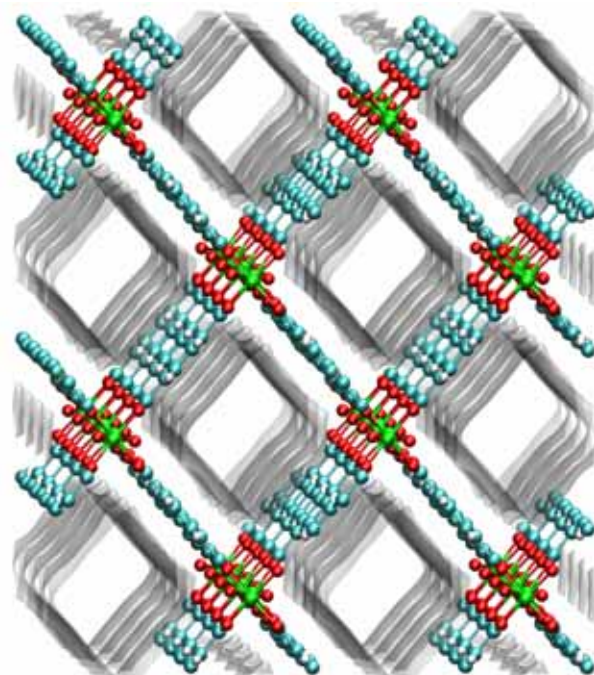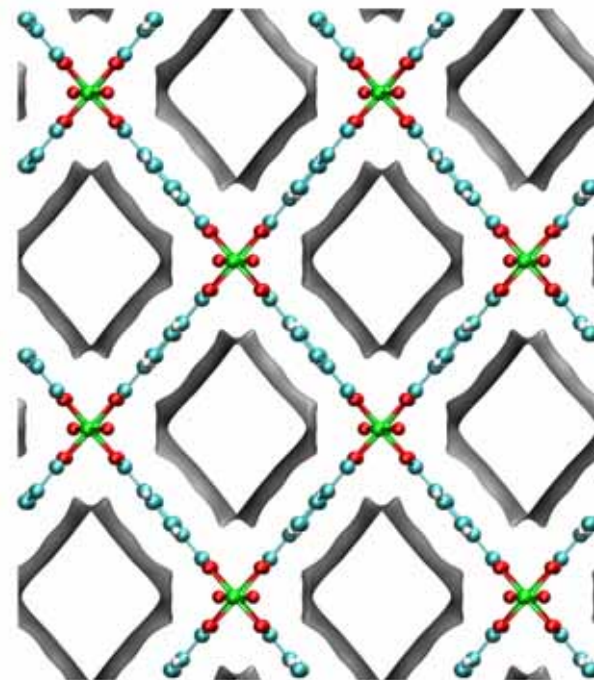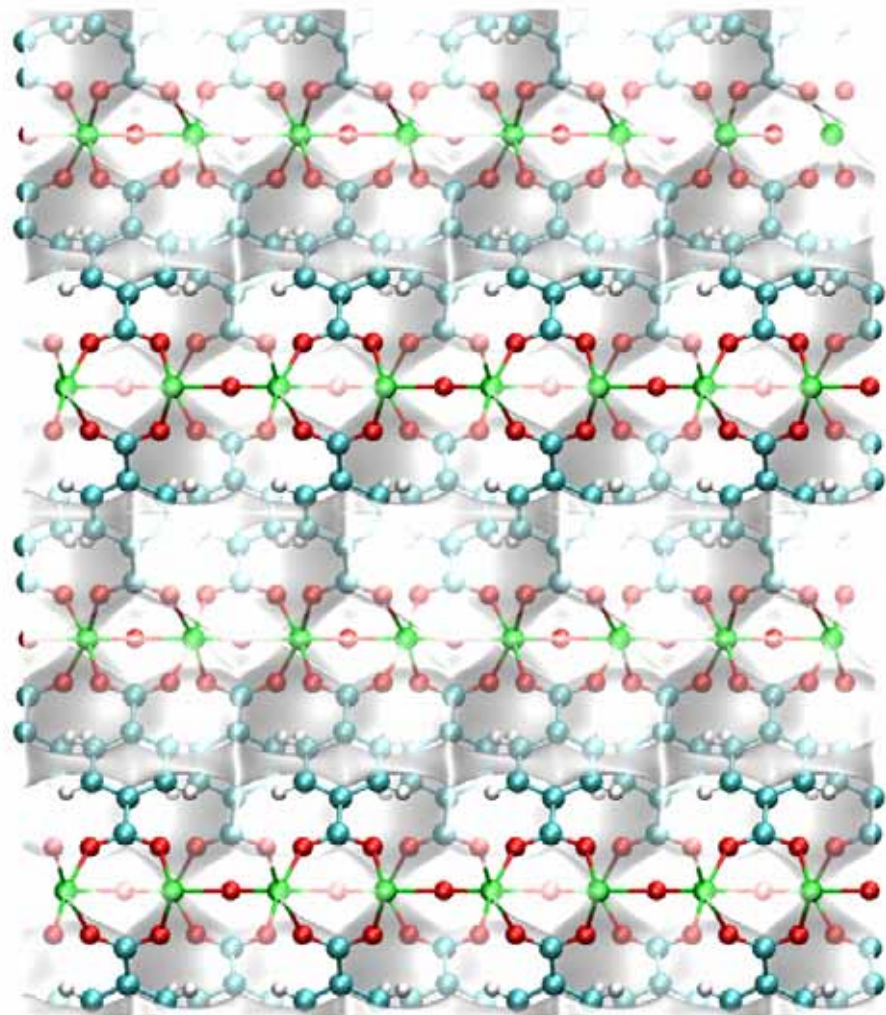
Figure 73

Figure 74

**MIL – 47, with pore landscape**
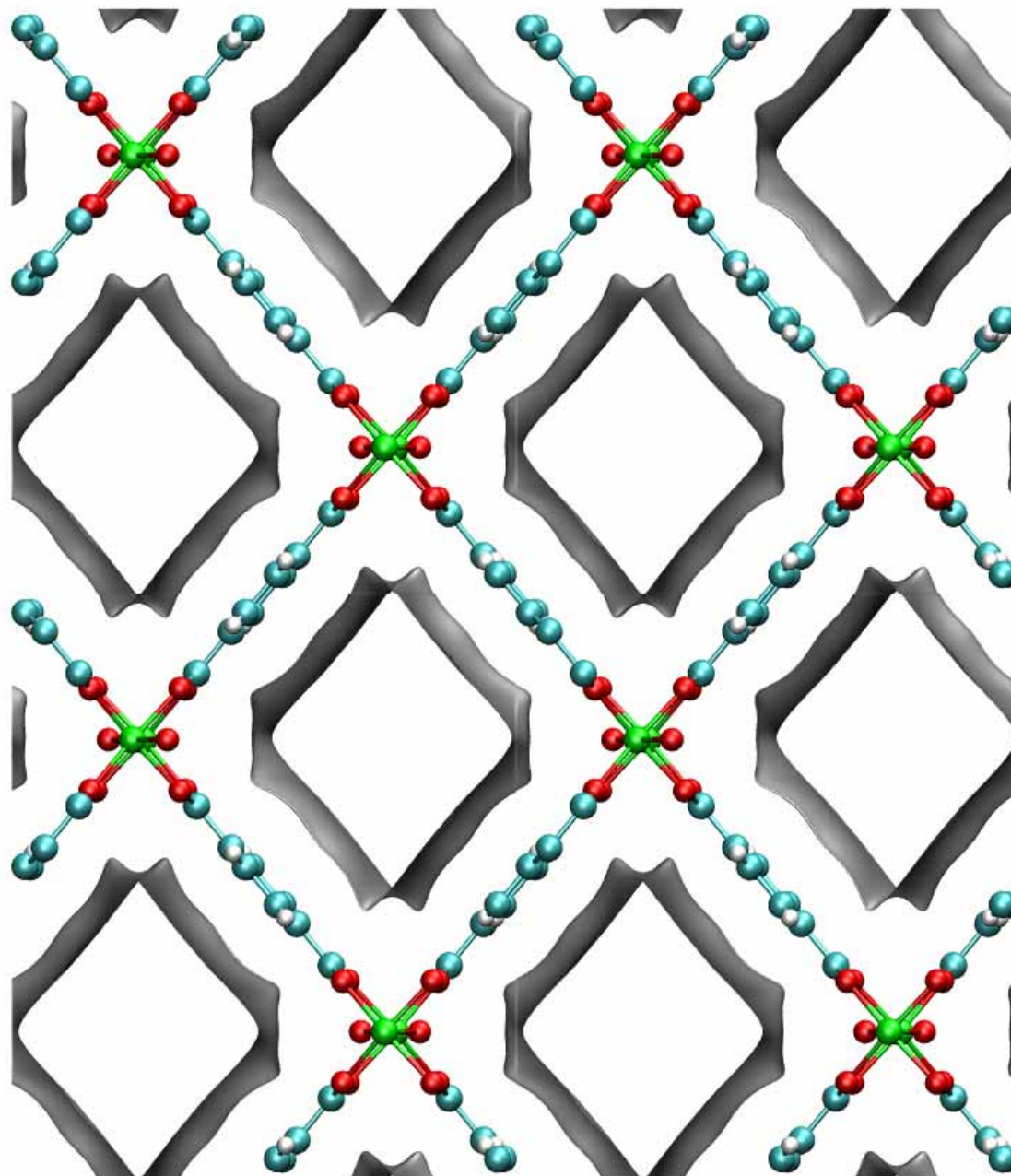
# MIL – 47
## pore landscape

Figure 75
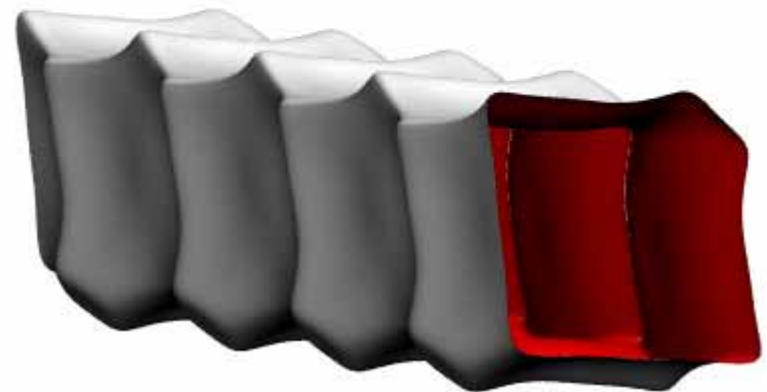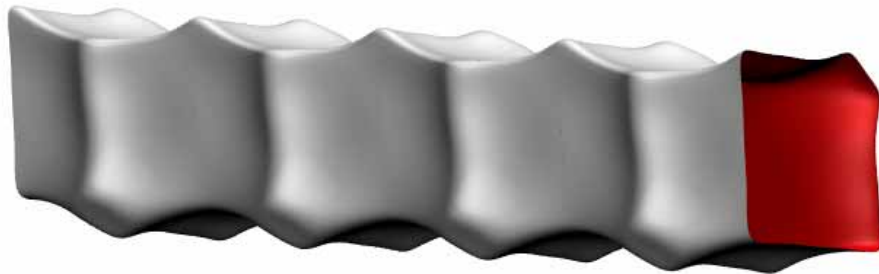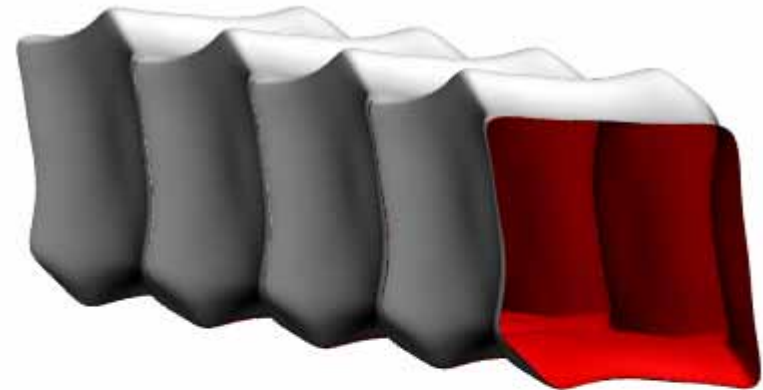
Figure 76
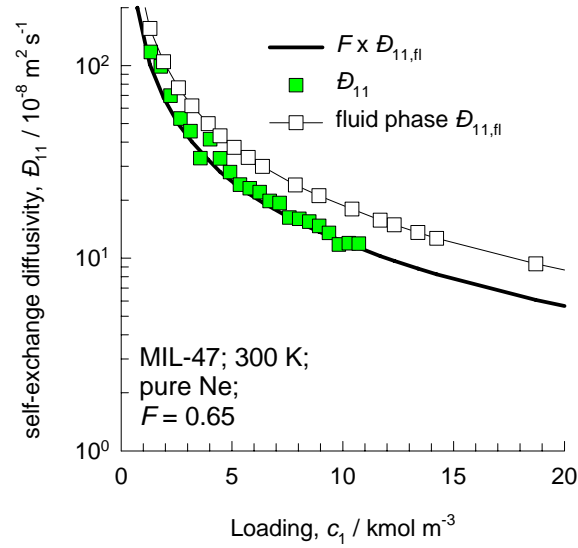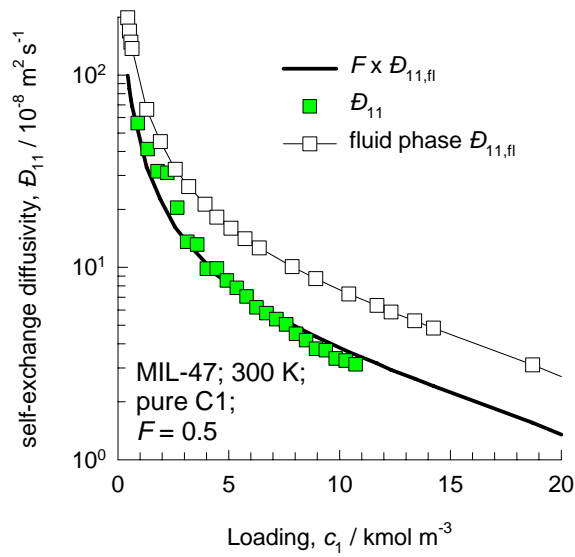
Data for MIL-47 for pure components
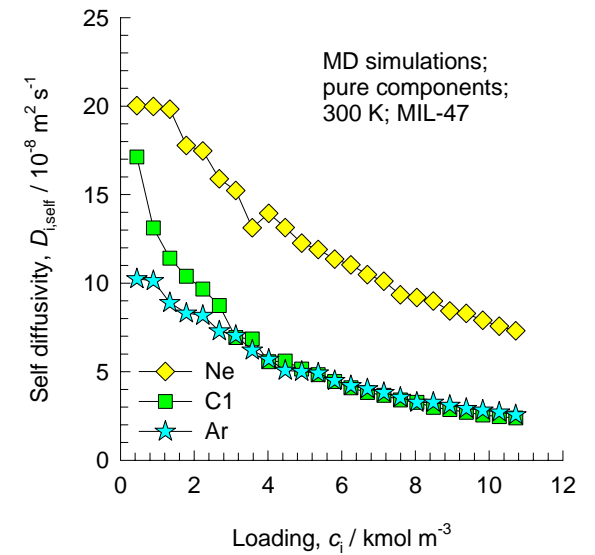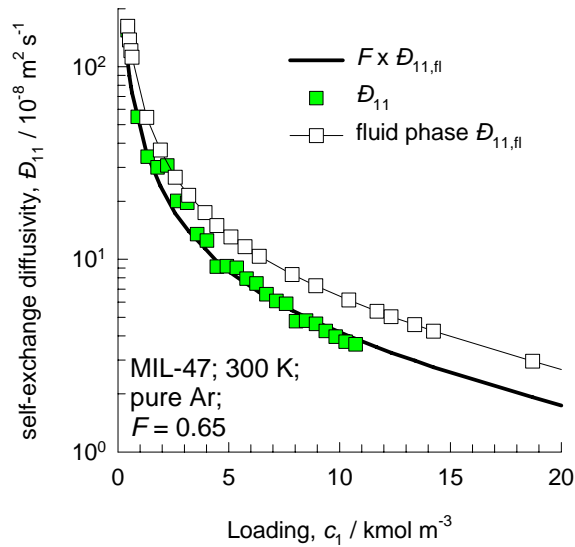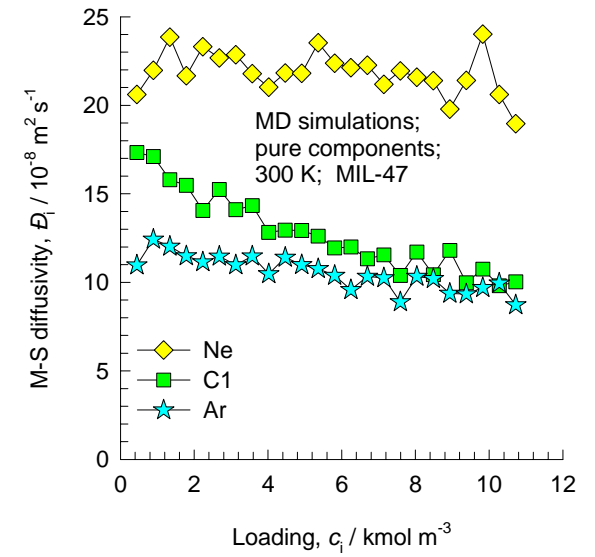
Figure 77

# Data for MIL-47 for binary mixtures



---
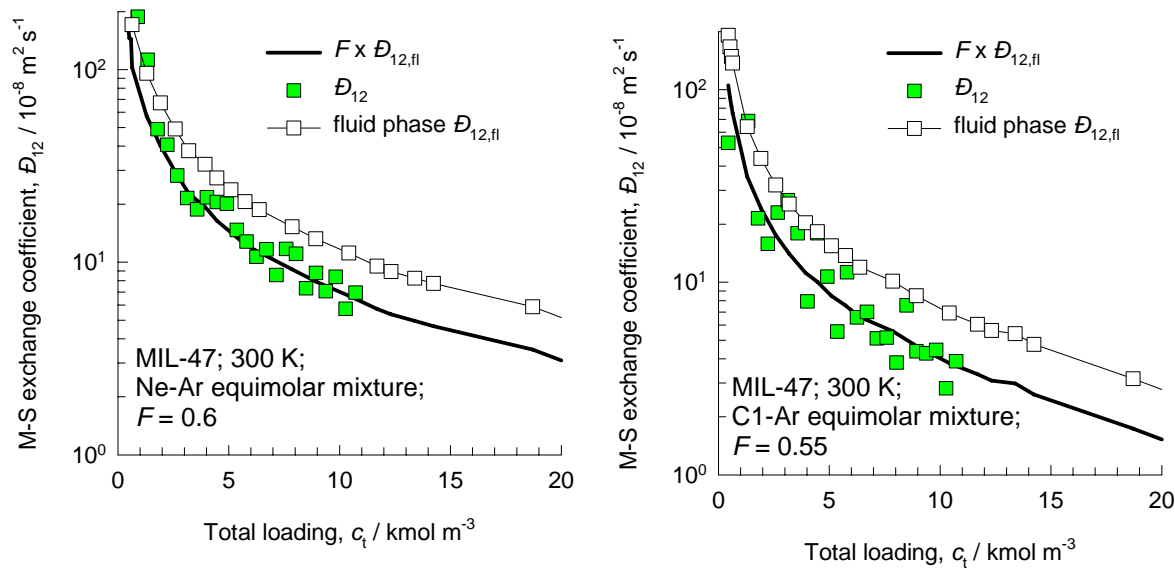
# Test of Darken and Vignes interpolation formulae for MIL-47

Figure 78

Prediction of $D_{i,self}$ and $\Delta_{ij}$ in binary mixtures in MIL-47 using Vignes interpolation and M-S model
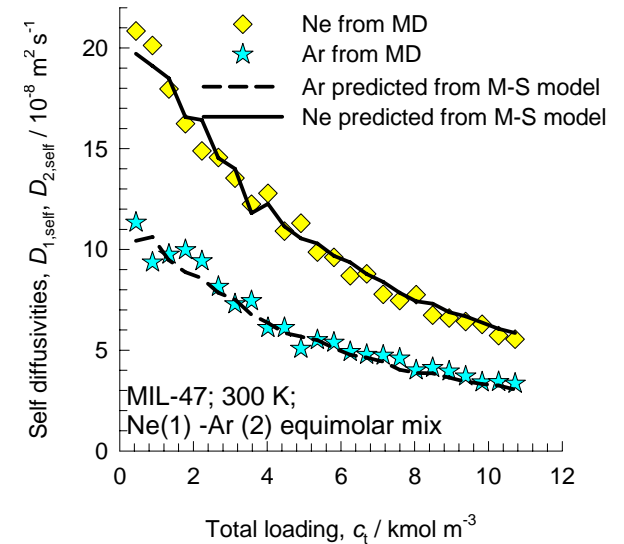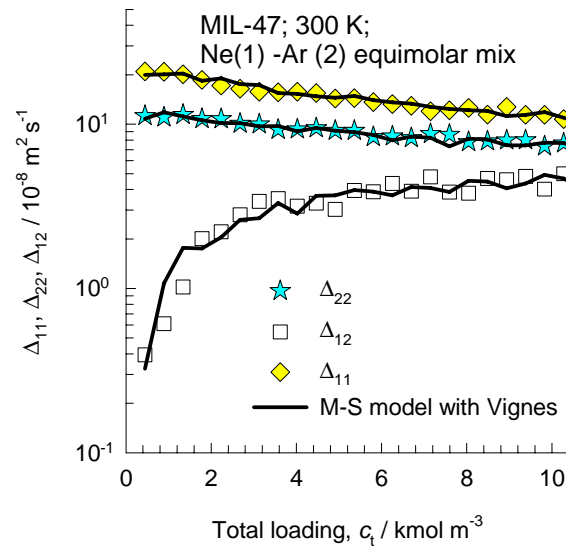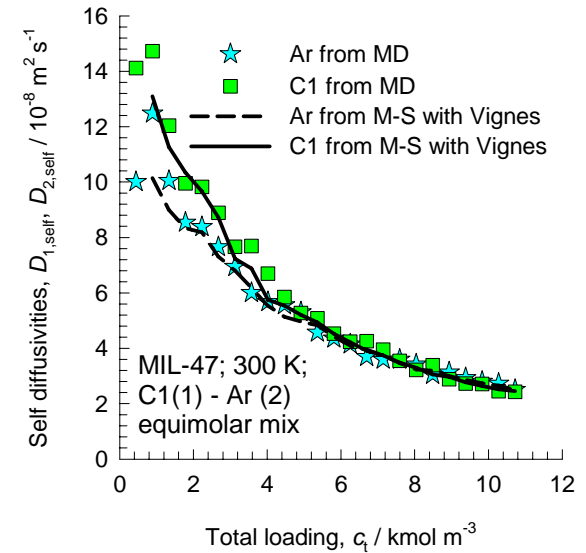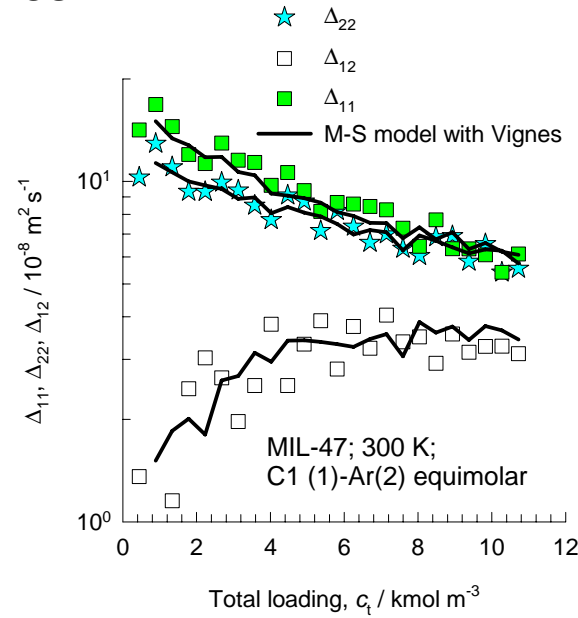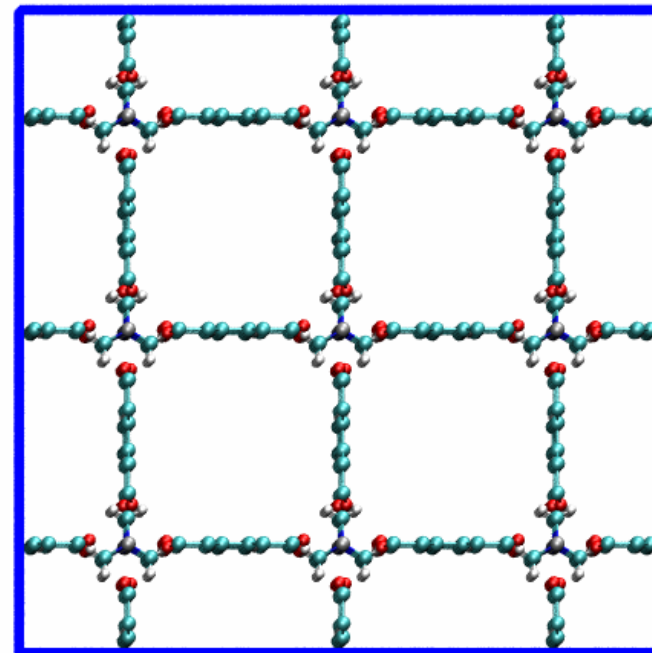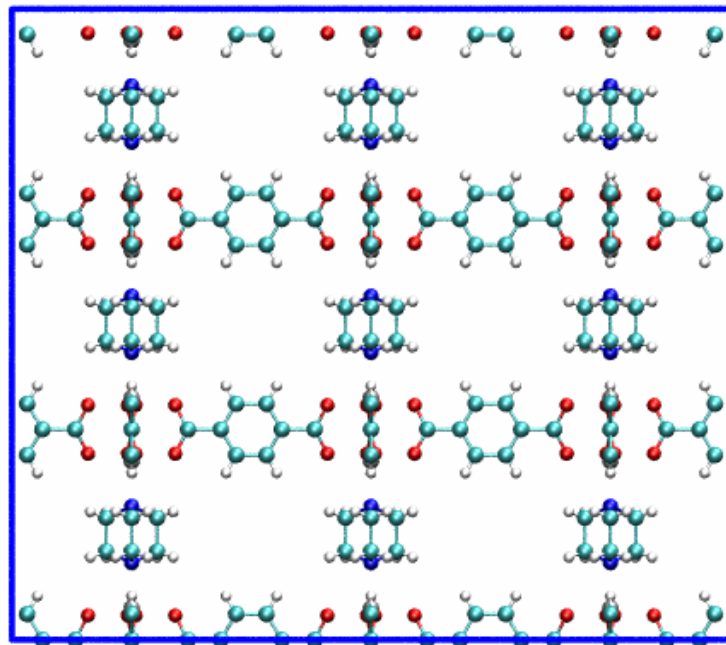
**Zn(bdc)dabco structure**
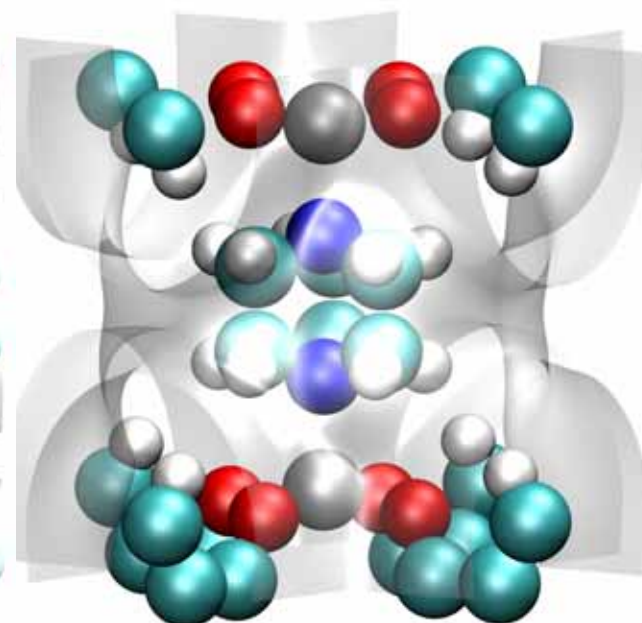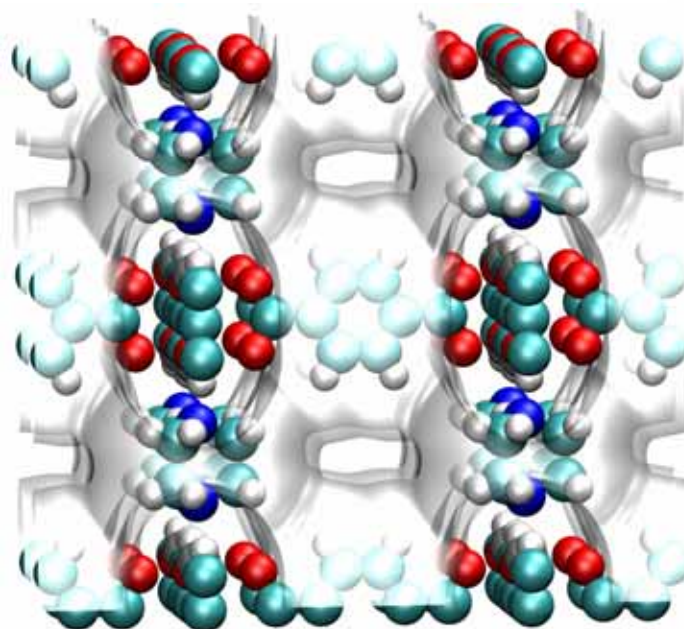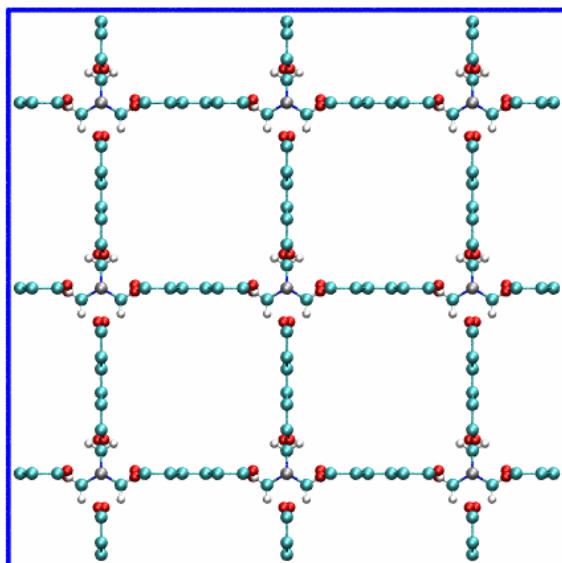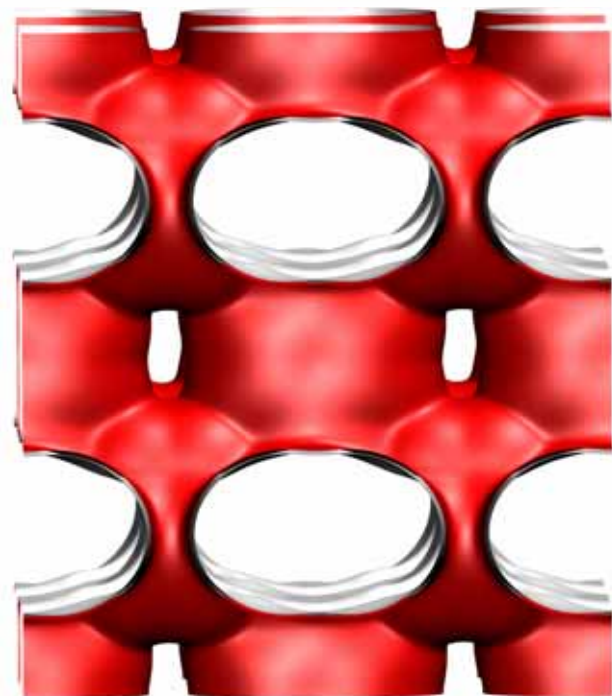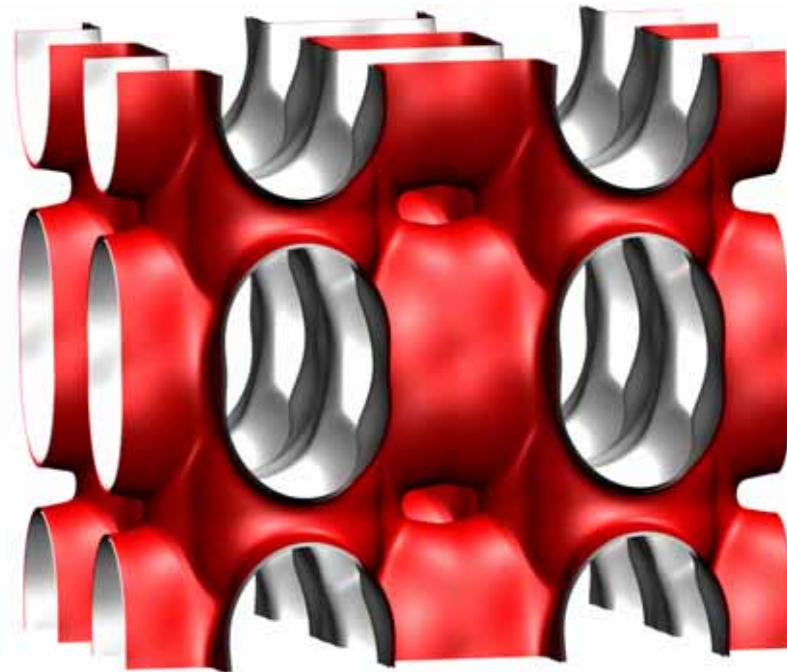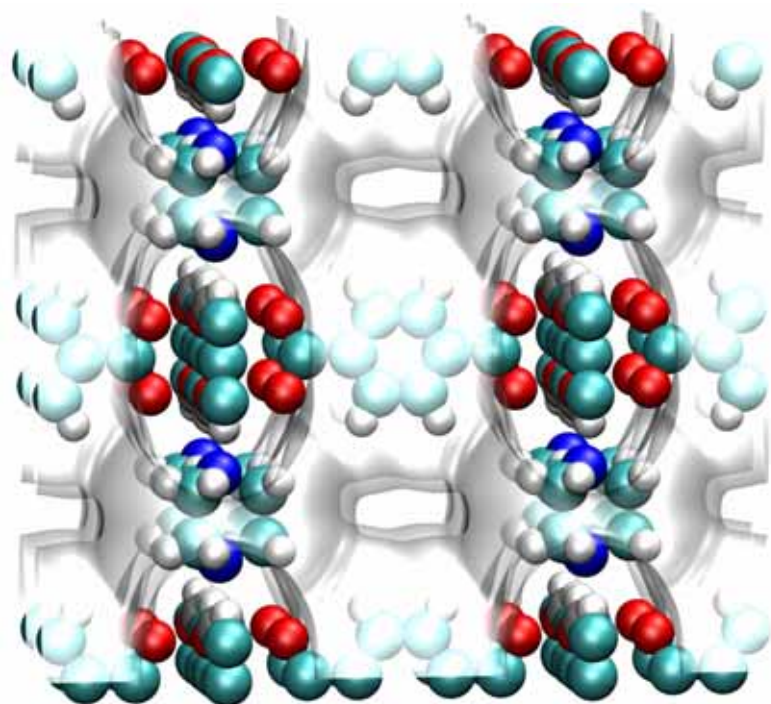
Figure 80

**Zn(bdc)dabco landscapes**
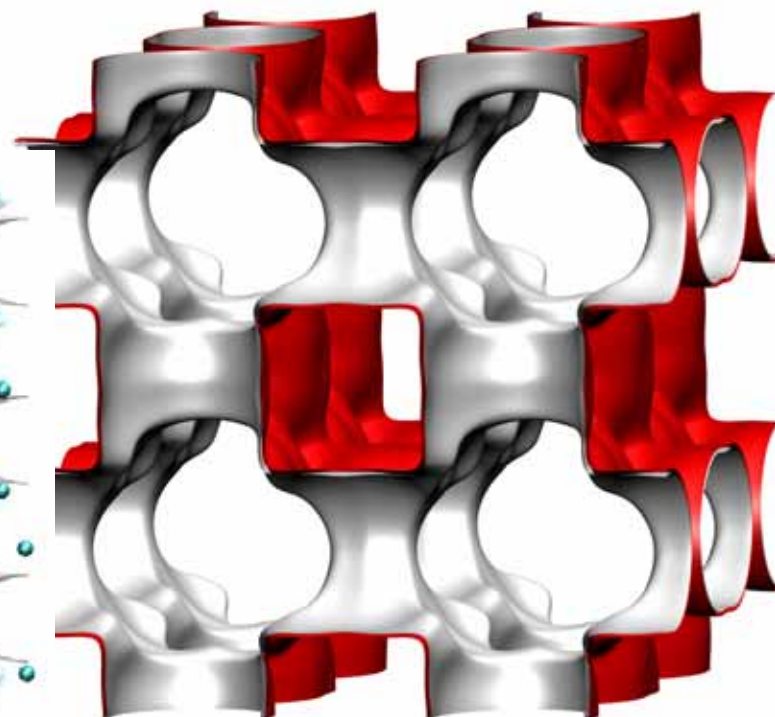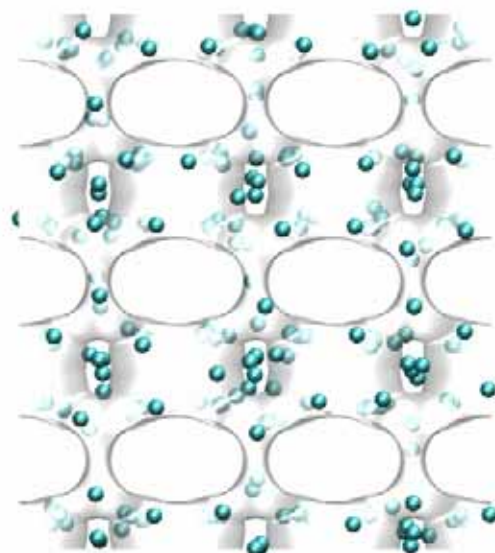
Figure 81
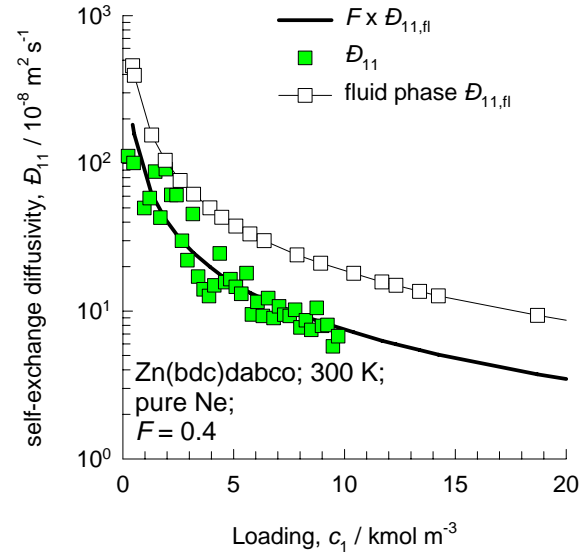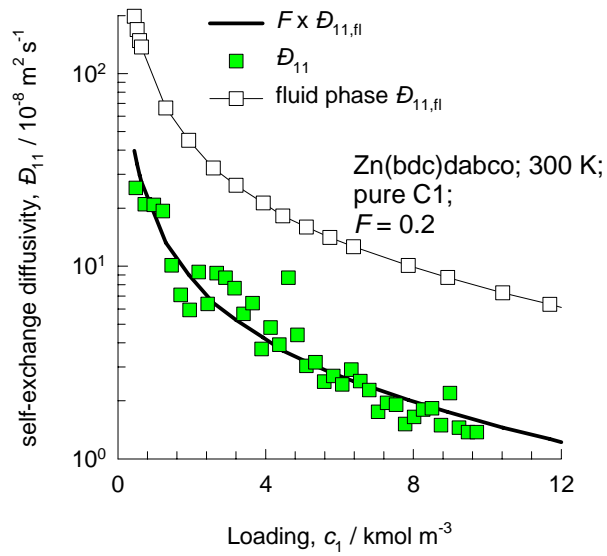


Data for Zn(bdc)dabco for pure components
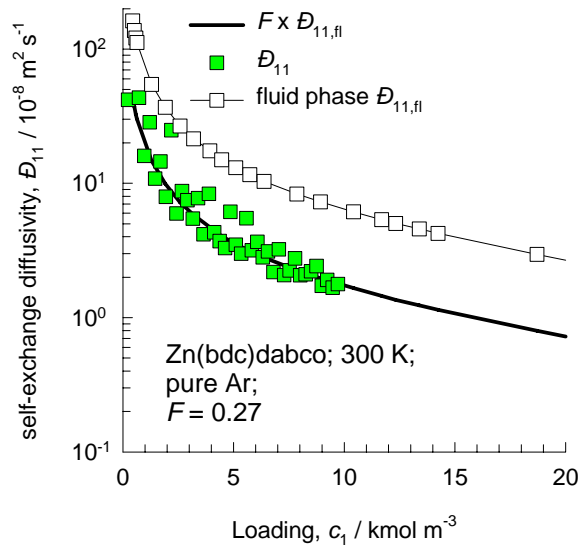
Comparison of simulated isotherm for C1 with experimental data of Senkovska and Kaskel, *Micro. Mesopor. Mat.*, 112, 108-115 (2008)
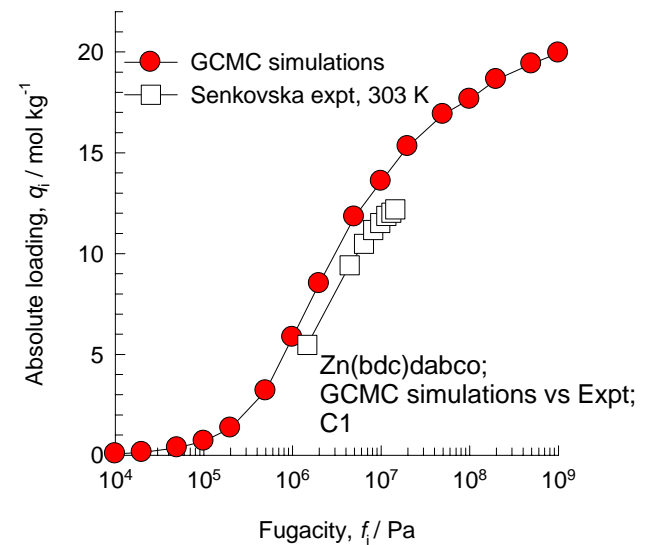
Figure 82
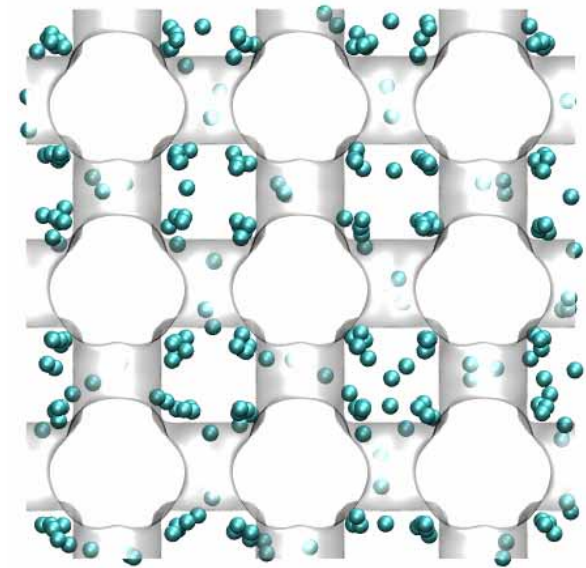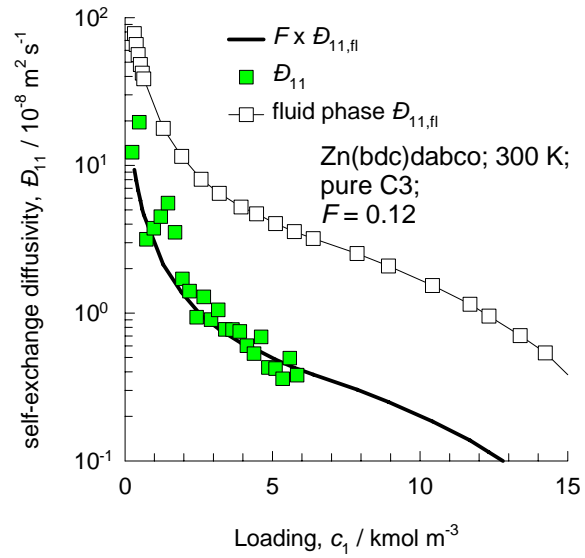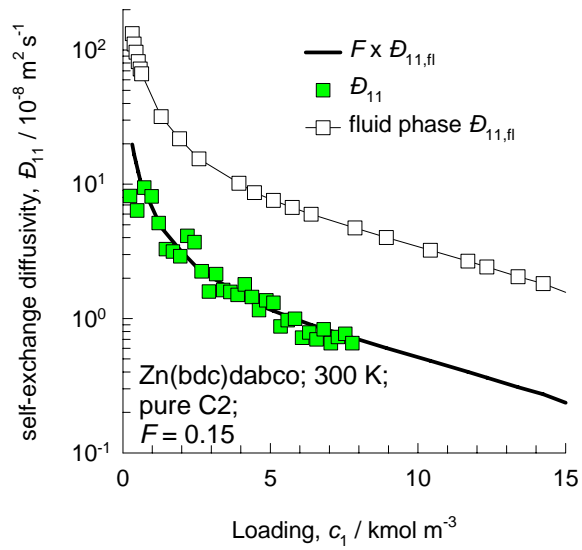
Data for Zn(bdc)dabco for pure components
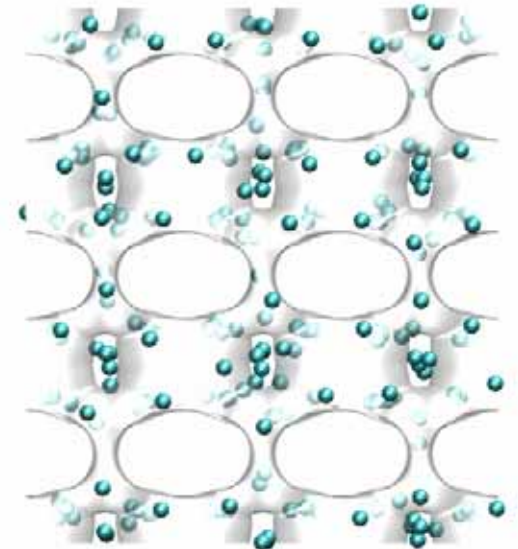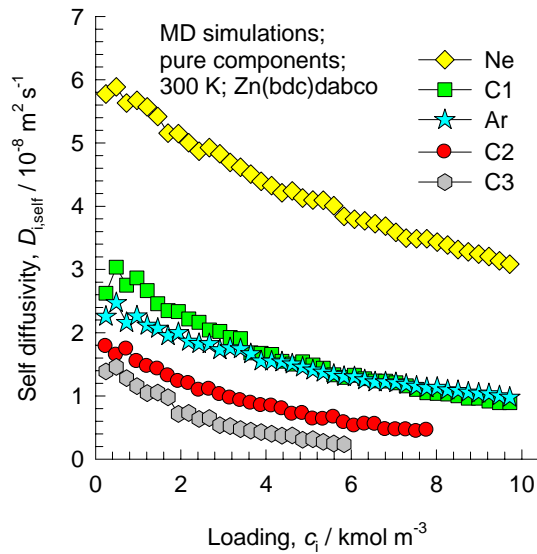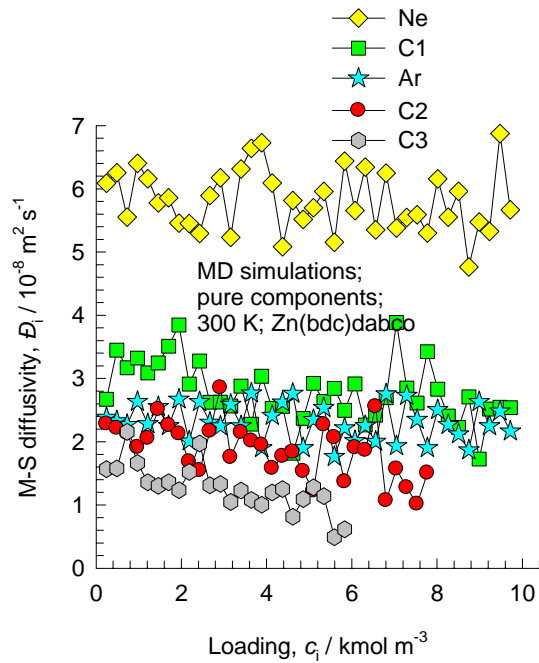
# Data for Zn(bdc)dabco for binary mixtures

Figure 83
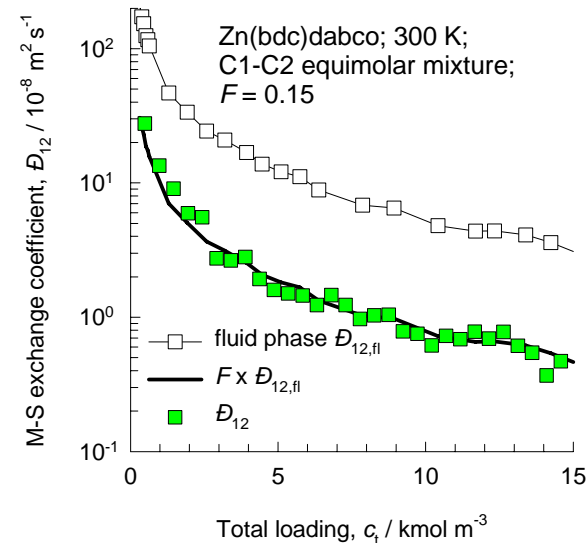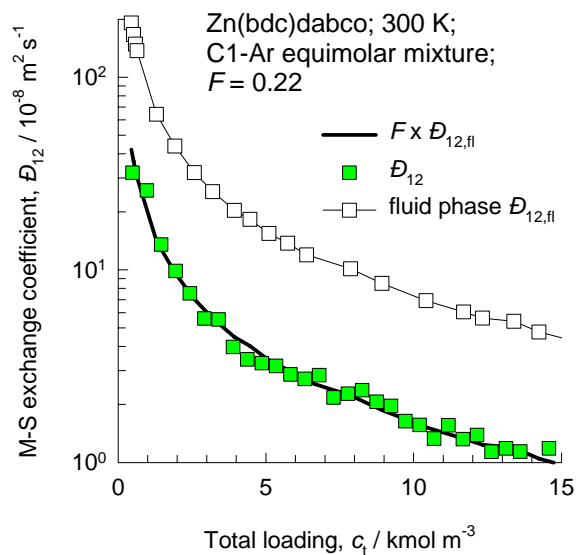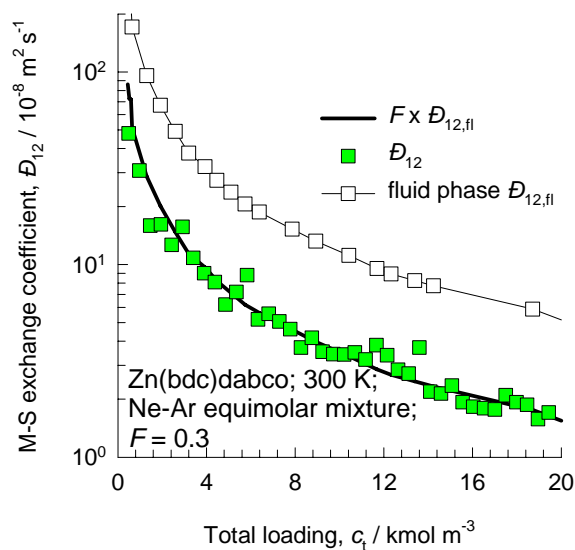


# Test of Darken and Vignes interpolation formulae for Zn(bdc)dabco

Figure 84
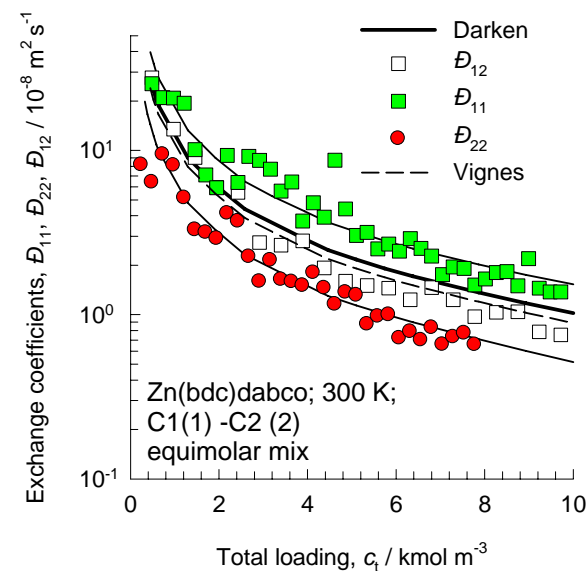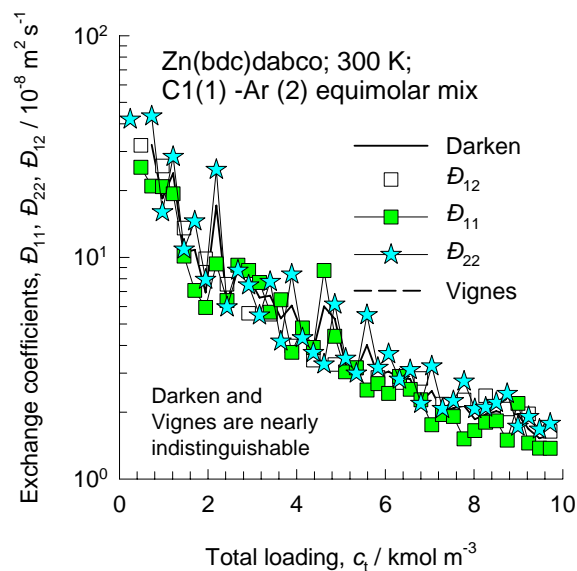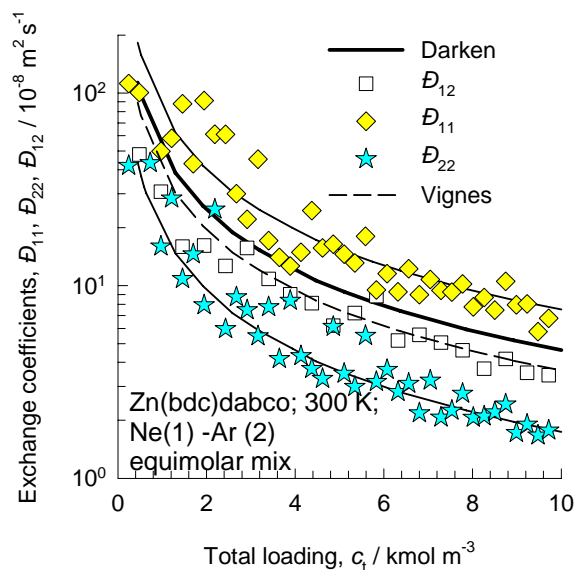
# Prediction of self diffusivities in binary mixture in Zn(bdc)dabco using Vignes interpolation and M-S model
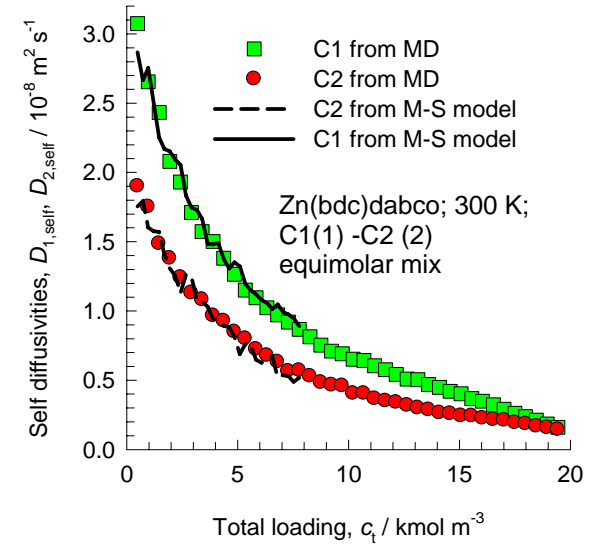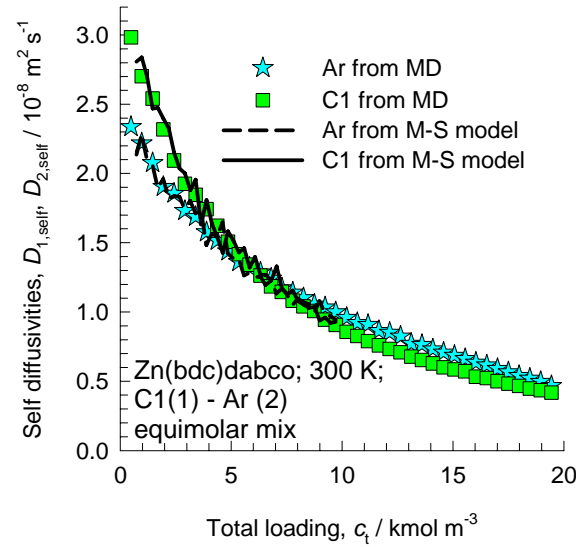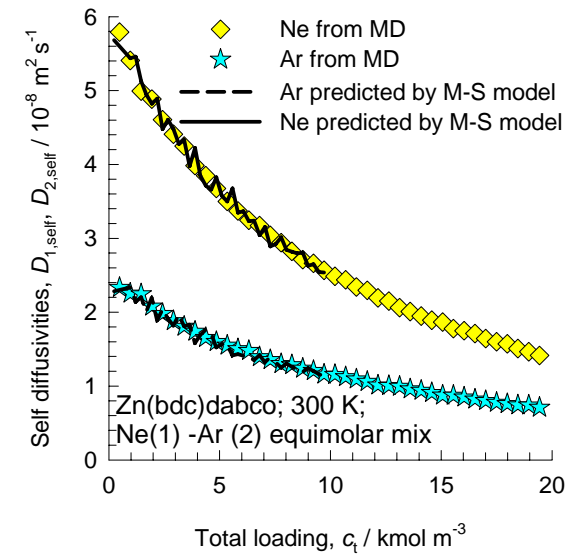
Figure 85

**Co(bdc)dabco structure**
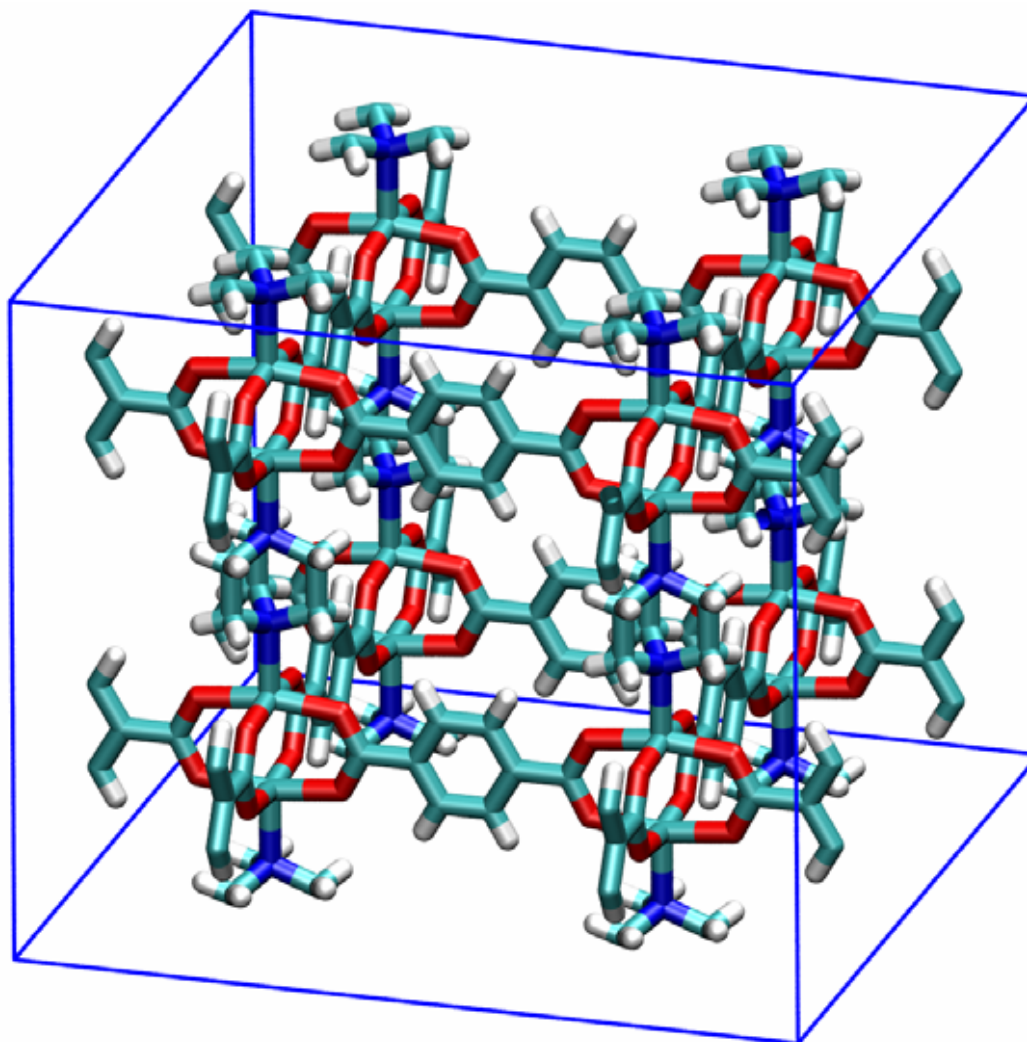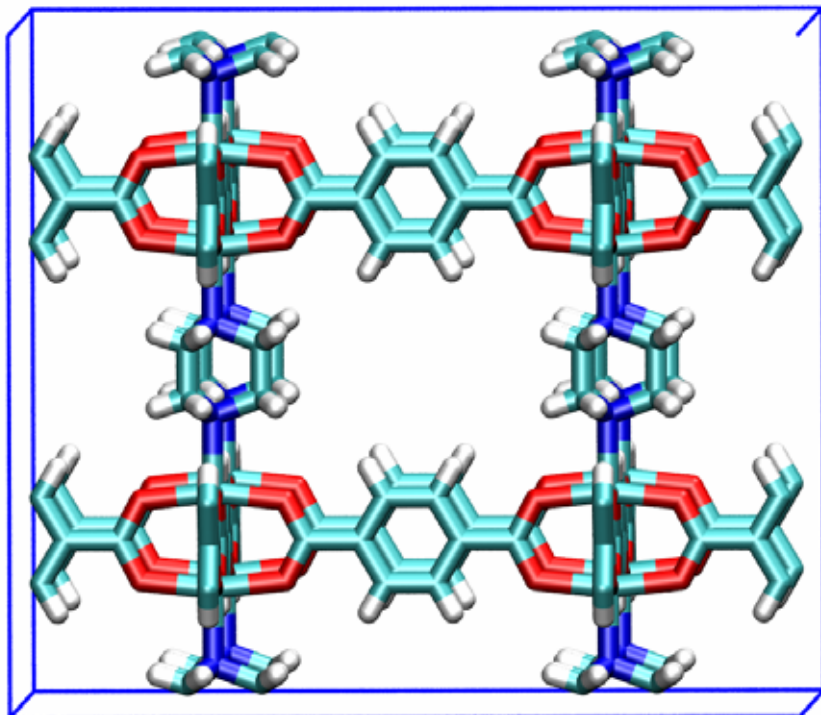
Figure 86
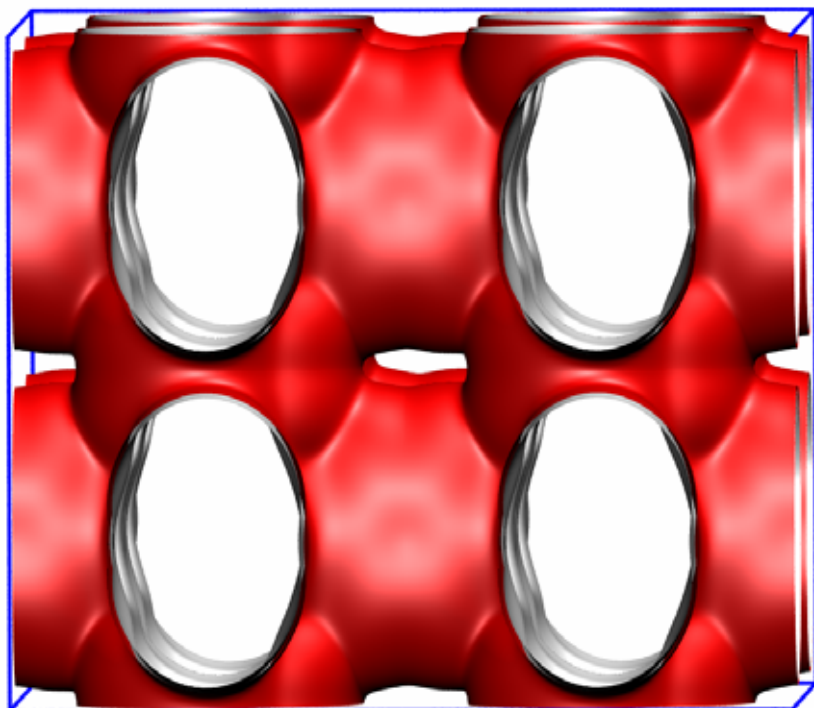
**Co(bdc)dabco landscapes**
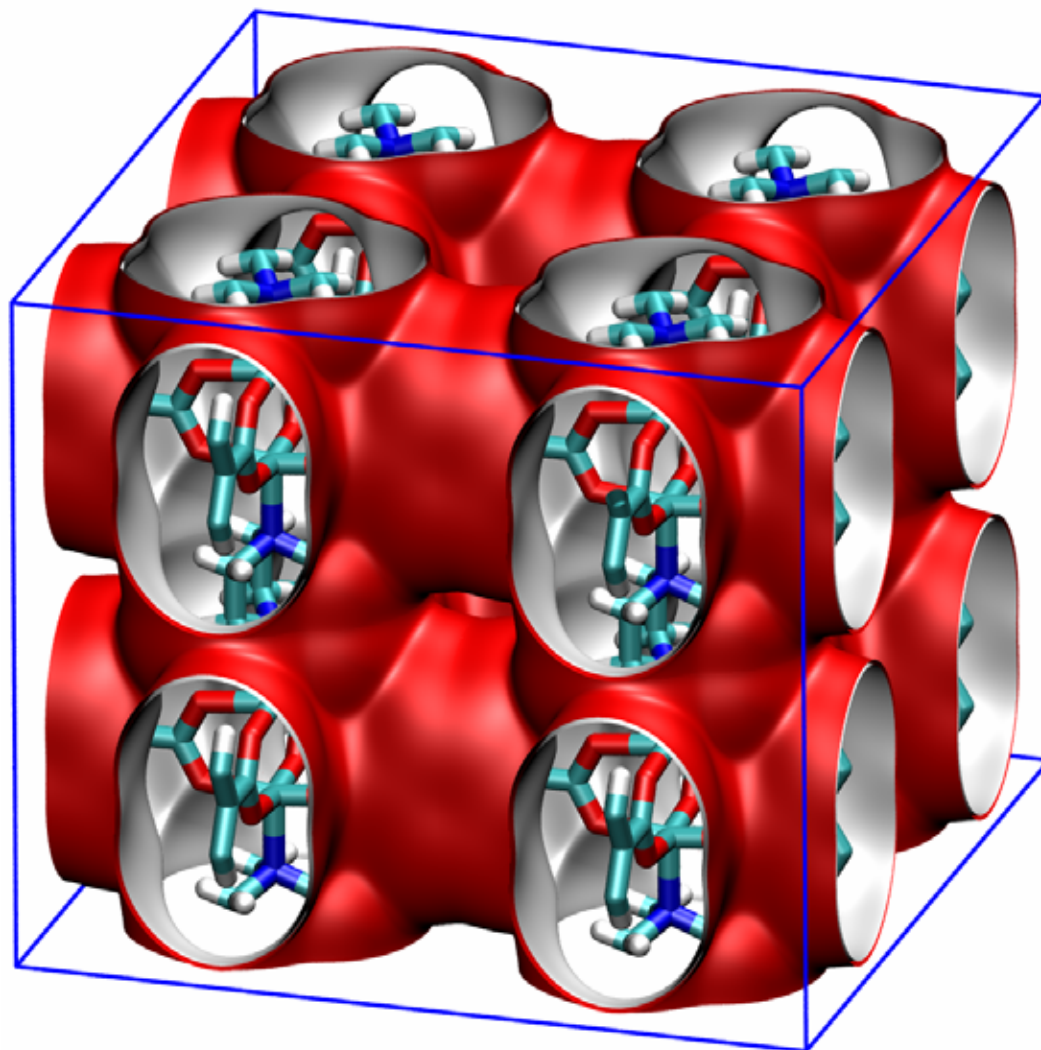
Figure 87
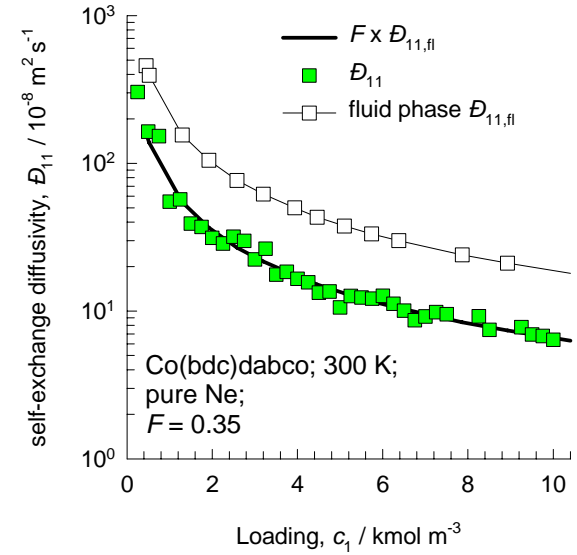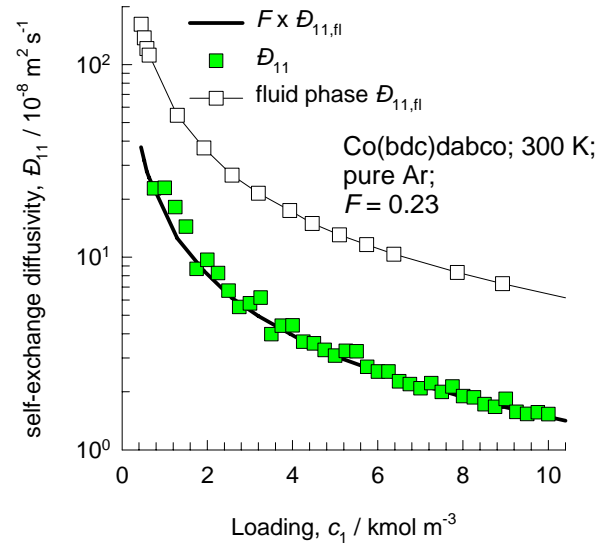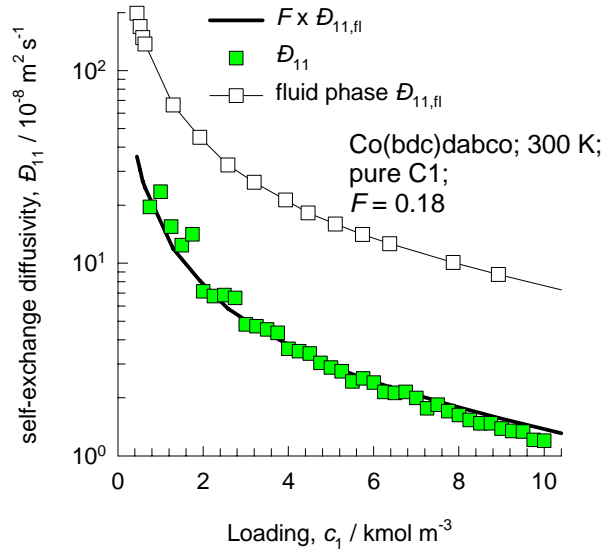


Data for Co(bdc)dabco for unary diffusion
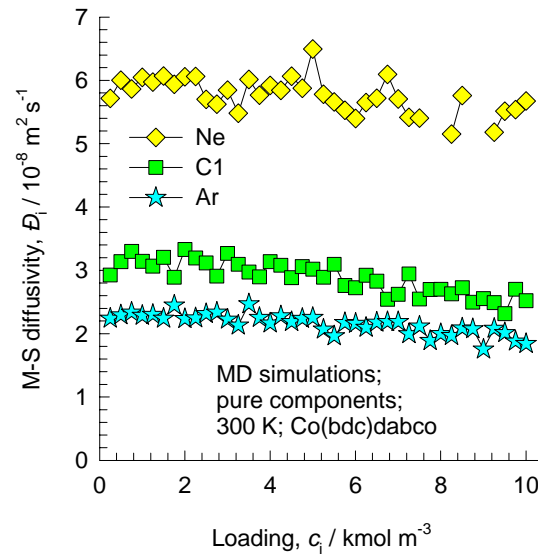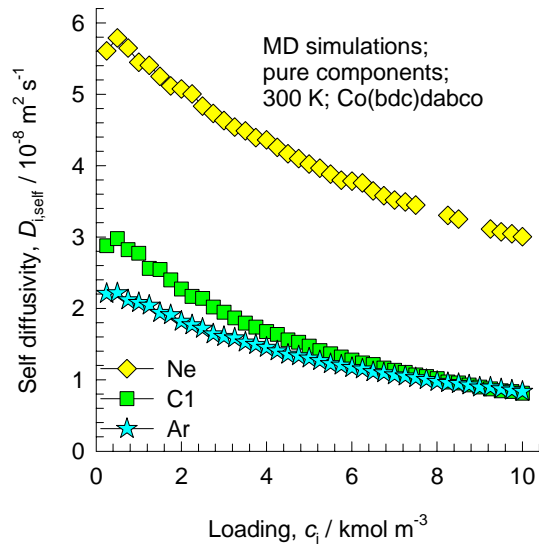
Comparison of simulated isotherm with experimental data of Wang et al, *Micro. Mesopor. Mat.*, 116, 653-657 (2008)
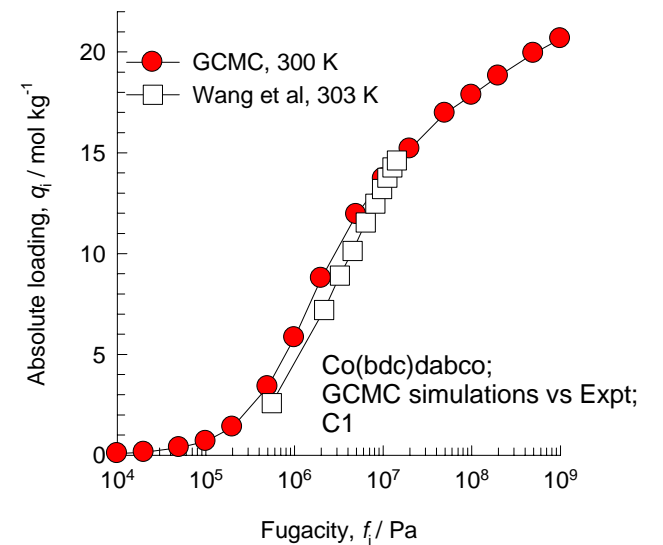
Figure 88

# Data for Co(bdc)dabco for binary mixtures



Co(bdc)dabco; 300 K;
Ne-Ar equimolar mixture;
$F = 0.3$

Co(bdc)dabco; 300 K;
C1-Ar equimolar mixture;
$F = 0.18$
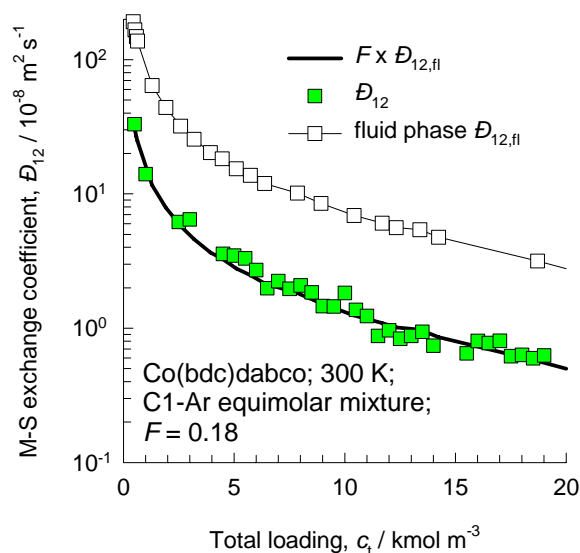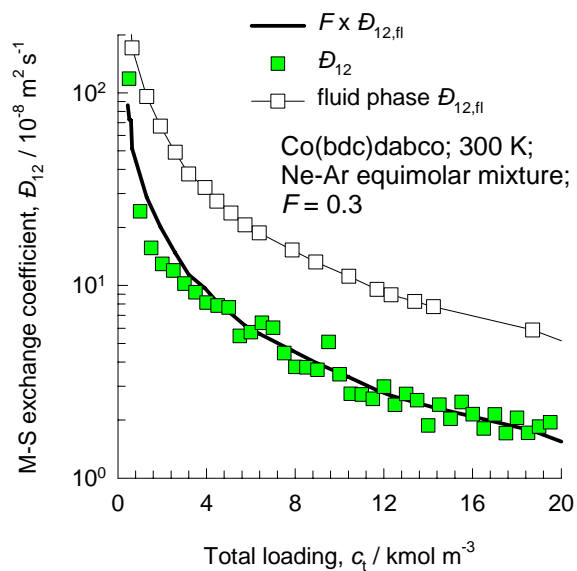
## Test of Darken and Vignes interpolation formulae for Co(bdc)dabco



Co(bdc)dabco; 300 K;
Ne(1) -Ar (2) equimolar mix

Co(bdc)dabco; 300 K;
C1(1) -Ar (2) equimolar mix
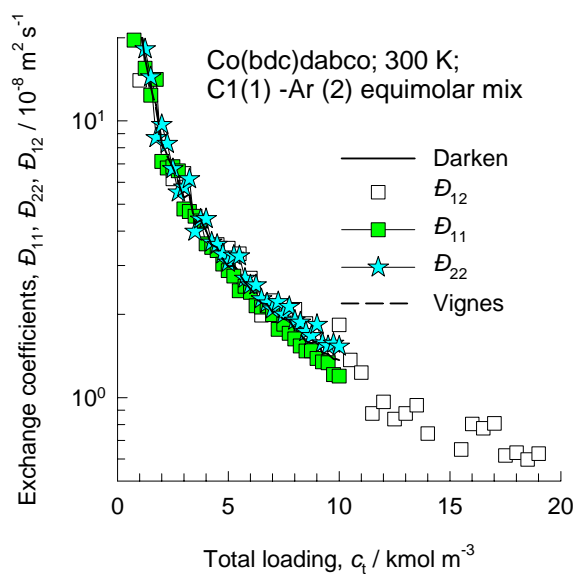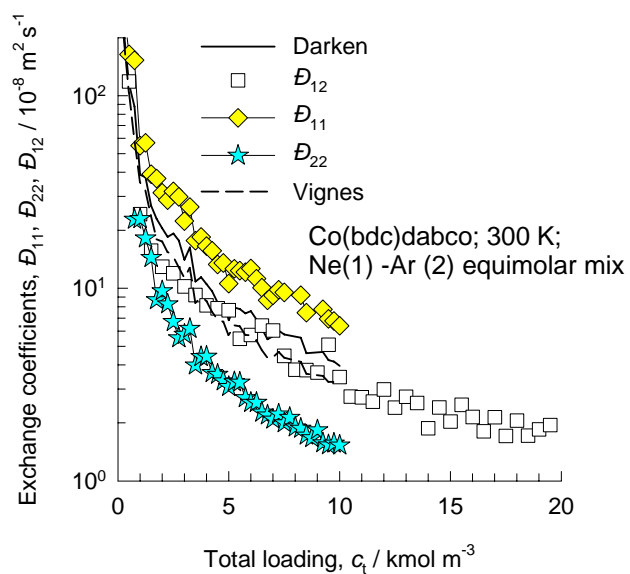
Figure 89

Prediction of $D_{i,self}$ and $\Delta_{ij}$ in binary mixtures in Co(bdc)dabco using Vignes interpolation and M-S model
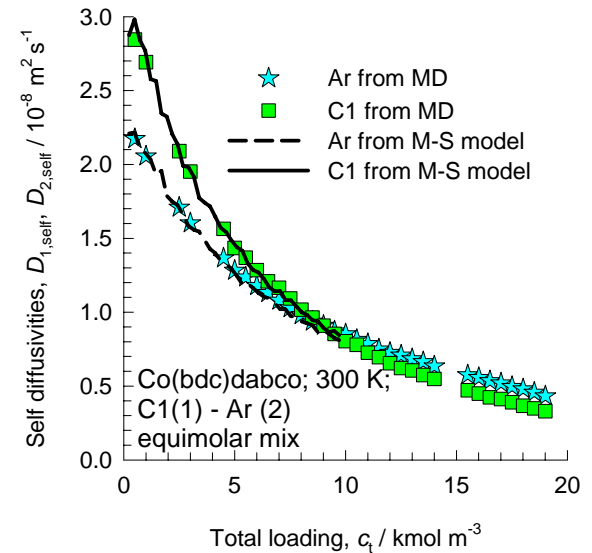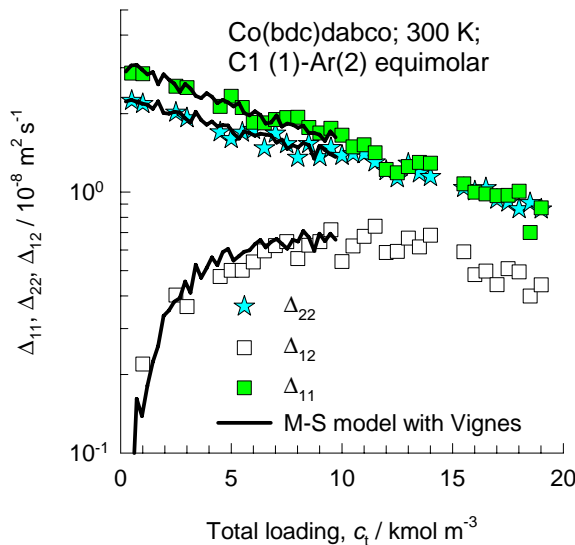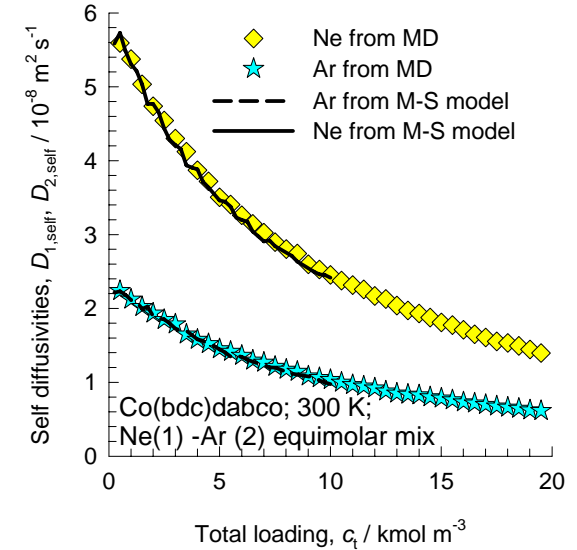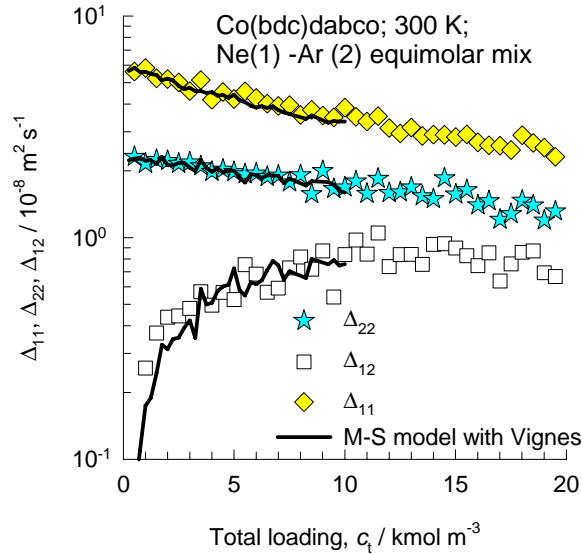
# Unit cell for Co-FA = 4 channel segments

Figure 90
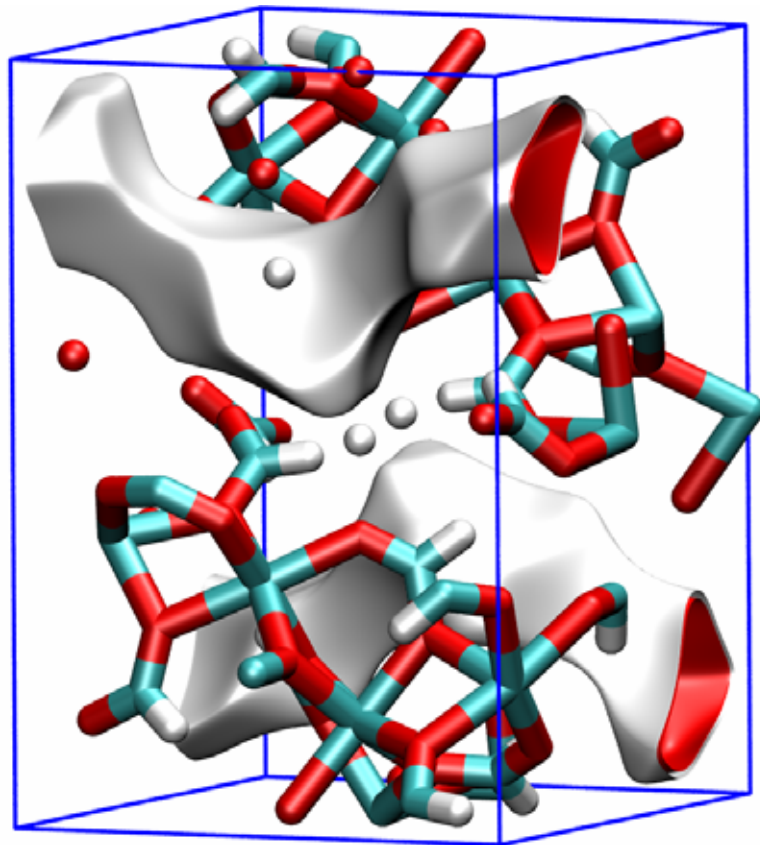


channel segment

C1

C2

C3

nC4 (low P)

nC4 (high P)

nC5

nC6

nC7

Except at very high pressures, each channel segment is occupied by one molecule as shown in the snapshots
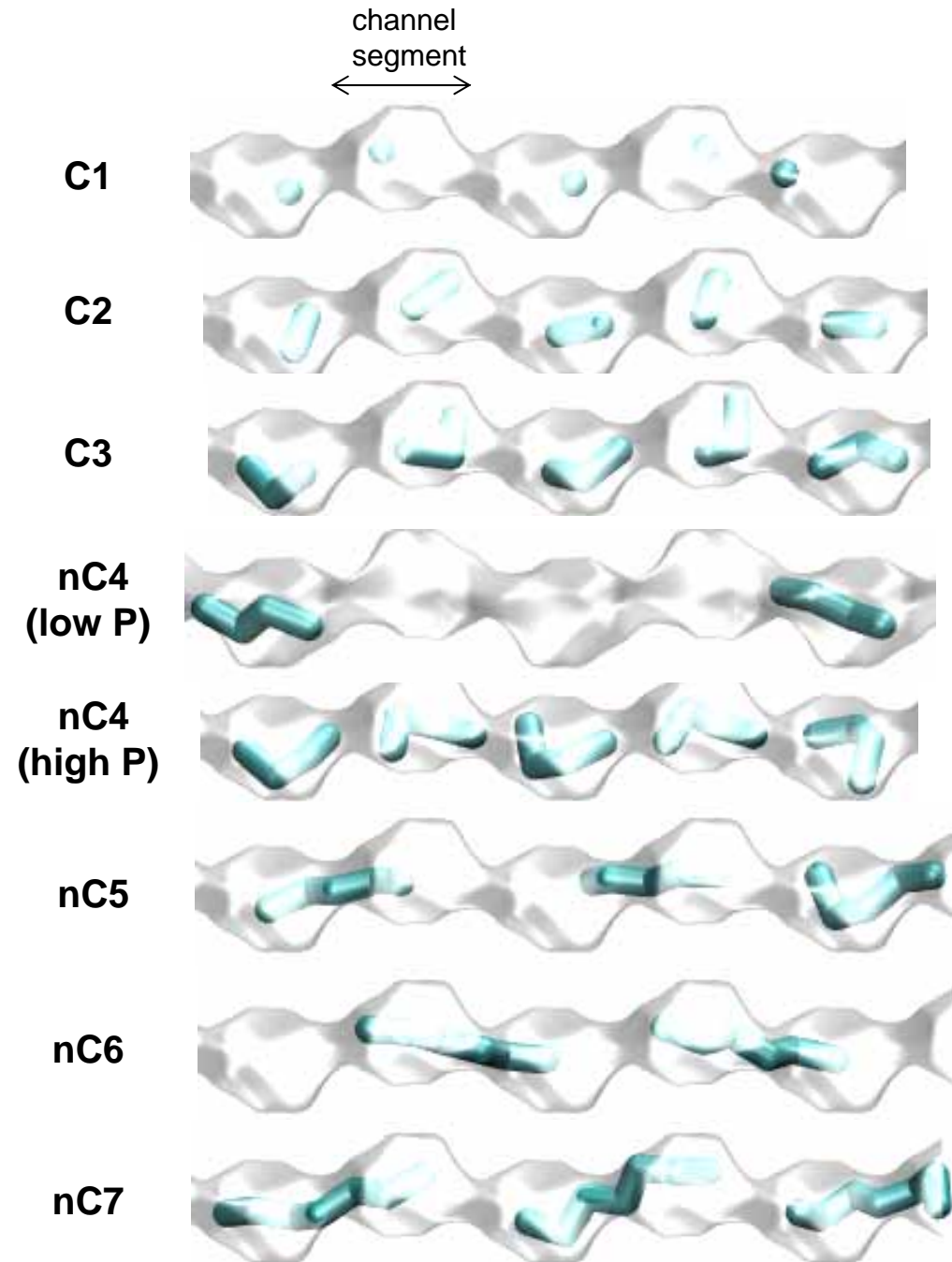
Figure 91
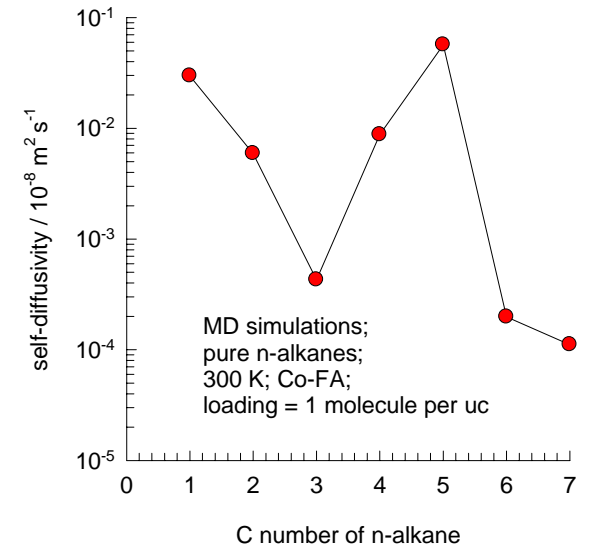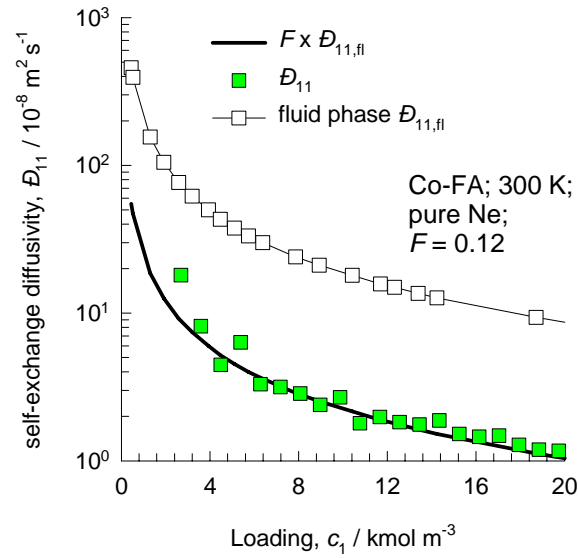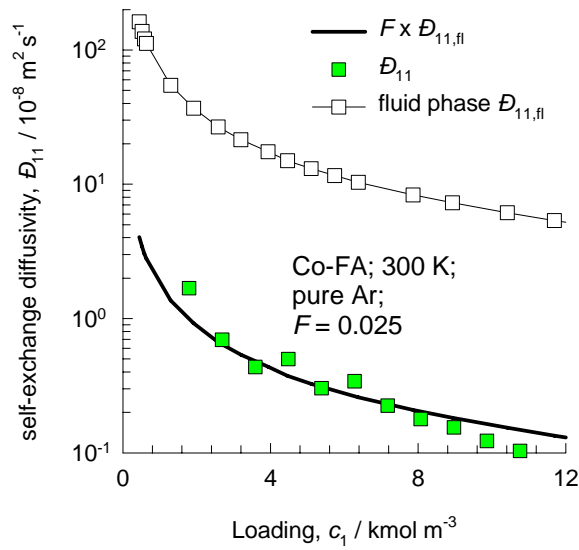
Data for Co-FA for unary diffusion

Hierarchy of diffusivities of n-alkanes in Co-FA is non-monotonic
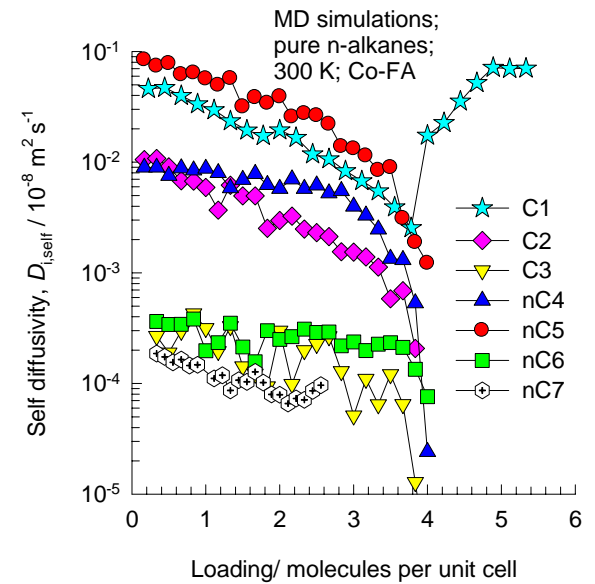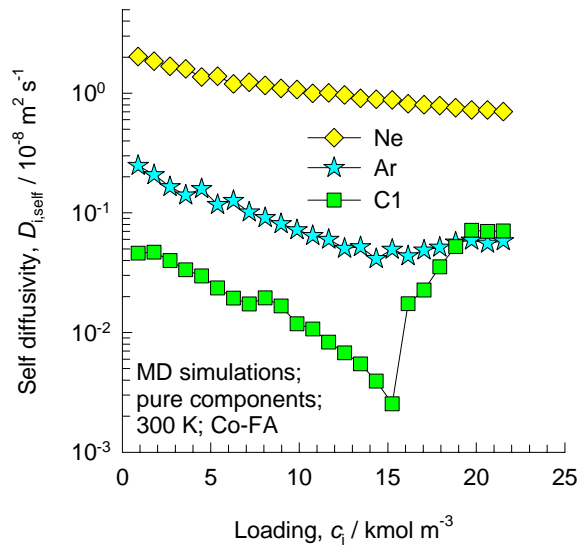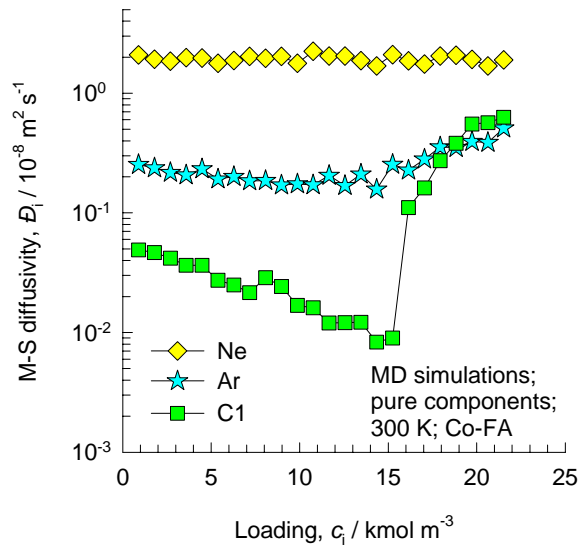
Figure 92

## Data for Co-FA for mixture diffusion
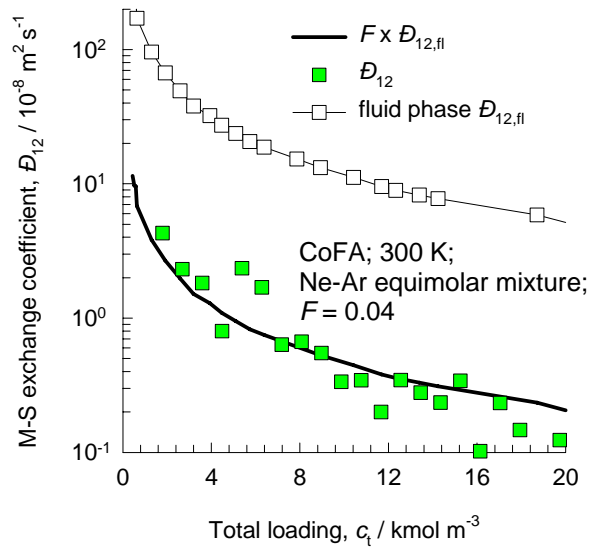
M-S exchange coefficient, $Đ_{12}$ / $10^{-8}$ m$^2$ s$^{-1}$

Total loading, $c_t$ / kmol m$^{-3}$

- $F \times Đ_{12,fl}$
- $Đ_{12}$
- fluid phase $Đ_{12,fl}$

CoFA; 300 K;
Ne-Ar equimolar mixture;
$F = 0.04$

## Test of Darken and Vignes interpolation formulae for Co-FA

Exchange coefficients, $Đ_{11}$, $Đ_{22}$, $Đ_{12}$ / $10^{-8}$ m$^2$ s$^{-1}$

Co-FA; 300 K;
Ne(1) -Ar (2)
equimolar mix

- Darken
- $Đ_{12}$
- $Đ_{11}$
- $Đ_{22}$
- Vignes

Total loading, $c_t$ / kmol m$^{-3}$
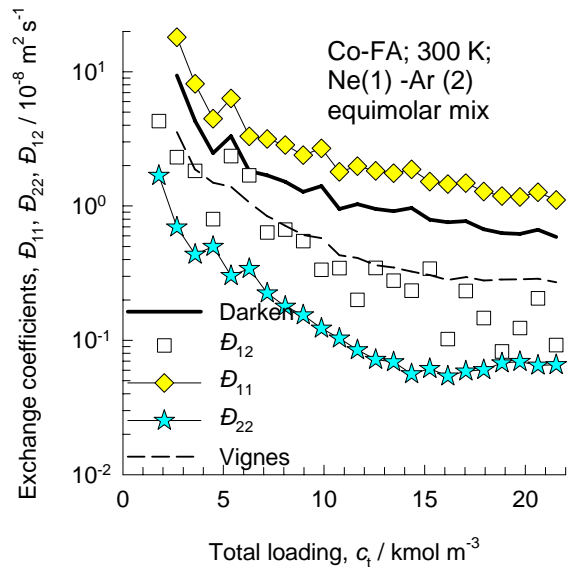
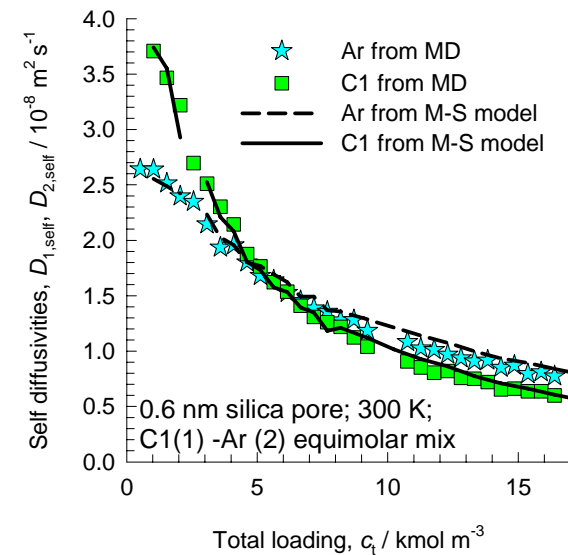## Self-diffusivities of binary mixture in Co-FA

Unary diffusion data

$$\frac{1}{D_{1,self}} = \frac{1}{Đ_1} + \frac{x_1}{Đ_{11}} + \frac{x_2}{Đ_{12}}$$

$$\frac{1}{D_{2,self}} = \frac{1}{Đ_2} + \frac{x_2}{Đ_{22}} + \frac{x_1}{Đ_{12}}$$
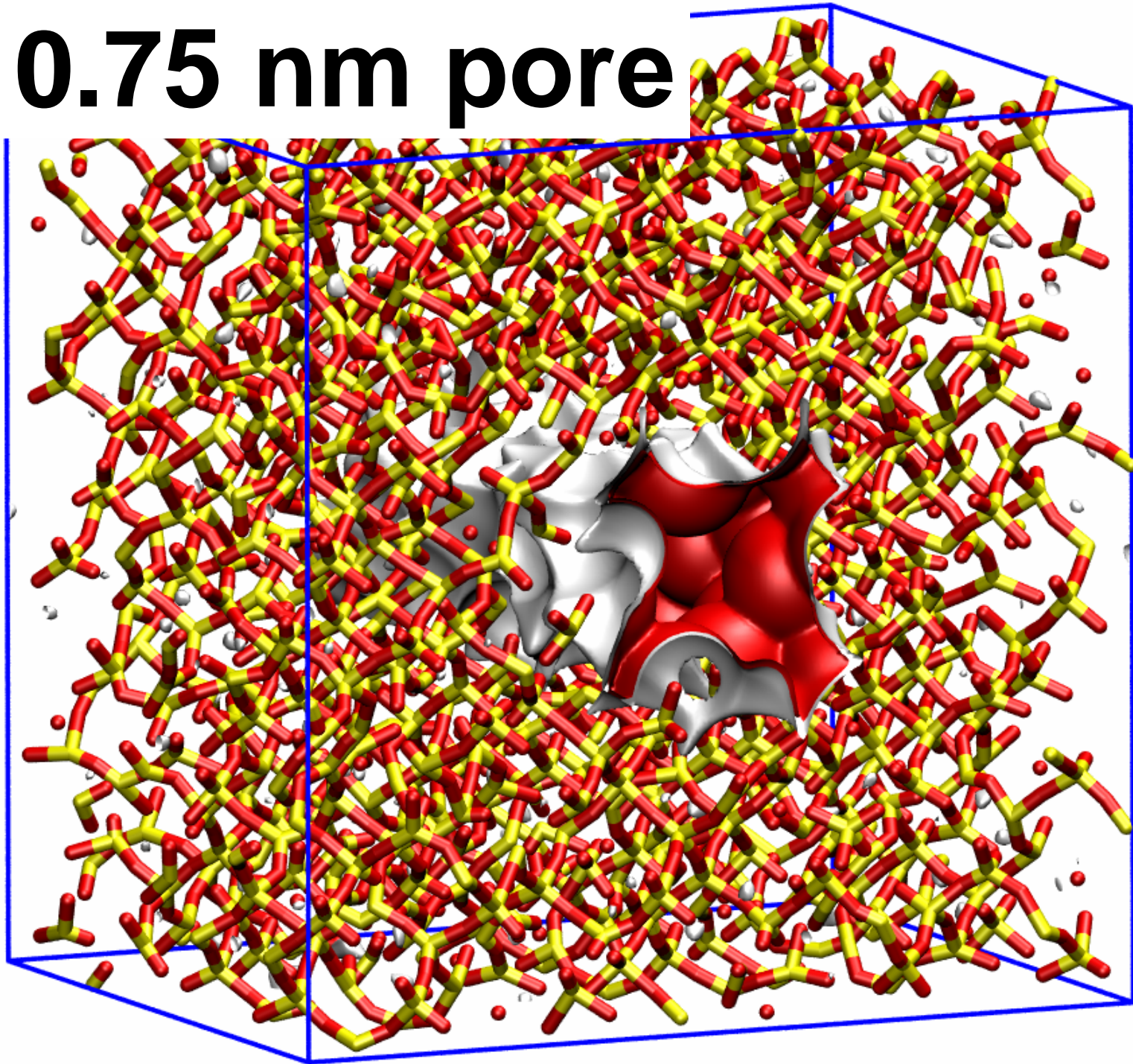
Vignes interpolation
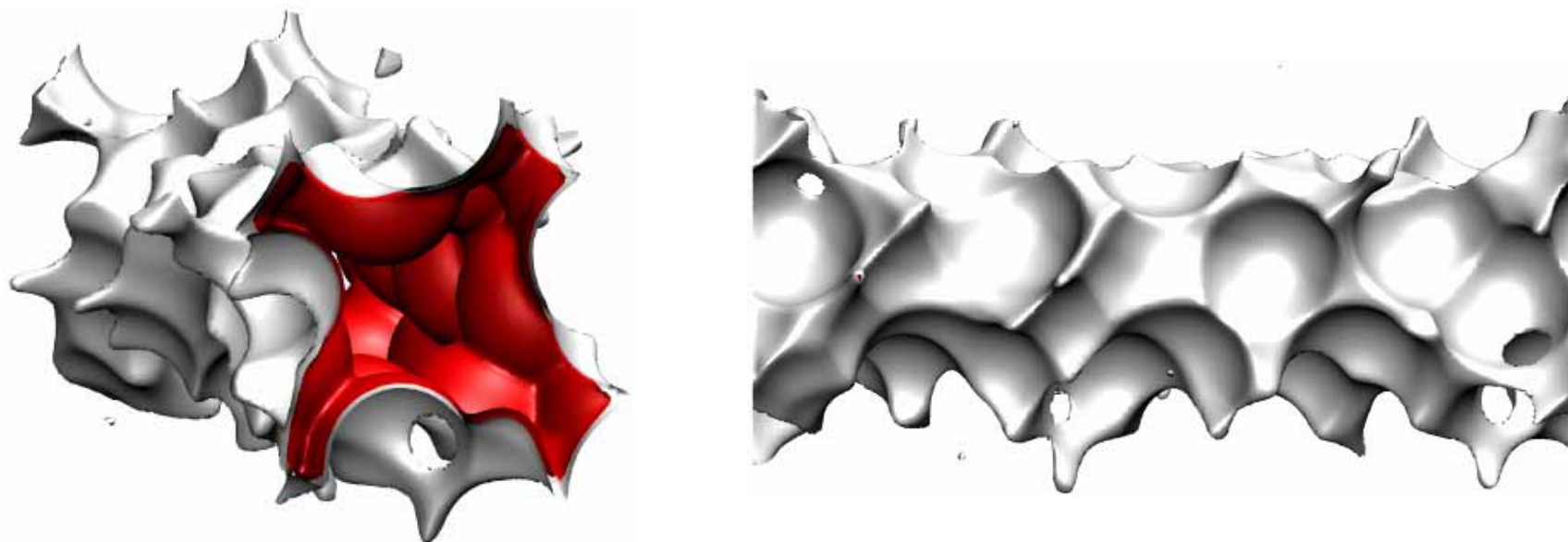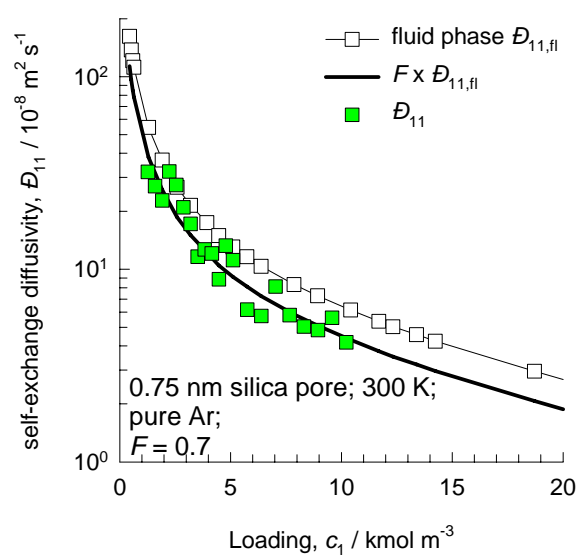
Predictions ( lines) are compared with MD (symbols)

Self diffusivities, $D_{1,self}$, $D_{2,self}$ / $10^{-8}$ m$^2$ s$^{-1}$

Co-FA; 300 K;
Ne(1) -Ar (2) equimolar mix

- Ne from MD
- Ar from MD
- Ar predicted from M-S model
- Ne predicted by M-S model

Total loading, $c_t$ / kmol m$^{-3}$

# Unit cell for Mn-FA
# = 4 channel segments

Figure 93



Except at very high pressures, each channel segment is occupied by one molecule as shown in the snapshots

Channel segment
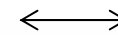
C1

C2

C3

nC4

nC5

nC6
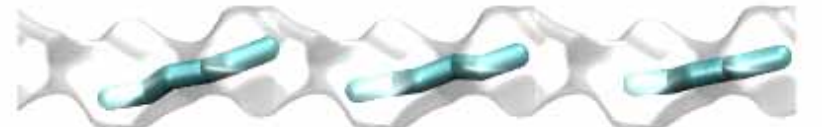
Data for Mn-FA for unary diffusion
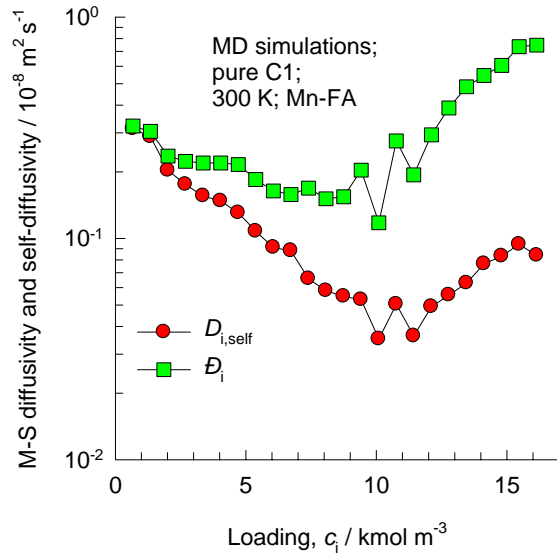
Hierarchy of diffusivities of n-alkanes in Mn-FA is non-monotonic
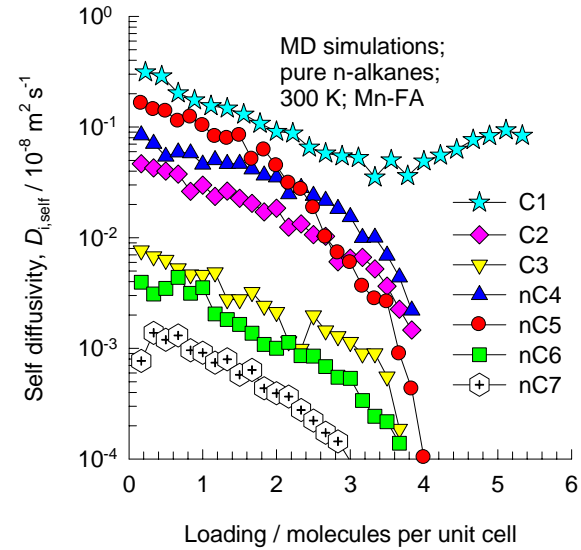
Figure 94

Data for Mn-FA for mixture diffusion
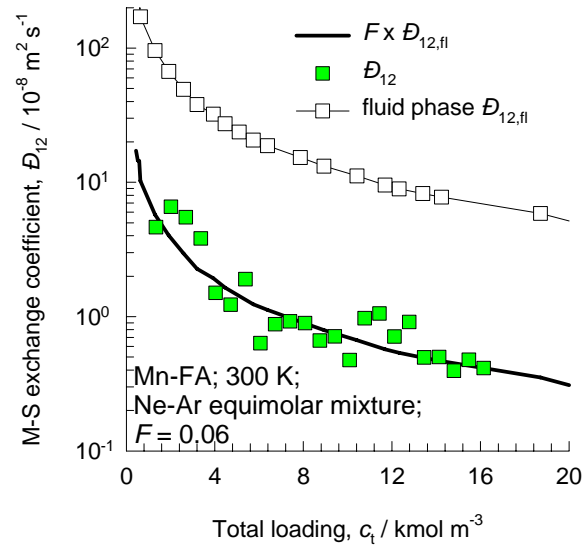
Figure 95
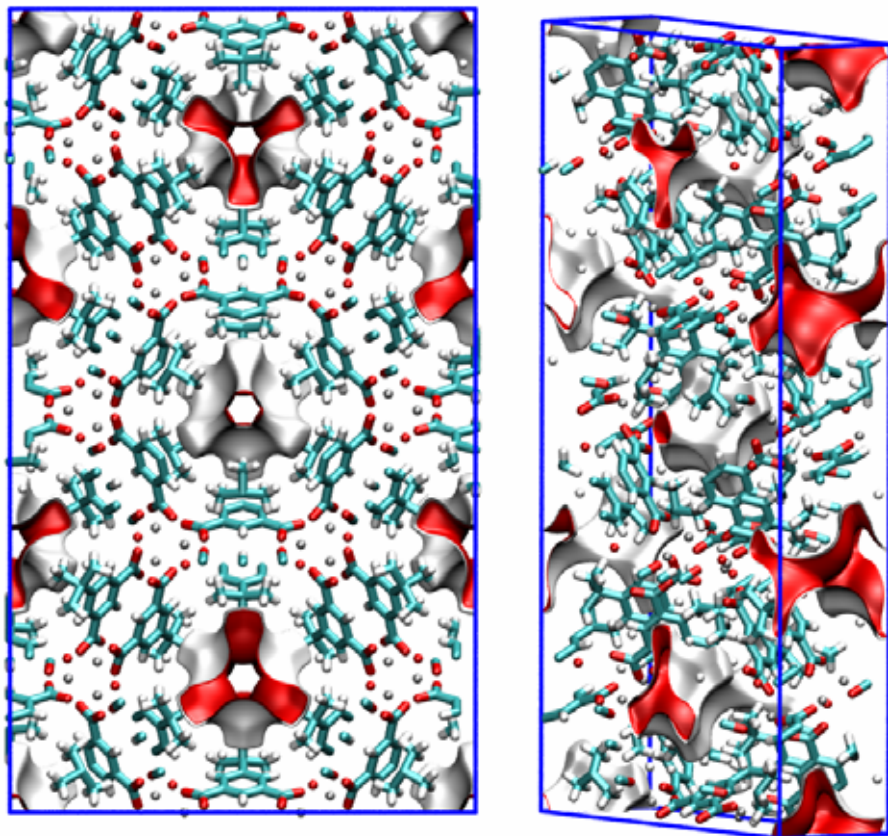
**Unit cell
for Zn(tbip)
= 6 channel segments**

Figure 96
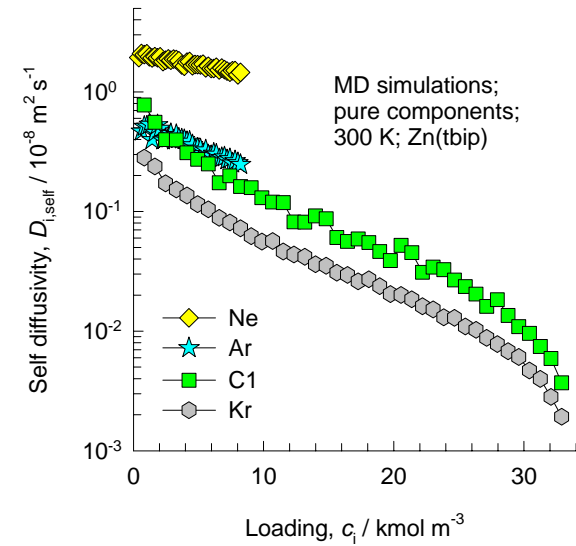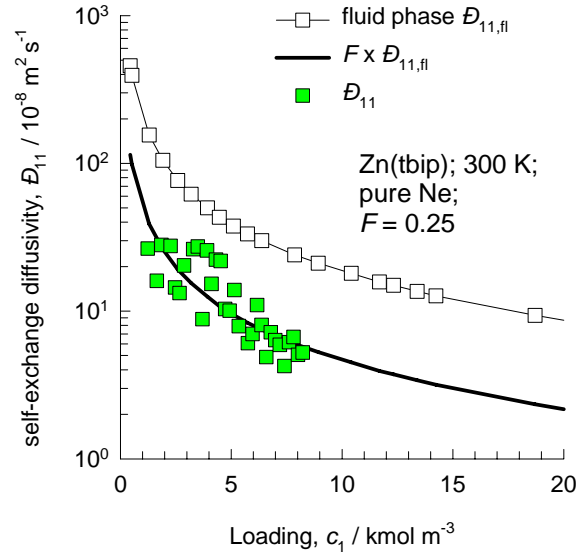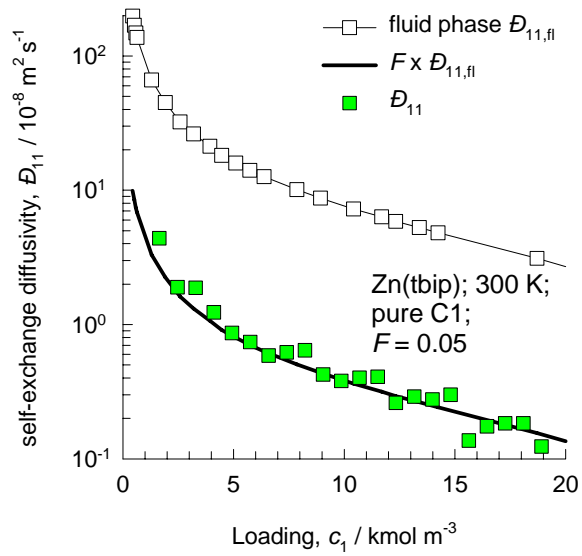
Data for Zn(tbip) for unary diffusion
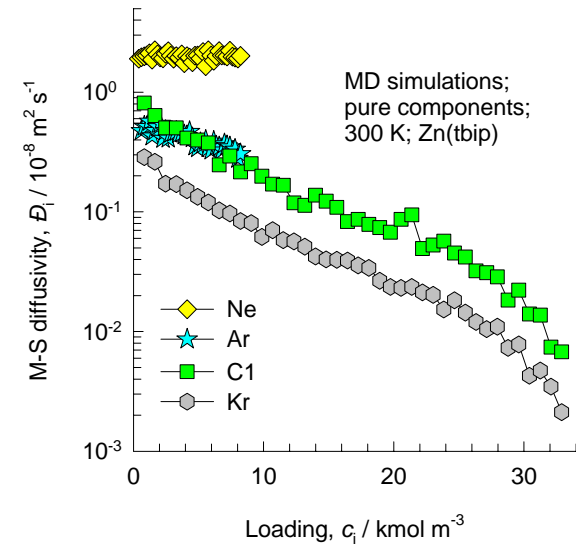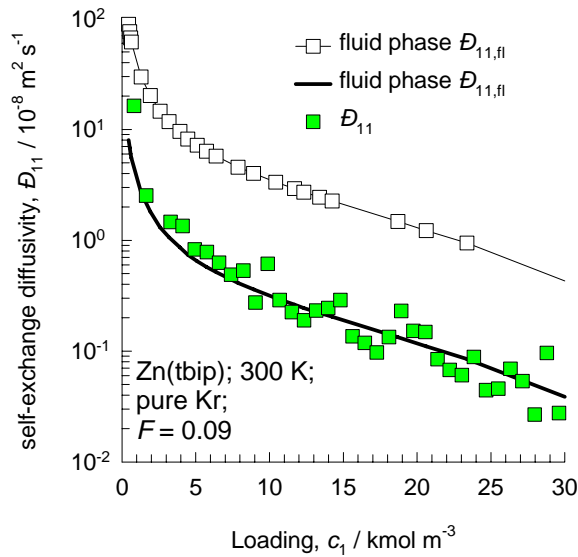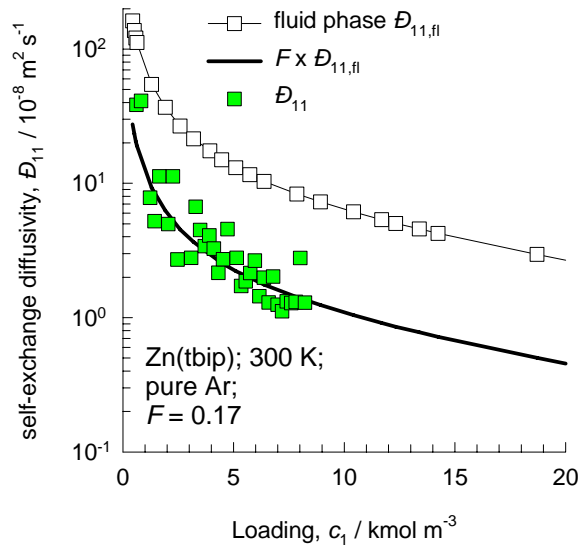
# Data for Zn(tbip) for mixture diffusion
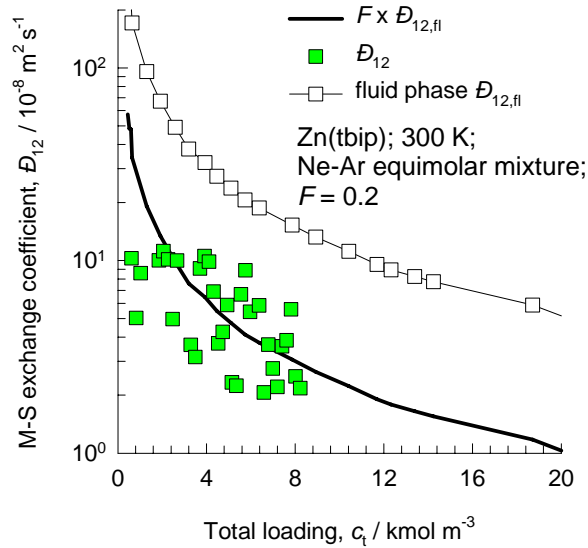
Figure 97



Zn(tbip); 300 K;
Ne-Ar equimolar mixture;
$F$ = 0.2

- $F \times Đ_{12,fl}$
- $Đ_{12}$
- fluid phase $Đ_{12,fl}$

## Test of Darken and Vignes interpolation formulae for Zn(tbip)



Zn(tbip); 300 K;
Ne(1) -Ar (2)
equimolar mix

- Darken
- $Đ_{12}$
- $Đ_{11}$
- $Đ_{22}$
- Vignes

# Self- diffusivities of binary mixture in Zn(tbip)

Unary diffusion data

$$\frac{1}{D_{1,self}} = \frac{1}{Đ_1} + \frac{x_1}{Đ_{11}} + \frac{x_2}{Đ_{12}}$$

$$\frac{1}{D_{2,self}} = \frac{1}{Đ_2} + \frac{x_2}{Đ_{22}} + \frac{x_1}{Đ_{12}}$$

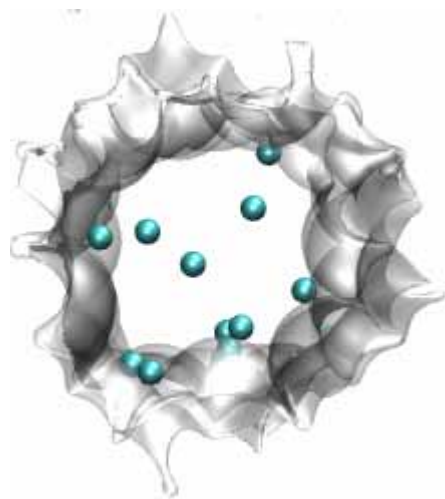Vignes interpolation
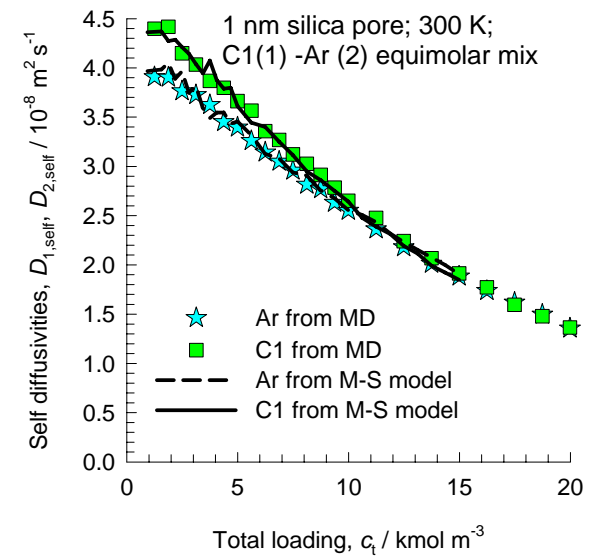
Predictions ( lines) are compared with MD (symbols)



Zn(tbip); 300 K;
Ne(1) -Ar (2) equimolar mix

- Ne from MD
- Ar from MD
- Ar predicted by M-S model
- Ne predicted by M-S model

Figure 98

# MIL – 53, with pore landscape
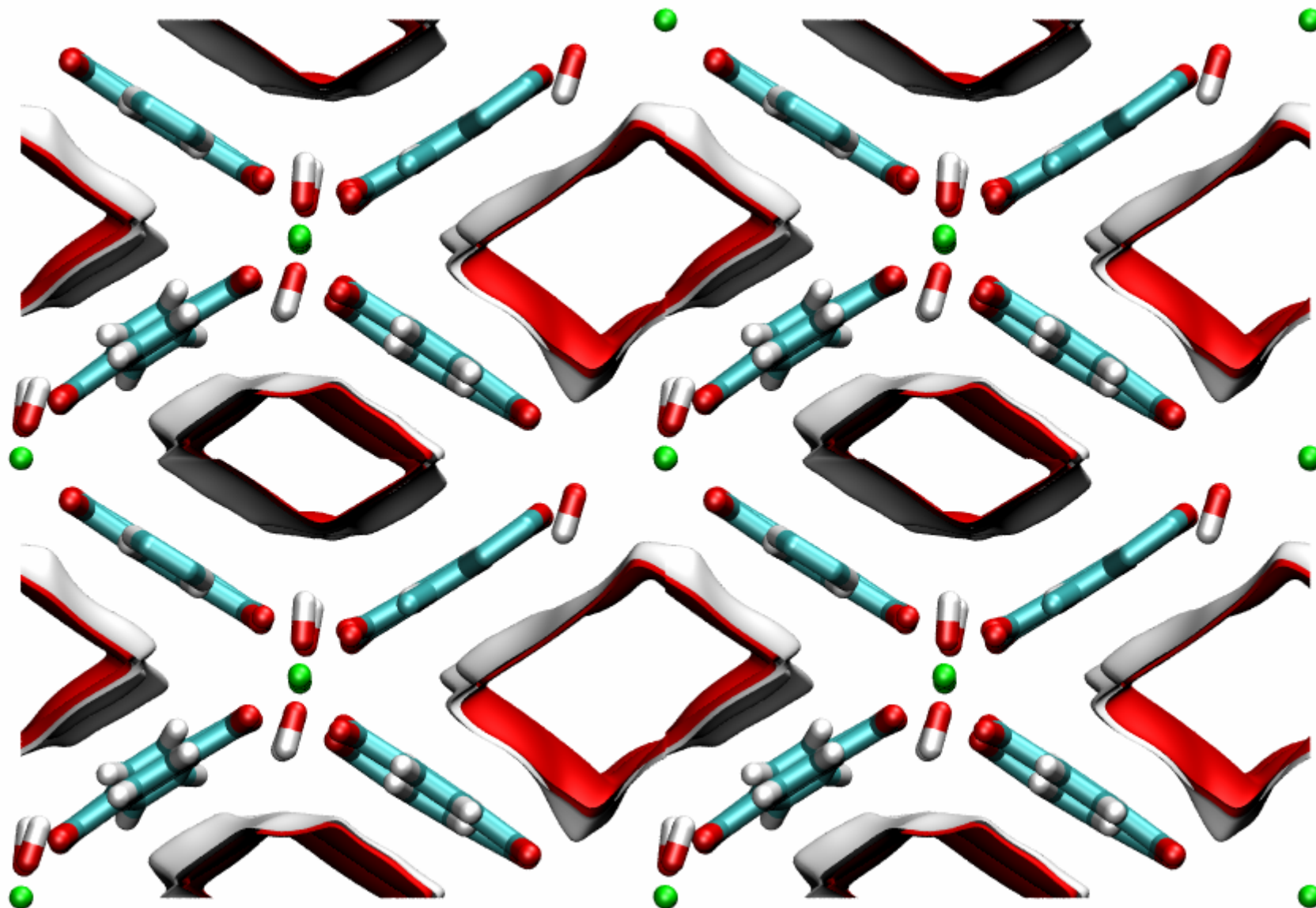
Figure 99

# MIL – 53 (Fe) with pore landscape
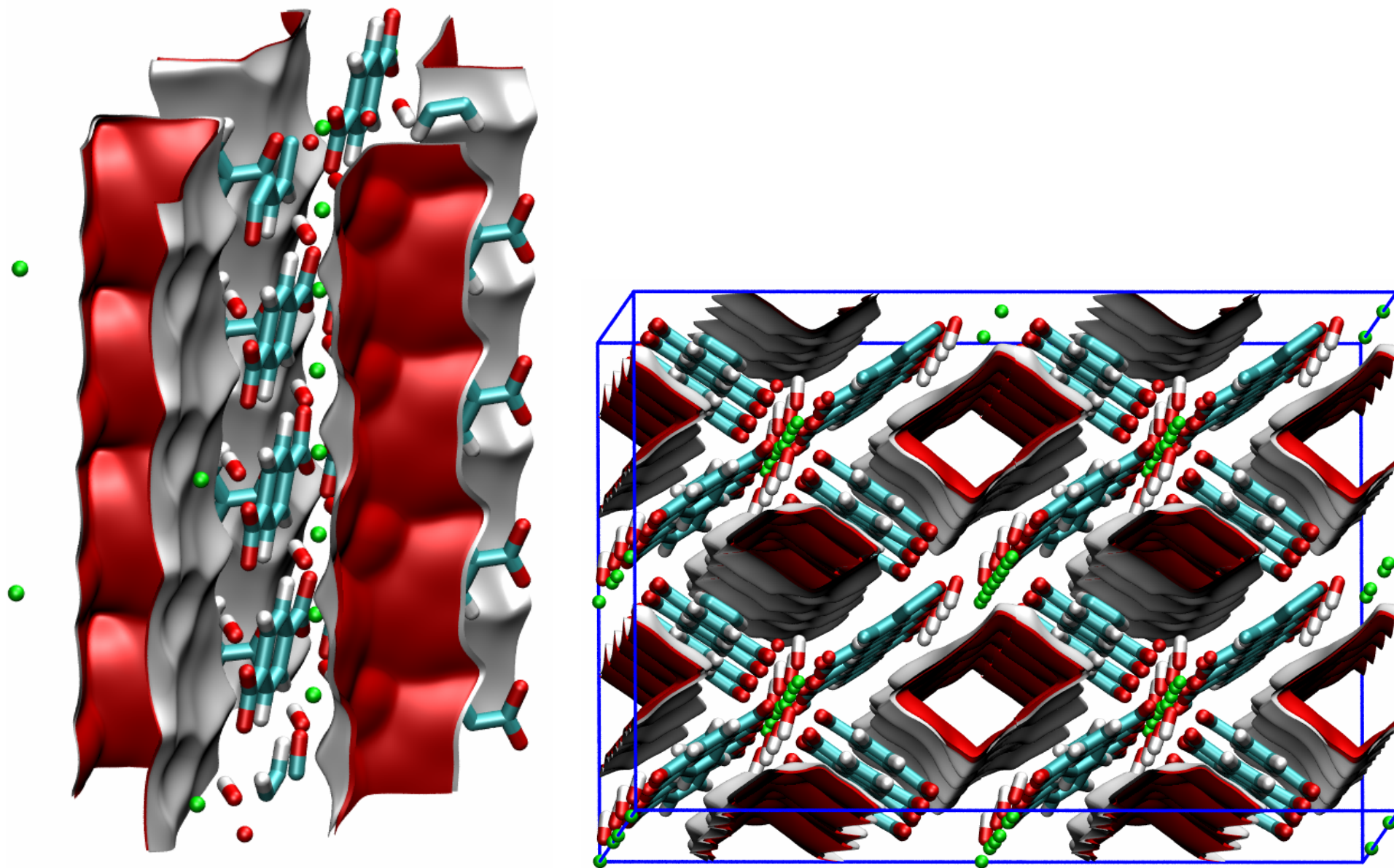
Figure 100
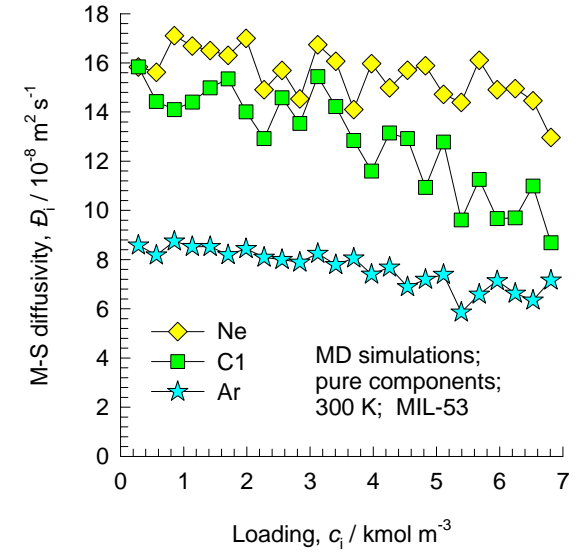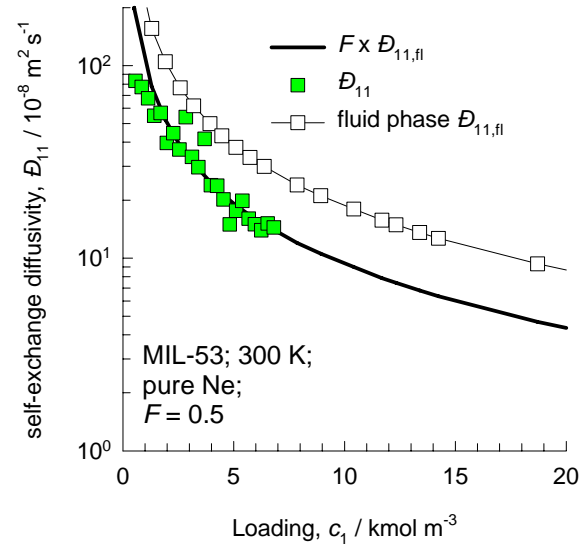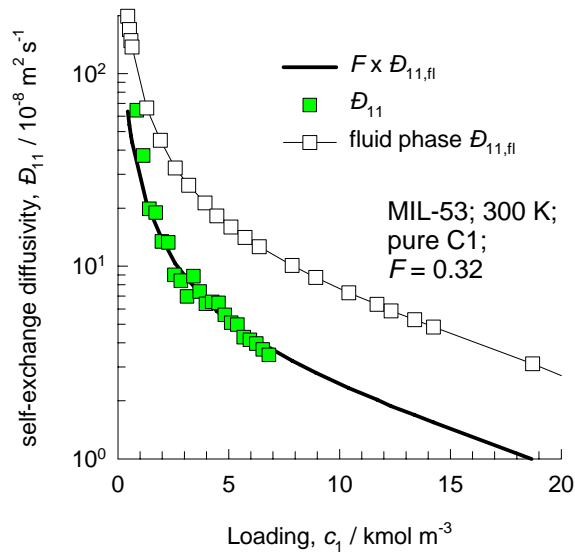
Data for MIL-53 (Fe) for pure components

# Figure 101

# Data for MIL-53 (Fe) for binary mixtures
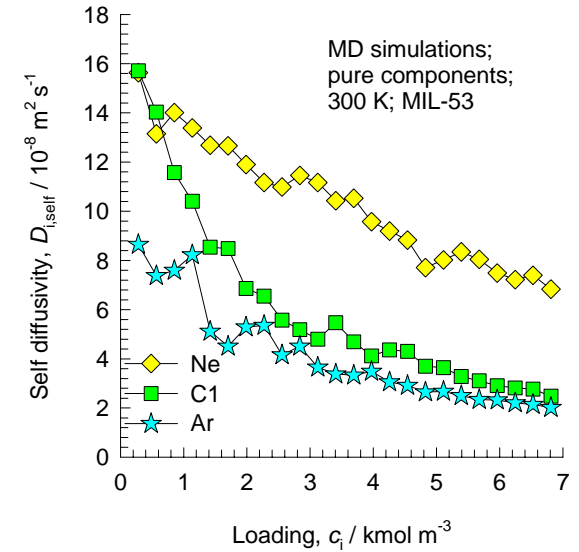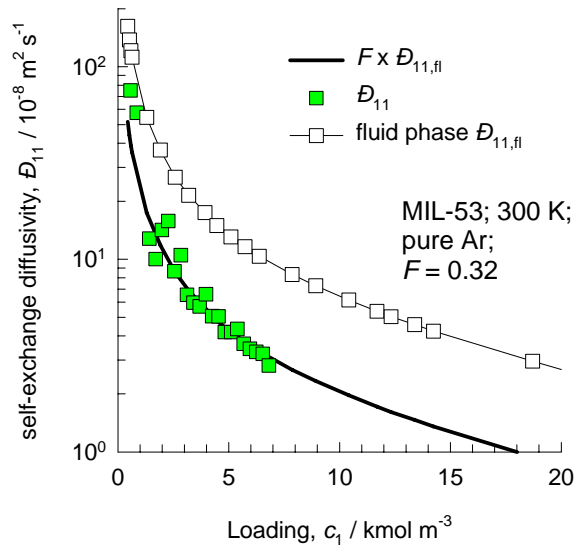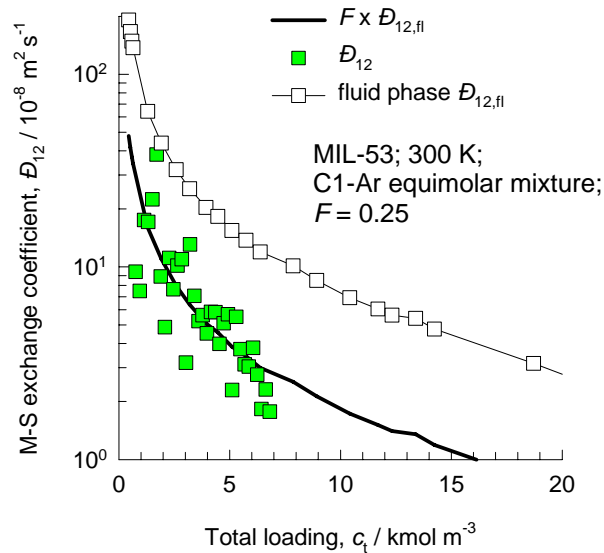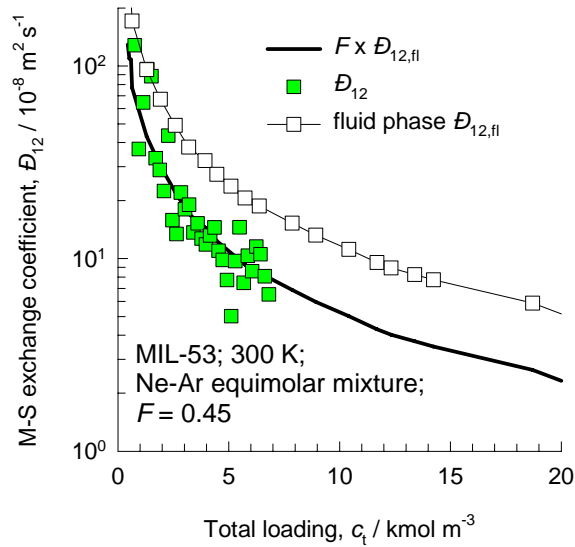
## Self- diffusivities of binary mixture in MIL-53 (Fe)

Unary diffusion data

$$\frac{1}{D_{1,self}} = \frac{1}{\text{Đ}_1} + \frac{x_1}{\text{Đ}_{11}} + \frac{x_2}{\text{Đ}_{12}}$$

$$\frac{1}{D_{2,self}} = \frac{1}{\text{Đ}_2} + \frac{x_2}{\text{Đ}_{22}} + \frac{x_1}{\text{Đ}_{12}}$$

Vignes interpolation

Predictions ( lines) are compared with MD (symbols)

## Test of Darken and Vignes interpolation formulae for MIL-53 (Fe)
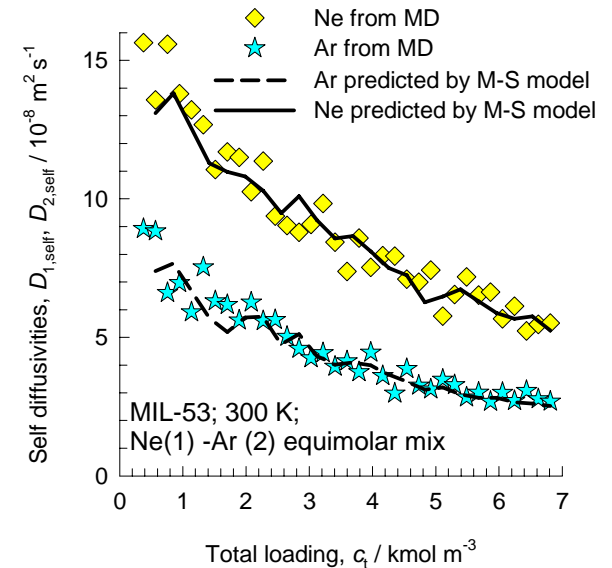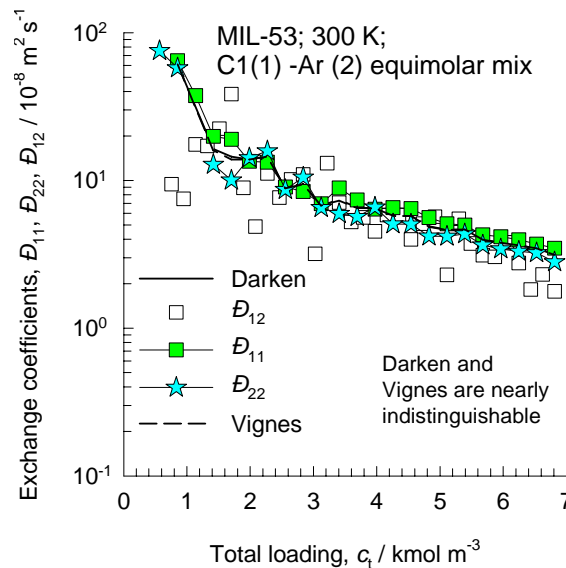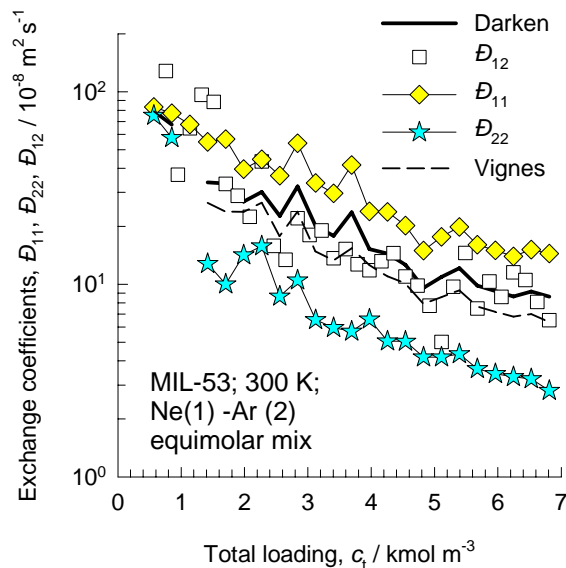
Figure 102
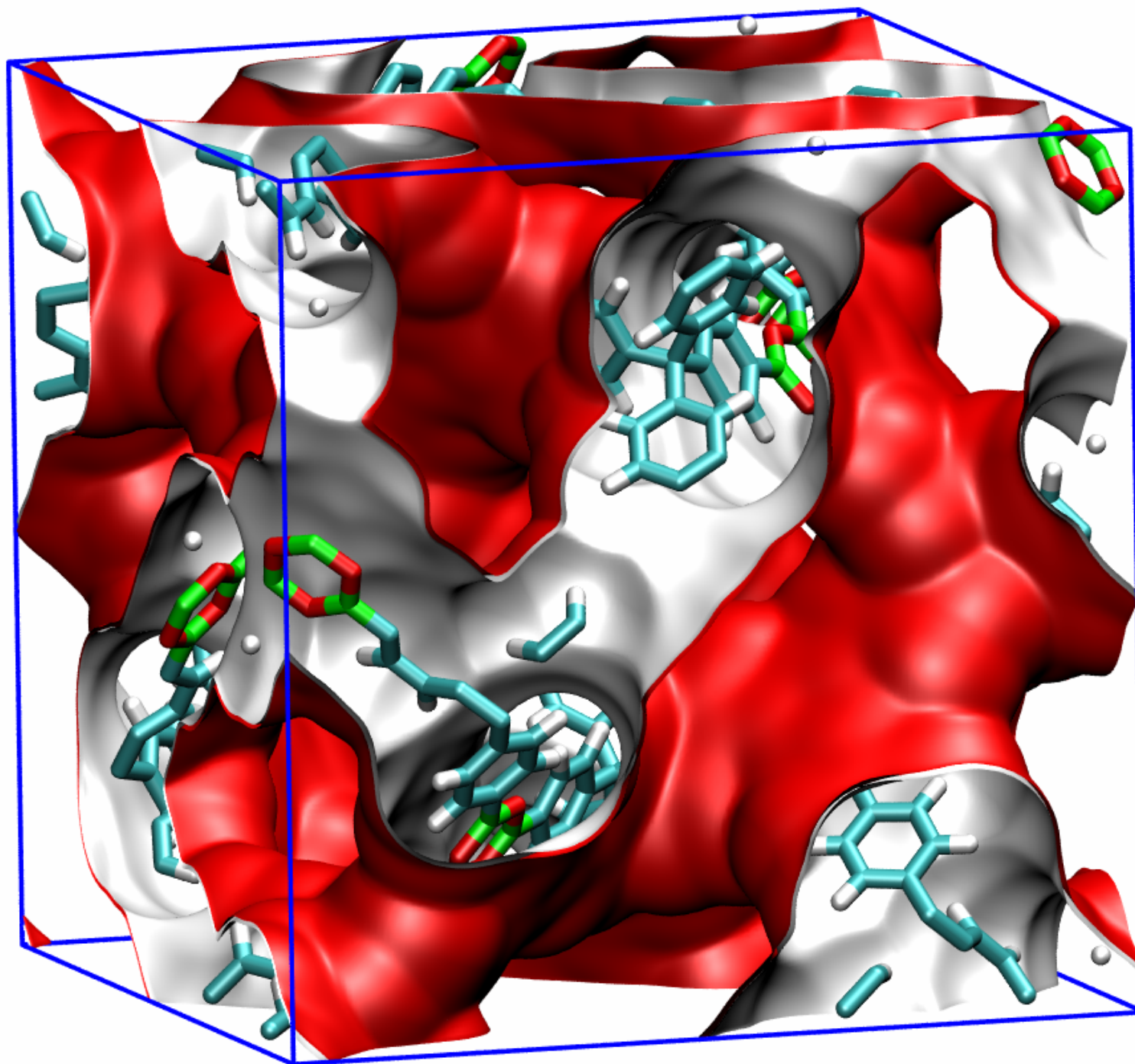
Unit cell
for COF-102

Figure 103
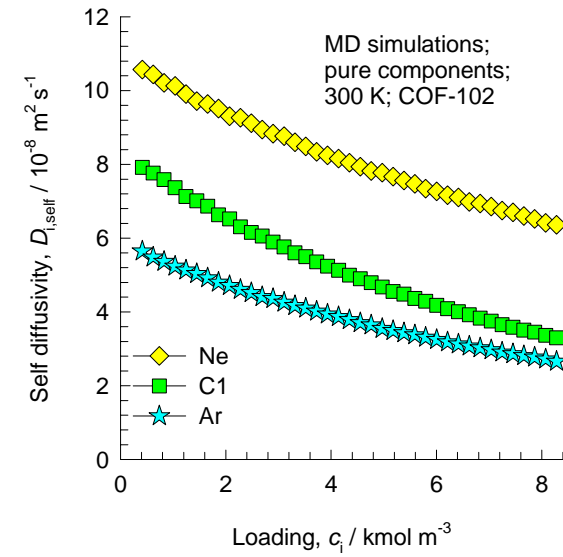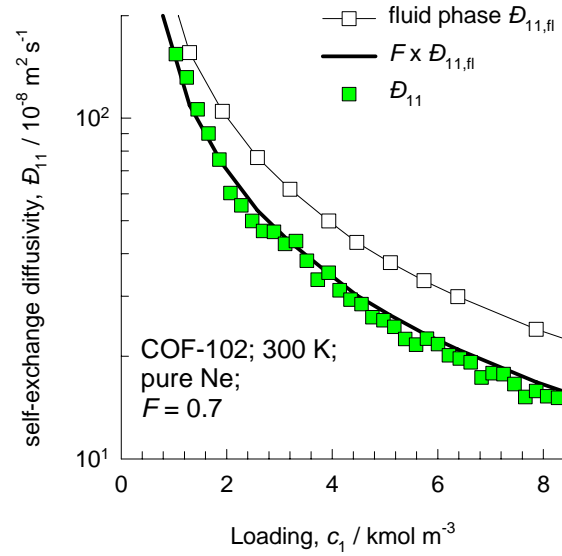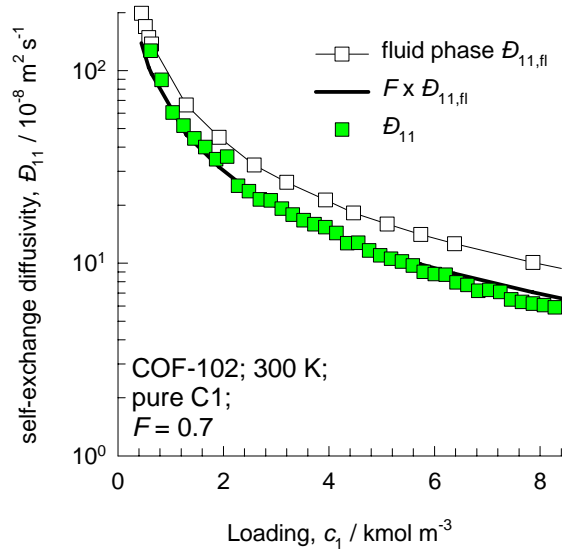
Data for COF-102 for unary diffusion
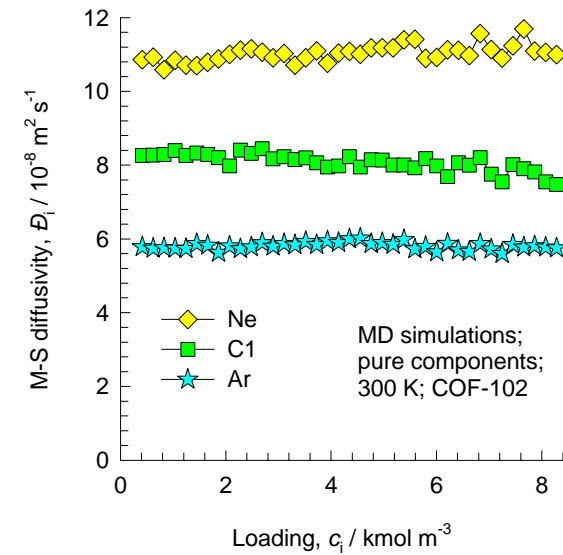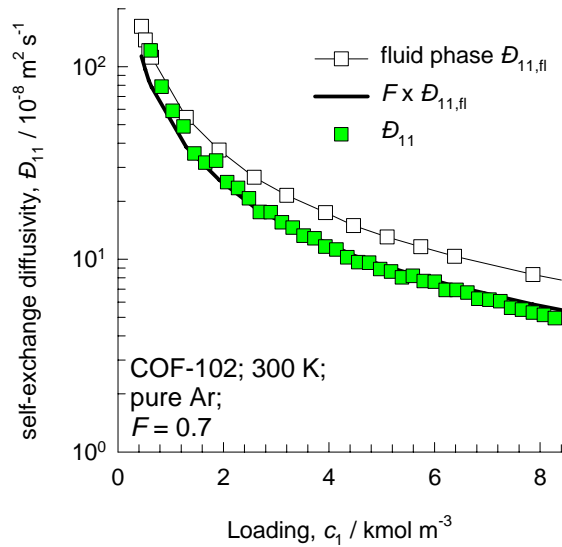
Figure 104

# Data for COF-102 for mixture diffusion
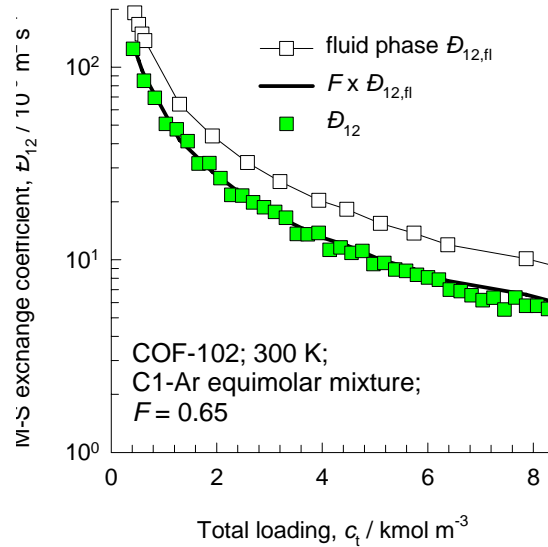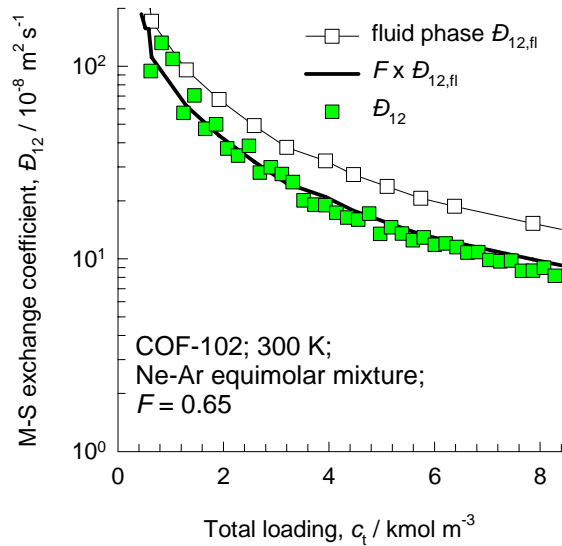


# Test of Darken and Vignes interpolation formulae for COF-102

Figure 105

Prediction of $D_{i,self}$ and $\Delta_{ij}$ in binary mixtures in COF-102 using Vignes interpolation and M-S model
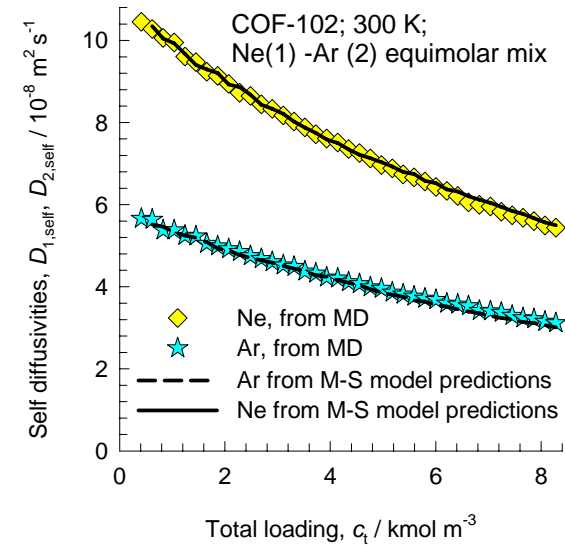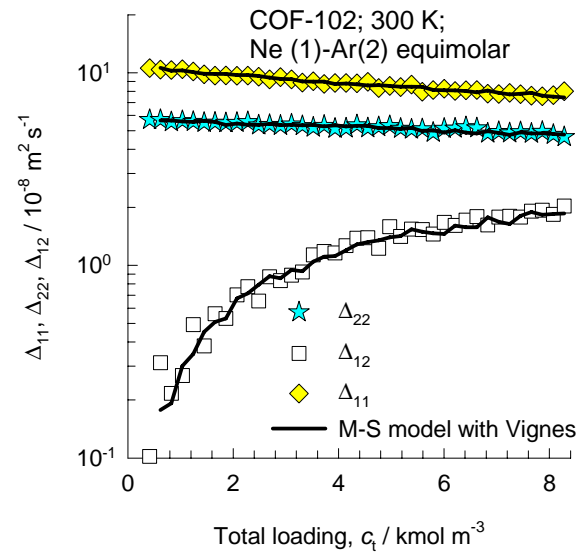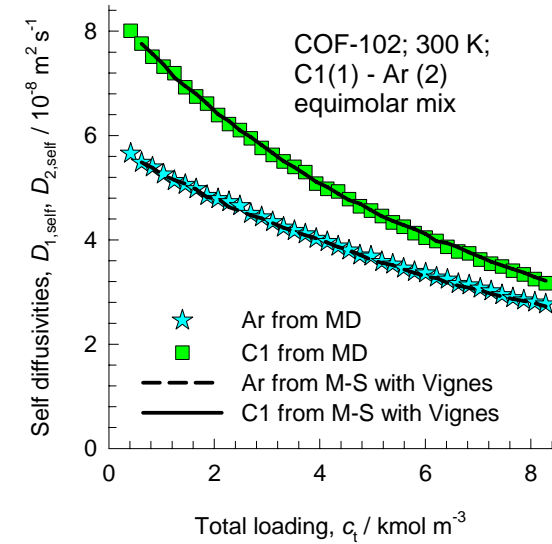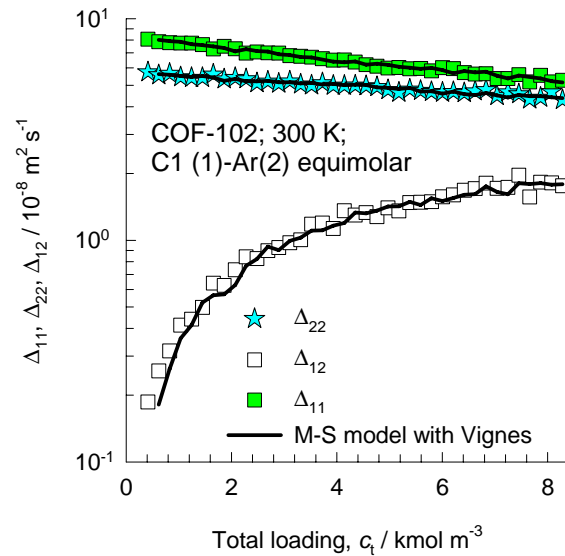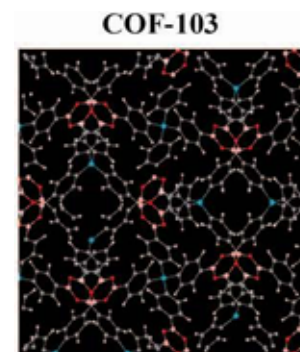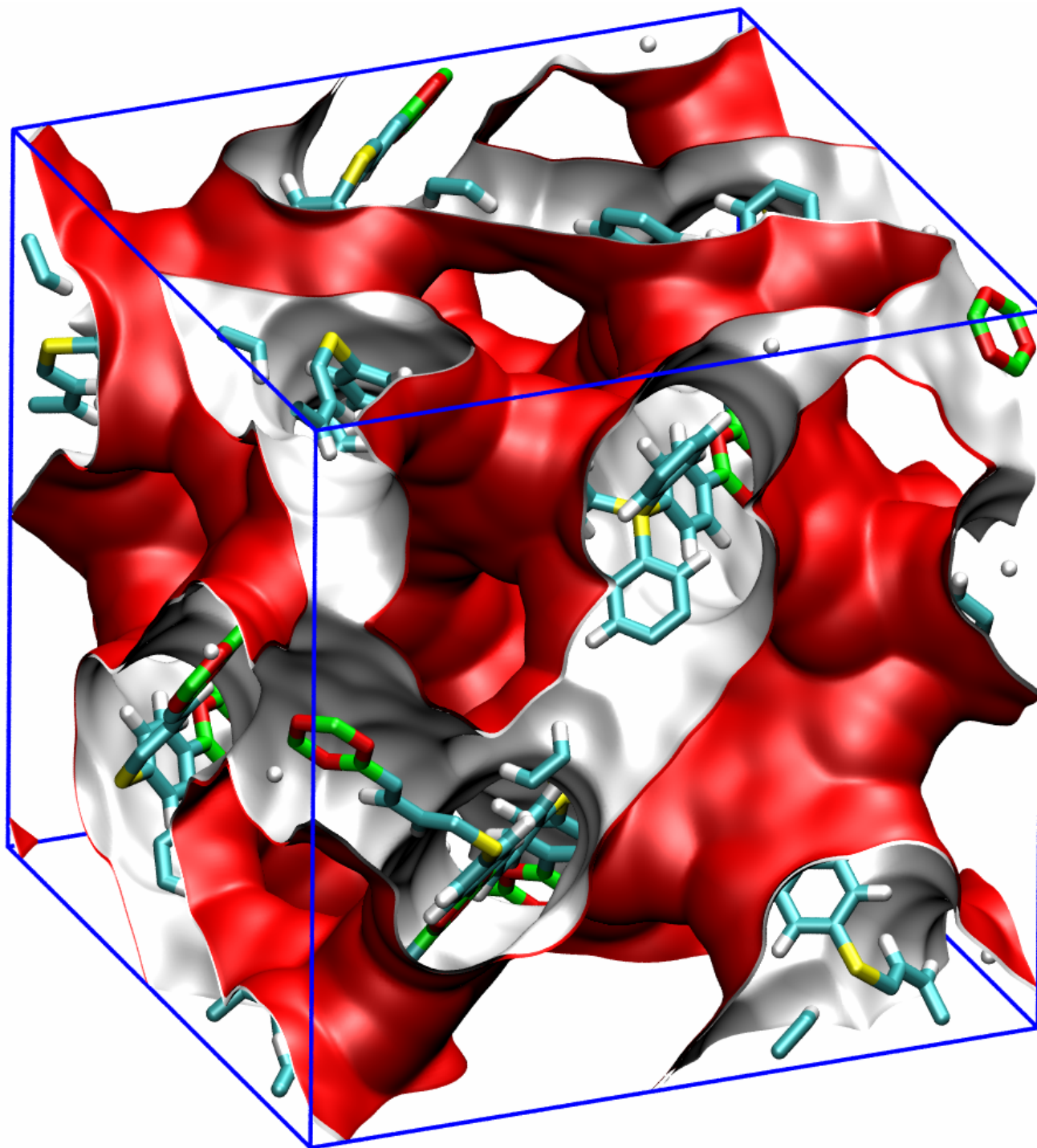
Figure 106

COF-103

Unit cell
for COF-103

Figure 107
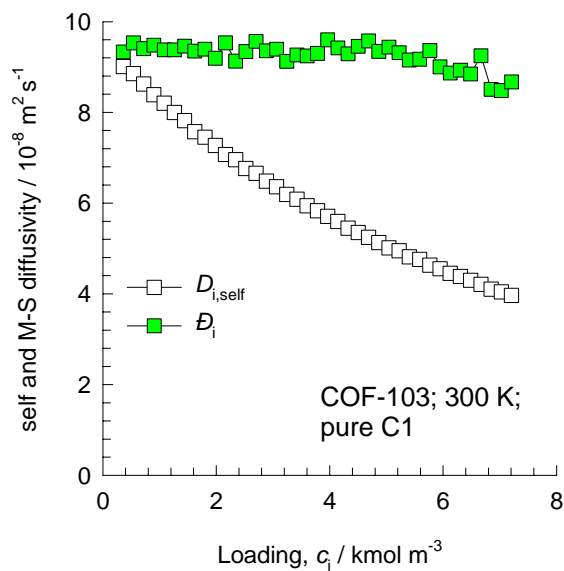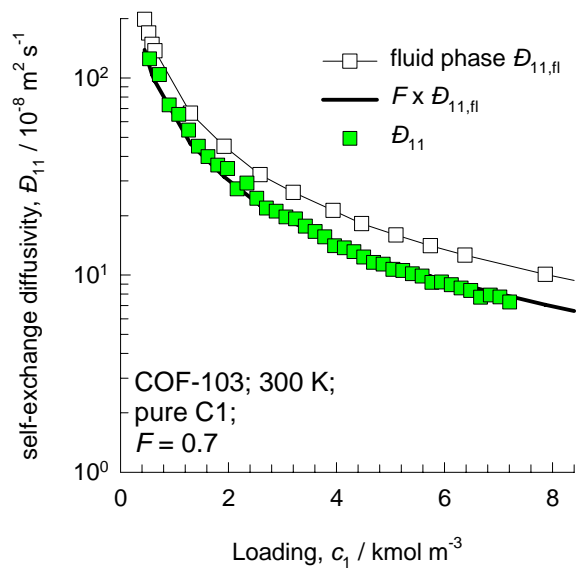
Data for COF-103
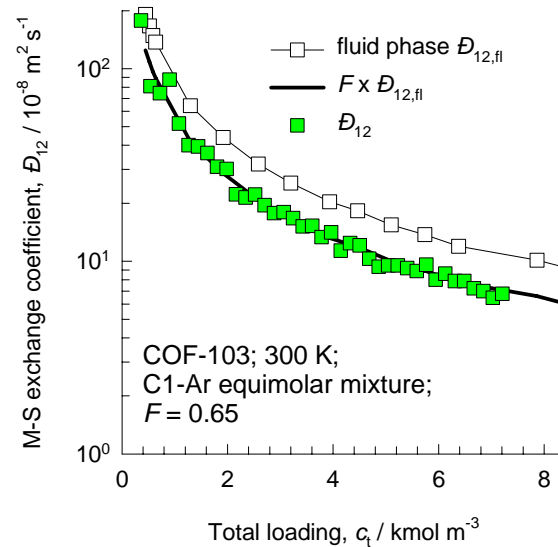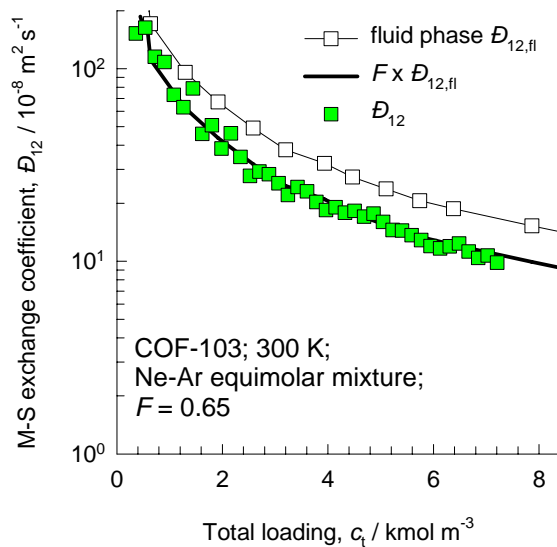
Figure 108
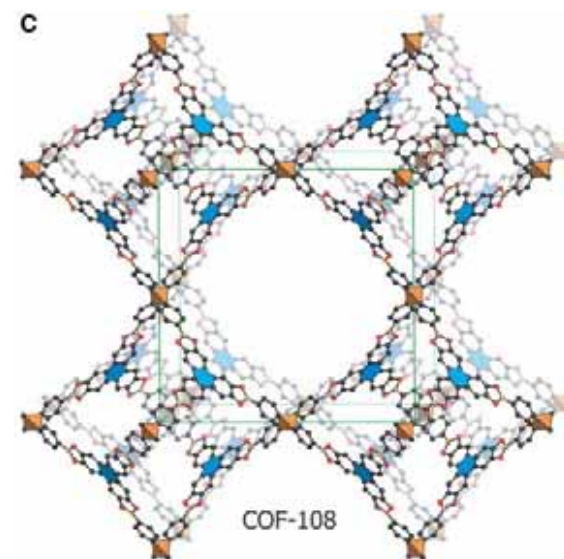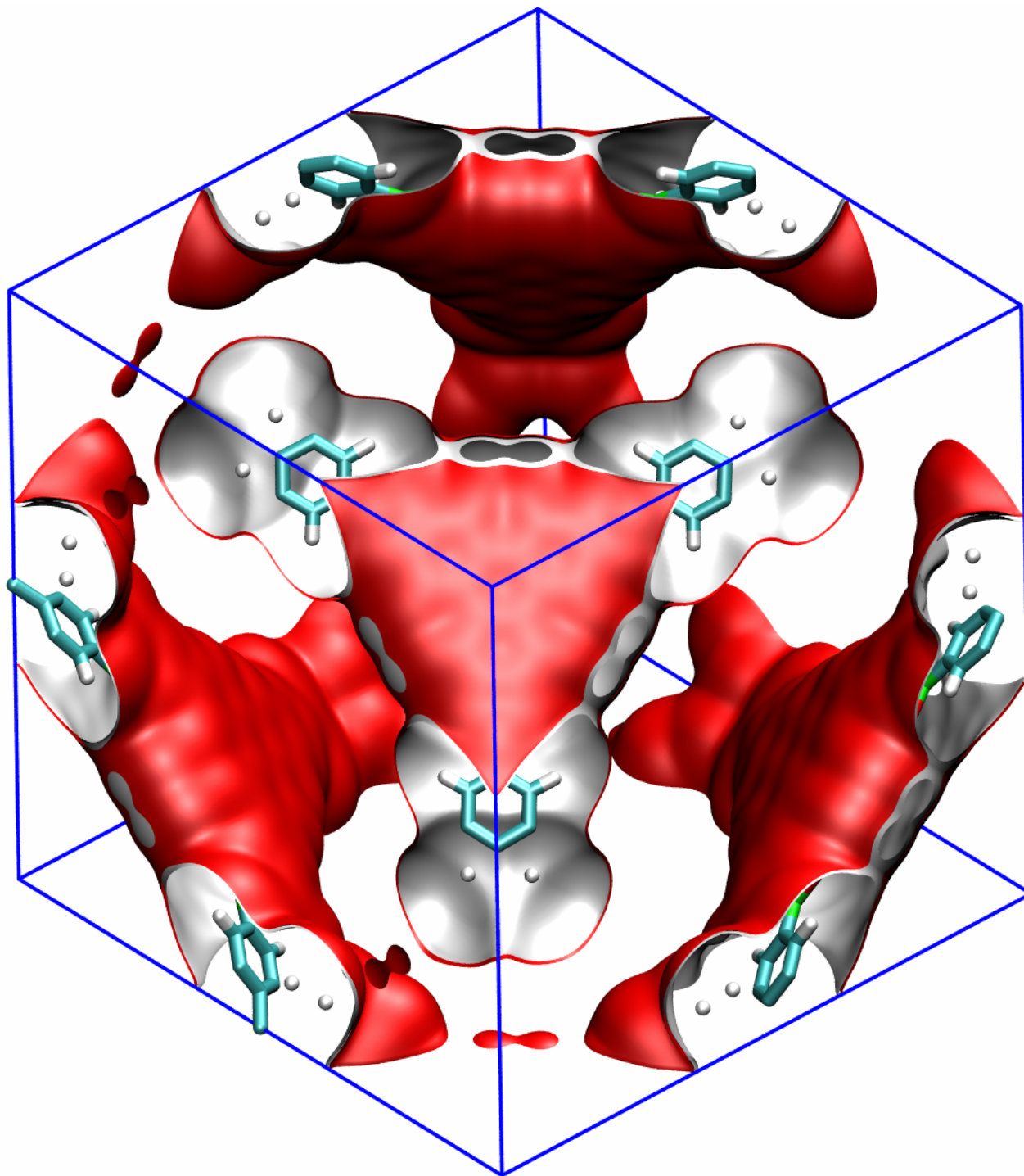
Unit cell
for COF-108

Figure 109
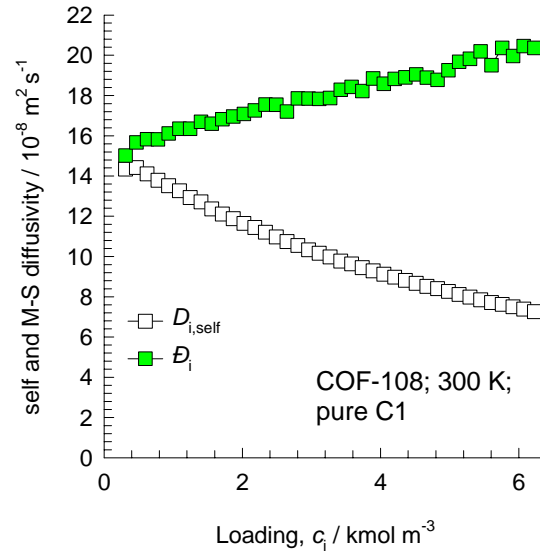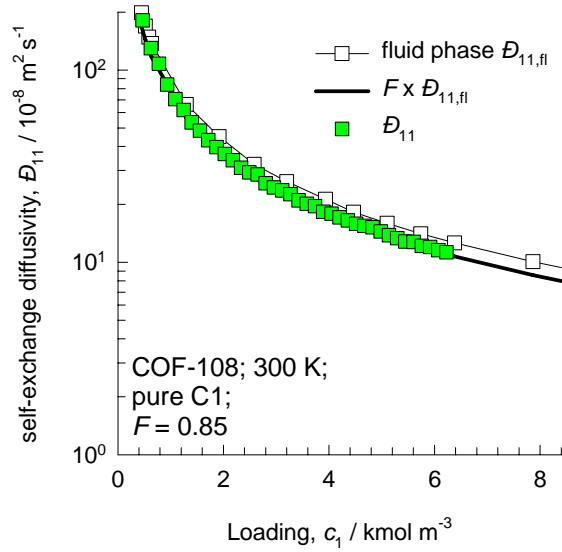
Data for COF-108
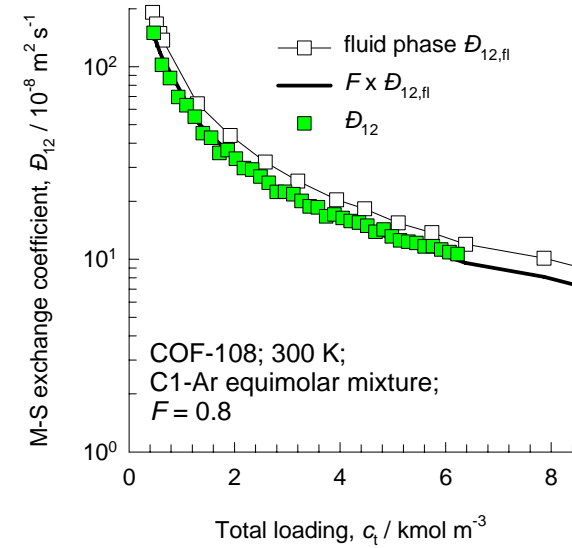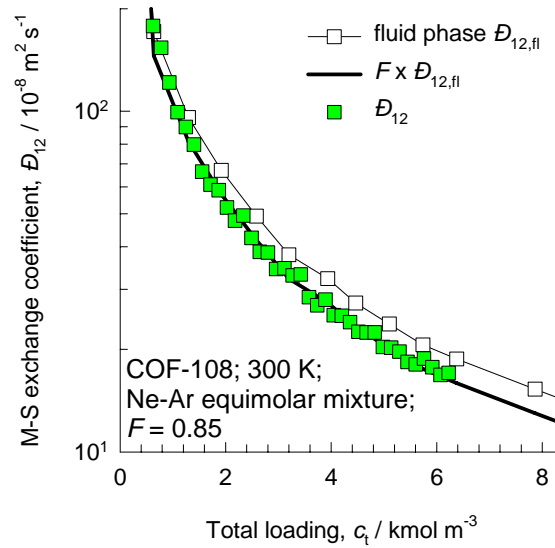
**0.6 nm pore**
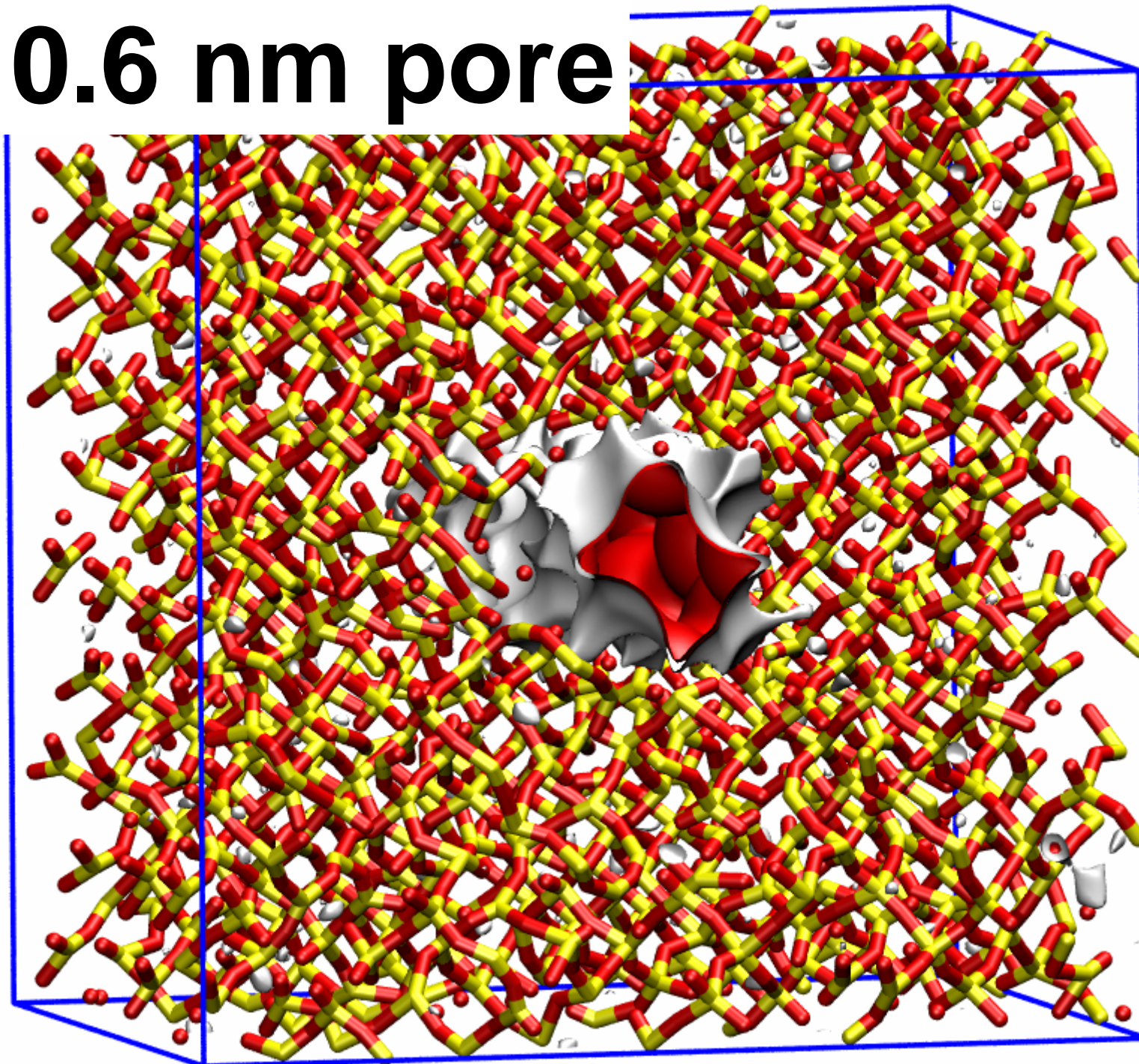
Figure 110

# 0.6 nm pore, 300 K

Figure 111
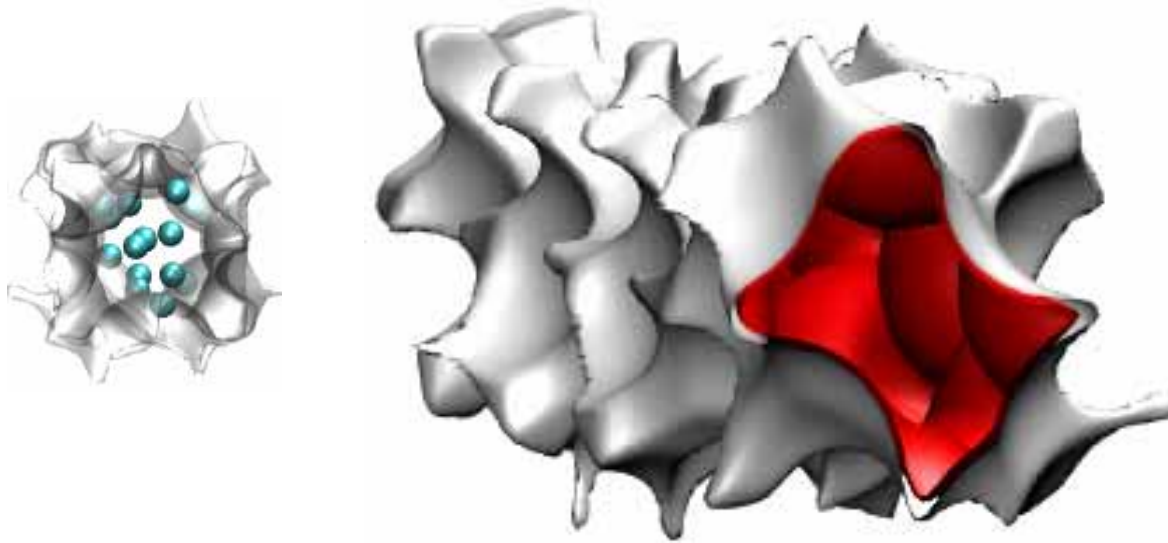


Data for unary diffusion in 0.6 nm silica pore
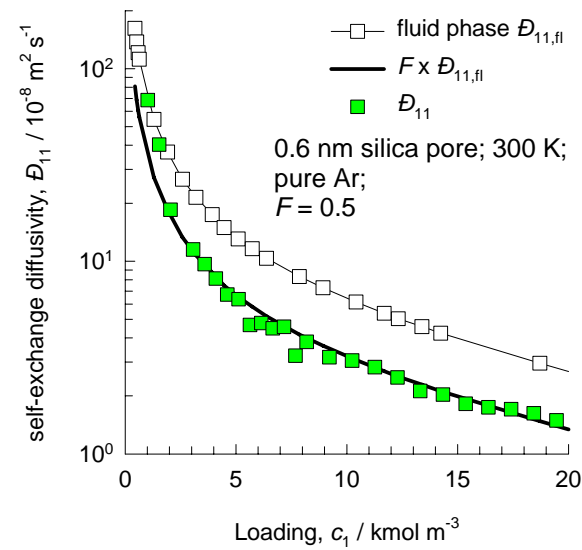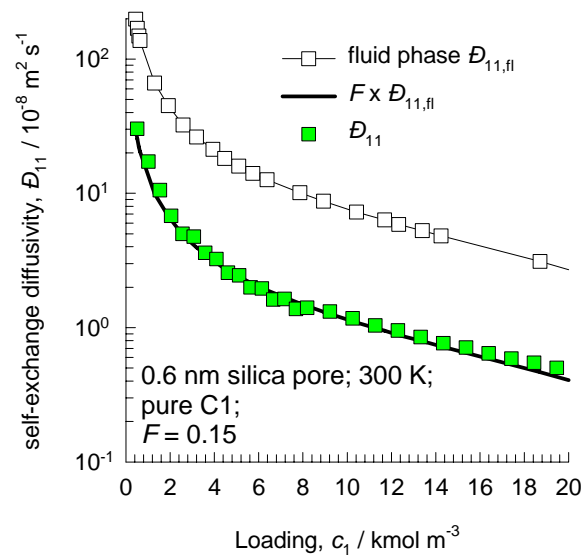
# Binary mixture data for 0.6 nm pore, 300 K

Figure 112
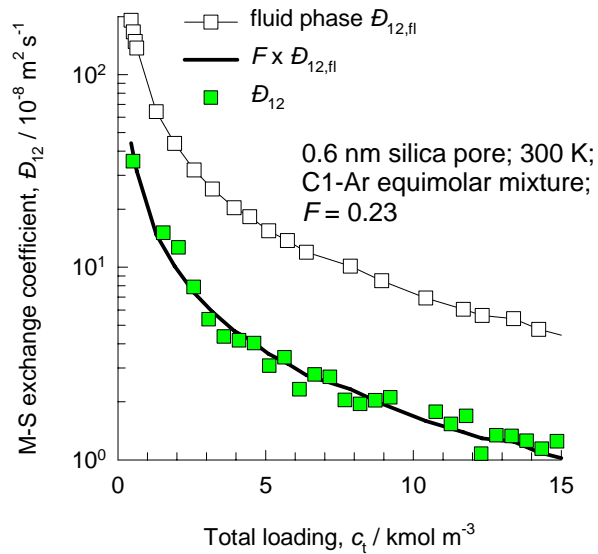


M-S exchange coefficient, $Ð_{12}$ / $10^{-8}$ m$^2$ s$^{-1}$

Total loading, $c_t$ / kmol m$^{-3}$

- □ fluid phase $Ð_{12,fl}$
- — $F \times Ð_{12,fl}$
- ■ $Ð_{12}$

0.6 nm silica pore; 300 K;
C1-Ar equimolar mixture;
$F = 0.23$
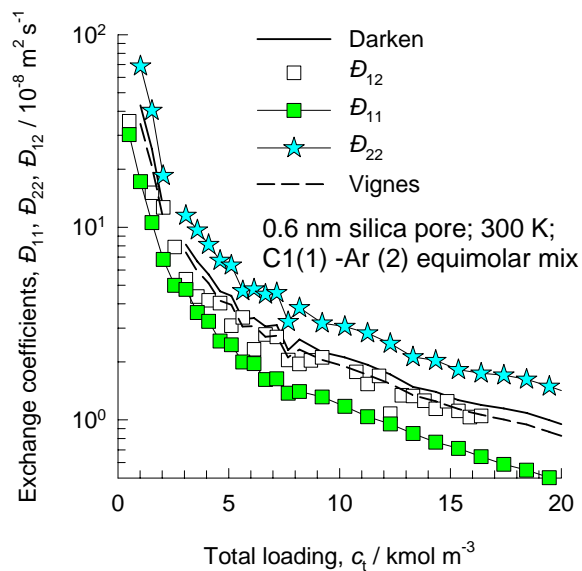
## Self- diffusivities of binary mixture in 0.6 nm pore

Unary diffusion data

$$\frac{1}{D_{1,self}} = \frac{1}{Ð_1} + \frac{x_1}{Ð_{11}} + \frac{x_2}{Ð_{12}}$$

$$\frac{1}{D_{2,self}} = \frac{1}{Ð_2} + \frac{x_2}{Ð_{22}} + \frac{x_1}{Ð_{12}}$$
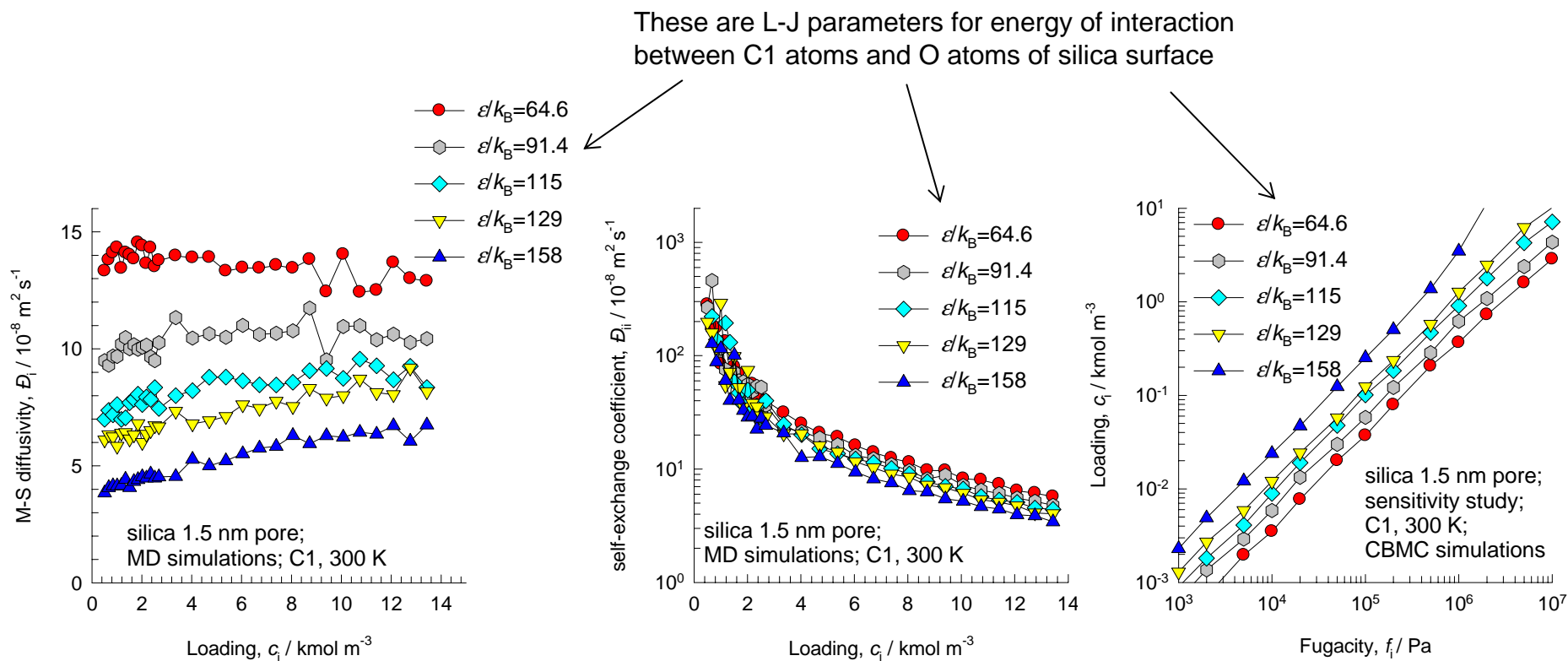
Vignes interpolation

Predictions ( lines) are compared with MD (symbols)

## Test of Darken and Vignes interpolation formulae



Exchange coefficients, $Ð_{11}$, $Ð_{22}$, $Ð_{12}$ / $10^{-8}$ m$^2$ s$^{-1}$

Total loading, $c_t$ / kmol m$^{-3}$

- — Darken
- □ $Ð_{12}$
- ■ $Ð_{11}$
- ★ $Ð_{22}$
- - - Vignes

0.6 nm silica pore; 300 K;
C1(1) -Ar (2) equimolar mix



Self diffusivities, $D_{1,self}$, $D_{2,self}$ / $10^{-8}$ m$^2$ s$^{-1}$

Total loading, $c_t$ / kmol m$^{-3}$

- ★ Ar from MD
- ■ C1 from MD
- - - Ar from M-S model
- — C1 from M-S model

0.6 nm silica pore; 300 K;
C1(1) -Ar (2) equimolar mix

0.75 nm pore

Figure 113

Figure 114

# 0.75 nm pore, 300 K



Data for unary diffusion in 0.75 nm silica pore



Left plot legend:
- fluid phase $Đ_{11,fl}$
- $F \times Đ_{11,fl}$
- $Đ_{11}$

0.75 nm silica pore; 300 K;
pure C1;
$F = 0.32$

y-axis: self-exchange diffusivity, $Đ_{11}$ / $10^{-8}$ m$^2$ s$^{-1}$
x-axis: Loading, $c_1$ / kmol m$^{-3}$

Right plot legend:
- fluid phase $Đ_{11,fl}$
- $F \times Đ_{11,fl}$
- $Đ_{11}$

0.75 nm silica pore; 300 K;
pure Ar;
$F = 0.7$

y-axis: self-exchange diffusivity, $Đ_{11}$ / $10^{-8}$ m$^2$ s$^{-1}$
x-axis: Loading, $c_1$ / kmol m$^{-3}$
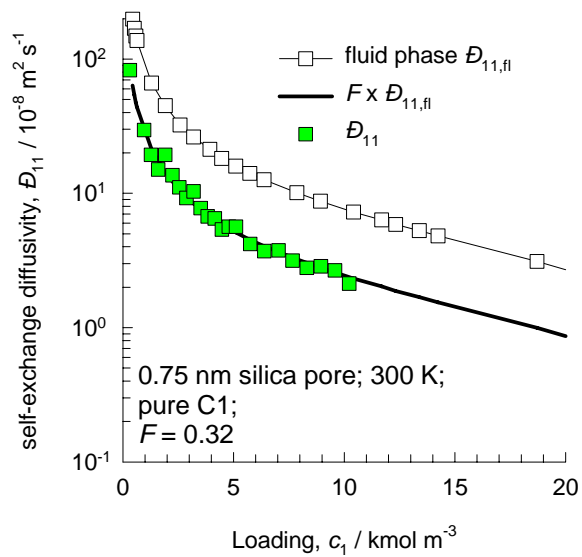
# Binary mixture data for 0.75 nm pore, 300 K

Figure 115
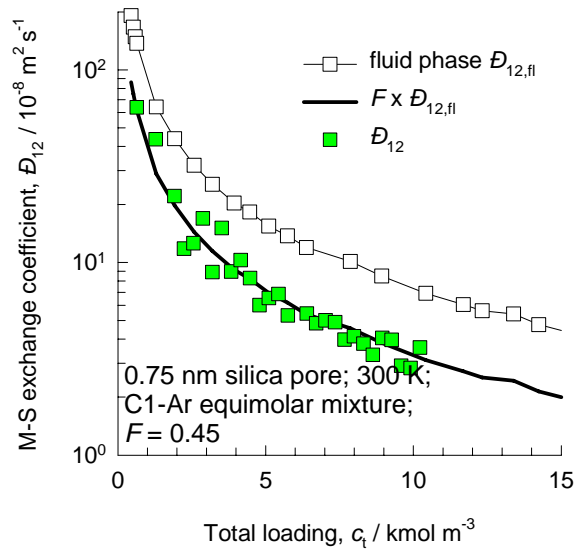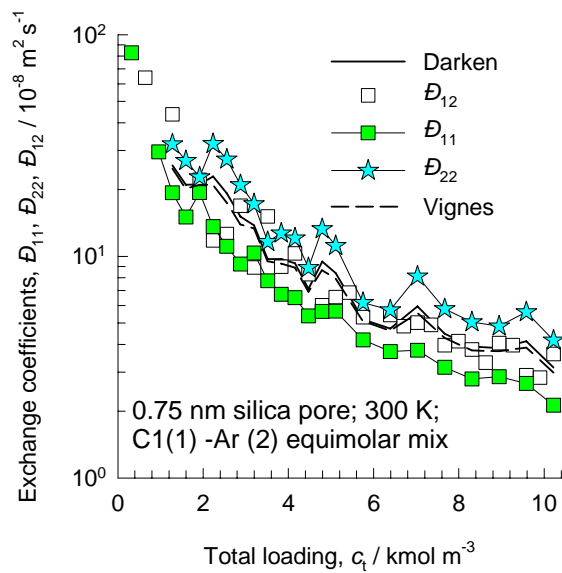


Self- diffusivities of binary mixture in 0.75 nm pore

Unary diffusion data

$$\frac{1}{D_{1,self}} = \frac{1}{\bar{D}_1} + \frac{x_1}{\bar{D}_{11}} + \frac{x_2}{\bar{D}_{12}}$$

$$\frac{1}{D_{2,self}} = \frac{1}{\bar{D}_2} + \frac{x_2}{\bar{D}_{22}} + \frac{x_1}{\bar{D}_{12}}$$

Vignes interpolation

Predictions ( lines) are compared with MD (symbols)

0.75 nm silica pore; 300 K; C1-Ar equimolar mixture; $F = 0.45$

Test of Darken and Vignes interpolation formulae

0.75 nm silica pore; 300 K; C1(1) -Ar (2) equimolar mix

0.75 nm silica pore; 300 K; C1(1) -Ar (2) equimolar mix
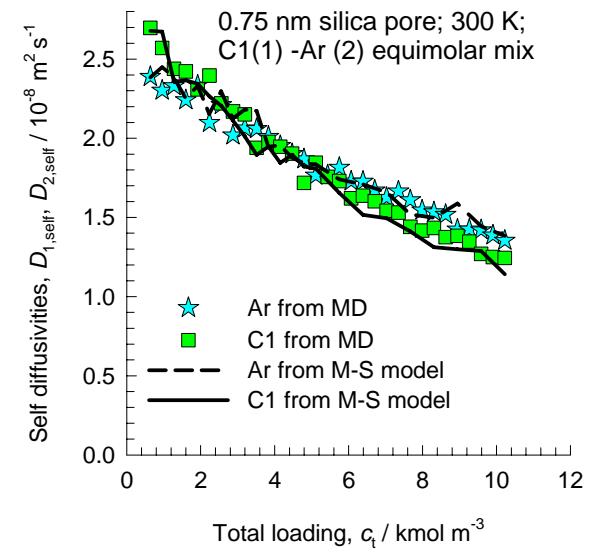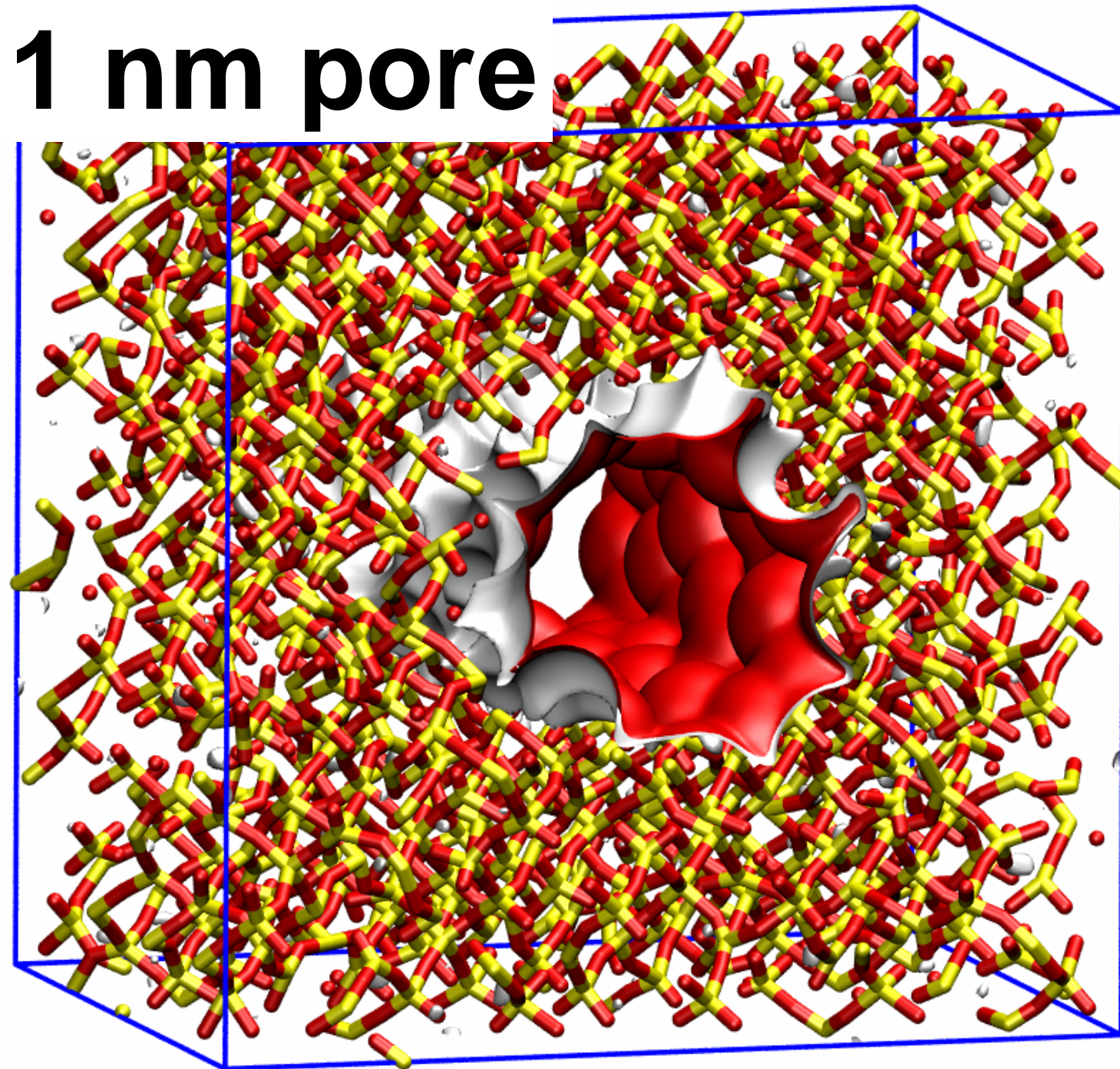
1 nm pore

Figure 116

Figure 117
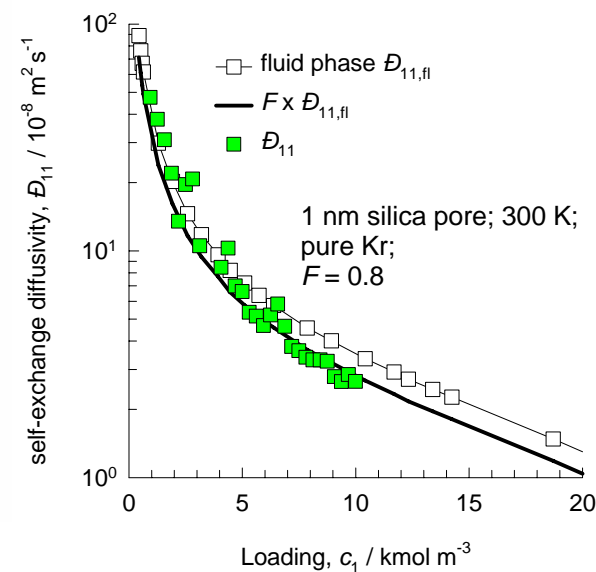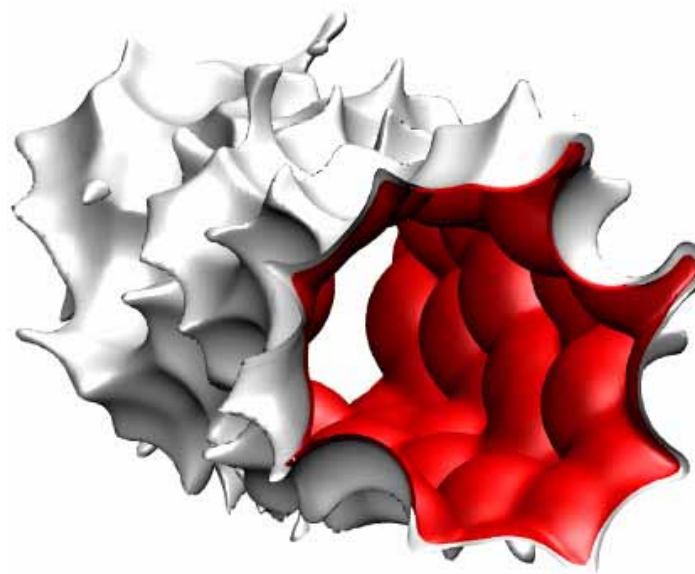
# 1 nm pore, 300 K



## Data for unary diffusion in 1 nm silica pore
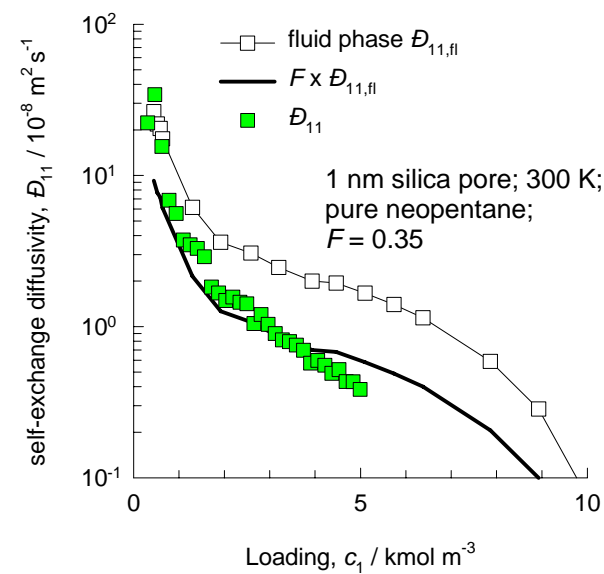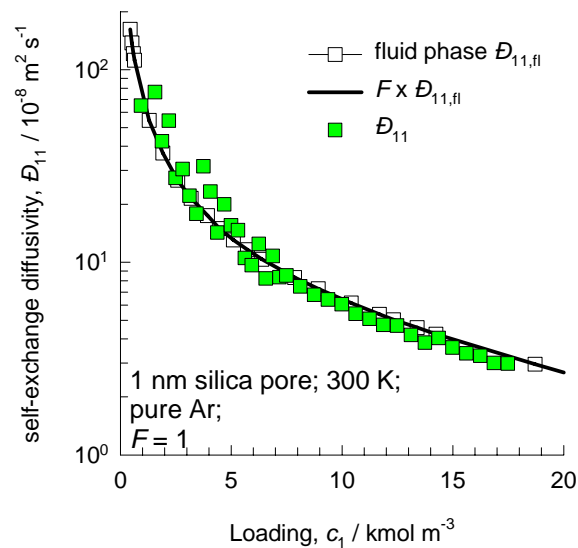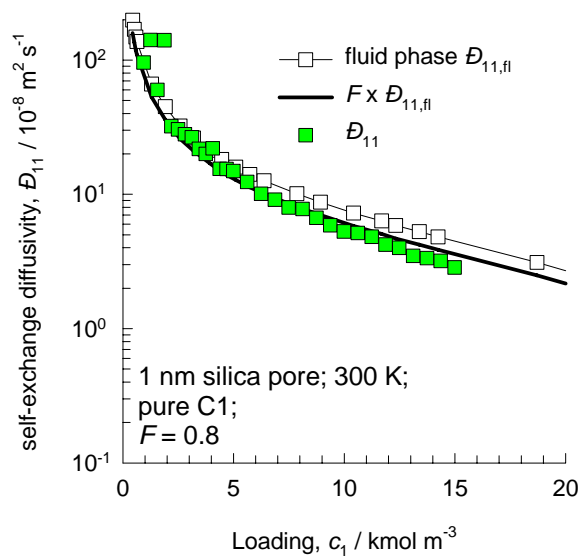
# Binary mixture data for 1 nm pore, 300 K

Figure 118
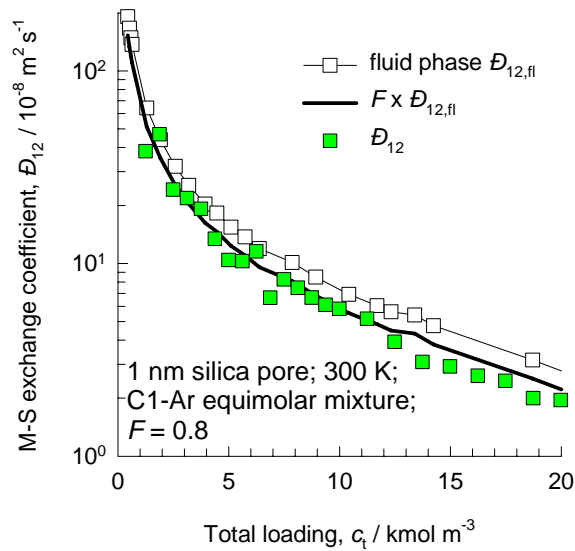


**M-S exchange coefficient chart (top left):**
- fluid phase $Đ_{12,fl}$
- $F \times Đ_{12,fl}$
- $Đ_{12}$

1 nm silica pore; 300 K; C1-Ar equimolar mixture; $F = 0.8$

x-axis: Total loading, $c_t$ / kmol m$^{-3}$
y-axis: M-S exchange coefficient, $Đ_{12}$ / $10^{-8}$ m$^2$ s$^{-1}$
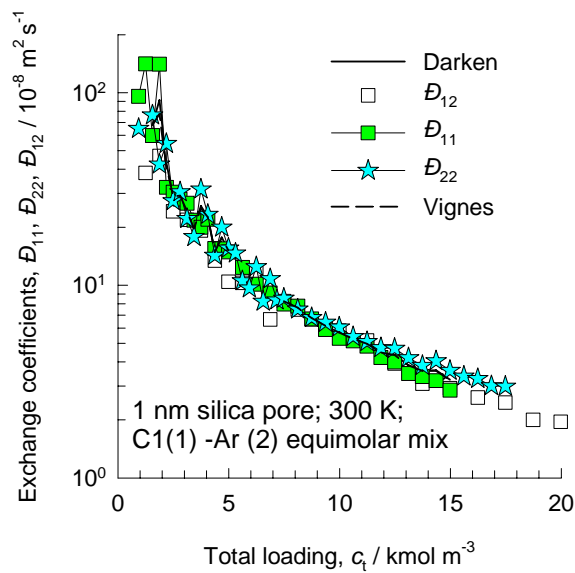
Self- diffusivities of binary mixture in 1 nm pore

Unary diffusion data

$$\frac{1}{D_{1,self}} = \frac{1}{Đ_1} + \frac{x_1}{Đ_{11}} + \frac{x_2}{Đ_{12}}$$

$$\frac{1}{D_{2,self}} = \frac{1}{Đ_2} + \frac{x_2}{Đ_{22}} + \frac{x_1}{Đ_{12}}$$

Vignes interpolation

Predictions ( lines) are compared with MD (symbols)

## Test of Darken and Vignes interpolation formulae

**Exchange coefficients chart (bottom left):**
- Darken
- $Đ_{12}$
- $Đ_{11}$
- $Đ_{22}$
- Vignes

1 nm silica pore; 300 K; C1(1) -Ar (2) equimolar mix

x-axis: Total loading, $c_t$ / kmol m$^{-3}$
y-axis: Exchange coefficients, $Đ_{11}$, $Đ_{22}$, $Đ_{12}$ / $10^{-8}$ m$^2$ s$^{-1}$

**Self diffusivities chart (bottom right):**
1 nm silica pore; 300 K; C1(1) -Ar (2) equimolar mix
- Ar from MD
- C1 from MD
- Ar from M-S model
- C1 from M-S model

x-axis: Total loading, $c_t$ / kmol m$^{-3}$
y-axis: Self diffusivities, $D_{1,self}$, $D_{2,self}$ / $10^{-8}$ m$^2$ s$^{-1}$

1.5 nm pore

Figure 119

# 1.5 nm pore, 300 K

Figure 120
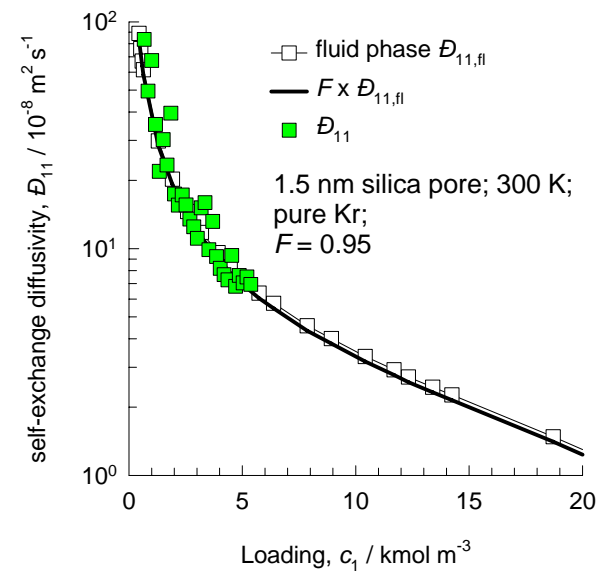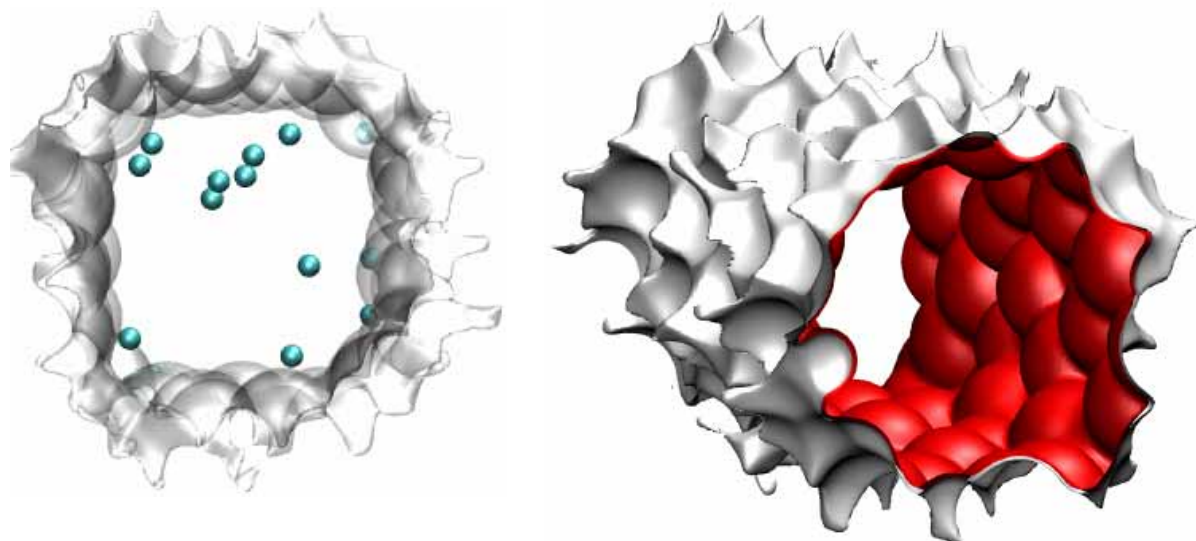


Data for unary diffusion in 1.5 nm silica pore
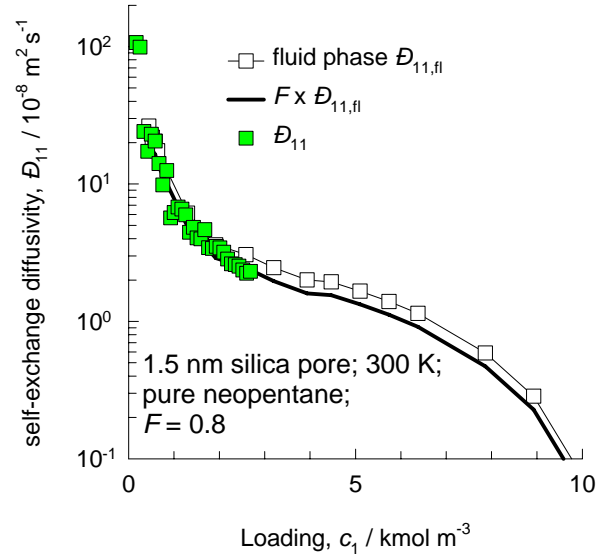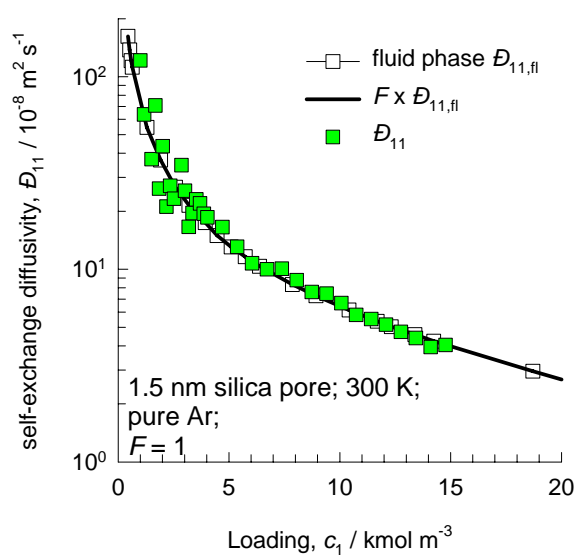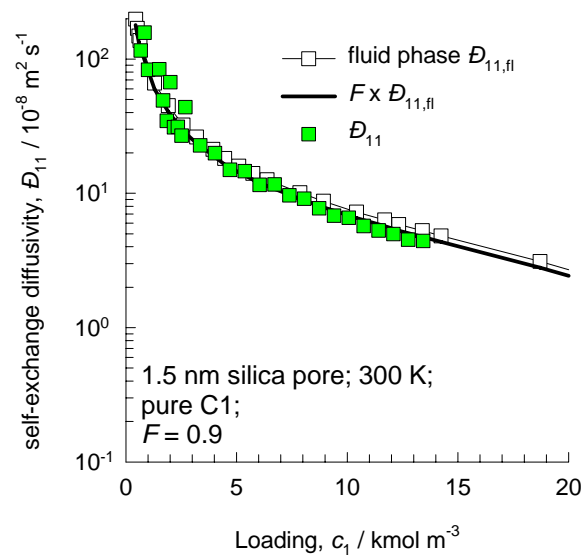
# Binary mixture data for 1.5 nm pore, 300 K

Figure 121
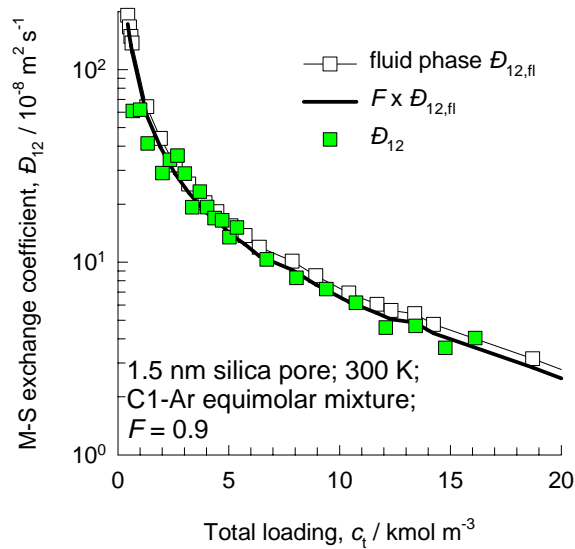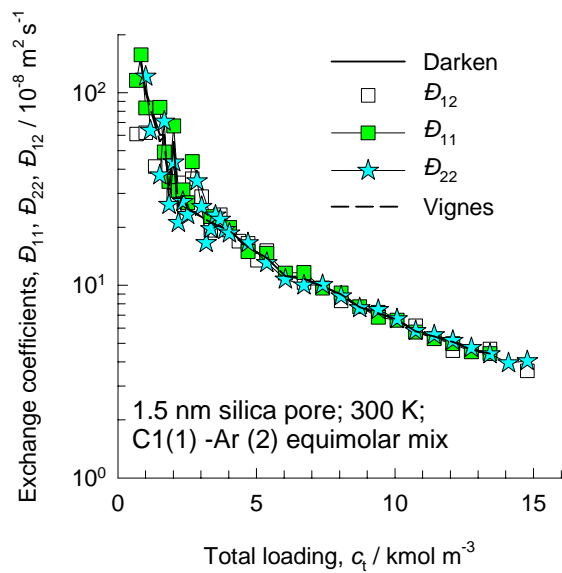
Self- diffusivities of binary mixture in 1.5 nm pore

Unary diffusion data

$$\frac{1}{D_{1,self}} = \frac{1}{\DJ_1} + \frac{x_1}{\DJ_{11}} + \frac{x_2}{\DJ_{12}}$$

$$\frac{1}{D_{2,self}} = \frac{1}{\DJ_2} + \frac{x_2}{\DJ_{22}} + \frac{x_1}{\DJ_{12}}$$

Vignes interpolation

Predictions ( lines) are compared with MD (symbols)

Test of Darken and Vignes interpolation formulae

Figure 122

# 1.5 nm pore, 300 K, sensitivity analysis

Here are the results of the
sensitivity analysis using
the parameters in Table 10
of supplementary material.

These are L-J parameters for energy of interaction
between C1 atoms and O atoms of silica surface

Figure 123

# 1.5 nm pore, 300 K, sensitivity analysis



In each case the self-exchange coefficient in the pore is compared with the corresponding fluid phase diffusivity using the force field parameters in Table 11 of supplementary material. These results show that the factor $F_i = 0.9$, irrespective of the Lennard-Jones energy parameter.
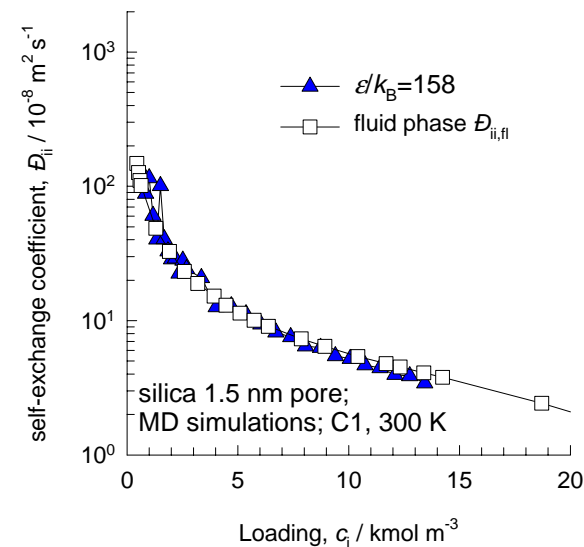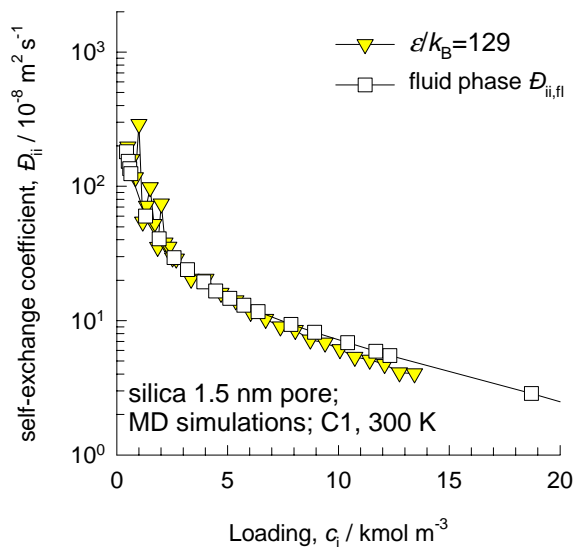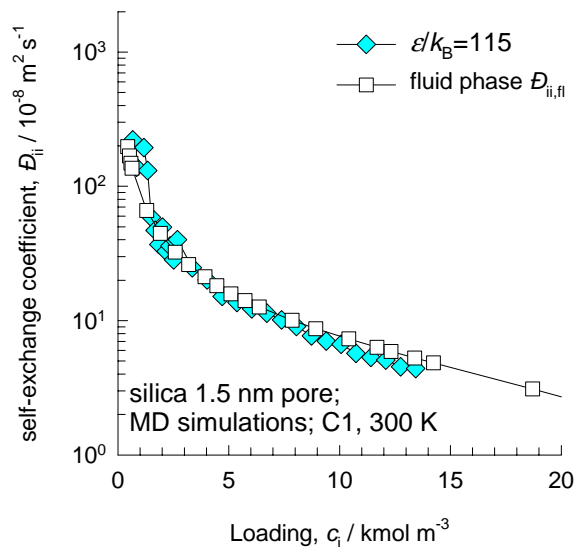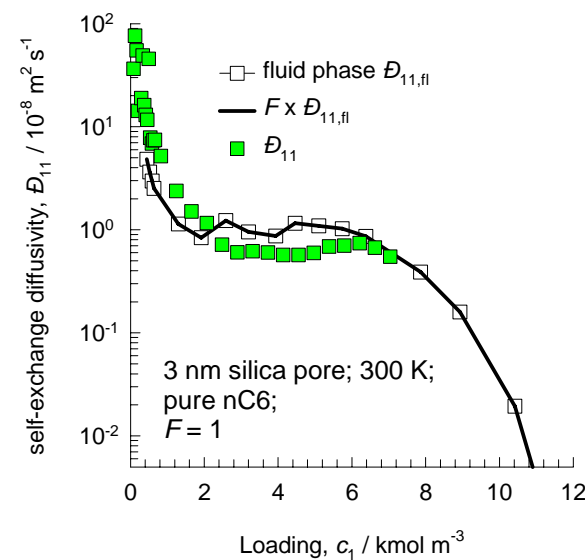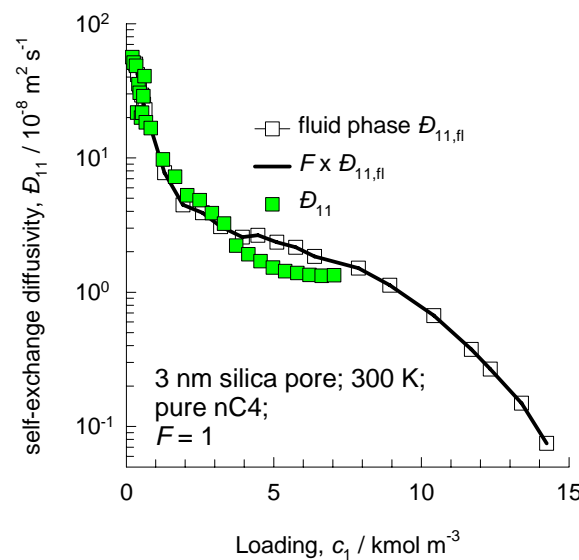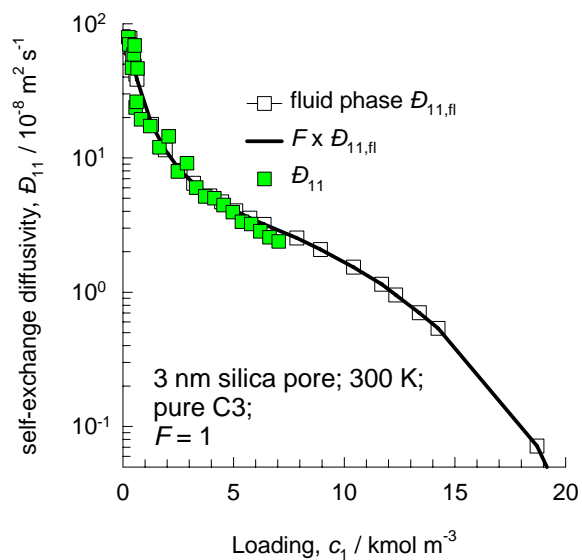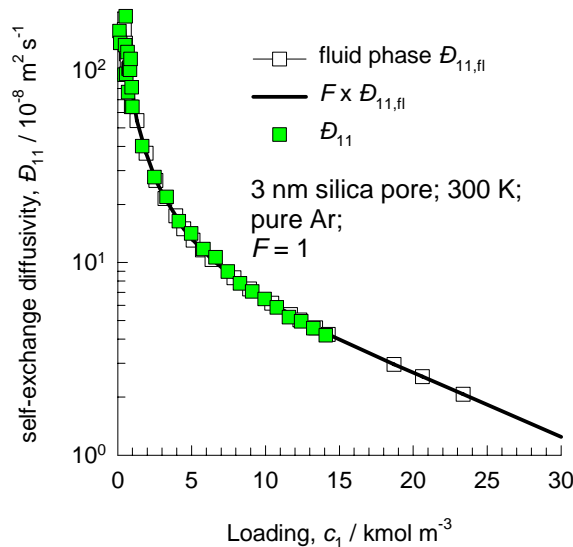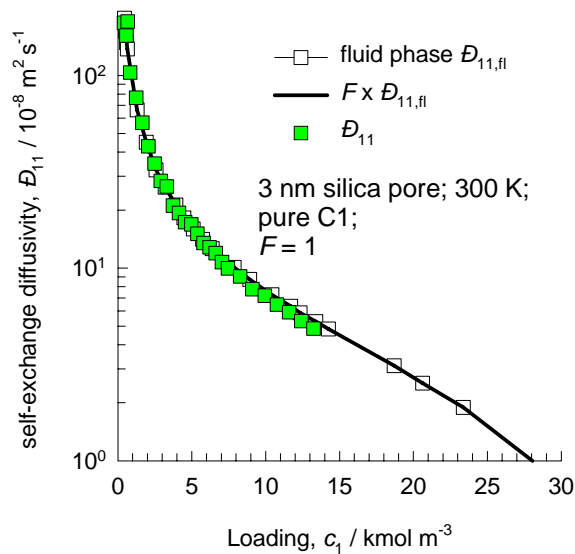
**2 nm pore**

Figure 124
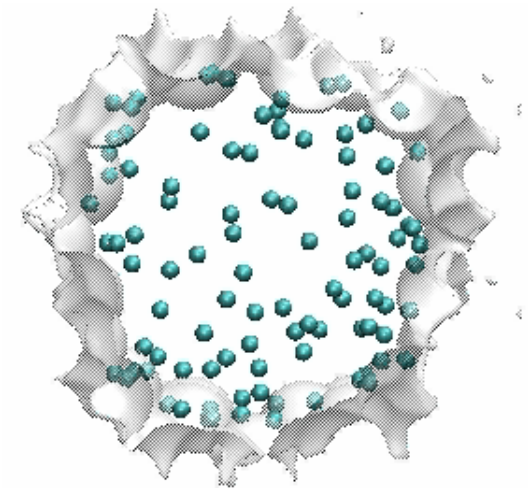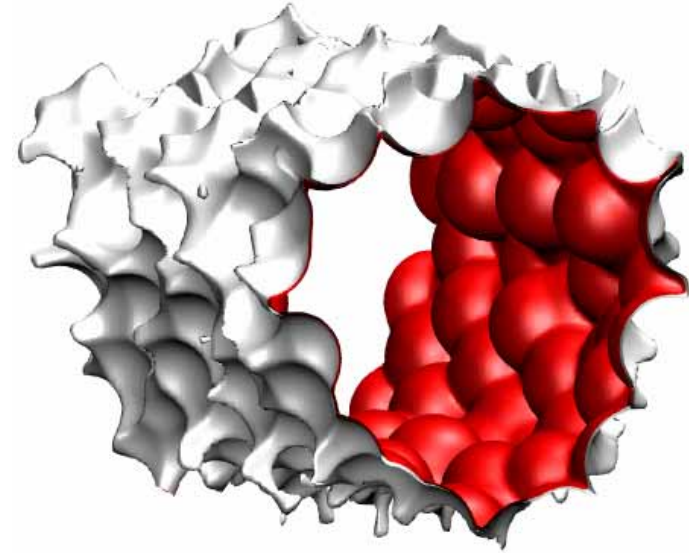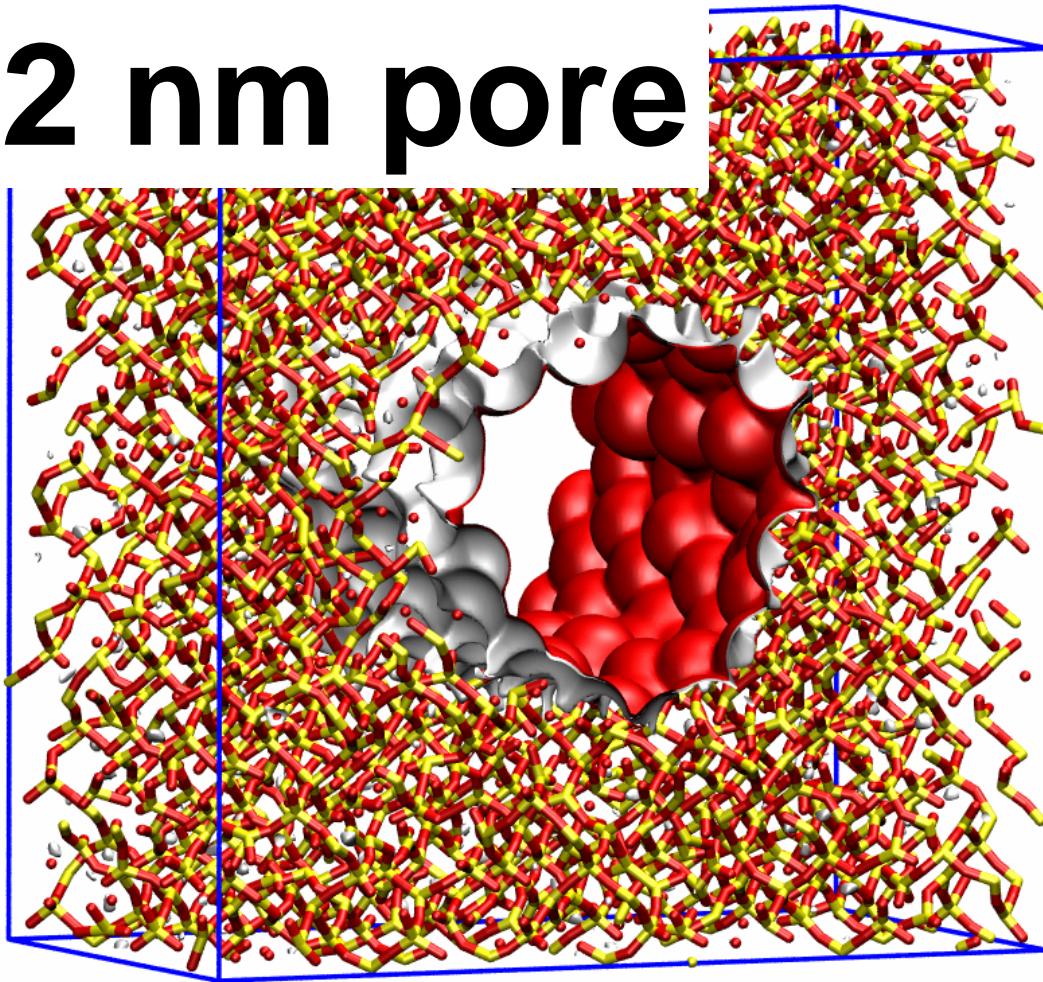
# 2 nm pore, 300 K

Figure 125
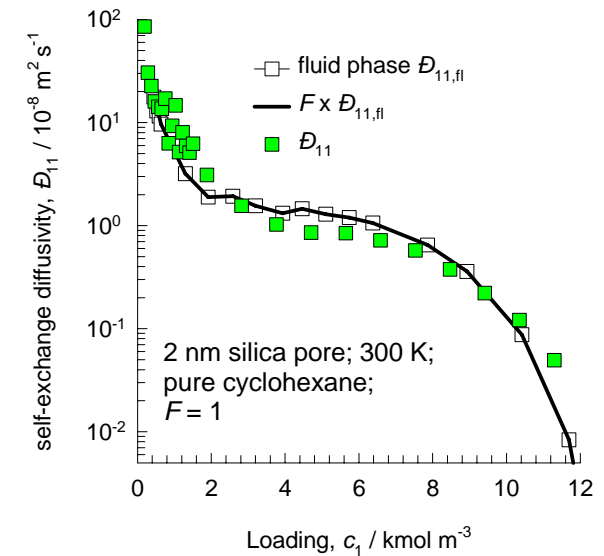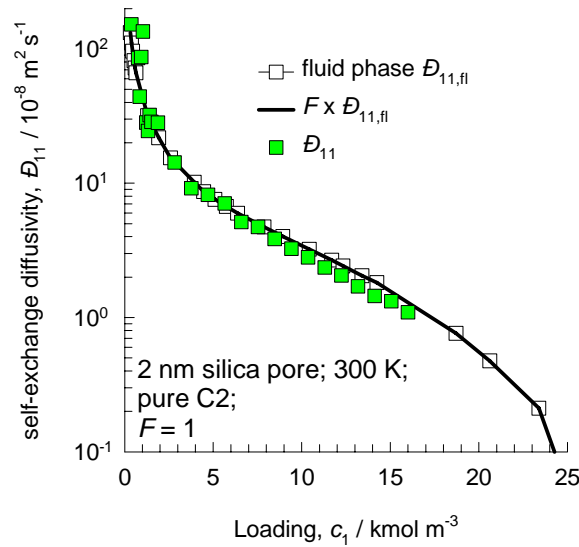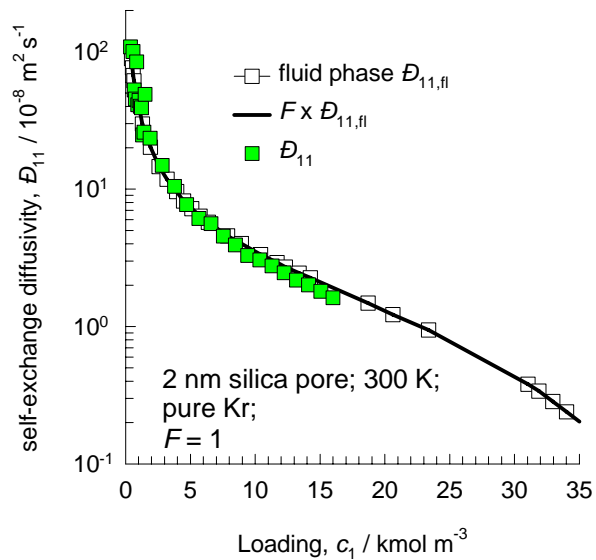


Data for unary diffusion of a variety of molecules in 2 nm silica pore
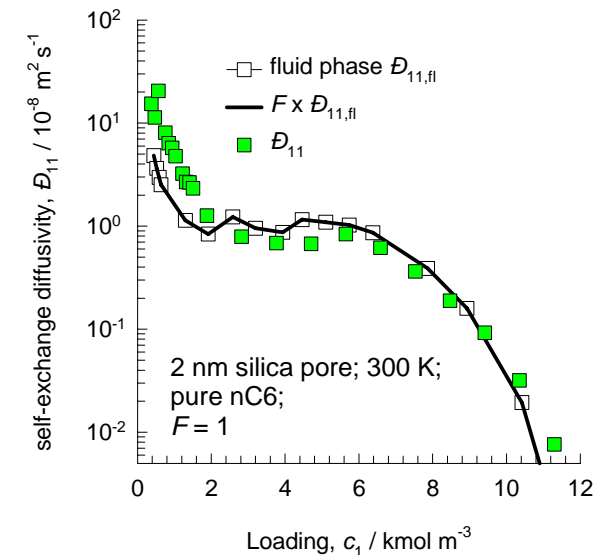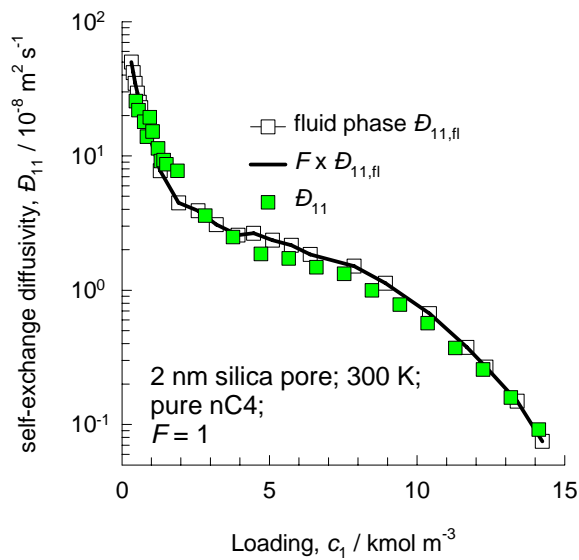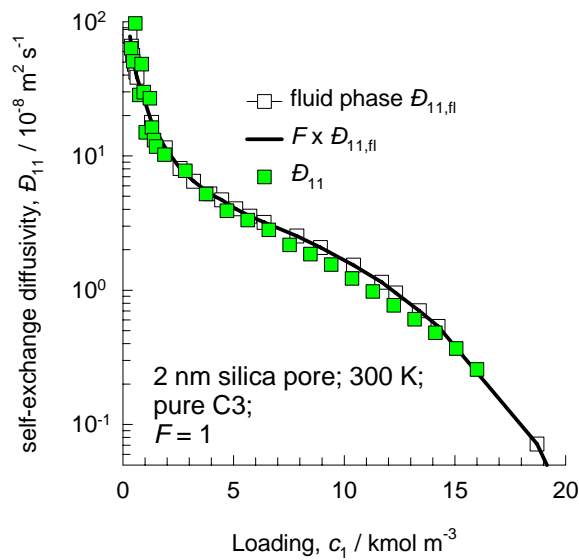
# Unary diffusion data for 2 nm pore, 300 K

Figure 126
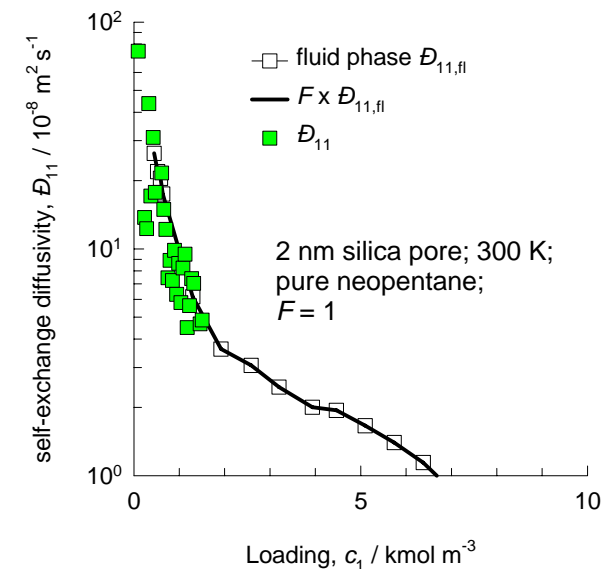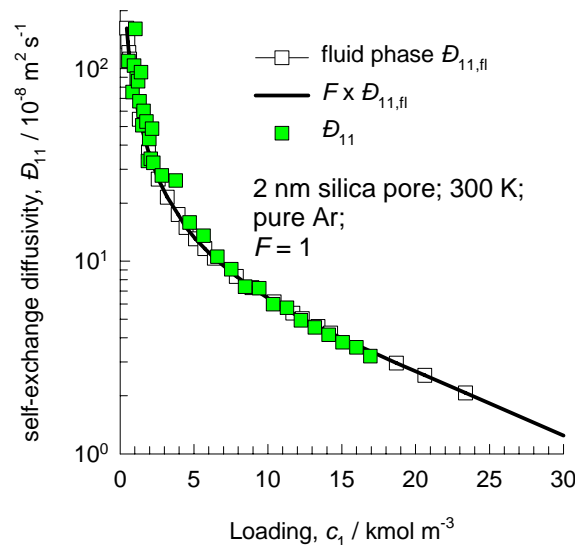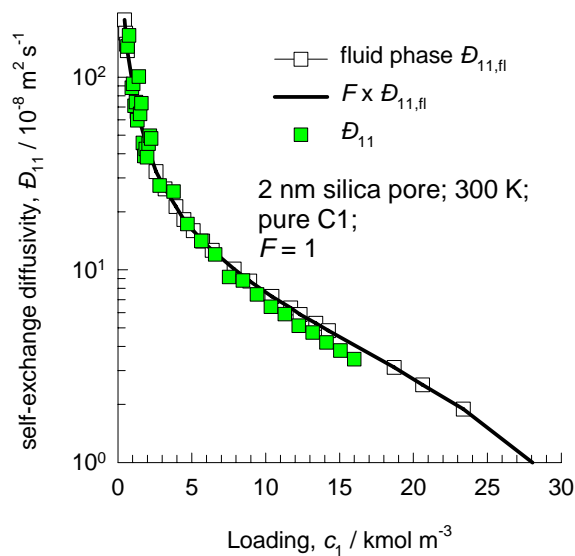


Test of Darken and Vignes interpolation formulae for binary mixture in 2 nm pore
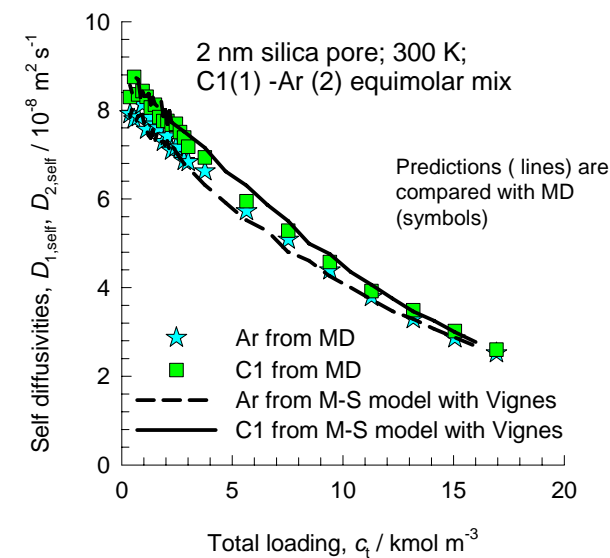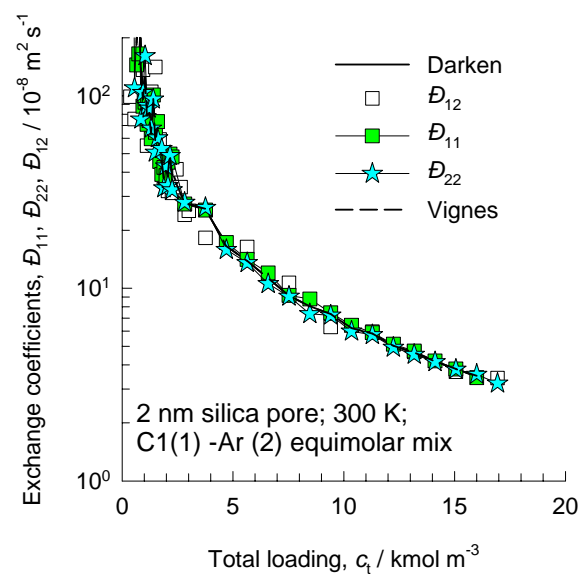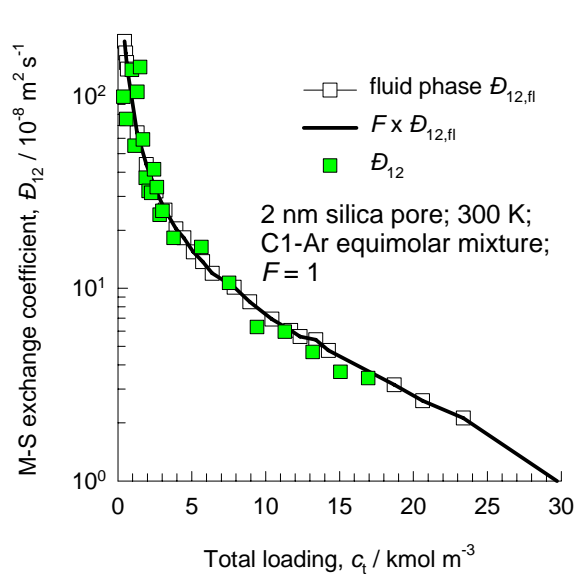
Here are the results of the sensitivity analysis using the parameters in Table 10 of supplementary material.

These are L-J parameters for energy of interaction between C1 atoms and O atoms of silica surface
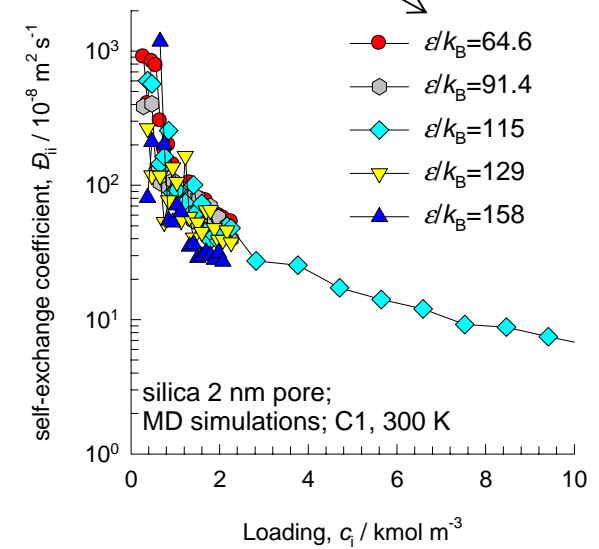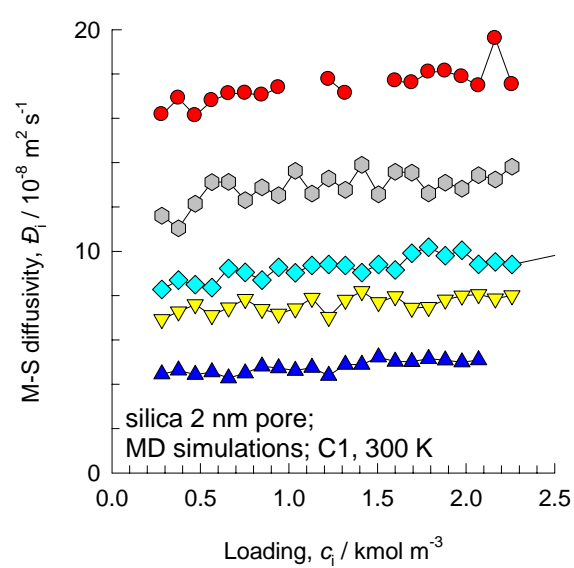
Figure 128

# 2 nm pore, 300 K, sensitivity analysis
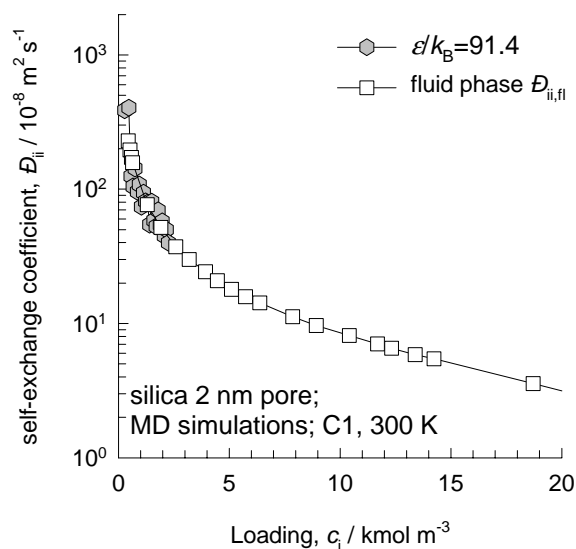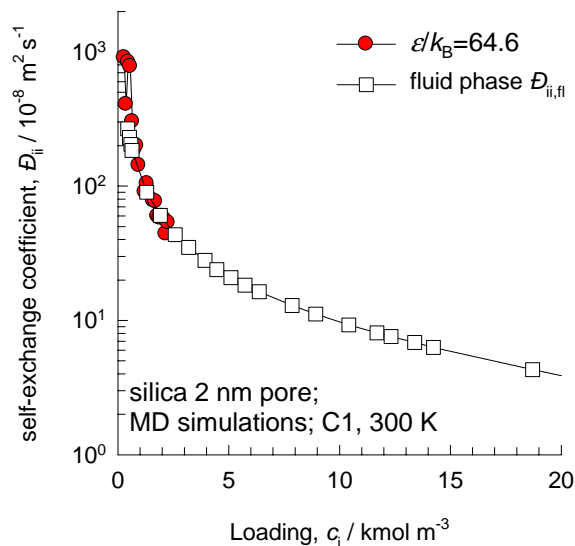


In each case the self-exchange coefficient in the pore is compared with the corresponding fluid phase diffusivity using the force field parameters in Table 10 of supplementary material. These results show that the factor $F_i = 1$, irrespective of the Lennard-Jones energy parameter.

# 2 nm pore, data at varying temperatures

Figure 129



2 nm silicapore; MD simulations

C1, 2 nm pore
Ar, 2 nm pore



silica nanopore; vary $T$; MD simulations

C1, 2 nm pore
Ar, 2 nm pore

parity

L-J parameter for energy of interaction between C1 atoms and O atoms of silica surface

The ratio of the zero-loading M-S diffusivity inside the 2 nm pore to that of the Knudsen diffusivity is plotted against $\varepsilon/k_BT$. These results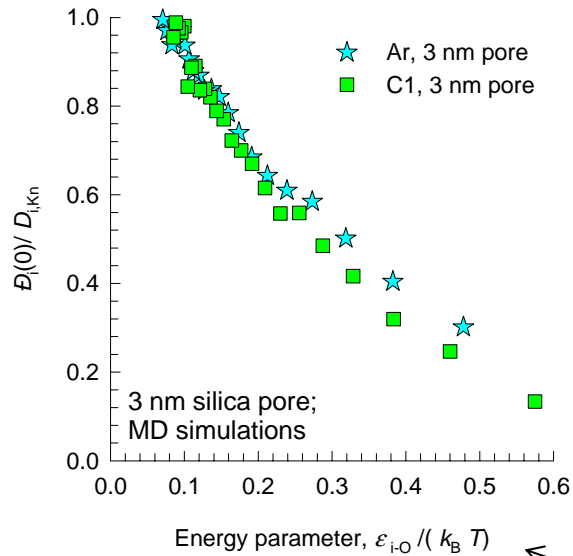 again show that the stronger the adsorption strength, quantified by $\varepsilon/k_BT$, the larger is the deviation from the classical Knudsen diffusivity formula.



2 nm silicapore; vary $T$; MD simulations

$Đ_i(0)$, C1
$Đ_i(0)$, Ar
$D_{i,Kn}$, Ar
$D_{i,Kn}$, C1
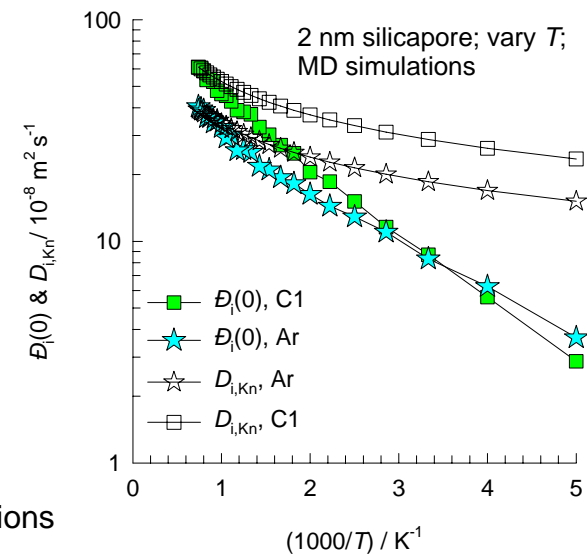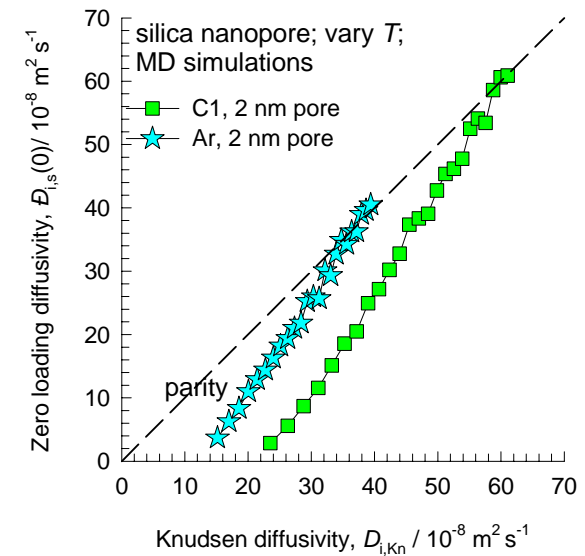
Arrhenius plots
Comparison of Knudsen formula with MD simulations

# 3 nm pore



Figure 130
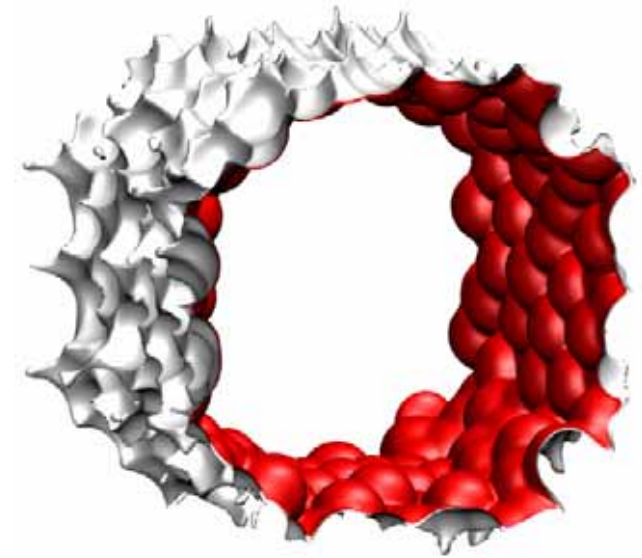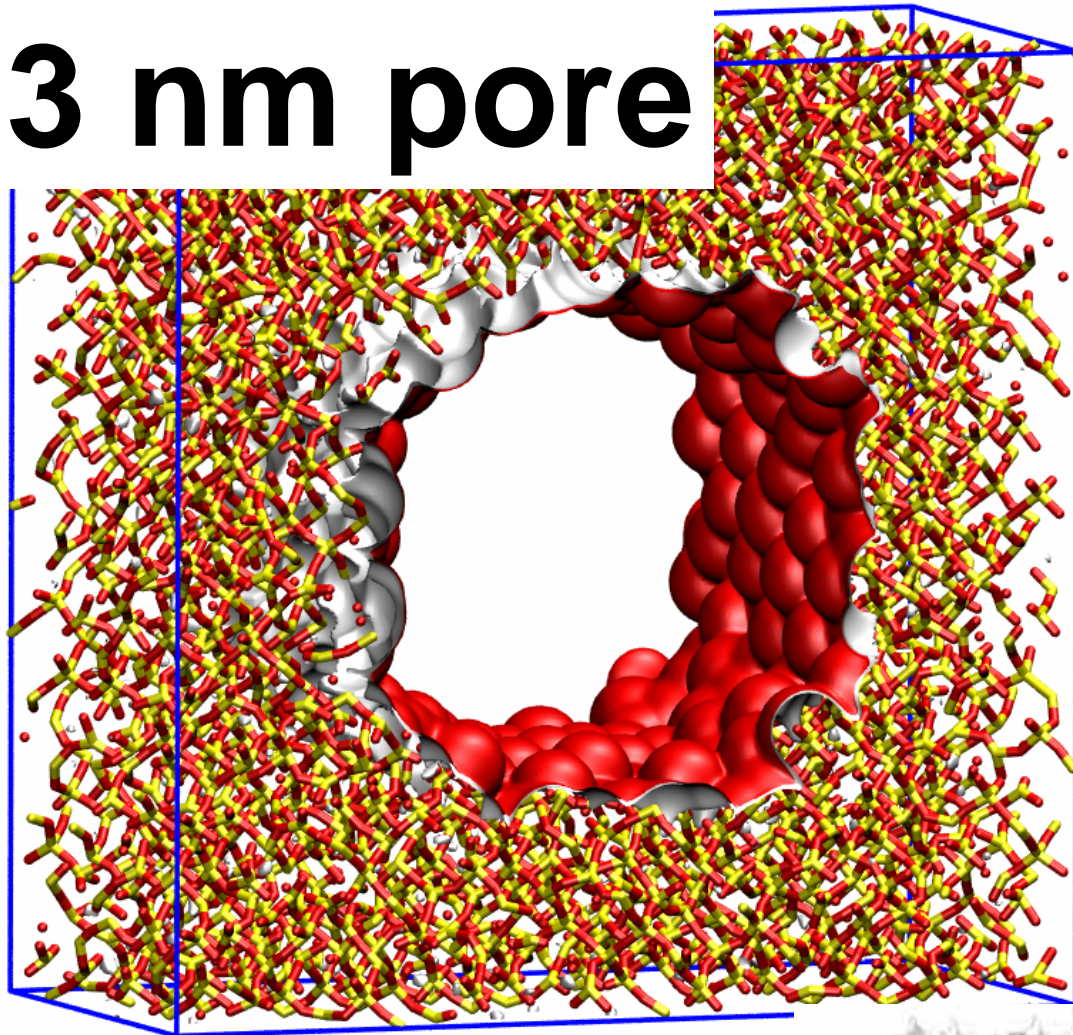


The radial distribution of concentrations for C1 and Ar in 3 nm pore.



3 nm silica pore; 300 K; average loading = 6.62 kmol m$^{-3}$
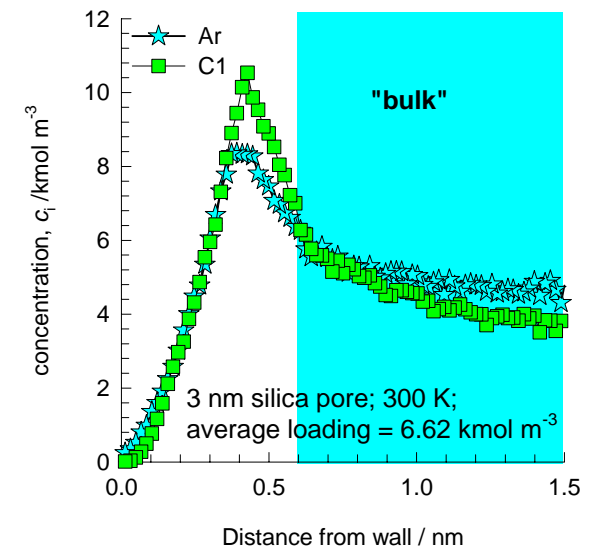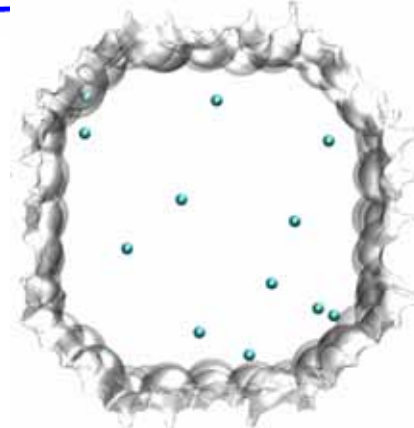
Figure 131
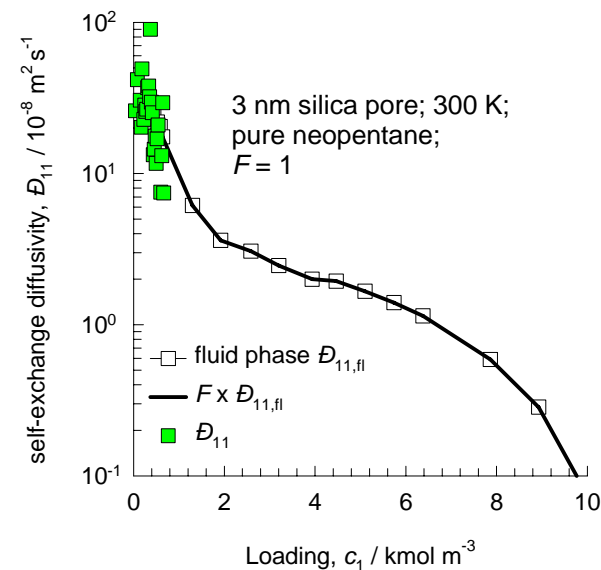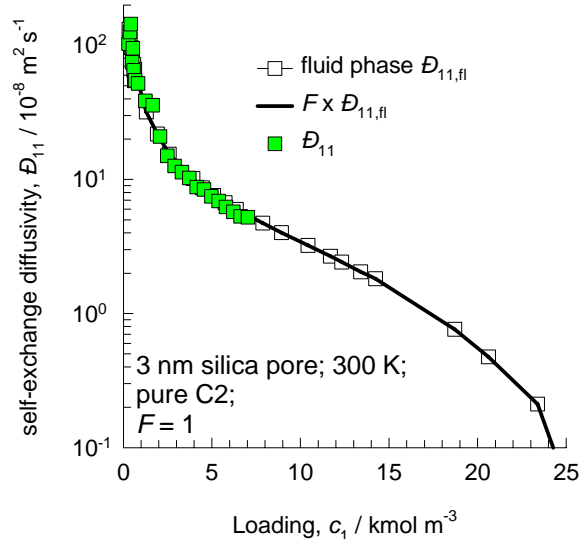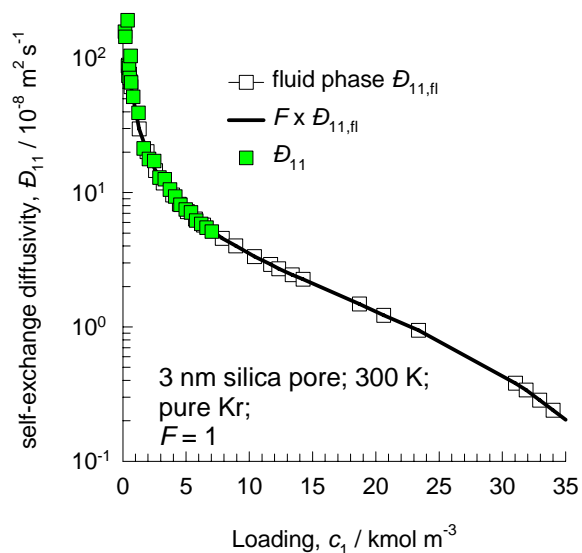
# 3 nm pore, 300 K



Data for unary diffusion of a variety of molecules in 3 nm silica pore

# Unary diffusion data for 3 nm pore, 300 K

Figure 132



Self- diffusivities of binary mixture in 3 nm pore

Unary diffusion data

$$\frac{1}{D_{1,self}} = \frac{1}{Ð_1} + \frac{x_1}{Ð_{11}} + \frac{x_2}{Ð_{12}}$$

$$\frac{1}{D_{2,self}} = \frac{1}{Ð_2} + \frac{x_2}{Ð_{22}} + \frac{x_1}{Ð_{12}}$$

Vignes interpolation

Predictions ( lines) are compared with MD (symbols)

Test of Darken and Vignes interpolation formulae for binary mixture in 3 nm pore

Figure 133

# 3 nm pore, 300 K, sensitivity analysis

Here are the results of the sensitivity analysis using the parameters in Table 11 of supplementary material.

These are L-J parameters for energy of interaction between C1 atoms and O atoms of silica surface

Figure 134

# 3 nm pore, 300 K, sensitivity analysis

In each case the self-exchange coefficient in the pore is compared with the corresponding fluid phase diffusivity using the force field parameters in Table 11 of supplementary material. These results show that the factor $F_i = 1$, irrespective of the Lennard-Jones energy parameter.

# 3 nm pore, data at varying temperatures

Figure 135



L-J parameter for energy of interaction between C1 atoms and O atoms of silica surface

The ratio of the zero-loading M-S diffusivity inside the 3 nm pore to that of the Knudsen diffusivity is plotted against $\varepsilon/k_B T$. These results again show that the stronger the adsorption strength, quantified by $\varepsilon/k_B T$, the larger is the deviation from the classical Knudsen diffusivity formula.
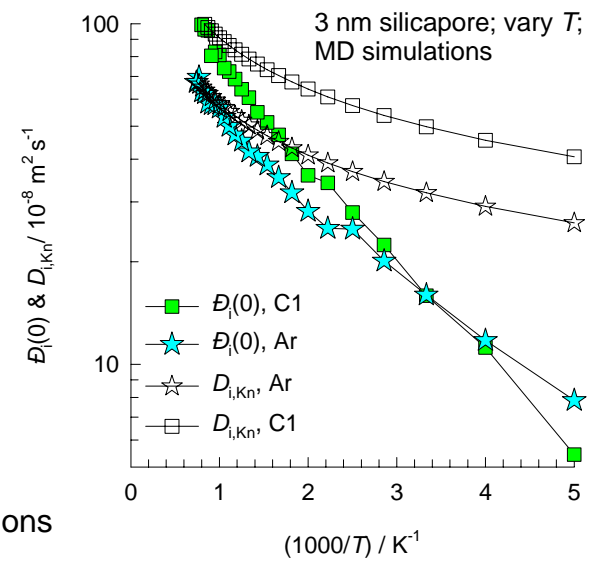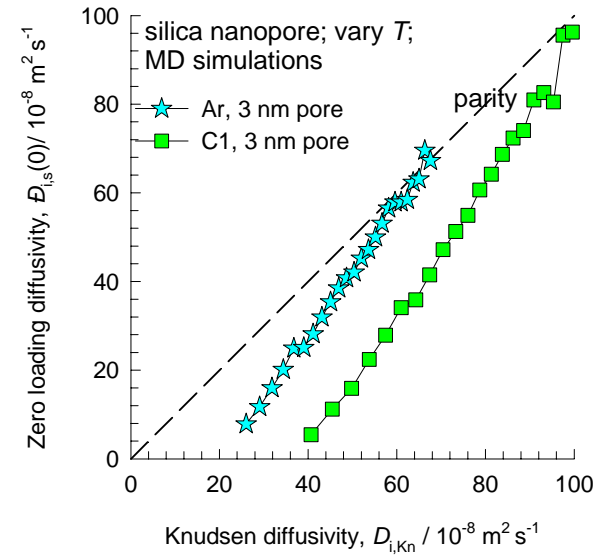
Arrhenius plots
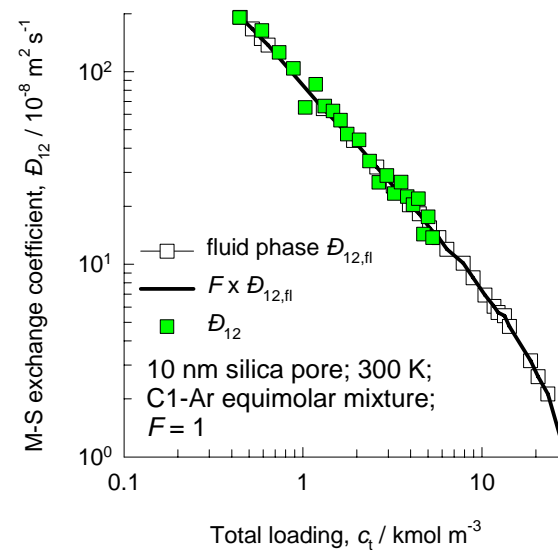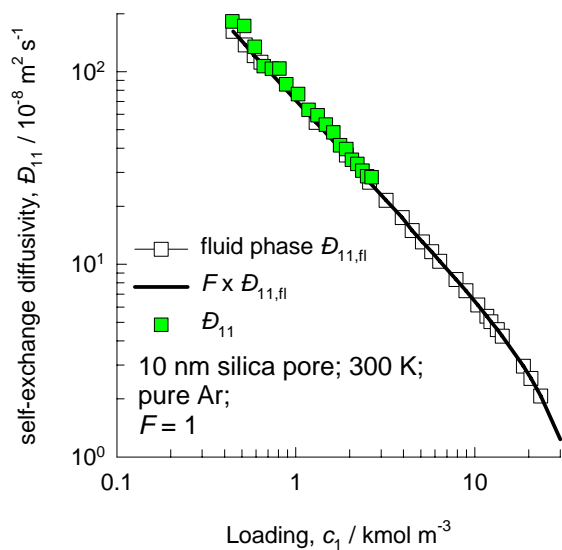Comparison of Knudsen formula with MD simulations
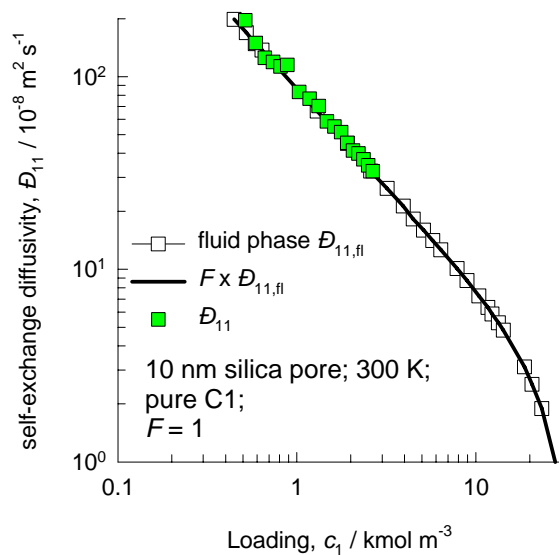
**4 nm pore, 300 K**

**5.8 nm pore, 300 K**

Figure 136
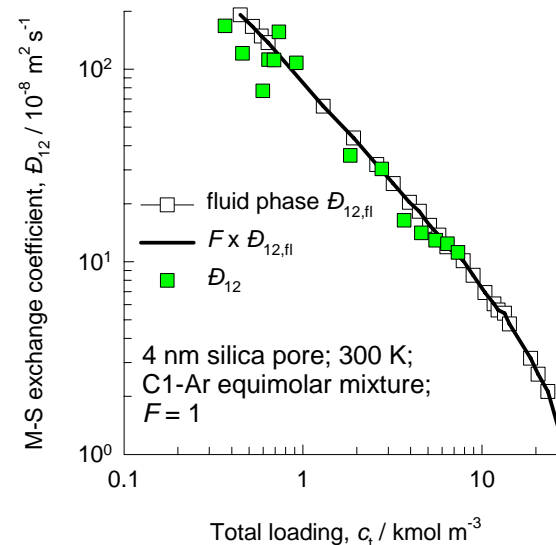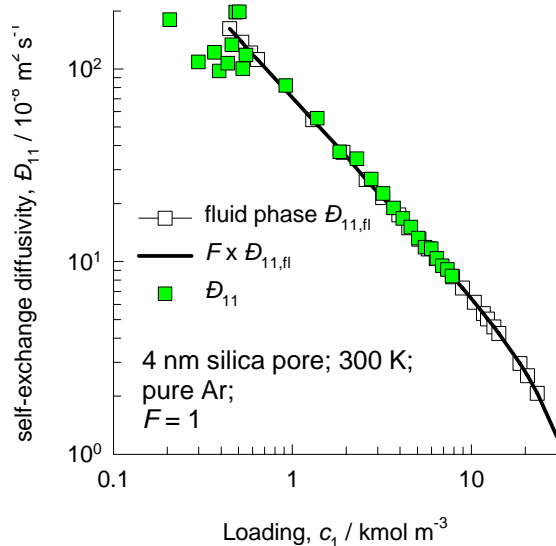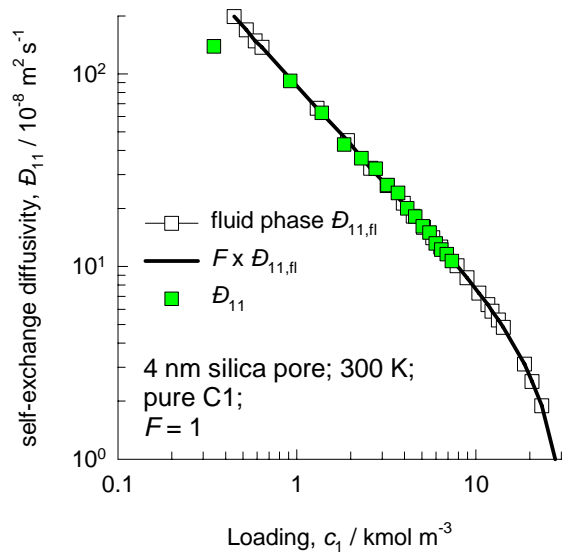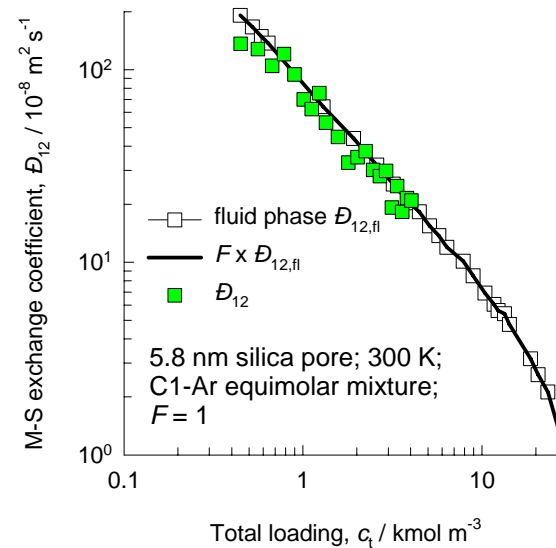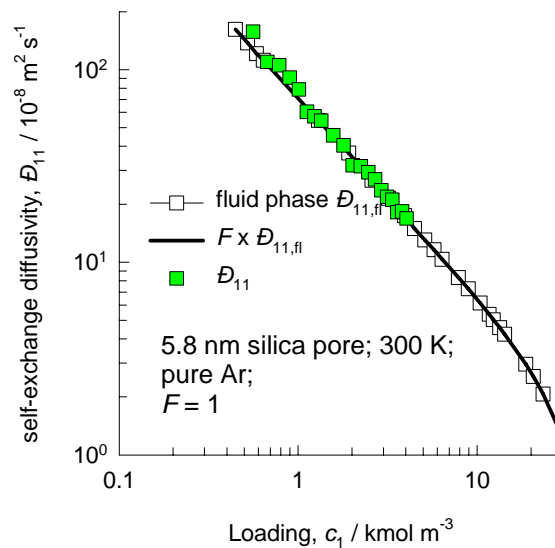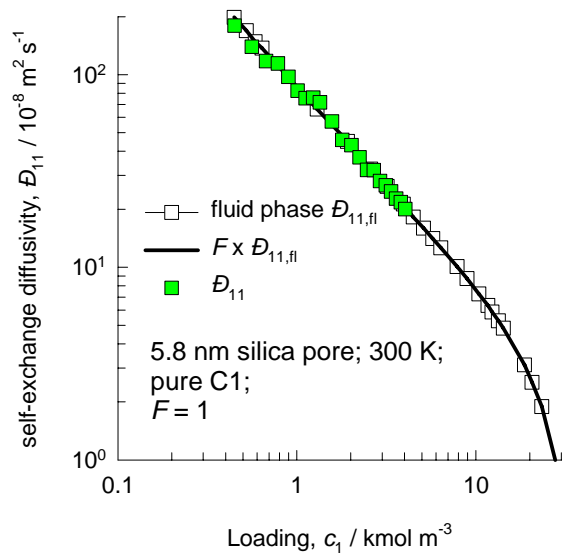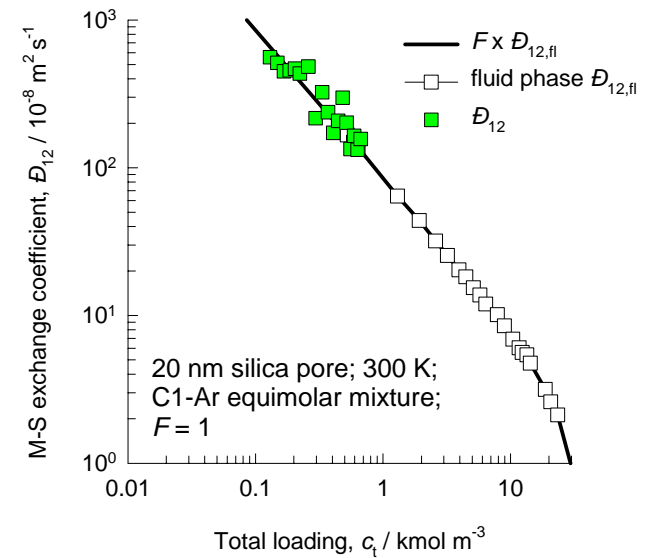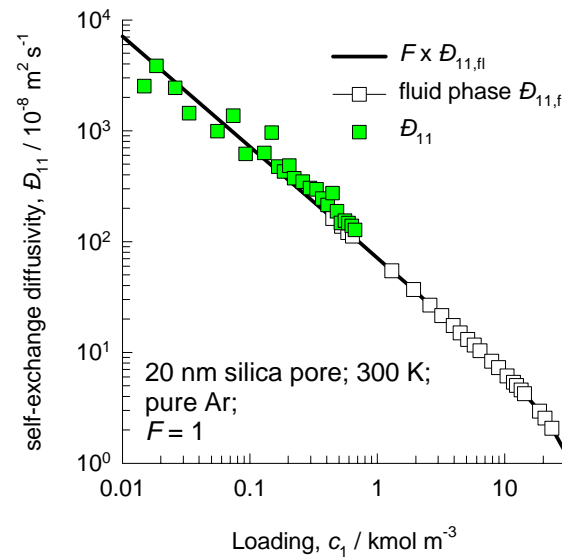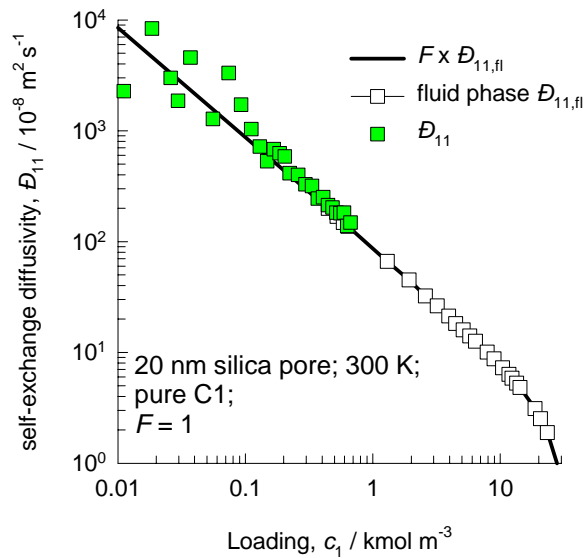
# 7.6 nm pore, 300 K

## Figure 137
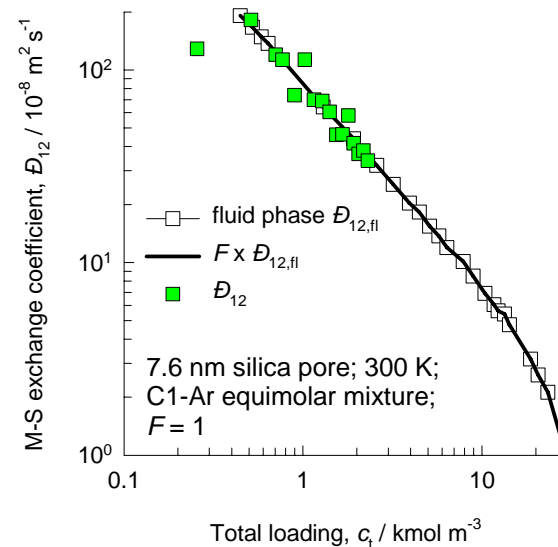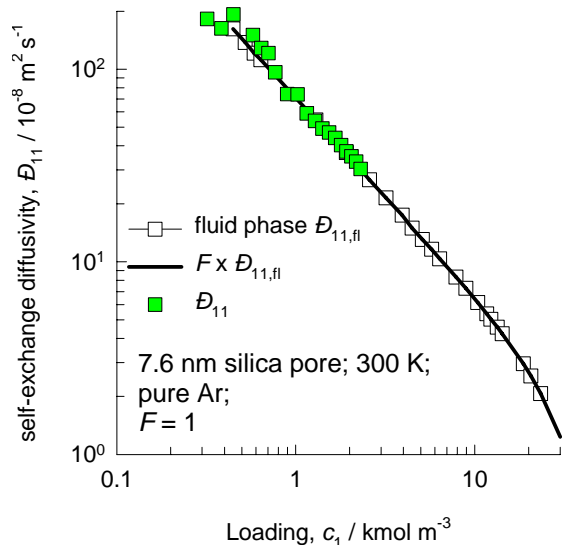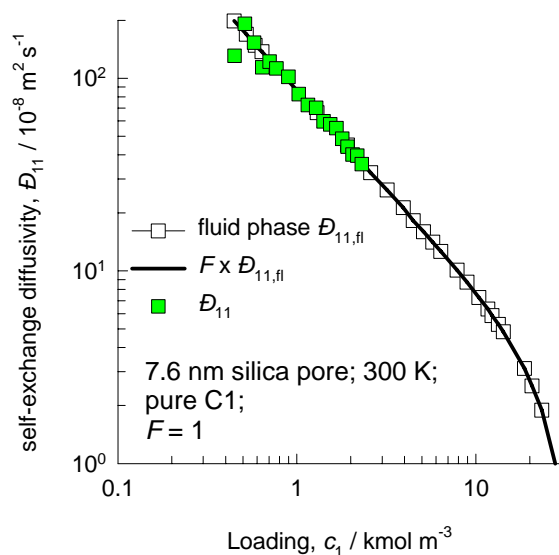
10 nm pore, 300 K

# 20 nm pore, 300 K

Figure 138



# 30 nm pore, 300 K